1990

Impact on Ceramic Faced Armour

TR diss
1994

Impact on Ceramic Faced Armour

BIBLIOTHEEK TECHNISCHE UNIVERSITEIT
Prometheusplein 1
2628 ZC
DELFT

Proefschrift

ter verkrijging van de graad van doctor
aan de Technische Universiteit Delft,
op gezag van de Rector Magnificus,
Prof. drs. P.A. Schenck,
in het openbaar te verdedigen
ten overstaan van
een commissie aangewezen door
het College van Dekanen
op donderdag 28 november 1991 te 14:00 uur

door

Paulus Cornelis den Reijer,

geboren te 's-Gravenhage,
vliegtuigbouwkundig ingenieur.

Dit proefschrift is goedgekeurd door de promotor:
Prof. dr. J. Arbocz

aan mijn ouders:
Philo & Cor

"I have little patience with scientists who take a board of wood,
look for its thinnest part,
and drill a great number of holes where drilling is easy."

Albert Einstein
quoted by Philipp Frank in "Einstein's Philosophy of Science",
Reviews of Modern Physics, Vol.21, No.3, 1949.

CONTENTS

PRINCIPAL SYMBOLS

A	cross-section
$A^{\star}$	radial cross-section (see figure 2.6)
A_0	initial projectile cross-section
c	plastic wave velocity
D_p	projectile diameter
f	uniformly distributed load on back-up plate per unit area
$\vec{T}$	vector function
F	impact load per unit of undeformed projectile area
h_b	back-up plate thickness
h_c	ceramic facing thickness
I	momentum
K_c	ceramic's bulk modulus
l	length
l'	deformed length
L	length of projectile
L_{ela}	length of projectile elastic remainder
L_{ero}	length of projectile after erosion phase
m_c	mass of comminuted ceramic in front of the projectile
M_{eject}	mass of ejected comminuted ceramic
M_p	projectile mass after erosion
M_{plas}	fully plastic bending moment per unit length
M_R	plastic bending moment per unit length
M_{r_h}	plastic bending moment per unit length
M_θ	plastic hoop moment per unit length
$\hat{M}_\theta$	averaged plastic hoop moment per unit length
N	membrane force per unit length
N'	membrane force per unit length
N_{plas}	fully plastic membrane force per unit length
P	additional resistance to penetration due to ceramic bulking
Q	shear force per unit length
Q'	shear force per unit length
Q_{plas}	fully plastic shear force per unit area
Q_{ps}	reduced plastic shear force per unit length
r	radial position from symmetry axis
r_h	radial position of moving back-up plate plastic hinge
r_{hole}	ejection hole radius
R	radial position of fixed back-up plate plastic hinge

R_{rigid}	radial position of moving plastic hinge at moment of model initiation
t	time
$t_{breakup}$	ceramic facing breakup time
u_{cela}	ceramic's elastic wave velocity
u_{pela}	projectile material's elastic wave velocity
u_{plas}	projectile material's plastic wave velocity
v	projectile velocity (rear end)
v'	velocity
v^*	radial velocity
v_0	initial projectile velocity
v_{50}	ballistic limit velocity
v_{eject}	velocity of ejected comminuted ceramic
V_{plas}	additional volume created by plastic deformation
V_{proj}	volume occupied by projectile
V_w	additional volume created by outer annular plate section deformation
V_{w_0}	additional volume created by central plate section deformation
Vol	available volume for comminuted ceramic
Vol_0	volume occupied by comminuted ceramic in pressureless situation
$Vol_{0_{ini}}$	Vol_0 at $t = t_{breakup}$
Vol_{eject}	volume of ejected comminuted ceramic
Vol_{ini}	ceramic conoid volume at $t = t_{breakup}$
w	outer annular section back-up plate deformation
w_0	central back-up plate deformation
w_0'	back-up plate deformation at inner periphery of the outer annular plate section ($r = r_h$)
w_{pi}	back-up plate deformation at moment of plug initiation
x	projectile/ceramic interface position
x'	projectile/plug position
$\dot{x}_{ini}$	initial projectile/ceramic interface velocity (at $t = t_{breakup}$)
x_{pi}	projectile position at moment of plug initiation
$\vec{Y}$	vector function
α	ceramic conoid (half) angle
β	parameter in force function
γ	shear strain or parameter in force function
ε_r	radial strain
θ	angle

μ_b	back-up plate's areal density
μ_c	ceramic layer's areal density
ρ_b	back-up plate's density
ρ_c	ceramic's density
ρ_c'	strongly comminuted ceramic's density
ρ_p	projectile's density
σ	dynamic stress
σ'	dynamic stress
σ_y	dynamic yield stress of projectile or yield stress of back-up plate material
$(\dot{})$	$d( )/dt$
$(\ddot{})$	$d^2( )/dt^2$

1. INTRODUCTION

Many objects, such as the case-wall of a centrifugal separator, an aircraft turbine or a spacecraft, are always in danger of being damaged by high-speed impacts and need to be protected. The protective material's weight has to be minimal, especially for aerospace applications. Much effort has therefore been made to clarify the behaviour of the materials involved, in attempts to increase safety and decrease the accompanying weight penalty. Fortunately, the development of such protective materials can benefit significantly from the experience and knowledge gained from the evolution of armour materials over the centuries.

Ancient man had various skins and furs available for protection against the environment and antagonists. The Sumerians favoured the use of leather capes and leather helmets in very ancient times (2800 B.C.). The Assyrians (1100-600 B.C.) are generally considered the most advanced of the ancients in the scope and sophistication of their armour. They used felt, wool, leather, wood, iron and bronze.
As the weapon designers were constantly improving the terminal effects of their projectiles, the armours were becoming thicker and heavier. During World War I, the first modern tank appeared. It was armoured with flat rolled steel plates. The increased weight of the armour reduced the mobility of its user. Hence, armour materials research was stimulated to find solutions for the major problems associated with armours: penetrability, weight and expense.

In 1918 for example, hard enamel on a metal was found to improve the resulting bullet resistance (Laible, 1980). High helicopter losses during the Vietnam war especially intensified the research and development on lightweight armour materials in the United States of America. Armour materials were required giving the same ballistic protection as afforded by standard homogeneous steel armour, but at half the weight (Abbot, 1968; Alesi & Barron, 1968; Rolston *et al.*, 1968; Taussig, 1970). In the search for these improved armours, ceramic materials were considered.
In the broadest sense, the term ceramics encompasses all inorganic materials, except metals and metal alloys, and can range from a dense polycrystalline substance to a vitreous glass. Many ceramic materials are stiff, brittle, very hard and stronger in compression than in tension. These properties make ceramic materials suitable for armour applications. Unfortunately, when projectiles are fired onto single ceramic tiles, they are only able to provide a limited amount of protection. Their brittle behaviour and poor tensile strength cause failure and prevent them from absorbing any significant amount of energy. By supporting the ceramic facing with a ductile back-up plate however, the performance of the armour is dramatically increased. The performance of a specific armour concept is characterized by the panel's ballistic limit velocity (v_{50}). This velocity is an approximation of the projectile velocity at which 50% of the impacts would result in complete penetrations and 50% in partial penetrations. For example, a single 11.4 mm thick tile of AD-85 alumina has a ballistic limit velocity of only 390 m/s. The ballistic limit velocity of an armour faced with 6.35 mm AD-85 alumina supported by 6.35 mm aluminum, which has the

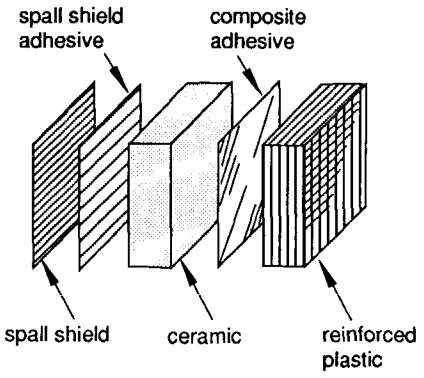

Figure 1.1 Ceramic composite armour (expanded view).

same areal density, is 650 m/s when impacted by an identical projectile (Mayseless *et al.*, 1987).
The function of the ceramic facing in armours like this is to destroy the tip of the projectile, to spread the load over a large area of back-up plate and to decelerate the projectile. The role of the back-plate is to support the ceramic and to bring the projectile and ceramic debris to rest. Using this principle, the Goodyear Aerospace Corporation developed a ceramic composite armour in 1963 which matched the performance of standard homogeneous steel but at half the weight. This armour, presented in figure 1.1, consisted of a ceramic facing backed by glass-reinforced plastic and could defeat a 7.62 mm armour piercing (AP) projectile.

Many companies and research institutes were motivated to develop other ceramic faced armours with even better performance. The works of Wilkins *et al.* (1967-1978), Florence & Ahrens (1967), Florence (1969), and Bodine *et al.* (1969) covering both experimental and theoretical studies on the relative effectiveness of various ceramics against armour piercing projectiles, resulted in a fair understanding of the penetration mechanisms dominating the impact event.

Experiments with lightweight armour systems are essential to improve the understanding of the penetration mechanisms. Unfortunately, the complexity and brevity of the impact process in ceramic faced armours, the event is completed within 0.0001 s (for a 7.62 mm AP projectile impacting at 840 m/s), make instrumentation very difficult. Soon after impact, fine ceramic and projectile debris are ejected from the impacted area and obscure the view for optical high-speed cameras. Only the back-up plate motion can be observed easily optically before perforation. Aside from debris problems, it is impossible to obtain information regarding the actual projectile penetration into the ceramic faced armour using an optical technique. As a result, most experimental data available in literature on impact onto ceramic faced armours is limited to ballistic limit velocity determinations. Detailed data regarding the projectile and armour behaviour throughout the impact event are very scarce.

The experimental work by Wilkins and his colleages in the seventies is the most comprehensive in the field. In addition to ballistic limit velocity experiments, they conducted flash X-ray experiments with ceramic faced armours to obtain detailed information on the penetration process. They carried out their experiments with 2-inch wide strips of ceramic faced armour. By setting up their flash X-ray system in plane with the armour's front surface (normal to the projectile's line of flight), the resulting shadowgraphs presented information regarding projectile rear-end position, projectile armour penetration and armour deformation and projectile erosion. Strips wider than 2 inches could not be used because of the limited penetrating power of the X-ray system. To the author's knowledge, the work published by Wilkins *et al.* in literature with respect to the information presented on the projectile and armour behaviour is unique to this date.
Unfortunately, some of the data presented by Wilkins contradict other data presented by him (Wilkins, 1988; Den Reijer, 1989). In addition, recent experiments at TNO's Prins Maurits Laboratory have shown that the reduction of the lateral dimensions of the ceramic armours, as done by Wilkins to allow X-ray penetration, can influence the performance of an armour panel in a negative way. As a result, there is doubt as to whether the flash radiographs presented by Wilkins can be considered as fully representative for the performance of full-size panels.

The recent availability of ceramics and back-up plate materials with outstanding performances at acceptable prices has lead to a renewed interest in lightweight protective materials over the past five years. An example of this new interest was the National Technology Project "Ballistisch Arall" carried out by a consortium of Dutch companies, led by AKZO. The project was sponsored by the Dutch Ministry of Defence, and started in 1987. The goal of this project was to develop a family of ceramic faced armours using arall for the back-up plate. Arall, aramid aluminium laminate, is a Delft University of Technology invention. The multiple layers of metal and fibre-reinforced composites in it, allow the back-up plate to be optimized for the special impact loading. Even though many projectiles were considered in this project, most emphasis was placed on defeating the 7.62 mm armour piercing (AP) projectile.

In the past, the design of such ceramic armour systems was based predominantly on experimental ballistic performance data. However, the large number of parameters influencing such an armour's performance render the sole use of traditional experimental ballistic performance data inefficient. The most fruitful results can be expected when the experiments are supplemented by an analytical approach, which includes the dynamic mechanisms accounting for the behaviour of these armours. The advantage of an analytical approach, over the use of empirical models, scaling procedures and hydrocode computations, is easily advocated. Empirical models need to be supported by a huge amount of experimental data in order to be able to accurately predict ballistic limit velocities of specific armour and projectile configurations. More detailed information than the v_{50} cannot easily be supplied by such models. By using geometric scaling, empirical models become more versatile, although such procedures do not allow the projectile geometry, armour geometry,

armour composition or impact velocity to be varied independently. Hydrocode simulations, on the other hand, have the potential of providing the most detailed information on the progress of a penetration process (Anderson, 1987). An enormous effort to develop brittle material response models for use within hydrocodes, is being pursued at many laboratories (Mescall & Tracy, 1986; Van der Graaf, 1988; Johnson & Holmquist, 1990). The tuning of the code predictions with experimental data is still necessary at the moment. Unfortunately, the long CPU execution times make the use of hydrocodes for parameter studies and ballistic limit velocity computations impractical to engineers in the development process of these protective materials. An analytic model requires only a limited amount of experimental data, yet is able to present the user with details of the penetration process in addition to the prediction of the ballistic limit velocity. The use of an analytic model allows a user to conduct parameter studies by varying projectile and armour composition, geometry and materials completely independently, without the immediate necessity to support this by experimental data.

Hence, the "Ballistisch Arall" project aimed at a theoretical and experimental approach to achieve its goal. Its theoretical approach included the development of an analytic penetration model for ceramic faced armours. This model was intended to increase the "feeling" for the important parameters in the impact process. As such, it was expected to be able to examine the effect on the ballistic limit velocity of (limited) variations of the projectile and armour geometry and properties about a reference ceramic faced armour with a (laminated) metal back-up plate. The model was also expected to present the user with details on the penetration process, such that the influence of back-up plate related properties could be assessed. In addition, the model was required to execute quickly enough on a personal computer (PC-AT) to allow it to be used as an engineering tool.

In this thesis, a combination of theoretical and experimental work on ceramic faced armours is presented. The development of the above-mentioned penetration model, ALARM (Analytic Lightweight Armour Response Model), is described. The results obtained with the model are compared with experimental data. The model's potential as an engineering tool is illustrated by examples of parameter studies.
In order to improve the understanding of the penetration process of projectiles into ceramic faced armours, experiments were conducted. They supplied information regarding projectile erosion, armour penetration and armour deformation throughout the impact event. The novel experimental technique used for these experiments, the test results and their analyses are subjects of this thesis too. The results of the experiments were also used to evaluate and to validate the proposed description of the penetration process in the analytical model.

2. MODELLING IMPACT ON CERAMIC FACED ARMOUR

2.1. Introduction

Over the years, only a few analytic penetration models for impact on ceramic faced armour were presented in literature. In 1969, Florence published a model which yielded a very simple formula for the ballistic limit velocity of a ceramic faced armour. Prior & Hetherington presented a paper in 1986 where they reviewed Florence's model and described the initial development of a model to simulate the impact of a soft-core (ball) projectile onto a ceramic-GFRP (Glass Fibre-Reinforced Plastic) composite armour. These models were not capable of fulfilling the requirements set by the "Ballistisch Arall" project. They do represent the state-of-the-art with respect to ceramic faced armour modelling at the time that the model presented in this thesis was developed.
Recently, Ravid *et al.* (1989) presented a paper in which they proposed a procedure to use their analytic model for the early stage of high-velocity impact, and their two-dimensional, five stage, analytic model for the penetration and perforation of moderate thickness viscoplastic plates by rigid projectiles, for the case of ballistic impact of ceramic armour with a metallic back-up plate. Very recently, Woodward (1990) proposed a one-dimensional model for the penetration into ceramic faced armour, using a lumped mass model. The analytic penetration model presented in this thesis was developed independently from the work by Ravid *et al.* and Woodward. A description of the model together with a comparison of model calculations with experimental data was first published by the author in 1989.

In this chapter, a phenomenological description of the penetration process of projectiles into ceramic faced armours is presented. The most characteristic mechanisms responsible for the behaviour of these armours are isolated and addressed. The important armour material properties are identified. Based on these observations, a number of general assumptions and simplifications are proposed for use within the analytic model. Subsequently, the projectile behaviour and armour response are modelled, bearing in mind that:

- the model's scope of application is limited to the family of ceramic faced armours and projectiles that satisfy the following criterion: the thickness of the ceramic facing, the thickness of the back-up plate and the diameter of the projectile have to be of the same order,
- the model is developed for ceramic faced armours with a (layered) metal back-up plate,
- the model has to present the user with details on the penetration process, such that the influence of back-up plate properties can be assessed, and
- the model is required to execute quickly on a personal computer (PC-AT) so as to allow its use as an engineering model.

The proposed resisting force model, which simulates the loading experienced by the projectile and the armour during their interaction process, is presented next. The resulting set of differential equations, describing the penetration model, are solved numerically. The numerical solution technique and the outline of the Fortran-77 ALARM program are described. The model's capabilities are illustrated by the comparison of computed and experimentally determined ballistic limit velocities, at the end of this chapter.

2.2. A phenomenological description of projectile penetration into ceramic faced armours

Following Bodine *et al.* (1969), the impact process of a projectile into a ceramic faced armour can be simplified by discussing the process on two time-scales. The first time-scale encompasses the time required for no more than a few stress wave reflections through the armour plate and thus is of the order of a few microseconds. This period of observation can be denoted as the shock-wave period. The second time-scale, encompasses the subsequent structural response period of the armour and is terminated when the armour is defeated or has arrested the projectile.

The penetration process into a ceramic faced armour during the shock-wave period will be described first. When a hard core (armour piercing) projectile impacts a ceramic faced armour at a velocity of approximately 800 m/s, shock degradation of the armour and shatter of the projectile may result. Shock degradation of an armour, by inducing extensive microfracture, results from the propagation of a high pressure wave followed by a rarefaction wave through the ceramic. Shocks above the ceramic's Hugoniot elastic limit (HEL) are known to induce damage in ceramics (Bless, 1987). The high stress wave induced in the projectile results in a radial expansion and fragmentation of the projectile tip. This phenomenon is called bullet shatter or bullet splash. The extent of the shock degradation and projectile shatter depends on the shape and intensity of the initial shock wave and resulting rarefaction waves.
In the ceramic, a fracture front starts to propagate into the material ahead of the projectile. According to Frechette & Cline (1970), the initial damage to the ceramic originates at the impact surface at a number of points situated roughly in a circle around the centre of contact with the projectile. From these points fracture spreads to form a group of shallow coaxial cylindrical cracks, some of which join to complete a shallow cylinder. The cylindrical cracks flare quickly into a conoid which tends to intersect the back-up plate. The shape of these cracks strongly resemble the Hertzian-type of conoid cracks (Evans, 1973). They propagate at a velocity substantially lower than the sonic velocity of the material. The projectile continues to erode or flatten during this fracturing process, while the actual penetration into the ceramic remains slight. This is illustrated by the results of a HEMP finite difference computer calculation in figure 2.1 (Wilkins, 1968). Fracture of the ceramic also originates at the ceramic's back-face. According to Wilkins, the fracture in the ceramic at its back-up plate interface is a result of tension in the ceramic as it follows the motion of the back-

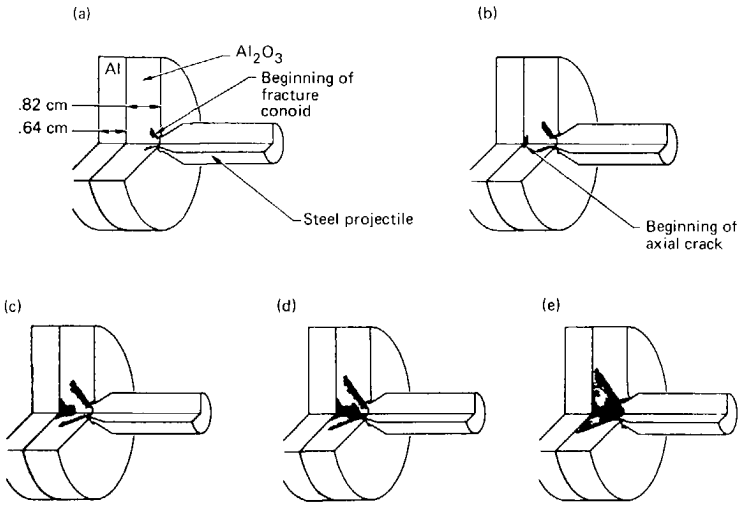

Figure 2.1 Calculation of development of fracture and axial crack in a ceramic faced lightweight armour (Wilkins, 1968).

up plate after the reflection of the shock wave. Hence, a few microseconds after impact a ceramic fracture conoid has formed in front of the impacting projectile. The angle of this fracture conoid depends on the dynamic loading conditions in the ceramic material, but is typically of the order of 65 degrees.

The structural response period of the armour follows. The projectile attempts to penetrate through the comminuted ceramic. Projectile erosion may continue to take place, depending on the resistance the projectile experiences from the armour. Fractured ceramic is pushed away and out through the impact hole. The ceramic conoid effectively distributes the concentrated impact load over a large area of back-up plate. The back-up plate deflects under the applied load, and thus creates space for the comminuted ceramic to move as well. As the projectile continues its penetration, the impact load is spread over an increasingly smaller area of the back-up plate by the deteriorating fracture conoid. The back-up plate has to be able to carry this load and dissipate the energy by plastic deformation. At some moment in time, depending on the back-up plate's properties, the plate reaches its limits of energy absorption, and failure, either by plug shearing or strain failure, may become evident. The penetration sequence presented in figure 2.2, which was calculated by Wilkins using the HEMP-code, illustrates the given description of events.

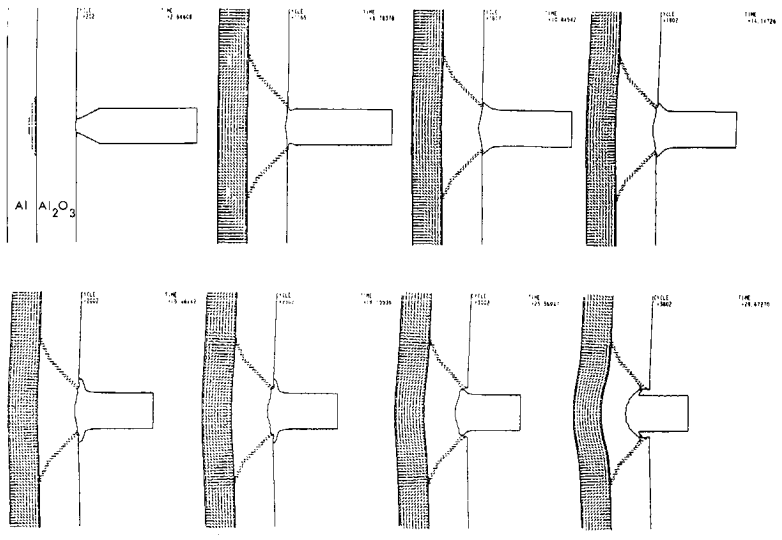

Figure 2.2 Calculated penetration of an armour consisting of 8.6 mm thick AD-85 alumina and 6.3 mm thick 6061-T6 aluminium. The steel projectile had an impact velocity of 853 m/s (Wilkins, 1968).

2.3. The important mechanisms

Projectile mass erosion is a very important mechanism by which a ceramic faced armour can defeat penetration. Wilkins has shown that much of the energy that the projectile loses in the initial stages of impact is not absorbed by the armour, but is consumed by erosion of the projectile, as is illustrated in figure 2.3. This erosion implies a physical separation of material from the projectile so that its momentum no longer contributes to armour perforation. As a consequence, the back-up plate may have to absorb only some sixty per cent of the initial kinetic energy.

Studies by Mayseless *et al.* (1987) and O'Donnell *et al.* (1990) have shown that a negligible amount of projectile kinetic energy is dissipated in the fracturing process of the ceramic facing. Nevertheless, the ceramic fracturing process remains very important. The lateral extend of the fracture conoid and the type of fractures influence the armour's performance. In addition, the time necessary to complete this fracturing process can influence the duration of the projectile mass erosion. A calculation by Wilkins *et al.* (1969) showed that a two-microsecond delay in the completion of the fracturing process, resulted in a noticeably extended projectile mass erosion, and thus a better armour performance.

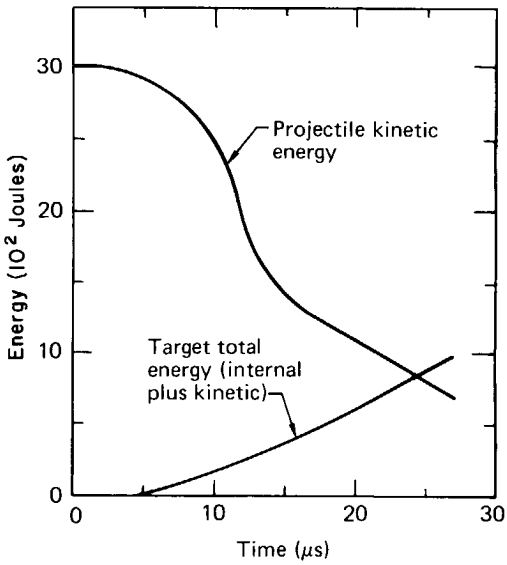

Figure 2.3 Energy-versus-time curve for a sharp steel projectile impacting an armour composed of 8.6 mm AD-85 alumina bonded to 6.3 mm thick 6061-T6 aluminium at a velocity of 853 m/s (Wilkins, 1968).

The confinement of the broken and comminuted ceramic in the ceramic conoid contributes significantly to the penetration resistance of the armour. Johnson (1972) concluded that the conoid filled with fractured ceramic is effective in defeating bullets at velocities up to around 850 m/s because of the aluminium back-up plate which possesses sufficient ductility to accommodate deflection under impact, yet restrains and holds the conoid in place so that even when the ceramic is fractured its penetration resistance is little impaired. Bless (1987) supports this by his observations that as long as the fractured alumina cannot expand, it retains much of its initial shear strength and cannot be easily penetrated. Hence, the ceramic, even when fractured, remains able to distribute the high impact load over a large section of the back-up plate.

The important role that the broken ceramic plays in penetration resistance can also be concluded from experiments carried out by Woidneck (1978), who compared the ballistic resistance of aluminium and aramid. Impacted at an equal areal density of 15 kg/m^2 by a 3 gram blunt steel cylinder, the ballistic limit velocity of the aluminium plate was 280 m/s, while the aramid plate had a ballistic limit velocity of 700 m/s. Because, at equal total armour weight, including ceramic, the performance of these armours is comparable, the ceramic layer must fulfil a more important function when backed by a metallic (less-flexible) plate. The broken ceramic is capable of fulfilling this

function because the metal back-up plate restrains the broken ceramic from moving out of the projectile's path to a much greater extent than the aramid plate does. Unfortunately, the mechanism by which the projectile penetrates through the comminuted ceramic has not become completely clear from the experimental evidence presented in literature.

The ceramic facing is usually bonded to the back-up plate. This bond may have an effect on the support given to the ceramic material by the back-up plate, and thus on the ceramic fracturing process. Wilkins (1968) investigated the role of the bond between ceramic and back-up plate. The compressibility of the bonding layer will allow tensions to occur in the ceramic depending on the thickness of the bonding layer. These tensions are caused by the poor support given to the ceramic by the bond. Therefore, a too thick bonding layer may result in a poor ballistic performance of the armour. The ballistic performance of (thinly) bonded and unbonded ground ceramics can be expected to be the same. The performance of some ceramic materials, with irregular surfaces, increases when a bonding layer is used. Wilkins concluded that in those cases the bonding layer had no structural effect on the armour. The irregular surface of the ceramic material benefitted from the bonding layer as it filled in the voids and served as a coupling medium between ceramic and back-up plate.

Because of the large amount of energy that has to be absorbed by the back-up plate, and because of the importance of confinement for the broken ceramic's penetration resistance properties, the back-up plate's behaviour is very important as well. Experimental observations indicate that for much of the motion, the backing remains bonded to the ceramic at some radius outside the base of the conoidal volume and thus confines most of the backing's kinetic energy absorption within this area. For laminated back-up plates, delamination can occur. This allows an increasing amount of backing material to be deformed. Provided that the back-up plate is not separated from the facing over the entire panel, and provided reasonably large deflections are tolerable, this is an effective energy absorption mechanism.

2.4. The important armour material properties

An enormous amount of scientific research is directed towards the correlation of mechanical properties and ballistic performance, especially for the ceramics. So far, a group of static properties, not one unique property, are identified to influence the ballistic performance of armour ceramics. The properties are: (high) hardness, (high) sonic velocities, (high) Young's modulus, (low) Poisson's ratio, (low) density, and (low) porosity (Viechnicki *et al.*,1987; Slavin *et al.*, 1988). High sonic velocities relate to the ability of the material to remove energy from the impact point. The hardness of the armour should be greater than that of the penetrator though above a minimum threshold value; no further increase is beneficial. The low Poisson's ratio probably reflects the way the cumulative damage forms in the ceramic during the initial compressive failure during penetration. The impedance, a property that governs wave

propagation in a material is increased by the high Young's modulus and low density. According to Semple (1976), ballistic performance increases as porosity decreases.

Of course, the ceramic's tensile and compressive strength are also very important for a good ballistic performance. Unfortunately, the tensile strength, measured indirectly through flexural testing, and the compressive strength are not found to have any apparent relationship to performance. This is caused by the fact that traditional mechanical behaviour tests are designed to measure the weakest portions of a sample. These measures of strength therefore reflect the flaws inherent in the ceramic. For the ballistics application, the strength of the individual grains and grain boundaries are responsible for the performance.

The difficulty in determining material properties important to the impact event is enhanced by the fact that the projectile interacts with the confined but broken and comminuted ceramic for a considerable amount of time, as is illustrated in figure 2.2. Hence, in addition to the above-mentioned material properties, a number of unconventional properties such as the pressure increase in the ceramic due to the bulking of the fractured material (dilatation), the friction, flow, and the abrasive properties of the finely fragmented material, are expected to influence the ceramic's penetration resistance (Mescall & Tracy, 1986; Shockey *et al.*, 1990; Johnson & Holmquist, 1990). The importance of these unconventional properties are expected to increase with ceramic confinement.

In Wilkins' second progress report on light armour (1967), he stated that the back-up plate has to have: low density, to allow for a large plate thickness, high tensile strength, and sufficient bulk and rigidity moduli, to prevent ceramic failure at the back-up plate interface from the first stress waves. In 1968 he supplemented this statement by the observation that an optimum back-up plate is made of a material that is stiff when deflected, but not so stiff that a shear failure will occur.

2.5. General assumptions and simplifications for the model

The fracturing process of the ceramic facing during the shock-wave period of the impact process has been shown to be very important. The ideal Hertzian-type fracture trajectories depend on the elastic properties of the projectile and the brittle facing, but in the dynamic impact situation the cracks travel through a time varying stress field and deviate from the ideal path. In the extreme overload situation of the impact event, it is very difficult to model the sequence of cracking. Therefore, in the present model, primarily the structural response period is modelled. Such an approach is similar to the one used by Florence (1969) and Prior & Hetherington (1986) for their models.

Hence, it is assumed that the ceramic fracture conoid exists at the moment that the model is initiated, that the projectile has not yet penetrated the armour, and that the projectile has lost some mass and velocity. This "start" situation is illustrated in

figure 2.4. The fracture conoid angle is assumed to be known. According to Wilkins (1967) and Florence (1969), this assumption is correct for impacts in the ballistic range (around 800 m/s). Recently, Townsend & Field (1987) observed a small velocity dependence of the conoid angle. Here, the angle is taken to be velocity independent.

The impacting projectile is simulated by a blunt cylinder. It is assumed that the projectile does not break up into large fragments during impact. The projectile is allowed to erode mass during the penetration process.

In order to be able to carry out ballistic limit velocity computations, the projectile mass erosion and velocity reduction during the shock-wave period of the penetration process have to be accounted for. A so-called pre-model phase is added to the model which calculates the projectile mass erosion and velocity reduction that occur during the shock-wave period. Neither the support given by the back-up plate to the ceramic facing during the ceramic fracturing process, nor the (possible) effects of a thin, thick or no bond between the ceramic facing and the back-up plate, nor the effects of projectile nose shape, are taken into account in the pre-model phase.

Another simplification is the assumption that the area of backing over which the impact load is spread varies in time, such that as the projectile approaches the back-up plate and the amount of ceramic between the back-up plate and projectile reduces, the spread of load occurs over a progressively smaller area. It is proposed that this area is dependent only on the invariant conoid angle and the projectile's relative position to the back-up plate. This assumption was also used by Prior & Hetherington (1986). That the impact load is initially spread over a large area of back-up plate is illustrated by the sequence of views presented in figure 2.5. This figure shows the interface of an alumina (Al_2O_3) armour as seen through a glass back-up plate during impact of a sharp projectile (Wilkins *et al.*, 1969). The breakout of the large fracture conoid can be seen clearly.

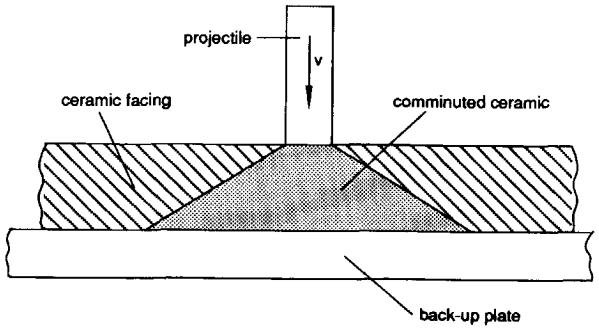

Figure 2.4 Start situation for the penetration model.

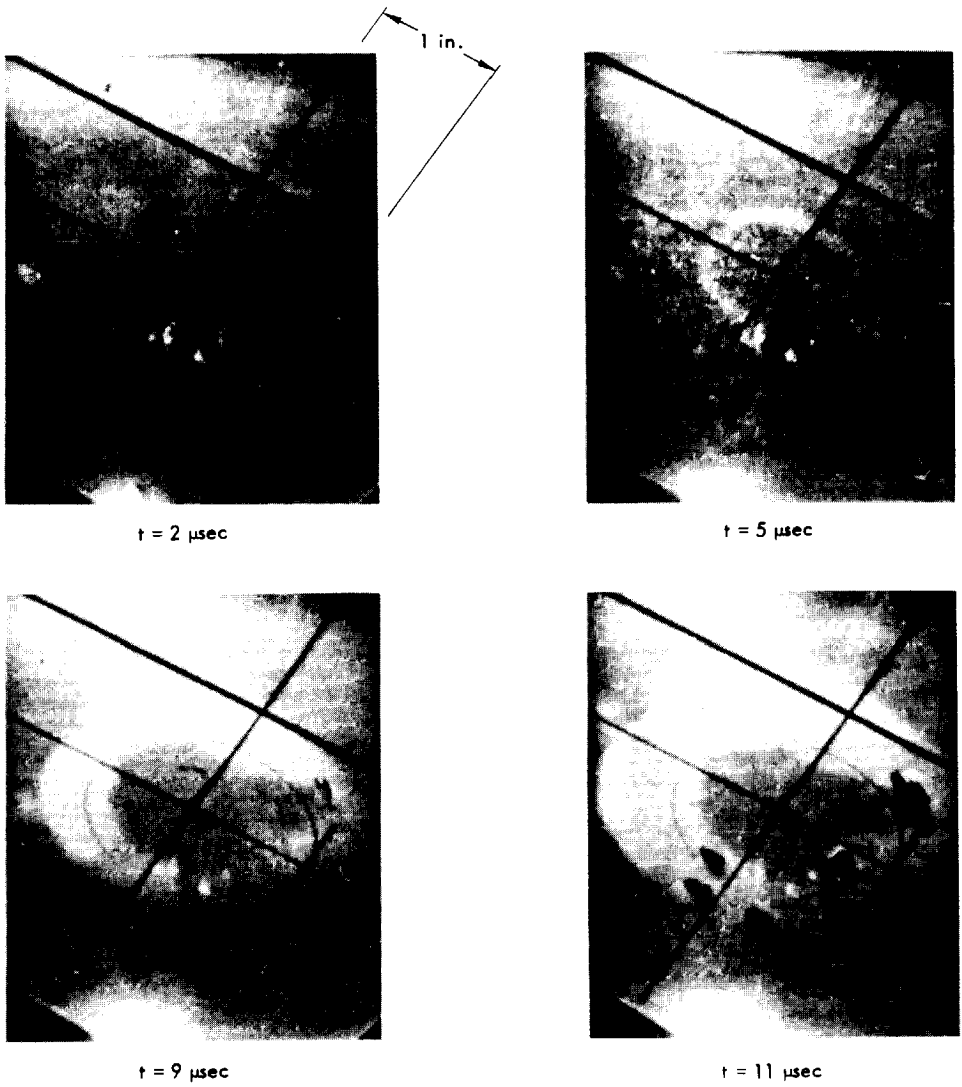

Figure 2.5 Experimental breakout of fracture conoid in an armour of alumina supported by a glass back-up plate (Wilkins *et al.*, 1969).

Because the back-up plate is initially loaded over an area with a radius several times larger than its thickness, it is assumed that the bulging of the comminuted ceramic is geometrically constrained to the deformation of the back-up plate. Hence, the ceramic layer is not allowed to deform (or bulge) into the upper surface of the back-up plate.

With the broken ceramic's penetration resisting properties being so dependent on confinement, and because of the large amount of energy that has to be absorbed by the back-up plate, the back-up plate's behaviour has to include bending, shearing, and stretching. Due to the large (plastic) deformations witnessed in experiments (Van Riet, 1988) and the computational constraints set for the model, the back-up plate behaviour is approximated by using a simplified rigid-perfectly plastic approach to structural deformation, whereby the entire back-up plate deformation field is described using two circular plastic hinges. The plastic hinge theory is commonly used for dynamically loaded structures, see for example Jones (1968) or Johnson (1972), and allows for relatively simple expressions for the back-up plate behaviour.

2.6. Outline of the analytic penetration model

A two-stage penetration model is formulated based on the observations, assumptions and simplifications presented in the previous paragraphs. This model primarily describes the projectile/armour interaction processes during the structural response period of the penetration event. It is assumed that the ceramic fracture conoid has completed its development at the moment of model initiation. The initial conditions for the model are obtained from a simplified analysis of the shock-wave period of the penetration process.

The stages described here are presented in detail in the sections following this outline.

2.6.1. The initial conditions

As the projectile impacts the armour, shock degradation of the armour and shatter of the projectile result. The ceramic facing develops a fracture conoid. During this fracturing process it is assumed that the projectile is practically unable to penetrate the armour and erodes mass. The response of the armour's back-up plate is assumed to be negligibly small. The formation of the fracture conoid is assumed to be completed when the fracture front that follows the tensile wave that was created by the reflection of the initial shock wave at the ceramic/back-up plate interface, reaches the ceramic's front surface.
The projectile mass erosion and velocity reduction that occur during this fracturing process are approximated and taken into account when the first stage of the penetration model is started. It is assumed that the projectile is penetrating the armour at a small (user-given) velocity at the moment of initiation of the first stage of the penetration model.

2.6.2. The first stage of the penetration model

In the first stage of the penetration model, the projectile is allowed to penetrate through the broken and comminuted ceramic. The projectile may either continue to erode mass, to mushroom or to be rigid, depending on the resistance it experiences during penetration. The penetration resisting force from the ceramic is proposed to be given by a semi-empirical relation which accounts for the drag, but also includes confinement and bulking (dilatational) effects of the comminuted ceramic. It is assumed that the very strong bulking of the ceramic material that occurs during the formation of the fracture conoid is limited to a small area directly in front of the projectile. The magnitude of this bulking and the associated pressure build-up at the moment of initiation of the first stage of the penetration model is taken to be such, that the eroding projectile which is penetrating at the initial penetration velocity is in equilibrium with the resisting force from the ceramic. During the penetration process, the confinement of the ceramic is increased by the penetrating projectile, whereas on the other hand, it is released by ejection of ceramic material through the impact hole and by deformation of the back-up plate. It is proposed that the back-up plate is loaded by the impacting projectile over an area that varies in time, such that as the projectile gets closer to the back-up plate, the amount of ceramic between the projectile and the back-up plate reduces and the spread of load occurs over an increasingly smaller area. The comminuted ceramic in the conoidal volume in front of the projectile is assumed to be constrained in its motion by the underlying back-up plate.
The back-up plate deformation is modelled by the use of circular plastic hinges. In certain impact situations, the shear load on the periphery of the loaded section of the back-up plate reaches the material's shear yield strength. Whenever this occurs the shear load that is being transferred to the surrounding back-up plate is limited to this maximum value by means of the shear deformation model.
This stage of the penetration model ends either when the shear strain in the back-up plate reaches a critical value, or when the projectile has (almost) completely penetrated the comminuted ceramic, or when the projectile's penetration velocity is matched by the back-up plate's deformation velocity.

2.6.3. The second stage of the penetration model

In the second stage, the projectile is assumed to be rigid and will no longer erode or mushroom. The plug shearing deformation mechanism is initiated in either of the following cases: when the shear strain in the back-up plate has reached the limiting value, when the projectile's penetration velocity is matched by the back-up plate's deformation velocity in the shear deformation model, or when the projectile has reached the forward face of the back-up plate. A projectile/plug combination is assumed to be formed instantaneously with a velocity that is obtained from a momentum balance. The projectile/plug combination is decelerated by the shear force acting on the plug's periphery. The plug shearing may result in the complete separation of the plug from the surrounding back-up plate. When this occurs, the armour is

defeated and the execution of the penetration model is stopped. On the other hand, the projectile/plug and the surrounding back-up plate may arrive at the same velocity, at which time plug shearing is assumed to stop. The projectile/plug/back-up plate ensemble is then decelerated by the forces in the back-up plate, using the membrane deformation model. This membrane deformation mechanism is also initiated when, at the end of the first stage of the penetration model, the shear deformation model is not active and the projectile penetration velocity is matched by the back-up plate's deformation velocity. As the projectile/plug/back-up plate ensemble is being decelerated, the back-up plate stretches. This may result in the back-up plate's failure strain being reached. When this occurs, the armour has failed and the execution of the penetration model is stopped. On the other hand, the projectile may be brought to rest by the back-up plate. In this situation the projectile is defeated by the armour and the execution of penetration model is stopped.

2.7. The pre-model projectile mass erosion and velocity reduction

At the time that the model begins its computations it is assumed that the ceramic material is already broken up. A certain amount of time is needed for this ceramic breakup, which of course depends on the specific armour material properties such as wave velocities, yield stress, strain behaviour and, of course, strength and shape of the impact shock wave. During the ceramic break-up phase, which according to Wilkins (1968) takes approximately 6 μs for a lightweight armour consisting of an 8.6 mm thick Al_2O_3 facing supported by 6 mm thick Al 6061-T6, the ceramic presents an almost impenetrable barrier, as can be seen in figure 2.1. The projectile will hardly penetrate the armour during this phase, hence it erodes and loses mass and velocity. If the model is to be used for ballistic limit velocity predictions, an estimate is required for this initial erosion and velocity decrease.

Here, a simple formalism is used to estimate the time span in which the ceramic presents an impenetrable barrier to the projectile. It is assumed that the ceramic's break-up time depends on the time that the fracture front following the reflected compressive (shock) wave needs to traverse the ceramic. It is known (Hornemann *et al.*, 1984) that this fracture front travels at a velocity significantly below the ceramic's longitudinal sonic velocity, $u_{c_{ela}}$. Here, it is assumed that the fracture wave moves at 1/5 of the velocity of the longitudinal sonic velocity (Kennedy *et al.*, 1986). Hence, by taking into account that the impact shock wave has to travel through the ceramic and reflect from the back face before the fracture front starts to travel through the facing, the following expression for the break-up time is arrived at:

$$t_{breakup} = \frac{h_c}{u_{c_{ela}}} + \frac{5h_c}{u_{c_{ela}}} = \frac{6h_c}{u_{c_{ela}}} \qquad (2.1)$$

The break-up times calculated with this equation match those presented by Wilkins.

The actual mass erosion and velocity reduction is approximated by using the mass erosion equations derived in section 2.8.2 with $\dot{x}$, the velocity of the projectile/armour interface, set to zero (neglecting penetration).

2.8. Modelling the projectile response

2.8.1. Introduction

At the impact velocities necessary to penetrate ceramic faced lightweight armours, the initial pressures at the projectile/armour interface are much higher than the dynamic flow stress in the projectile (Wilkins *et al.*, 1969). Projectile erosion and/or breakup generally results, which is an essential defeat mechanism of lightweight armours. In the present description it is assumed that the projectile erodes and does not break up into a discrete number of fragments during penetration, although some armour piercing projectiles do.
The projectile behaviour is divided into three phases; a mass erosion (flowing) phase, where the nose of the projectile disintegrates or spatters, with modelling based on the equations of White (1984) for missile impact; a mushrooming phase where the projectile deforms to a mushroom shape, with modelling based on Yatteau's work for the Thick Plate Penetration Model (1985); and a rigid body penetration phase. The frequently used approach towards the modelling of projectile mass erosion by using Bernoulli's equation (Tate, 1967) was not adopted here. Such an approach considers equilibrium along the central streamline of the flowfields of the projectile and the armour only, and is not compatible with the mushrooming and rigid body projectile models used here. The mushrooming phase provides for a continuous transition from the mass erosion model towards rigid body penetration. Omission of the mushrooming phase would lead to an unallowable discontinuous projectile/armour interaction. It is assumed that the projectile material behaves rigid-perfectly plastic and it is thus assumed to be incompressible.

2.8.2. The mass erosion (flowing) model

It is known from experiments (Florence & Ahrens, 1967; Wilkins *et al.*, 1967-78) that at high velocities ductile materials spatter or flow out parallel to the armour surface. This erosion implies a physical separation of material so that its momentum no longer contributes to armour perforation. In practice with brittle penetrator materials, this may happen in chunks, but as the physics of such a process is not developed yet, it is assumed that projectile erosion is governed by plastic flow of the penetrator material.

At some time after impact, (at time greater than $t_{breakup}$) the eroding projectile, with length L, cross-section A_0 and velocity v, is penetrating the armour at a velocity $\dot{x}$. The material in the rear-end of the projectile is moving towards the armour and is

assumed to encounter at some moment what can be termed as a standing plastic wave, a discontinuity of force, velocity, and cross-section, which is stationary relative to the (moving) projectile/armour interface. This plastic wave has a velocity $c = (v-\dot{x})$ relative to the moving tail. By moving through the wave front, the material experiences an increase of cross-section to A, and a corresponding decrease in velocity to v'. The plastic wave is assumed to be located at a very short distance δ ($\delta << \sqrt{A_0}$) from the projectile/armour interface. The material is assumed to flow away laterally from the impact zone after passing the plastic wave. The eroding projectile's deformation is illustrated in figure 2.6. Rod erosion occurs as long as the velocity of the undeformed rear-portion of the rod relative to the projectile/armour interface $v-\dot{x}$, exceeds the velocity u_{plas}, at which velocity plastic deformations propagate in the rod.

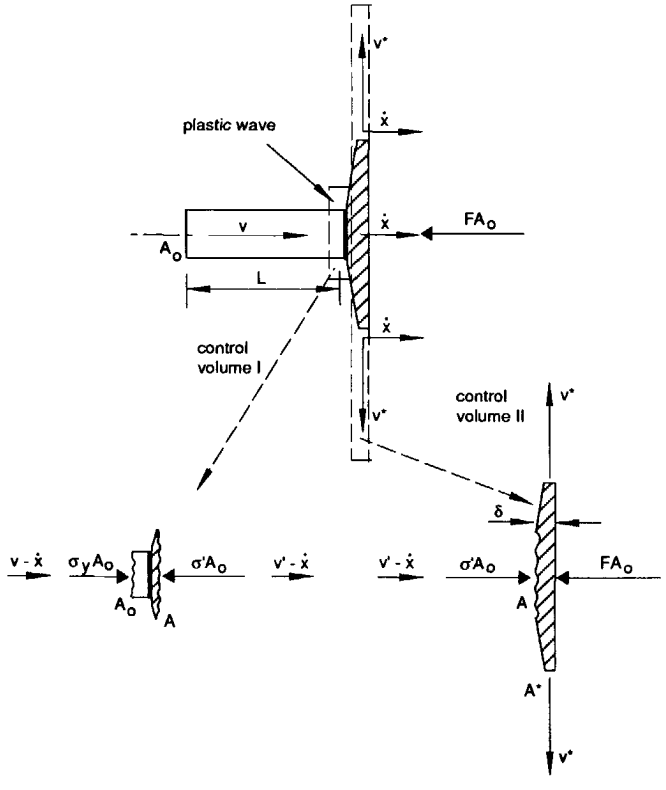

Figure 2.6 The projectile mass erosion mechanism.

First, the situation around the plastic wave is considered. Applying the equation of continuity across the wave yields

$$(v - \dot{x}) A_0 = (v' - \dot{x}) A \tag{2.2}$$

By definition, there is no change of momentum across the plastic wave. Hence

$$\rho_p (v - \dot{x}) v A_0 - \rho_p (v' - \dot{x}) v' A + \sigma_y A_0 - \sigma' A_0 = 0 \tag{2.3}$$

where ρ_p is the projectile material's density, σ_y is the dynamic yield stress of the projectile material, and $\sigma' A_0$ represents the force acting on the right-hand side boundary of the control volume.
By using equation (2.2), the above equation becomes

$$\rho_p (v - \dot{x}) v - \rho_p (v - \dot{x}) v' + \sigma_y - \sigma' = 0 \tag{2.4}$$

Next, the projectile material between the plastic wave and the armour (control volume II) is considered. Since the plastic wave is stationary relative to the projectile/armour interface and the projectile material is incompressible, conservation of mass yields

$$\rho_p (v' - \dot{x}) A = \rho_p A^* v^* \tag{2.5}$$

where v^* is the velocity of the material flowing parallel to the armour surface at a radius corresponding to the cross-section A^*.

Because the plastic wave is assumed to be located at a very short distance δ ($\delta << \sqrt{A_0}$) from the projectile/armour interface, the momentum of the projectile material inside control volume II is neglected when equating the momentum fluxes through the boundaries of this control volume to the forces acting on it. Hence

$$\rho_p A (v' - \dot{x}) v' - \rho_p A^* v^* \dot{x} + \sigma' A_0 - F A_0 = 0 \tag{2.6}$$

Using equation (2.5), this equation is rewritten as follows

$$\rho_p A (v' - \dot{x}) v' - \rho_p A (v' - \dot{x}) \dot{x} + \sigma' A_0 - F A_0 = 0 \qquad (2.7)$$

Substitution of the expression for σ' as given by equation (2.4), using equation (2.2), and some straightforward manipulations, results in the following equation

$$\rho_p (v - \dot{x}) v - \rho_p (v - \dot{x}) \dot{x} + \sigma_y = F \qquad (2.8)$$

or rewritten,

$$\rho_p (v - \dot{x})^2 + \sigma_y = F \qquad (2.9)$$

where F is the load per unit of undeformed projectile area exerted on the projectile during penetration of the comminuted ceramic. An expression for this load will be described in section 2.10.

There remain two other equations for the projectile's behaviour. While the projectile is being consumed, its retardation is given by

$$\frac{dv}{dt} = -\frac{\sigma_y}{\rho_p L} \qquad (2.10)$$

where L is the current length of the projectile. The rate of decrease of projectile length is given by

$$\frac{dL}{dt} = -(v - \dot{x}) \qquad (2.11)$$

which is also a direct measure for the mass erosion rate, since all material passing through the plastic wave is assumed to be separated from the projectile.

2.8.3. The mushrooming model

When decrease of the comminuted ceramic's resistance causes the projectile's relative impact velocity v-$\dot{x}$, to fall below the projectile material's plastic wave velocity u_{plas}, the relative displacement between the rear-end of the projectile and the projectile/armour interface can start to be accommodated by plastic deformation of the projectile. Hence mass erosion is assumed to stop. The mushrooming situation is illustrated in figure 2.7. The plastic wave starts to travel through the projectile towards its rear-end, yielding plastic deformation of the projectile material as it passes the plastic wave. In this analysis it is postulated that the tail section (rear-end) of the projectile has the uniform velocity v, while the mushroomed section of the projectile has a uniform velocity $\dot{x}$.

Consider the change of momentum of the deformed section of the projectile, shown separately in figure 2.7. The equation for the momentum flux is given by

$$\frac{dI}{dt} = \rho_p A_0 u_{plas} v + \sigma_y A_0 - F A_0 \tag{2.12}$$

where,

$$I = \rho_p A_0 (L_{ero} - L_{ela}) \dot{x} \tag{2.13}$$

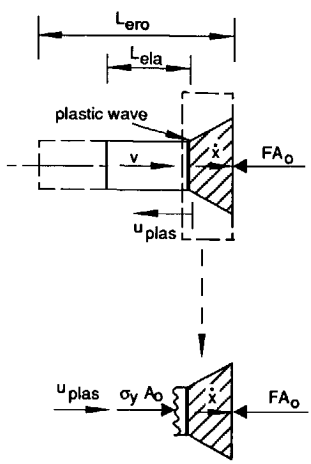

Figure 2.7 The projectile mushrooming mechanism.

In this equation, L_{ero} represents the remaining length of the projectile at the end of the mass erosion phase. L_{ela} is the length of the projectile not yet influenced by the plastic wave.
Substitution of the above equation into equation (2.12) yields

$$\frac{d}{dt}\left[\rho_p \, (L_{ero} - L_{ela}) \, \dot{x}\right] = \rho_p \, u_{plas} \, v + \sigma_y - F \tag{2.14}$$

Taking into account that L_{ero} is a constant, differentiation yields the following equation:

$$\rho_p \, \ddot{x} \, (L_{ero} - L_{ela}) - \rho_p \, \dot{x} \, \frac{d}{dt} L_{ela} = \rho_p \, u_{plas} \, v + \sigma_y - F \tag{2.15}$$

Since

$$\frac{d}{dt} L_{ela} = - u_{plas} \tag{2.16}$$

equation (2.16) can be rewritten as follows:

$$\ddot{x} = \frac{1}{(L_{ero} - L_{ela})} \left[u_{plas} \, (v - \dot{x}) + \frac{1}{\rho_p} (\sigma_y - F) \right] \tag{2.17}$$

The retardation of the rear-end of the projectile during the mushrooming deformation phase is given by equation (2.10).

2.8.4. The rigid body model

At a certain moment, the velocity of the elastic remainder of the projectile v, has become equal to the velocity of the deformed (mushroomed) section of the projectile, $\dot{x}$. From that moment on it is assumed that the projectile behaves as a rigid body.
At the moment that the mass erosion phase ends, the projectile's mass (M_p) is given by $\rho_p \, A_0 \, L_{ero}$. Using Newton's second law then yields the following equation for the motion of the rigid body projectile remainder,

$$\ddot{x} = \frac{-F}{\rho_p \, L_{ero}} \tag{2.18}$$

Since the projectile is a rigid body, its rear-end velocity v, and acceleration $\dot{v}$, are identical to $\dot{x}$ and $\ddot{x}$.

2.9. Modelling the armour response

2.9.1. Introduction

As stated in section 2.5, the armour's response to the impact event is modelled primarily for the structural response period of time. The response of the armour to the impacting projectile is approximated by four deformation models using a simplified rigid-perfectly plastic approach to structural deformation. It is assumed that the back-up plate deformation field can be approximated by using a very simple deformation mechanism based on two circular plastic hinges.
This approximate and simplified approach to the structural deformation of the armour was preferred above a more refined (elastic-plastic) approach, because a more complicated approach towards the structural response of the armour is not expected to contribute significantly to the accuracy of the result due to the large number of uncertainties which remain associated with the armour's response at this moment, such as the magnitude of the impact load, the ceramic conoid deterioration and the associated impact load distribution through the comminuted ceramic conoid over the back-up plate.
The initial deformation of the back-up plate is modelled by the use of circular plastic bending hinges. This is the first model. In certain loading situations, the shear load on the boundary of the central section of the back-up plate (i.e. the area of back-up plate loaded by the projectile) reaches the material's shear yield strength, requiring the use of a shear deformation model, which effectively limits the shear load being transferred to the unloaded section of the back-up plate. This is the second model. When the shear strain reaches a critical value, or as the projectile impacts the back-up plate, a plug may be sheared off by use of the plug shearing model. On the other hand, if the back-up plate and projectile obtain identical velocities, they are decelerated by the forces in the back-up plate modelled by the fourth model, namely the membrane deformation model. The equations of motion for these deformation models are discussed in detail. In addition, some back-up plate related topics such as the calculation of the radial strain and the use of a multi-layer back-up plate are addressed as well.

2.9.2. Initial armour response model

An illustration of the situation some time after impact is given in figure 2.8. In this figure, the back-up plate is represented by a solid line. It is assumed that the motion of the armour remains limited to an area with a radius R, which is somewhat larger than the initial base radius R_{rigid} of the comminuted ceramic conoid. It is also assumed that the area of backing over which the impact load is spread varies in time, such that as the projectile approaches the back-up plate and the amount of ceramic between

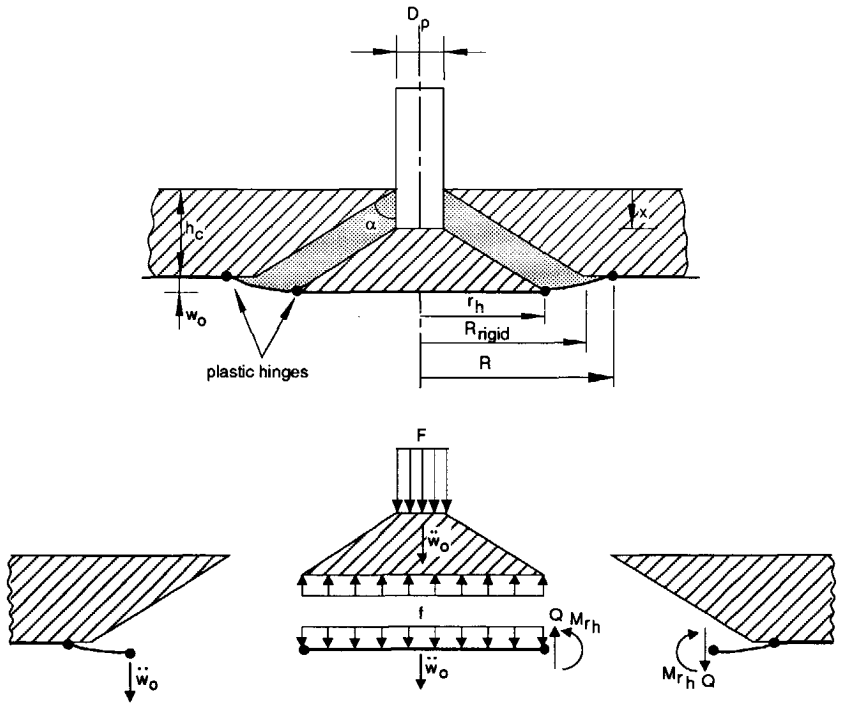

Figure 2.8 The initial armour response model.

projectile and back-up plate reduces (as the conoid deteriorates) the load is spread over a progressively smaller area of back-up plate. It is proposed that this area, with radius $r_h(t)$ is dependent only on the invariable conoid angle and the projectile's relative position to the back-up plate.

It is also assumed that the deformation and velocity fields of the section of the back-up plate supporting the deteriorating ceramic conoid ($0 < r < r_h$) are uniform. The velocity field of the back-up plate outside this area ($r_h < r < R$) is assumed to be linear. These deformation and velocity fields are obtained by assuming circular plastic hinges to be located at $r = R$ and $r = r_h$. The hinge at R effectively restricts the amount of back-up plate affected by the impact. The hinge at $r_h(t)$ is a so-called moving circular hinge. This hinge is located at the edge of the loaded area of the back-up plate. In view of the observations by Griffith & Vanzant (1961) that the material of a circular plate tends to move in a transverse sense at high rates of dynamic loading, the displacements in the direction r of the undeformed plate are neglected in the analysis.

For a specific ceramic conoid angle α, projectile diameter D_p, position of the projectile tip x(t), and back-up plate central deformation $w_0(t)$, the radius of the area of back-up plate over which the impact load is spread, $r_h(t)$, is given by

$$r_h(t) = \frac{D_p}{2} + \left(h_c - \left(x(t) - w_0(t)\right)\right) \tan \alpha \qquad (2.19)$$

where D_p is the projectile's diameter and h_c the thickness of the ceramic facing.
At the moment of model initiation, $x(t_{breakup}) = 0$ and $w_0(t_{breakup}) = 0$. Hence,

$$r_h(t_{breakup}) = \frac{D_p}{2} + h_c \tan \alpha = R_{rigid} \qquad (2.20)$$

Some time after impact, the mass of the comminuted ceramic in the conoid in front of the projectile, see figure 2.8, is given by

$$m_c(t) = \frac{1}{3}\pi \rho_c \left(h_c - \left(x(t) - w_0(t)\right)\right)\left[\frac{D_p^2}{4} + \frac{D_p}{2} r_h(t) + r_h^2(t)\right] \qquad (2.21)$$

where ρ_c is the ceramic's original density. The effect of bulking (dilatation) on the mass of the comminuted ceramic in the conoid in front of the projectile is assumed to be small and is neglected in the above equation.

The impact load acts on the top of the ceramic conoid. The motion of the material in the ceramic conoid in front of the projectile is assumed to be constrained by the motion of the underlying centre section of the back-up plate ($0 < r < r_h$). Hence, it is loaded on top by the uniformly distributed impact load per unit of undeformed projectile area F, and (in the opposite direction) by the unknown load f per unit area, which is assumed to be uniformly distributed over the base area of the deteriorating ceramic conoid. This base load f, is the result of the back-up plate's reluctance to deform and accelerate.
Hence, the equation of motion for the comminuted ceramic in the conoid in front of the projectile can be obtained and is given by

$$\frac{1}{3}\pi \rho_c \left(h_c - (x - w_0)\right)\left[\frac{D_p^2}{4} + \frac{D_p}{2} r_h + r_h^2\right] \ddot{w}_0 = F \pi \frac{D_p^2}{4} - f \pi r_h^2 \qquad (2.22)$$

where ($\ddot{}$) denotes $d^2( ) / dt^2$.

By rewriting equation (2.22), the following expression for the (unknown) load f, is obtained:

$$f = \frac{1}{r_h}\left[F\frac{D_p^2}{4} - \frac{1}{3}\rho_c \ddot{w}_0 \left(h_c - (x - w_0) \right)\left(\frac{D_p^2}{4} + \frac{D_p}{2} r_h + r_h^2 \right)\right] \qquad (2.23)$$

As indicated, the back-up plate deformation mechanism is approximated by the use of two circular plastic bending hinges. It is assumed that the loaded centre section of the back-up plate deforms uniformly, and at some moment after impact moves at a velocity $\dot{w}_0$. The velocity field of the back-up plate outside this area ($r_h < r < R$) is assumed to be linear and is thus given by

$$\dot{w}(r,t) = \frac{(R-r)}{\left(R-r_h(t)\right)}\,\dot{w}_0(t) \qquad (2.24)$$

The acceleration of this annular plate section ($r_h < r < R$) is fully determined by the above equation and given by

$$\ddot{w}(r,t) = \frac{(R-r)}{\left(R-r_h(t)\right)}\,\ddot{w}_0(t) + \frac{(R-r)}{\left(R-r_h(t)\right)^2}\,\dot{r}_h(t)\,\dot{w}_0(t) \qquad (2.25)$$

This acceleration is the result of the loading on the periphery of this annular plate section.

As stated earlier, the back-up plate is assumed to be made from a rigid-perfectly plastic material. In principle, therefore, it is necessary to employ a multi-dimensional yield surface between the bending moments, membrane forces and shear forces in order to be able to solve the equilibrium equations for a plate made of this material. Onat & Prager (1954) have derived equations for the load carrying capacity of shells of revolution made from a rigid, perfectly plastic material which obeys Tresca's yield criterion and associated flow rule. However, these relations are very difficult to handle. Hodge (1960), therefore, proposed a two-moment limited interaction surface which maintains all interaction between force and force, and moment and moment, but neglects all interactions between force and moment. If it is assumed that yielding is controlled by the Tresca criterion, the result is a linear surface in four dimensional space.

However, even this yield criterion is considered too difficult to handle for the simple armour response model being developed here. Hence, an even more simplified yield criterion is required here. It is therefore proposed that for the situation where membrane forces are assumed to be dominated by bending moments, the interaction on the yield surface between moments and forces can be approximated by assuming an average value for these moments of two-thirds of the fully plastic moment. In the

situation where a bending moment is assumed to be dominated by a membrane force on a boundary, the membrane force is assumed to be fully plastic, whereas the bending moment is assumed to be reduced to zero. In a situation where shearing and bending occur, it is assumed that the interaction on the yield surface can be approximated by assuming an average value for the bending moments of two-thirds of the full plastic moment and the shear force to be fully plastic.
Use of this approximate and simplified yield criterion has given acceptable agreement when comparing the results of calculations using the penetration model with the experimentally observed back-up plate responses (see also chapter 5).

Now consider an element of the annular outer plate, as is shown in figure 2.9. On the boundaries it is loaded by radial moments M_R and M_{r_h}, a hoop moment M_θ, and shear forces Q and Q', all per unit distance along the edge of the element. The back-up plate thickness is given by h_b, while ρ_b denotes its density. The equation for rotational equilibrium by taking moments about the hinge positioned at r = R, see figure 2.9, is given by

$$\int_{r_h}^{R} \rho_b h_b \ddot{w} (R-r)\, r d\theta\, dr + \int_{r_h}^{R} M_\theta d\theta\, dr + M_R R d\theta + $$

$$+ M_{r_h} r_h d\theta - Q(R-r_h) r_h d\theta = 0 \qquad (2.26)$$

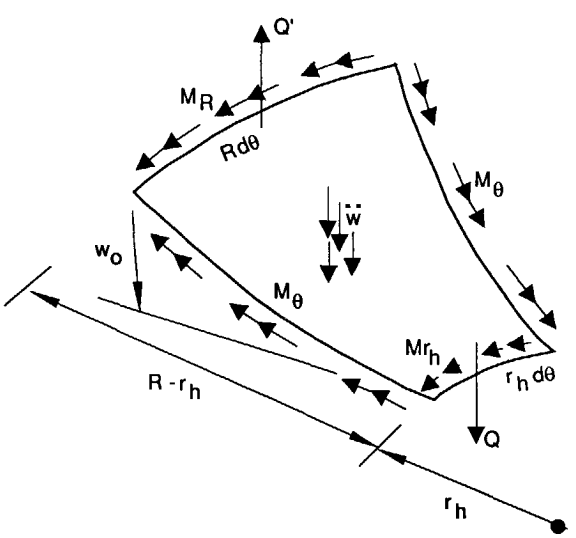

Figure 2.9 The loading situation on an outer annular segment of the back-up plate.

The rotary inertia effect is disregarded. Because the deformation of the back-up plate is assumed to be small, the contribution of the membrane forces is ignored.

After substitution of equation (2.25) into (2.26), and some straightforward manipulations and regrouping, the following equation is obtained for the shear load Q, on the periphery at $r = r_h$:

$$Q = \frac{\hat{M}_\theta}{r_h} + \frac{M_R R}{(R-r_h)r_h} + \frac{M_{r_h}}{(R-r_h)} + \left[\frac{\mu_b \ddot{w}_0}{(R-r_h)^2 r_h} + \frac{\mu_b \dot{w}_0 \dot{r}_h}{(R-r_h)^3 r_h} \right] \cdot \left[\frac{1}{12} R^4 - \frac{1}{2} R^2 r_h^2 + \frac{2}{3} r_h^3 R - \frac{1}{4} r_h^4 \right] \tag{2.27}$$

where

$$\hat{M}_\theta = \frac{1}{(R-r_h)} \int_{r_h}^{R} M_\theta \, dr \tag{2.28}$$

and μ_b denotes the areal density of the back-up plate ($= \rho_b h_b$).
According to the simplified yield criterion (including all the assumptions discussed on p. 26),

$$M_R = M_{r_h} = \hat{M}_\theta = \frac{2}{3} M_{plas} = \frac{1}{6} h_b^2 \sigma_y \tag{2.29}$$

where σ_y represents the yield strength of the back-up plate material, which is assumed to be strain-rate insensitive.

The acceleration of the centre section of the back-up plate can now be derived. This plate section is loaded by the uniformly distributed load per unit area f, on its top surface and by the shear load Q and radial moment M_{r_h} around its periphery as is illustrated in figure 2.8. Newtons equation of motion then yields

$$\ddot{w}_0 = \frac{1}{\mu_b} \left(f - \frac{2Q}{r_h} \right) \tag{2.30}$$

Substituting equations (2.23) and (2.27) into (2.30) yields the equation of motion for the centre section of the back-up plate:

$$\ddot{w}_0 = \frac{A}{B} \tag{2.31}$$

with

$$A = \frac{F D_p^2}{4\mu_b r_h^2} - \frac{8 R M_{plas}}{3 \mu_b r_h^2 (R - r_h)} + \\ - \frac{2 \dot{w}_0 \dot{r}_h}{(R-r_h)^3 r_h^2} \left[\frac{1}{12} R^4 - \frac{1}{2} R^2 r_h^2 + \frac{2}{3} r_h^3 R - \frac{1}{4} r_h^4 \right]$$

and

$$B = 1 + \frac{\rho_c (h - x + w_0)}{3 \mu_b r_h^2} \left[\frac{D_p^2}{4} + \frac{D_p}{2} r_h + r_h^2 \right] + \\ + \frac{2}{(R - r_h)^2 r_h^2} \left[\frac{1}{12} R^4 - \frac{1}{2} R^2 r_h^2 + \frac{2}{3} r_h^3 R - \frac{1}{4} r_h^4 \right]$$

This equation of motion for the response of the centre section of the back-up plate is valid for as long as the shear load per unit length Q is smaller than the back-up plate's shear strength per unit length Q_{plas} ($= h_b \tau_y$, with τ_y representing the shear strength of the back-up plate material). It can also be used only for as long as the projectile has not reached the back-up plate and the projectile's penetration velocity is not matched by the back-up plate's deformation velocity, because in these instances, the plug shearing or membrane deformation model is initiated. When the shear load per unit length Q exceeds Q_{plas}, the shear deformation model is initiated.

2.9.3. The shear model

In those situations where the shear load per unit length Q reaches the maximum value Q_{plas} ($= h_b \tau_y$), the back-up plate deformation is controlled by the shear model. This model effectively limits the shear load Q, that is transferred to the outer annular section ($r_h < r < R$) of the back-up plate at the location of the moving plastic hinge at $r = r_h$, as is illustrated in figure 2.10. This outside section therefore responds as if it

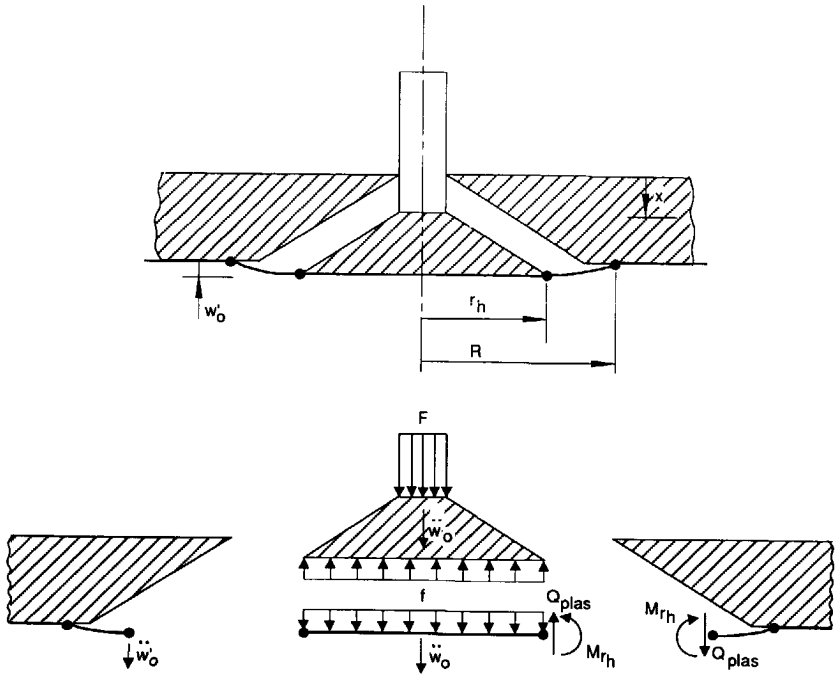

Figure 2.10 The shear deformation model.

were loaded by Q_{plas} only, whereas the centre section of the back-up plate ($0 < r < r_h$) is loaded by the load f on its surface and by Q_{plas} on its periphery.

Since the velocity field of the outer annular plate section of the back-up plate is assumed to be linear and given by equation (2.24), the entire motion of this plate section is related to the motion at its inner periphery ($r = r_h$).
Let w_0' denote the displacement of this outer annular plate section at the location of the moving plastic hinge. Using equation (2.27), substituting Q_{plas} for Q then yields the following equation for the acceleration of this annular plate section at the position of $r = r_h$:

$$\ddot{w}_0' = - \frac{\dot{w}_0' \dot{r}_h}{(R-r_h)} + \frac{A}{B} \qquad (2.32)$$

with

$$A = Q_{plas} (R-r_h)^2 r_h - \hat{M}_\theta (R-r_h)^2 - M_R (R-r_h) R - M_{r_h} (R-r_h) r_h$$

and

$$B = \mu_b \left(\frac{1}{12} R^4 - \frac{1}{2} R^2 r_h^2 + \frac{2}{3} r_h^3 R - \frac{1}{4} r_h^4 \right)$$

where according to the simplified yield criterion (see equation 2.29),

$$M_R = M_{r_h} = \hat{M}_\theta = \frac{2}{3} M_{plas}$$

The equation of motion for the (rigid) centre section of the back-up plate is given by,

$$\ddot{w}_0 = \frac{1}{\mu_b} \left(f - 2 \frac{Q_{plas}}{r_h} \right) \tag{2.33}$$

Substitution of equation (2.23) gives the following result

$$\ddot{w}_0 = \frac{A}{B} \tag{2.34}$$

with

$$A = \frac{F D_p^2}{4 \mu_b r_h^2} - \frac{2 Q_{plas}}{\mu_b r_h}$$

and

$$B = 1 + \frac{\rho_c}{3 \mu_b r_h^2} (h_c - x + w_0) \left(\frac{D_p^2}{4} + \frac{D_p}{2} r_h + r_h^2 \right)$$

During the shear deformation stage, the shear strain in the back-up plate, at the position of the plastic hinge at $r = r_h$, is given by

$$\gamma = \frac{\dot{w}_0' - \dot{w}_0}{\dot{r}_h} \tag{2.35}$$

When the shear strain exceeds a limiting value, or when the projectile reaches the back-up plate, or when the projectile's penetration velocity is matched by the deformation velocity of the centre section of the back-up plate, the plug shearing model is initiated. If, on the other hand, the shearing ends, the response model as described in the previous section is continued.

2.9.4. The plug shearing model

The plug shearing model is initiated by the shear model or when the projectile strikes the back-up plate. In experiments (Van Riet, 1987-1991) it is often observed that a small amount of ceramic material remains in front of the projectile as it plugs through the back-up plate, therefore the possibility is left open to initiate plugging as the distance between the projectile tip and back-up plate is less than a user-specified value.
It is assumed that a plug is instantaneously formed, with an initial velocity $\dot{x}'$, that is obtained from conservation of momentum. The plug consists of the remaining ceramic conoid in front of the projectile and the corresponding back-up plate section whose diameter is equal to the current ceramic conoid base diameter ($2r_h$). Projectile mass erosion or mushrooming is assumed to stop at the moment that this plug is formed.
The projectile/plug combination is decelerated by the shear load on its periphery. This shear load decreases as the contact area between the plug and the surrounding back-up plate reduces due to the plug shearing action. The surrounding back-up plate is accelerated by this shear load. Plug shearing can result in total plug separation from the surrounding back-up plate in which case the armour is assumed to have failed. When the sliding between the plug and back-up plate ends before complete separation, the membrane deformation model as described in section 2.9.5 is selected.

Just after plug formation, the projectile, the ceramic conoid in front of it, and the centre section of the back-up plate, are assumed to have the same velocity, $\dot{x}'$. By applying the conservation of momentum principle to the projectile, the ceramic conoid in front of it, and the corresponding back-up plate section, the following expression for the initial projectile/plug velocity is obtained.

$$\dot{x}' = \frac{A}{B} \tag{2.36}$$

with

$$A = M_p\left(\dot{x} + \frac{L_{ela}}{L_{ero}}(v - \dot{x})\right) + \dot{w}_0\left(\pi\mu_b r_h^2 + \frac{\pi\mu_c (r_h - \frac{D_p}{2})}{3(R_{rigid} - \frac{D_p}{2})}\left(\frac{D_p^2}{4} + \frac{D_p}{2}r_h + r_h^2\right)\right)$$

and

$$B = M_p + \pi\mu_b r_h^2 + \frac{\pi\mu_c (r_h - \frac{D_p}{2})}{3\,(R_{rigid} - \frac{D_p}{2})}\left(\frac{D_p^2}{4} + \frac{D_p}{2}r_h + r_h^2\right)$$

where, r_h is the radius of the back-up plate plug, which now has obtained a fixed value and M_p is the (eroded) projectile's mass.

The projectile/plug combination is decelerated by the shear load Q_{ps}, on its periphery, see figure 2.11. The magnitude of this shear load depends on the contact area between the plug and the surrounding back-up plate. It is given by

$$Q_{ps} = \left(\frac{h}{h_b}\right) Q_{plas} \tag{2.37}$$

with

$$h = h_b - \left(x' - x_{pi} - (w_0' - w_{pi}) \right) \tag{2.38}$$

where x_{pi} and w_{pi} are the displacements x and w_0 at the moment of plug initiation.

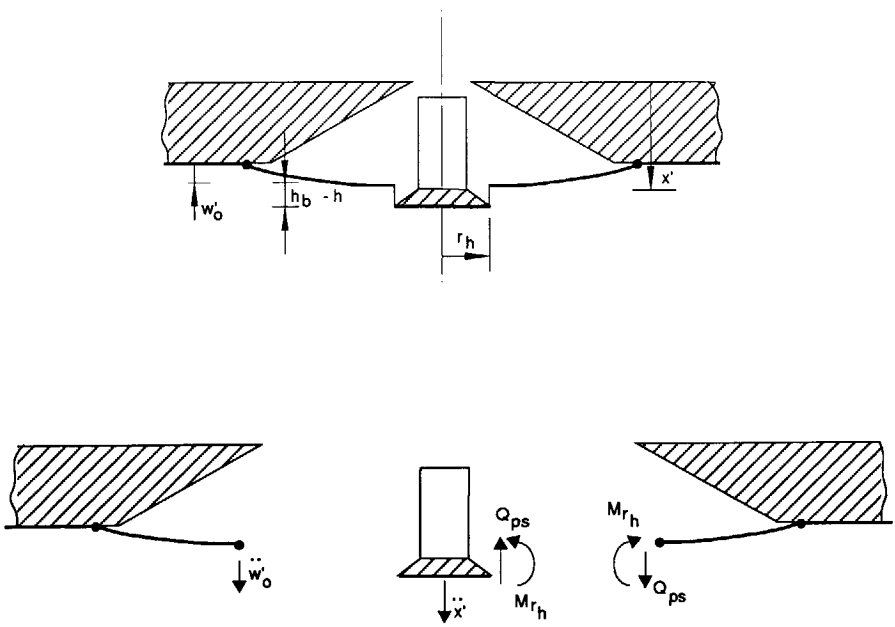

Figure 2.11 The plug shearing deformation model.

The equation of motion for the projectile/plug combination is easily obtained, and given by

$$\ddot{x}' = \frac{-2\pi r_h Q_{ps}}{\left(M_p + \pi\mu_b \dot{r}_h^2 + \frac{\pi\mu_c (r_h - \frac{D_p}{2})}{3 (R_{rigid} - \frac{D_p}{2})} (\frac{D_p^2}{4} + \frac{D_p}{2} r_h + r_h^2) \right)} \tag{2.39}$$

The equation of motion for the surrounding back-up plate (i.e. the outer annular section of the back-up plate) can be obtained from equation (2.32) by substitution of Q_{ps} for Q_{plas}, and taking into account that the hinge at r_h has come to rest ($\dot{r}_h = 0$). Thus, the acceleration of the surrounding back-up plate is given by

$$\ddot{w}_0' = - (R-r_h) \frac{\left(\hat{M}_\theta (R - r_h) + M_R R + M_{r_h} r_h - Q_{ps}(R - r_h) r_h \right)}{\mu_b \left(\frac{1}{12} R^4 - \frac{1}{2} R^2 r_h^2 + \frac{2}{3} r_h^3 R - \frac{1}{4} r_h^4 \right)} \tag{2.40}$$

where according to the simplified yield criterion (see also discussion on p. 26),

$$M_R = \hat{M}_\theta = \frac{2}{3} M_{plas}$$

and (2.41)

$$M_{r_h} = \frac{2}{3} \left(\frac{h}{h_b} \right)^2 M_{plas}$$

due to the reduced height of the contact area caused by the partial plug separation.

Plug separation is complete when

$$h_b - h = 0 \tag{2.42}$$

If, on the other hand, the relative velocity between the plug and the surrounding back-up plate becomes zero, the membrane deformation model is initiated.

2.9.5. The membrane deformation model

The membrane deformation model is activated when either the projectile's penetration velocity is matched by the back-up plate's deformation velocity in the initial armour response model, or the relative velocity between the projectile/plug combination and the surrounding back-up plate is reduced to zero. The outer annular back-up plate section is assumed to stretch as a membrane with bending continuing to occur in the circumferential direction and at the hinge positioned at r = R, see figure 2.12. The membrane deformation model ends when either the projectile/plug/back-up plate ensemble has come to rest, or when the back-up plate's failure strain is reached.
For simplicity, the ceramic conoid in front of the projectile and the corresponding back-up plate section are also denoted as the plug in the situation where a plug has not physically been formed.

As before, two equations of motion are derived. One for the projectile/plug combination and the other for the surrounding back-up plate. Both equations relate the acceleration to the (unknown) shear load on their shared periphery. However, the acceleration of the projectile/plug combination is identical to the acceleration of the surrounding back-up plate at $r = r_h$. Hence, elimination of the (unknown) shear load Q from either one of these equations yields the equation of motion for the entire ensemble.

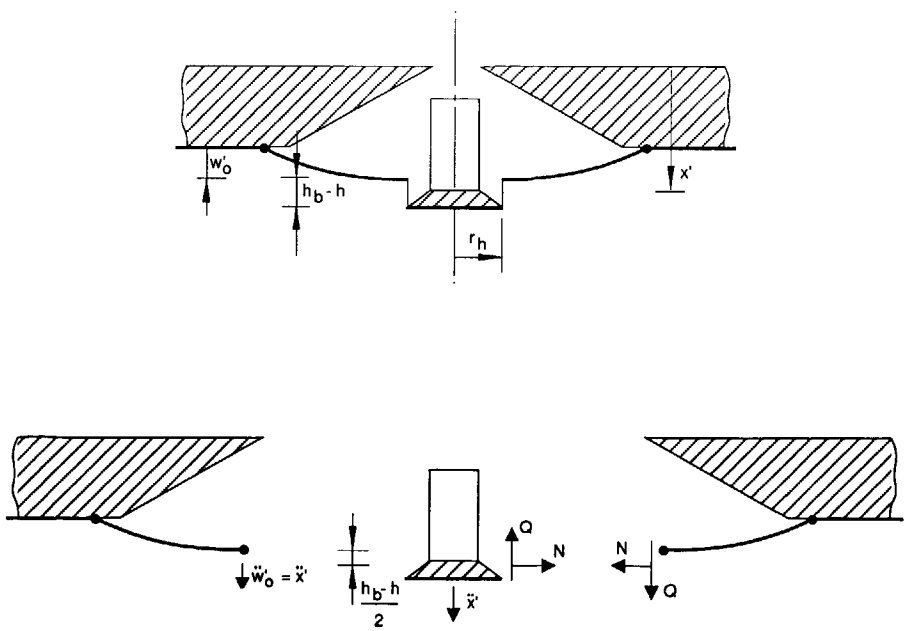

Figure 2.12 The membrane deformation model.

The projectile/plug combination is decelerated by an unknown shear load Q. Hence, Newton's equation of motion yields,

$$\left(M_p + \pi \mu_b r_h^2 + \frac{\pi \mu_c \left(r_h - \frac{D_p}{2} \right)}{3 \left(R_{rigid} - \frac{D_p}{2} \right)} \left[\frac{D_p^2}{4} + \frac{D_p}{2} r_h + r_h^2 \right] \right) \ddot{x}' = - 2\pi r_h Q \tag{2.43}$$

This same (unknown) shear load works, in the opposite direction, on the surrounding back-up plate ($r_h < r < R$). Consider an element of this annulus, as shown in figure 2.13. At its boundaries it is loaded by radial moments M_R and M_{r_h}, a hoop moment M_θ, the (unknown) shear forces Q, and Q', and the membrane forces N and N', all per unit length along the edge of the element.

Due to the (possible) plug shearing action, the membrane force N may be applied eccentrically from the middle plane of the plate. This offset is given by

$$w_{ecc} = \left(\frac{h_b - h}{2} \right) \tag{2.44}$$

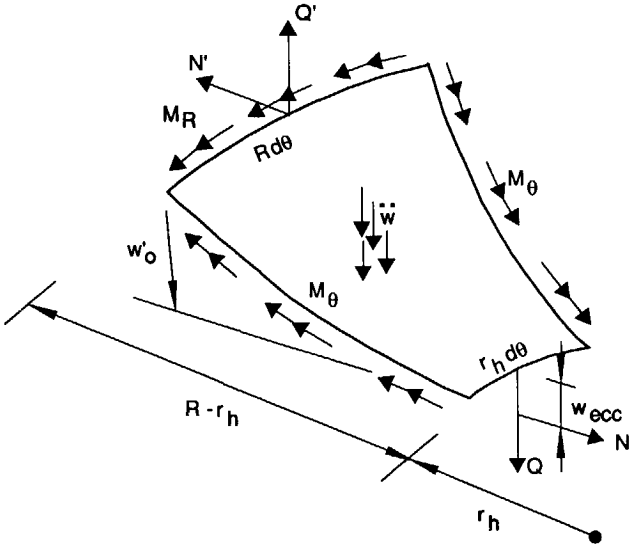

Figure 2.13 The loading situation on an outer annular segment of the back-up plate.

The equation of motion for this outer plate section is obtained from the equation for rotational equilibrium of this annulus, by taking moments about the hinge positioned at r = R, see figure 2.13:

$$\int_{r_h}^{R} \mu_b \frac{(R-r)}{(R-r_h)} \ddot{w}_0' \, (R-r) \, r d\theta \, dr + \int_{r_h}^{R} M_\theta d\theta \, dr + M_R R d\theta +$$

$$+ M_{r_h} r_h d\theta + N\left(w_0' + w_{ecc}\right) r_h d\theta - Q(R-r_h) r_h d\theta = 0 \quad (2.45)$$

Again, the rotary inertia effect is disregarded.

It is assumed that due to the stretching action, the bending moment M_{r_h} is dominated by the membrane force N across the full section of the plug/back-up plate periphery ($r = r_h$), whereas along the other peripheries the membrane forces are assumed to be dominated by the bending moments. Following the simplified yield criterion, the membrane force N is thus taken to be fully plastic, and is given by

$$N = \left(\frac{h}{h_b}\right) N_{plas} = \left(\frac{h}{h_b}\right) h_b \sigma_y \quad (2.46)$$

due to the reduced height of the contact area caused by the (possible) partial plug separation. Whereas according to the simplified yield criterion (see also discussion on p. 26) the bending moments are given by

$$M_R = \hat{M}_\theta = \frac{2}{3} M_{plas}$$

and (2.47)

$$M_{r_h} = 0$$

After some straightforward manipulations and regrouping, the following equation is obtained from equation (2.45) which relates the shear load Q to the acceleration $\ddot{w}_0'$ of the outer plate section on the periphery at $r = r_h$:

$$Q = \frac{4R - 2r_h}{3(R-r_h)r_h} M_{plas} + \frac{N\left(w_0' + w_{ecc}\right)}{(R-r_h)} +$$

$$+ \frac{\mu_b \ddot{w}_0'}{(R-r_h)^2 r_h} \left[\frac{1}{12} R^4 - \frac{1}{2} R^2 r_h^2 + \frac{2}{3} r_h^3 R - \frac{1}{4} r_h^4 \right] \quad (2.48)$$

With the acceleration of the centre section of the back-up plate $\ddot{x}'$ equal to the acceleration $\ddot{w}_0'$ of the outer back-up plate section at $r = r_h$, substitution of equation (2.48) into (2.43) and some regrouping yields the following equation for the motion of the entire projectile/plug /back-up plate ensemble.

$$\ddot{w}_0' = \ddot{x}' = \frac{A}{B} \quad (2.49)$$

with

$$A = -2 \left(\frac{4R - 2r_h}{3(R-r_h)} M_{plas} + \frac{\left(w_0' + w_{ecc}\right) r_h N}{(R-r_h)} \right)$$

and

$$B = \frac{1}{\pi} M_p + \mu_b r_h^2 + \frac{\mu_c \left(r_h - \frac{D_p}{2} \right)}{3 \left(R_{rigid} - \frac{D_p}{2} \right)} \left[\frac{D_p^2}{4} + \frac{D_p}{2} r_h + r_h^2 \right] +$$

$$+ \frac{2\mu_b}{(R-r_h)^2} \left(\frac{1}{12} R^4 - \frac{1}{2} R^2 r_h^2 + \frac{2}{3} r_h^3 R - \frac{1}{4} r_h^4 \right)$$

This equation of motion is used for as long as $\dot{w}_0'$ is positive and the radial failure strain in the back-up plate has not reached its limiting value.

2.9.6. Computing the radial strain

Because it is assumed that the back-up plate has a rigid-perfectly plastic behaviour, there is no direct relation between stress and strain. Here, the strain is approximated by examining the radial elongation of the back-up plate section between r = R and r = r_h. At r = r_h the back-up plate has a deformation of w_0'. The length of this segment is therefore approximated by

$$l' = \sqrt{(R - r_h)^2 + w_0'^2} \tag{2.50}$$

while the original undeformed length of this segment is given by

$$l = (R - r_h) \tag{2.51}$$

This yields the following expression for the radial strain:

$$\varepsilon_r = \frac{l' - l}{l} = \sqrt{1 + \left(\frac{w_0'}{R - r_h}\right)^2} - 1 \tag{2.52}$$

The strain in the circumferential direction is not taken into account because in view of the observations by Griffith & Vanzant (1961) the displacements in the direction r of the undeformed plate are neglected in the analysis.

2.9.7. The multi-layer back-up plate

A formalism was introduced which allows the description of layered multi-material back-up plates within the model. By layering the back-up plate the properties of the individual layers can be chosen such that an optimal performance of the armour is obtained. In the model the back-up plate is regarded as being one single plate. Inclusion of multi-layered back-up plates can therefore only be realized by translation of the individual layer's properties to single back-up plate properties. These back-up plate properties are: the plastic membrane force N_{plas}, the plastic shear force Q_{plas}, the plastic bending moment M_{plas}, the areal density μ_b, the limiting shear strain γ, and the radial failure strain ε_r.
The following formalism was chosen to simulate the behaviour of a multi-layered back-up plate. It is assumed that the individual layers are not bonded together. An individual layer of the multi-layered back-up plate may fail in either one of two modes i.e. the radial (normal) strain failure or the plug shearing failure mode.

At any moment, a single layer strain failure is allowed to occur on the basis of the overall back-up plate deformation. The consequence of a single layer strain failure is that that layer is assumed no longer to be able to carry any membrane force. This implies that in computing the overall membrane force carrying capabilities of the back-up plate, this layer is no longer taken into account. For all other properties, the presence of this layer is still accounted for. It is assumed that a strain-failed back-up plate layer is located such that, at the location of the plastic bending hinges, the layer is still forced to undergo the hinge motion.
When a plug is formed in the model and plug shearing commences, the properties of the deformed back-up plate section are modified as layers of the back-up plate are sheared off. These sheared off layers are assumed to be delaminated and no longer contribute to the remaining strength properties of the back-up plate. Of course, they do contribute to the mass of the plug in front of the projectile. In the deceleration phase of the back-up plate, sheared off layers are not taken into account.
With the exception of the strains, the overall back-up plate properties are simply obtained by summation of a given property over the number of contributing layers, as the layers are assumed not to be bonded in any way.

2.10. The resisting force from the ceramic

During penetration of the comminuted ceramic by the projectile, the ceramic exerts a force on the projectile. As was discussed in section 2.4, a number of material properties is known to influence the ceramic's resistance to penetration. However, no detailed information is available in the open literature, which accurately describes the force resisting the projectile's penetration.

The function for the resistive force from the comminuted ceramic is proposed to include drag, confinement and bulking (dilatation). It is given by:

$$F(t) = \frac{Vol_0}{Vol} \left(\beta \left(\dot{x} - \dot{w}_0 \right) + \gamma \right) + P \qquad (2.53)$$

F is defined as a force per unit of undeformed projectile area.

The first term of the above expression,

$$\frac{Vol_0}{Vol} \left(\beta \left(\dot{x} - \dot{w}_0 \right) + \gamma \right) \qquad (2.54)$$

describes the drag experienced during penetration. Vol is the volume available to all the comminuted ceramic and depends on the deformation of the back-up plate and the penetration of the projectile. Vol_0 represents the volume occupied by the comminuted

ceramic in the conoid in a pressureless environment and may change due to ceramic material ejection through the impact hole. Their ratio simulates the reduction of the drag force due to the fact that as more volume becomes available for the ceramic to move to, the resistance will decrease.
The term within the brackets is a special case of the general expression for the force experienced by projectiles during penetration of a sand-like medium (Allen *et al.*, 1957). It was obtained by Prior & Hetherington (1986) from a generalized theory due to Recht (1973), to describe the drag force during penetration of comminuted ceramic. According to Prior & Hetherington, the constant β is a function of the ceramic's bulk modulus and density whereas the constant γ is assumed to be a function of the Young's modulus, the shear strength and the yield strength. Due to the fact that the ceramic is comminuted at the moment of projectile penetration, its mechanical properties may differ from those of the intact bulk material. Therefore, the constants β and γ must be obtained by tuning the model to experimental ballistic limit velocity data.

The ceramic material in a relatively small area directly in front of the projectile is assumed to be very strongly fractured during the shock-wave period of the impact event. It is assumed that this strong comminution has caused significant bulking of this material. Due to the confinement of this bulked material to approximately the same volume that it occupied when unfractured, it is pressurized. This pressure forms an additional resistance to penetration by the projectile, and is represented by the second term in the expression for F. This additional resistance to penetration and its decay are approximated by

$$P = K_c \left(\frac{Vol_0 - Vol}{Vol_0} \right) \qquad \text{for } Vol \leqq Vol_0$$
$$P = 0 \qquad \text{for } Vol > Vol_0 \tag{2.55}$$

where K_c is the ceramic's bulk modulus.

Initially, $Vol_0 > Vol$ due to the bulking of the fractured material. It is very difficult to quantify Vol_0, and thus the additional resistance to penetration P. However, when the projectile penetration velocity is given at the moment that the model is initiated, equations (2.9) and (2.53) must hold and will yield the initial value of P. The initial value of Vol_0 ($Vol_{0_{ini}}$) can then be obtained through equation (2.55).

Experiments with sharp projectiles (Wilkins *et al.*, 1967-1978) have shown that ceramic faced armours present an almost impenetrable barrier to the projectile during the first few microseconds of impact. The penetration velocity just after this period, at the moment that the model is initiated (at $t = t_{breakup}$), is probably considerably lower than the impact velocity.

The initial projectile penetration velocity $\dot{x}_{ini}$, is assumed to be given by

$$\dot{x}_{ini} = \frac{v_0}{\left(1 + \frac{u_{c_{ela}} \rho_c}{u_{p_{ela}} \rho_p}\right)} \tag{2.56}$$

where v_0 represents the projectile velocity. $U_{c_{ela}}$ and $u_{p_{ela}}$ represent the ceramic's and the projectile's longitudinal sonic velocities. Although this equation is strictly speaking only valid at the moment of impact, it is used here as an approximation of the penetration velocity just after the shock-wave period of response. By changing the projectile's longitudinal sonic velocity, $u_{p_{ela}}$, the initial penetration velocity, can be reduced or increased to fit experimental observations.

With the initial penetration velocity $\dot{x}_{ini}$ given, the additional penetration resistance P can be quantified. Introduction of $\dot{x}_{ini}$, the expression for the resistive force F, equation (2.53), and the expression for P, equation (2.55), into equation (2.9) yields

$$\rho_p (v_0 - \dot{x}_{ini})^2 + \sigma_y = \frac{Vol_{0_{ini}}}{Vol_{ini}} \left(\beta (\dot{x}_{ini} - \dot{w}_0) + \gamma\right) + K_c \left(\frac{Vol_{0_{ini}} - Vol_{ini}}{Vol_{0_{ini}}}\right) \tag{2.57}$$

Multiplying both sides of this equation by $Vol_{ini} \cdot Vol_{0_{ini}}$, taking into account that $\dot{w}_0 = 0$ at this moment in time, and regrouping yields

$$Vol_{0_{ini}}^2 \left(\beta \dot{x}_{ini} + \gamma\right) + Vol_{0_{ini}} Vol_{ini} \left[K_c - \left(\rho_p (v_0 - \dot{x}_{ini})^2 + \sigma_y\right)\right] - K_c Vol_{ini}^2 = 0 \tag{2.58}$$

The only unknown in this equation is $Vol_{0_{ini}}$, since Vol_{ini}, the available volume for the comminuted ceramic at the moment of model initiation (see also figure 2.8) is given by

$$Vol_{ini} = \frac{1}{3} \pi h_c \left(\frac{D_p^2}{4} + \frac{D_p}{2} R_{rigid} + R_{rigid}^2\right) \tag{2.59}$$

Equation (2.58) presents the following solution for $Vol_{0_{ini}}$:

$$Vol_{0_{ini}} = \frac{Vol_{ini}}{2\,(\beta\,\dot{x}_{ini} + \gamma)} \left[\rho_p\,(v_0 - \dot{x}_{ini})^2 + \sigma_y - K_c + \right.$$

$$\left. + \sqrt{\left(\rho_p\,(v_0 - \dot{x}_{ini})^2 + \sigma_y - K_c\right)^2 + 4\,(\beta\,\dot{x}_{ini} + \gamma)\,K_c} \right] \qquad (2.60)$$

Substitution of this expression for $Vol_{0_{ini}}$ and the expression for Vol_{ini} into equation (2.55) presents the additional penetration resistance at the moment of model initiation.

In order to compute the penetration resistance decay, the equations which describe the changes of Vol and Vol_0 need to be obtained.
The volume available for the comminuted ceramic Vol, changes due to deformation of the back-up plate and penetration of the projectile. The volume Vol_0 occupied by the comminuted ceramic in a pressureless environment may change due to ceramic material ejection through the impact hole. Since the additional resistance to penetration was found to decay very rapidly, the equations describing the changes of Vol and Vol_0 need to be determined for the first stage of the penetration model only.

At the moment of model initiation, the conoidal volume available for the comminuted ceramic, is given by equation (2.59). The additional volume, created by deflection of the back-up plate, V_{plas}, can be subdivided into two parts ; V_{w_0}, the additional volume created because of the deflection of the central section ($0 < r < r_h$) of the back-up plate and V_w, the additional volume created because of the outside section's deflection ($r_h < r < R$) as is shown in figure 2.14. V_{plas} can thus be written as

$$V_{plas}(t) = V_w(t) + V_{w_0}(t) = \int_0^{2\pi} \int_{r_h(t)}^{R} w(r,t)\, r\,dr\,d\theta + \int_0^{2\pi} \int_0^{r_h(t)} w_0(t)\, r\,dr\,d\theta \qquad (2.61)$$

For application within the model, it is convenient to differentiate this equation with respect to time:

$$\frac{d}{dt} V_{plas}(t) = 2\pi \int_{r_h(t)}^{R} \dot{w}(r,t)\, r\,dr + 2\pi \dot{w}_0(t) \int_0^{r_h(t)} r\,dr - 2\pi\, r_h(t)\, \dot{r}_h(t) \left(w(r_h,t) - w_0(t)\right)$$

(2.62)

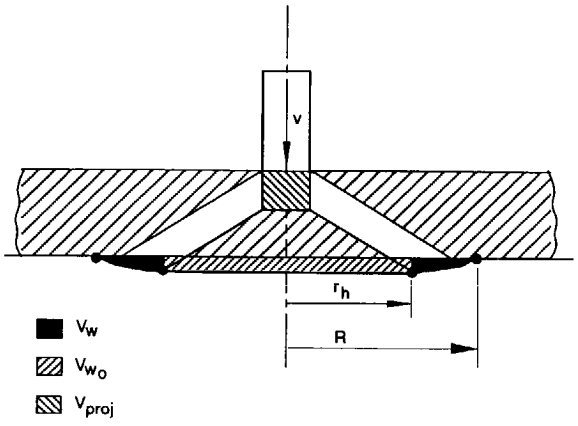

Figure 2.14 Location of additional volume for the comminuted ceramic due to penetration of the projectile and deformation of the back-up plate.

Since in the first stage of the penetration model

$$w(r_h,t) = w_0(t) \tag{2.63}$$

and using equation (2.24), equation (2.62) can be rewritten as

$$\frac{d}{dt}V_{plas} = \frac{2\pi\dot{w}_0'}{(R-r_h)}\left(\frac{1}{6}R^3 - \frac{1}{2}R\,r_h^2 + \frac{1}{3}r_h^3\right) + \pi\,\dot{w}_0\,r_h^2 \tag{2.64}$$

whereby for as long as the initial armour response model is active, $\dot{w}_0'$ is equal to $\dot{w}_0$.

The available volume for the comminuted ceramic also depends upon the projectile's penetration into the ceramic conoid. The amount of volume occupied by the projectile at any given moment during ceramic penetration is given by

$$V_{proj} = \pi\frac{D_p^2}{4}\,x \tag{2.65}$$

Hence, the ceramic conoid volume change due to projectile penetration is given by

$$\frac{d}{dt}V_{proj} = \pi\frac{D_p^2}{4}\,\dot{x} \tag{2.66}$$

Thus, the following expression is found for the change of the available volume for the comminuted ceramic in the first stage of the penetration model:

$$\frac{d}{dt} Vol = \frac{2\pi \dot{w}_0'}{(R - r_h)} \left(\frac{1}{6} R^3 - \frac{1}{2} R r_h^2 + \frac{1}{3} r_h^3 \right) + \pi \dot{w}_0 r_h^2 - \pi \frac{D_p^2}{4} \dot{x} \qquad (2.67)$$

Initially, Vol, is given by equation (2.59).

In experiments, it is often observed that comminuted ceramic ejects from the impact crater. See for example Florence & Ahrens (1967), or figure 3.1 which shows the impact of a 7.62 mm AP projectile onto a ceramic faced armour. Therefore, it is possible that through ejection of comminuted ceramic the confinement of the ceramic material within the conoidal volume decreases.
This option of release of confinement is implemented in the model, although discussions with Bless disclosed that the ejection of debris did not influence the armours resistance significantly during experiments carried out at the University of Dayton Research Institute (Den Reijer,1988).

Basically, the process is modelled by decreasing the mass and thus volume of the comminuted ceramic in the conoidal volume. Ejection of material is assumed to take place through a circular ring around the projectile impact zone. Figure 2.15 illustrates the assumed behaviour. Bernoulli's equation (Clancy, 1975) is used to get an estimate of the (relative) velocity of the ejected particles. It yields

$$P = \frac{1}{2} \rho_c' v_{eject}^2 \qquad (2.68)$$

where the density of the ejected, once strongly comminuted, ceramic is estimated by

$$\rho_c' = \frac{Vol_{ini}}{Vol_{0_{ini}}} \rho_c \qquad (2.69)$$

Thus, the (relative) velocity of the ejected particles is given by

$$v_{eject} = \sqrt{\frac{2P}{\rho_c'}} \qquad (2.70)$$

The mass (and volume) flux out of the impact crater is thus given by

$$\frac{d}{dt} M_{eject} = \rho_c' \frac{d}{dt} Vol_{eject} = \rho_c' \pi \left(r_{hole}^2 - \frac{D_p^2}{4} \right) (v_{eject} - \dot{x})$$

$$= \rho_c' \pi \left(r_{hole}^2 - \frac{D_p^2}{4} \right) \left(\sqrt{\frac{2P}{\rho_c'}} - \dot{x} \right) \qquad (2.71)$$

where, r_{hole} is the ejection hole radius.

Hence, the change of the volume of the comminuted ceramic in a pressureless environment due to ceramic ejection is given by

$$\frac{d}{dt} Vol_0 = - \pi \left(r_{hole}^2 - \frac{D_p^2}{4} \right) \left(\sqrt{\frac{2P}{\rho_c'}} - \dot{x} \right) \qquad (2.72)$$

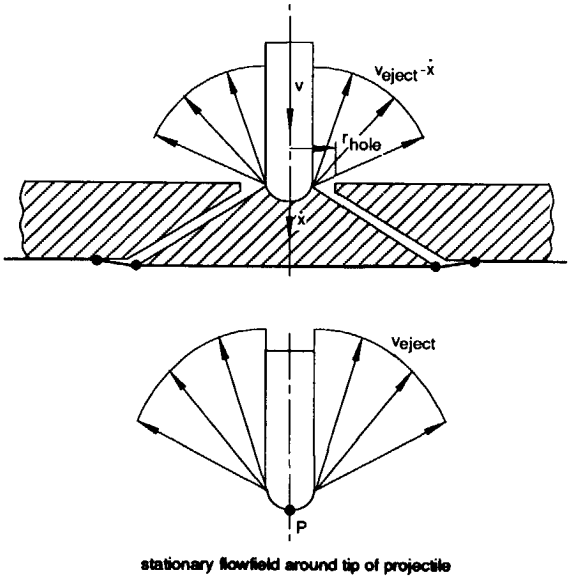

Figure 2.15 Assumed mechanism for the ejection of comminuted ceramic from the impact crater.

2.11. The Analytic Lightweight Armour Response Model (ALARM)

2.11.1. Introduction

The penetration model has been translated into a computer program. This program solves the set of differential equations governing the behaviour of armour and projectile during the impact event. It can be used to compute the penetration process for a single impact velocity, or to predict the ballistic limit velocity (v_{50}) of a specific armour concept. In the following sections a brief outline of the numerical procedure and of the program is presented.

2.11.2. The numerical solution technique

The differential equations derived for the ALARM model, can be represented by a set of maximal 12 first order nonlinear differential equations, schematically represented by,

$$\frac{d\vec{Y}}{dt} = \vec{f}\ (\vec{Y}; t) \tag{2.73}$$

These equations need to be integrated in time. A reliable procedure is required for the integration, with automatic truncation error control, and only a few derivative evaluations for every time step.
The Adams-Moulton predictor-corrector method was selected for this purpose (Gerald & Wheatley, 1984). Only two derivative evaluations are necessary for every time step. The Adams-Moulton method cannot be used to start the integration process. The Runge-Kutta-Gill method is used for this purpose (Gerald & Wheatley, 1984). Both methods have local truncation errors of the same order.
In the integration routine, the local truncation error is controlled as follows. The stepsize, Δt, is reduced whenever the local truncation error estimate exceeds a user-specified upper bound. In those cases the stepsize is reduced to $\Delta t/4$ and the integration process is restarted at $(t-\Delta t)$ by doing three steps of Runge-Kutta-Gill, followed by the Adams-Moulton steps.
If the local truncation error estimate is smaller than a specified lower bound, usually two per cent of the upper bound, the stepsize is increased from Δt to $2\Delta t$. The integration process is again restarted by doing three steps of Runge-Kutta-Gill.

2.11.3. Brief outline of the ALARM program

The ALARM program consists of 16 subroutines with approximately 1900 lines of Fortran-77 code. The personal computer executable is 140 Kb in size. The general flowchart of the program is presented in figure 2.16.
The main program is called BAL, the program starts in this routine. This routine calls INPUT, which reads and echos all input data. Consequently, BAL may calls V50 which, by calling the ALARM routine with different initial projectile velocities determines the ballistic limit velocity. The ALARM subroutine and all the routines it calls actually contain the ALARM model. The ALARM routine calls the BOUND subroutine which sets some constants and boundary conditions for the integration process, followed by a call to the INTEGR routine, the routine that actually controls the integration process. It selects the back-up plate deformation models, the projectile deformation models, checks for armour failure, projectile defeat and end-of-time. In the process it calls the routines BNDBAK and BNDPRO, where specific boundary conditions for the individual back-up plate and projectile deformation models are set. It also calls WSHAPE, which computes the back-up plate's deflected shape, and

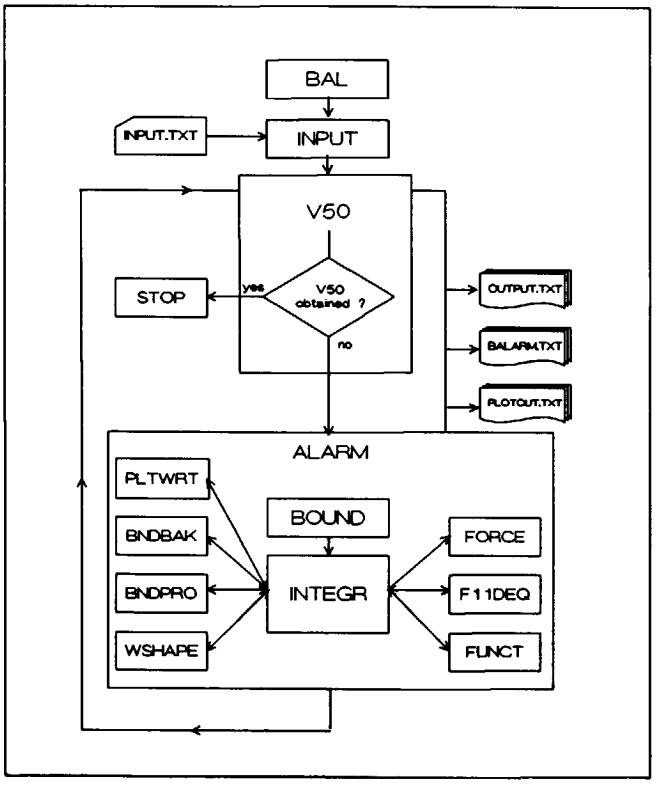

Figure 2.16 Schematic flow chart of the ALARM program lay-out.

PLTWRT, which creates a plotfile to be used by the plotting program. Most important, the INTEGR routine calls F11DEQ, the integration routine. This routine calls FUNCT. The FUNCT routine contains all the sets of first order nonlinear differential equations described governing the behaviour of projectile and armour. At certain instances the FUNCT routine calls the FORCE subroutine, which computes the comminuted ceramic's resisting force.

2.12. Comparison of experimental and analytical results

2.12.1. Introduction

An ALARM computation results in detailed data on the projectile erosion, armour penetration and armour deformation throughout the impact process. By variation of the impact velocity, the armour's ballistic limit velocity can be determined as well.
In order to assess the capabilities of the model, a detailed comparison of the computed results with experimental data is required. However, experimental data showing details of the penetration process are very scarce in literature. Wilkins (1968) presented the data shown in figure 2.17. This figure shows the position of the projectile, the armour penetration and the armour deformation throughout the penetration process for a pointed projectile impacting an armour of AD-85 alumina supported by aluminium at a velocity of 850 m/s. Unfortunately, comparison with Wilkins' own flash radiographs taken at early times after impact (16 μs), figure 2.18, revealed a discrepancy with the situation presented in figure 2.17. Wilkins (1988) confirmed the "plotting error" in this figure, but did not supply the correct data.

Hence, with no reliable detailed experimental data available, the ALARM model predictions can be compared with experimentally obtained ballistic limit velocities only. For this purpose, two series of Wilkins' ballistic limit velocity experiments with pointed .30" (7.62 mm) armour piercing projectile simulators impacting various armours of AD-85 and aluminium 6061-T6 were used. In addition, the influence of back-up plate bending stiffness is assessed. These comparisons served as the first overall checks of the validity of the model.

2.12.2. Simulation of Wilkins' ballistic limit velocity experiments

ALARM ballistic limit velocity computations were carried out for ceramic faced armours consisting of an AD-85 alumina facing, 8.6 mm or 7.9 mm thick, supported by several thicknesses of aluminium 6061-T6. In order to obtain results which compare well to the experiments, three parameters had to be tuned. Tuning of these parameters is necessary and inevitable, since no data was available which could be used in determining the value of the parameters in the ceramic resistance force function.

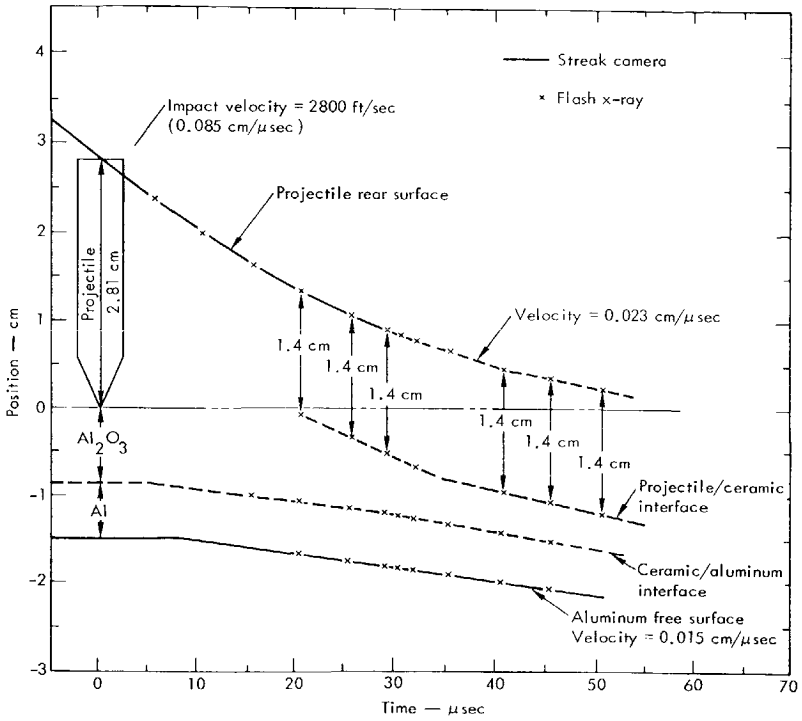

Figure 2.17 Position-versus-time curve of a 7.62 mm AP projectile simulator impacting an armour of 8.6 mm thick Coors AD-85 alumina backed by 6.3 mm thick 6061-T6 aluminium at 850 m/s (Wilkins, 1968).

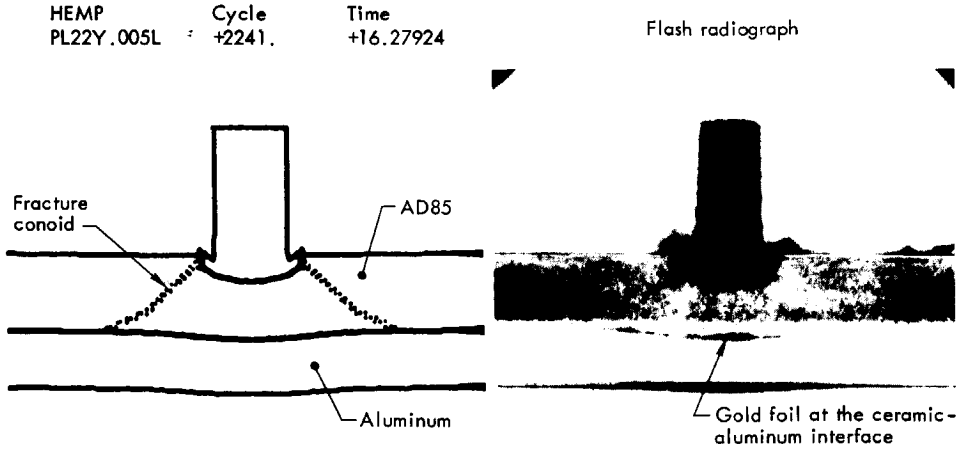

Figure 2.18 Comparison between calculation and experiment at 16 μs after impact of a 7.62 mm AP projectile simulator onto 8.6 mm thick AD-85 alumina bonded to 6.3 mm thick 6061-T6 aluminium. Impact velocity is 850 m/s (Wilkins *et al.*, 1969).

These three parameters are β, γ and r_{hole}. The values were obtained by trail and error and are given by,

β	$= 0.600$	10^7	(-)
γ	$= 0.675$	10^9	(-)
r_{hole}	$= 0.005$		(m)

Results of the ALARM computations are presented in table 2.1 while in figure 2.19 the computed ballistic limit velocities versus back-up plate thicknesses are presented for the above configurations.
The results obtained with other analytic penetration models for ceramic faced armours are also included in this figure to allow for comparison. Florence's model is based on a simplified back-up plate membrane deflection, and therefore, not capable of describing bending or plug shearing, which according to experimental observations are very important deformation mechanisms for armours with thicker (>5.5 mm) metallic back-up plates. Not surprisingly therefore, the ballistic limit velocities computed by Florence's model do not compare well to the experimental values. Recently, a comprehensive analytic model for projectile impact onto ceramic faced armours was proposed by Woodward (1990). In this publication, he compared his model predictions with the same set of experimental data as is done here. His model predictions are, therefore, included in figure 2.19 too.
For the two other analytic models, the one presented by Prior & Hetherington (1986) and the one presented by Ravid *et al.* (1989), no model predictions of the experimental data by Wilkins were available. Hence, they are not included in figure 2.19. The comparison presented in figure 2.19 shows that the predictions by the ALARM model match the experimental ballistic limit velocity data better than the predictions from the models by either Florence or Woodward.

Graphs with detailed information regarding the computed projectile mass erosion, projectile and back-up plate velocities and displacements, pressures on the projectile and strain in the back-up plate are presented in the figures 2.20, 2.21, 2.22 and 2.23, for armours with thin (3.1 mm), normal (5.0 mm, 6.3 mm) and thick (9.0 mm) aluminium 6061-T6 back-up plates. In each figure, five history plots are presented. In one of them (plot A), the projectile's rear-end velocity, projectile/armour interface velocity (projectile tip velocity) and back-up plate velocity are presented. Others show the projectile mass erosion (plot B), the load exerted on the armour (plot C), the position of the projectile/armour interface, the maximum back-up plate deformation and the maximum back-up plate deformation of the outer annular plate section at the location of the hinge at $r = r_h$ (plot D), and the accumulated strain in time (plot E).
Plot E in the figures 2.20 and 2.21 shows that the radial strain in the back-up plate reaches the limiting value of 13 per cent (for Al 6061-T6). Hence, the failure mode for armours with thin back-up plates is strain failure. This failure mode remains dominant for back-up plates up to 5.5 mm thick. For back-up plate thicknesses above 5.5 mm, a plug shearing failure mode appears to be dominant, as can be deduced from the figures 2.22 and 2.23. The radial strain history plots (E) in these figures

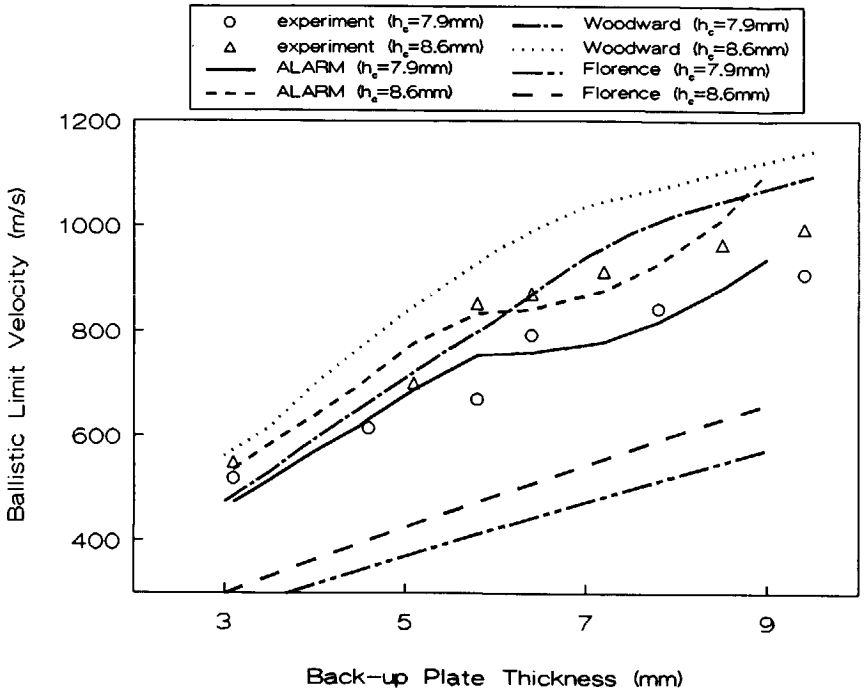

Figure 2.19 Comparison of ballistic limit velocities obtained by experiments (Wilkins, 1968), the ALARM model, Florence's model (1969) and Woodward's model (1990), for armours of AD-85 alumina backed by various thicknesses of 6061-T6 aluminium impacted by 7.62 mm AP projectile simulators at normal incidence.

show that the radial strain does not come close to the limiting value of 13 per cent (for Al 6061-T6). The back-up plate responses presented in plot D of these figures, do show a significant amount of plug shearing action as there arises a difference between the maximum back-up plate displacement (w_0) and the maximum back-up plate displacement of the outer annular back-up plate section at $r = r_h$ (w_0'). Although the projectile is brought to rest just before the plug separation is completed in these two figures, a slight increase of the initial impact velocity will show plug shearing as the failure mode.

The change in back-up plate failure mode at a back-up plate thickness of approximately 5.5 mm was also observed experimentally by Wilkins (1968).

When figure 2.19 is considered, it is observed that for back-up plate thicknesses from 5.5 mm through 9.0 mm the predicted ballistic limit velocities compare very well to the experimental values. For very thin (< 3.0 mm) and thick (> 9.0 mm) back-up plates the ALARM results deviate from the experimental values, mainly because of the description used for the back-up plate deformation. The ALARM back-up plate

deformation models are based on plastic bending hinges and are not accurate when used in describing membrane deformation, the primary deformation model for armours with very thin back-up plates. The very thick back-up plates are loaded on a relatively small area compared to the thickness of the back-up plate, making the use of plastic hinges to describe the deformation questionable.

Table 2.1 Comparison between ballistic limit velocities obtained with the ALARM model and experiments (Wilkins, 1968) for armours composed of Coors AD-85 alumina and aluminium 6061-T6, when impacted by an 8.5 gram 7.62 mm AP projectile simulator.

Back-up plate thickness	Ceramic thickness h_c = 8.6 mm		Ceramic thickness h_c = 7.9 mm	
[mm]	v_{50} ALARM [m/s]	v_{50} exp. [m/s]	v_{50} ALARM [m/s]	v_{50} exp. [m/s]
3.0	522			
3.1	536	549	473	518
3.5	583		515	
4.0	638		570	
4.5	696		619	
4.6	711		632	614
5.0	764		673	
5.1	777	701	689	
5.5	819		735	
5.8	834	853	754	670
6.0	836		758	
6.3	842	871	759	792
6.5	848		761	
7.0	869		773	
7.2	879	914	781	
7.5	901		797	
7.8	928		819	843
8.0	948		835	
8.5	1012	965	883	
9.0	1103		939	
9.4	1233	995	990	909
9.5	-		1004	

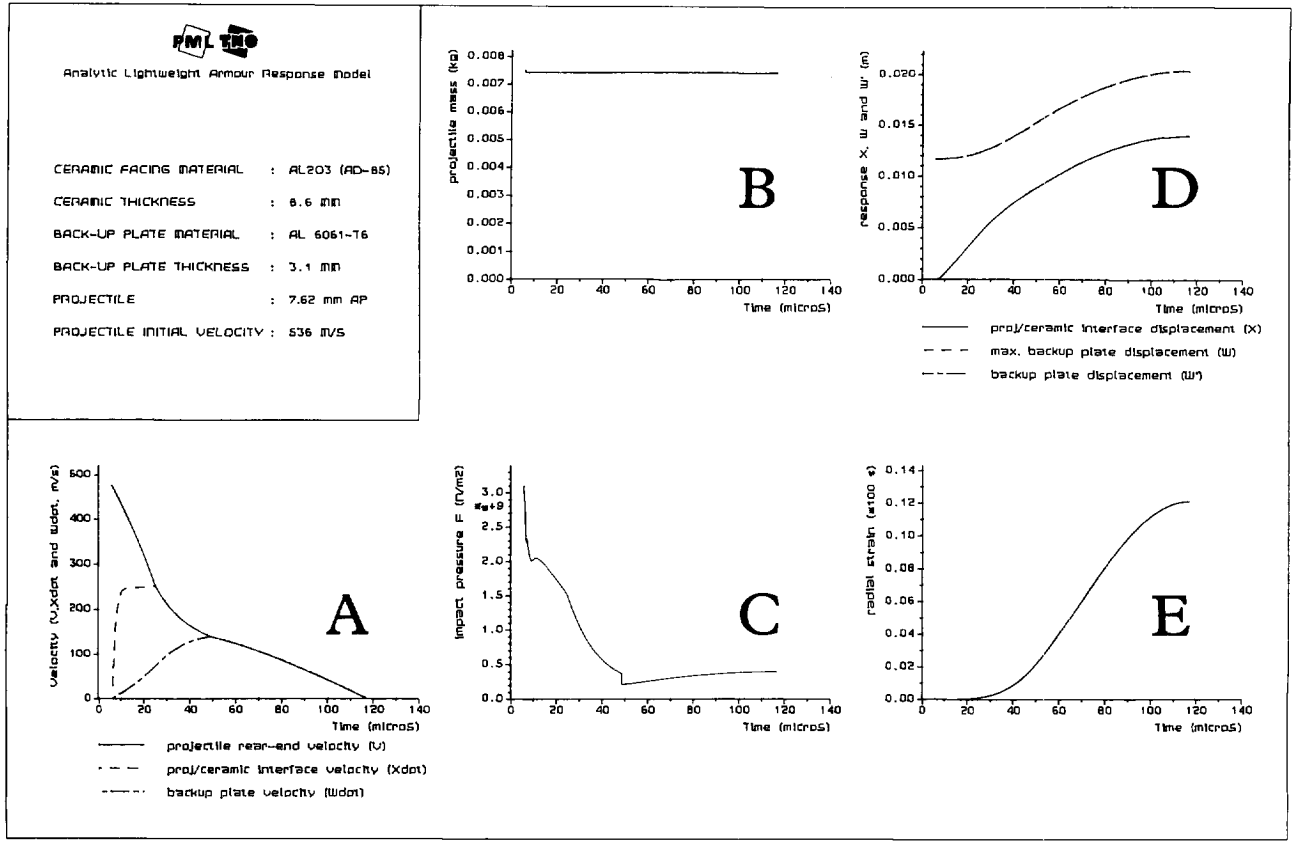

Figure 2.20 Computed mass, displacements, velocities, pressure and strain histories for an armour of 8.6 mm thick AD-85 alumina backed by 3.1 mm thick 6061-T6 aluminium, impacted by a 7.62 mm AP projectile simulator at a velocity of 536 m/s.

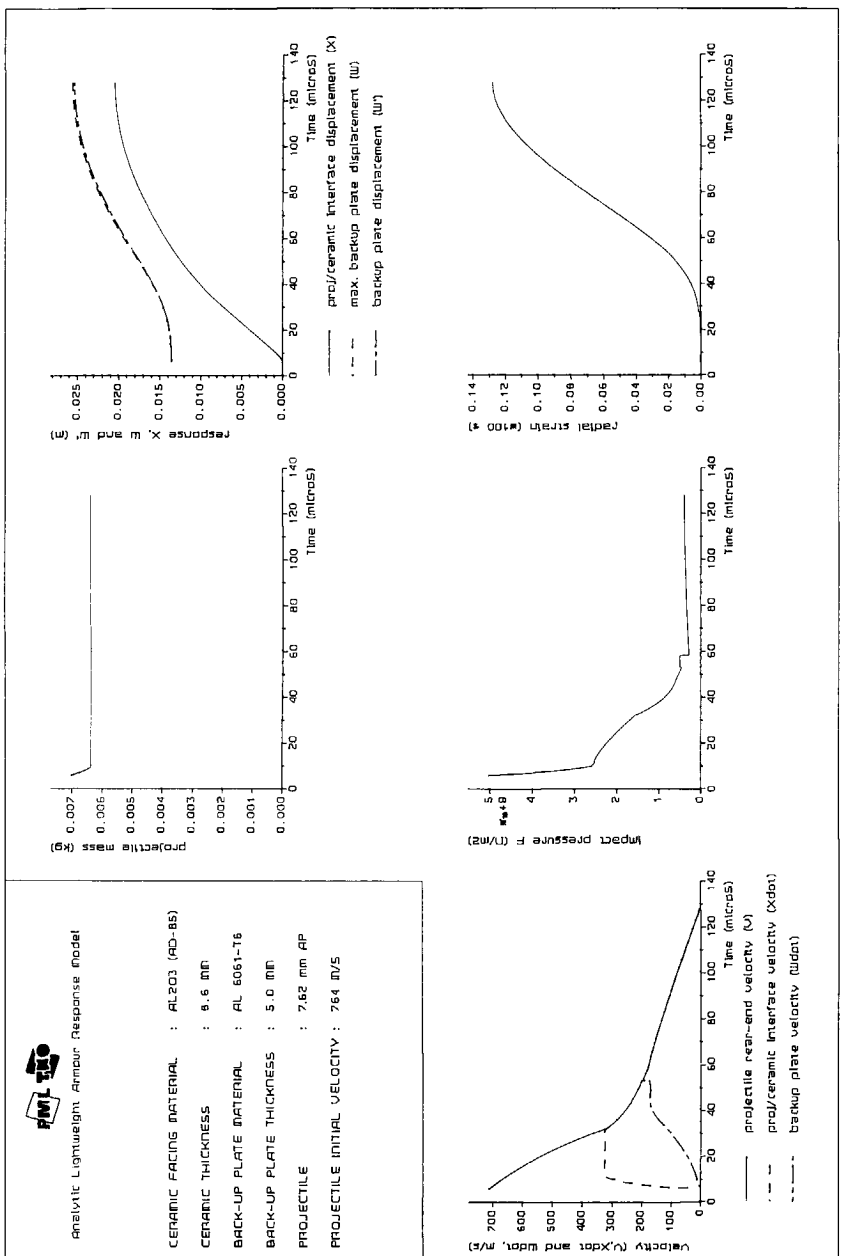

Figure 2.21 Computed mass, displacements, velocities, pressure and strain histories for an armour of 8.6 mm thick AD-85 alumina backed by 5.0 mm thick 6061-T6 aluminium, impacted by a 7.62 mm AP projectile simulator at a velocity of 764 m/s.

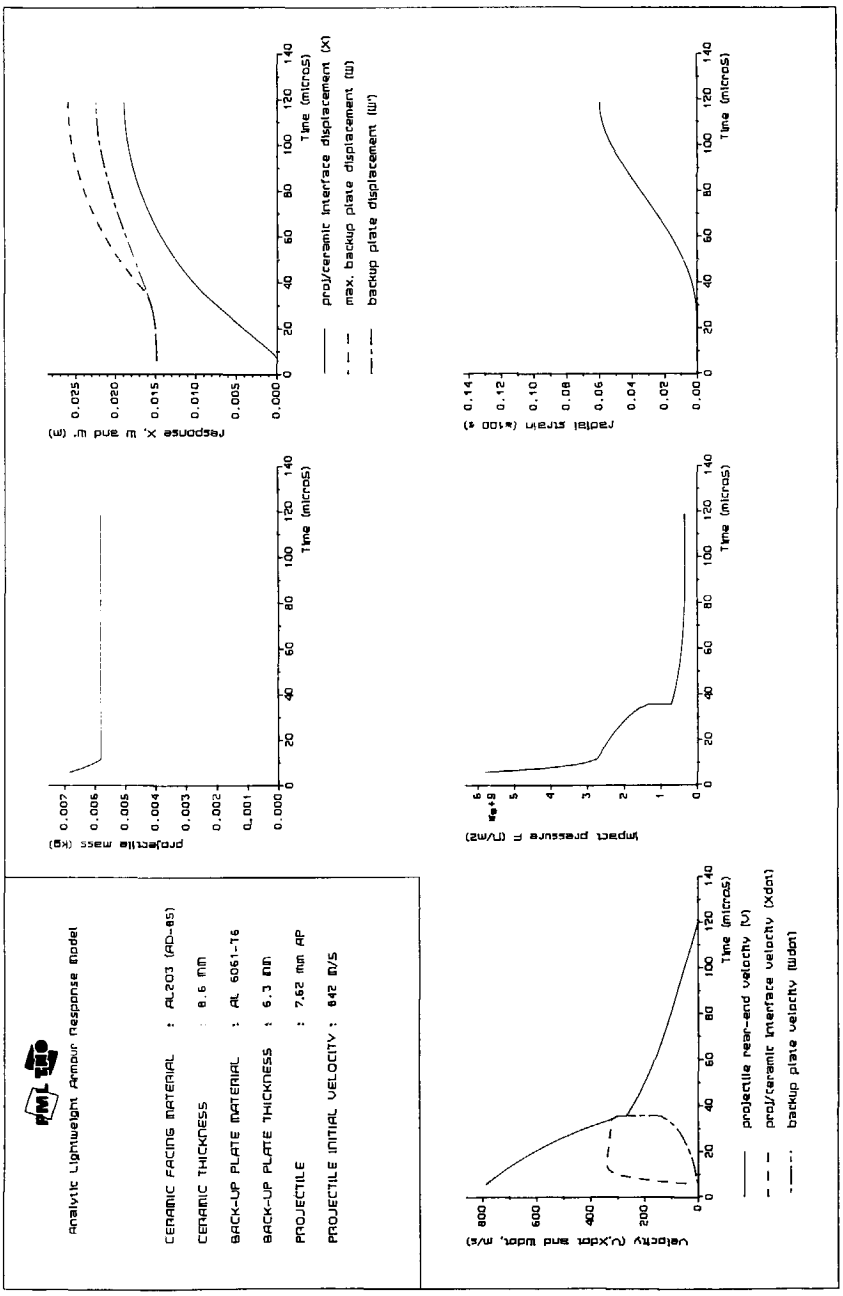

Figure 2.22 Computed mass, displacements, velocities, pressure and strain histories for an armour of 8.6 mm thick AD-85 alumina backed by 6.3 mm thick 6061-T6 aluminium, impacted by a 7.62 mm AP projectile simulator at a velocity of 842 m/s.

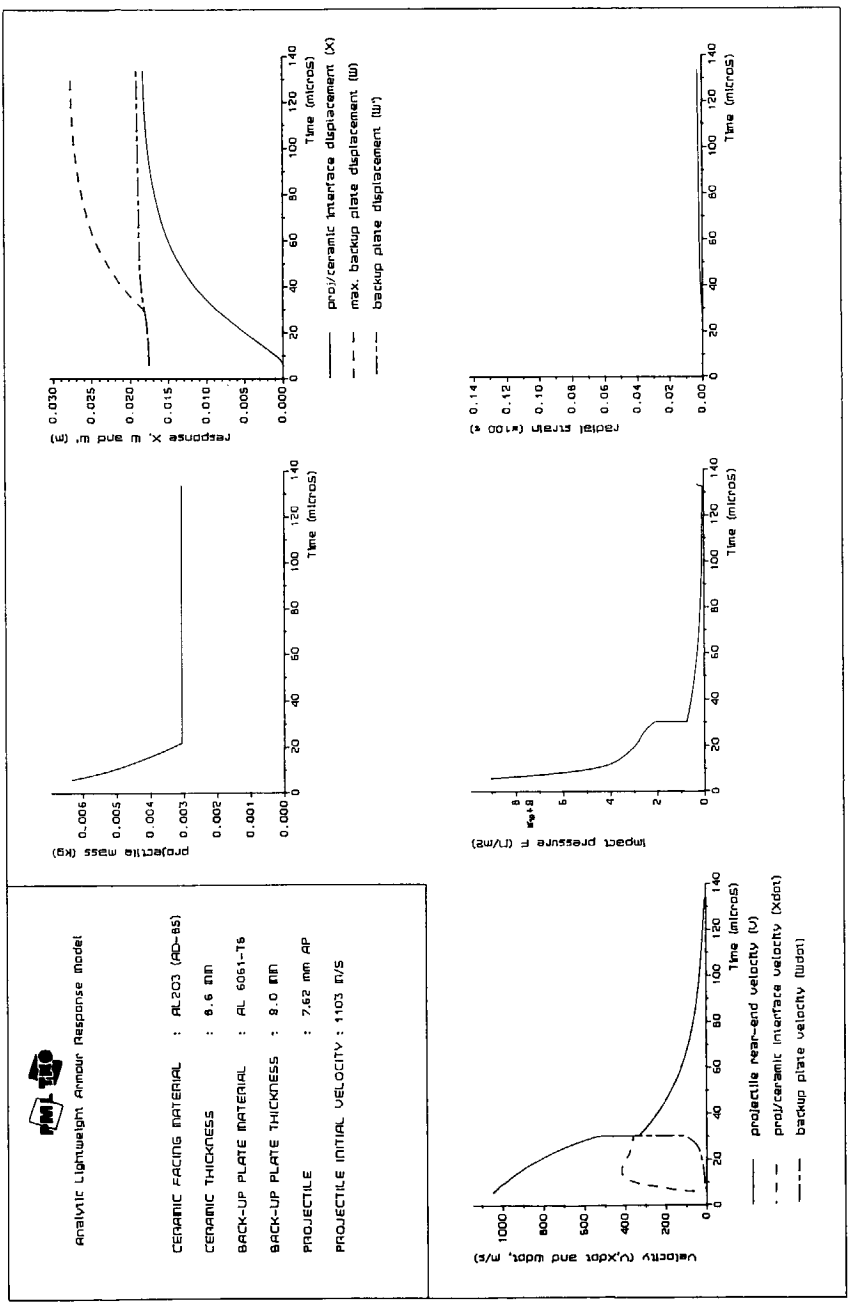

Figure 2.23 Computed mass, displacements, velocities, pressure and strain histories for an armour of 8.6 mm thick AD-85 alumina backed by 9.0 mm thick 6061-T6 aluminium, impacted by a 7.62 mm AP projectile simulator at a velocity of 1103 m/s.

2.12.3. A two-layer back-up plate

One of the reasons to develop a lightweight armour response model was to study the influence of back-up plate properties, such as bending stiffness. In the literature (Wilkins, 1968; Laible, 1980) it is reported that for an 8.6 mm thick layer alumina backed by two layers of 3.15 mm thick aluminium, the ballistic limit velocity drops almost 100 m/s as compared to the v_{50} of a similar armour with a single layer 6.3 mm thick back-up plate. According to Wilkins (1968), this drop in v_{50} is caused by the increased flexibility of the two-layer back-up plate which is less capable of confining the comminuted material inside the fracture conoid and thus allows the projectile to penetrate the armour more easily. The ALARM model was used to check whether it could reproduce this experimental result.

The model predicts an 80 m/s decrease of the ballistic limit velocity for an armour which consists of an 8.6 mm thick alumina facing backed by two layers of 3.15 mm thick aluminium 6061-T6 compared to the armour with a single 6.3 mm thick back-up plate. This is conform the experimental results. When the same ceramic facing is supported by two layers of 2.5 mm thick aluminium instead of a single 5.0 mm thick back-up plate, the ALARM model predicts the ballistic limit velocity to drop by 114 m/s. ALARM computations show a drop in the ballistic limit velocity of only 19 m/s, when the ceramic facing is supported by two layers of 4.5 mm thick aluminium instead of a single 9.0 mm thick back-up plate. Hence, the drop of the ballistic limit velocity due to layering of the back-up plate is found to depend on the armour configuration.

Understanding of this behaviour can be obtained by analysis of the back-up plate responses and failure modes for the two extreme situations. For the armour with the 5.0 mm thick back-up plate, the dominating failure mode is strain failure, as is illustrated by figure 2.21. Changing the stiffness of the back-up plate by layering it, increases its flexibility, causing a faster armour response and the strain failure to be reached even earlier. Hence, the increased flexibility results in an decreased energy dissipation by the back-up plate, and thus in a significantly lower ballistic limit velocity. For the armour with the 9.0 mm thick back-up plate, the plug shearing failure mode dominates. Only a limited amount of kinetic energy is dissipated by the back-up plate surrounding the plug, as is illustrated by figure 2.23. Hence, its energy dissipation can be improved. The increased flexibility of the layered back-up plate results in a reduced ceramic confinement and thus more projectile kinetic energy has to be dissipated by the armour. The increased flexibility, however, also facilitates back-up plate deformation, as is shown in figure 2.24. In this situation, the failure mode is not significantly changed by the increased flexibility. Hence, the back-up plate can decelerate the projectile for a longer period of time and can dissipate more energy before back-up plate failure occurs. The resulting drop in ballistic limit velocity of this layered armour is, therefore, not large (19 m/s) and shows that the increased flexibility of the layered back-up plate almost compensates the negative effects.

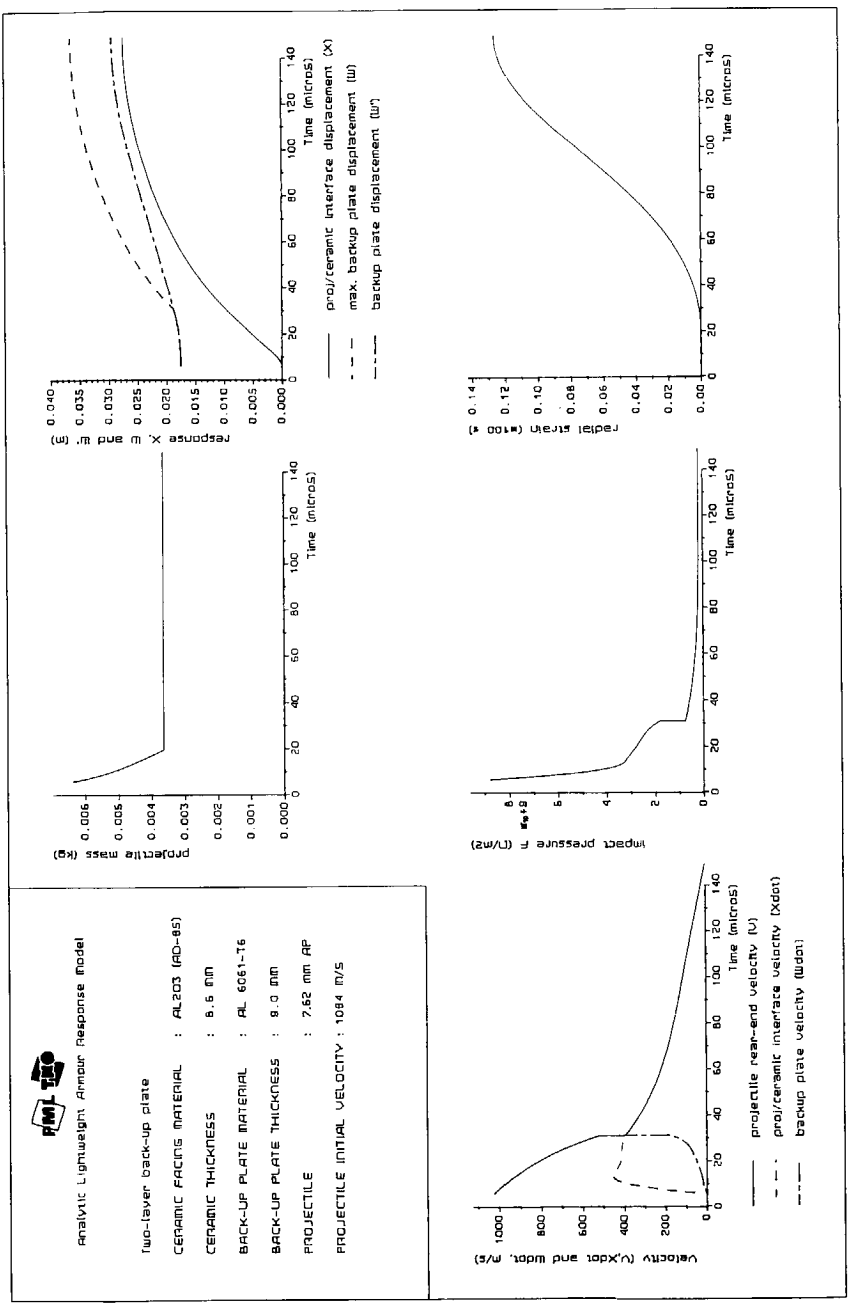

Figure 2.24 Computed mass, displacements, velocities, pressure and strain histories for an armour of 8.6 mm thick AD-85 alumina backed by two layers of 4.5 mm thick 6061-T6 aluminium, impacted by a 7.62 mm AP projectile simulator at a velocity of 1084 m/s.

The analysis of these simulations indicates that the magnitude of the drop in ballistic limit velocity of an armour with a two-layer back-up plate depends on the additional projectile kinetic energy that has to be dissipated by the armour due to the reduced ceramic confinement and the (additional) energy dissipation by the layered back-up plate.

2.13. Conclusions

A simple analytic model has been developed that is capable of carrying out ballistic limit velocity computations for ceramic faced lightweight armours. It describes the major phenomena, known to be of importance for the penetration process, such as: projectile mass erosion and mushrooming during ceramic penetration, time-dependent loading and load distribution on the back-up plate, deformation of the back-up plate and strain and shear failure modes for the back-up plate.
Although some parameters need to be tuned to insure that the computed armour and projectile behaviour compare to the experimentally obtained values, the model appears capable of describing the effect on the ballistic limit velocity of (limited) variations of the armour geometry and properties. The back-up plate failure modes as predicted by the model are in agreement with experimental observations.

3. IMPACT EXPERIMENTS ON CERAMIC FACED ARMOUR

3.1. Introduction

In the previous chapter, the available knowledge in literature was compiled in the attempt to form a consistent understanding of the penetration process of a projectile into a ceramic faced armour. Unfortunately, literature was found to be lacking in reliable and detailed experimental data on a number of important aspects of the projectile/armour interaction process.
For example, the penetration of the projectile through the comminuted ceramic inside the fracture conoid was not very well understood. Nor was the interaction between the ceramic layer and the back-up plate completely clear. Projectile mass erosion, a very important mechanism by which an armour can reduce the amount of kinetic energy that it has to absorb, forms another example of some controversy. Wilkins' analysis of flash radiographs in his third progress report on light armour (1968), shows the projectile eroding mass during the first 20 μs of the impact event. Ravid *et al.* (1989), however, assume that the projectile erodes only for a very short period of time (some 2.5 μs) and may break up into a number of fragments afterwards. Bless (Den Reijer, 1988) assumes that all mass erosion occurs during the time that the armour appears to behave like a rigid anvil (the so-called dwell-time), implying that all projectile mass erosion occurs as the projectile has not yet even started to penetrate the ceramic facing. According to Bless, this dwell-time is strongly dependent on the ceramic fracturing process.

Therefore, the main objective to carry out an experimental programme was to obtain information on the projectile/armour interaction process for a number of different projectiles and armour configurations. To fulfill this objective, the results of the experiments needed to show details of: the projectile erosion process, the penetration process into the armour, and the armour's response. The experimental data thus becoming available, could also be used for the verification and validation of the behaviour predicted by the ALARM model.

3.2. The experimental programme

The understanding of the pentration mechanisms dominating the impact event was expected to benefit most from impact experiments with simple projectiles and armours. Therefore, a blunt circular-cylindrical rod was used as a projectile with most of the experiments. The armours used consisted of a homogeneous ceramic facing supported by an aluminium back-up plate. The back-up plates were not reinforced by modern composite materials.

In order to study the influence of the back-up plate properties, armours with four types of back-up plates were used. A concept of 8.1 mm thick alumina, backed by 6.0 mm

aluminium, weighing 47 kg/m^2, was used as a base-line reference. This armour just defeats the 7.62 mm AP projectile at muzzle velocity (840 m/s).
Experiments were also carried out with armours consisting of an 8.1 mm thick ceramic facing supported by heavier, 8.0 mm thick, and lighter, 4.0 mm thick back-up plates. The thick back-up plate gives optimal support to the comminuted ceramic inside the conoid. The thin back-up plate cannot support the ceramic facing very well, but deforms and absorbs energy easily. Based on Wilkins' observations (1968), it was expected that the failure modes of these back-up plates differed. Hence, including armours with these back-up plates in the programme allowed study of the apparent differences in the projectile/armour interaction processes caused by these different back-up plates. The projectiles were also fired at a concept with two 3.0 mm thick layers of aluminium instead of the single 6.0 mm thick layer. According to literature (Wilkins, 1968; Laible, 1980), the two-layer back-up plate, which has a four-times lower bending stiffness than the single 6.0 mm thick back-up plate, would cause the armour's ballistic limit velocity to decrease by almost 100 m/s. Since the armour with the 6.0 mm thick aluminium back-up plate was designed such that its ballistic limit velocity lies slightly above the 7.62 mm AP projectile's muzzle velocity (840 m/s), the armour with the double back-up plate was expected to be defeated by the projectile. This presented the possibility to study projectile defeat and perforation at identical projectile velocity and armour areal density.

In order to obtain a complete overview of the projectile/armour interaction processes with these armours, the rods were fired into them at velocities just above and below their ballistic limit velocities.

The applicability of the results obtained with the rod projectiles for the 7.62 mm AP projectile impact situation had to be ensured. Therefore, the rod was to be designed such that it inflicted a similar response to the armour, with the same magnitude of stress and time-scale of events, as would result from a 7.62 mm AP projectile impact. In order to obtain references, a number of experiments were also conducted with standard 7.62 mm AP (hard-core) and 7.62 mm ball (soft-core) projectiles.

Thus, the experimental programme included the following series:

- steel rod impact on the four ceramic faced armour concepts, at velocities above and below the ballistic limit velocity.
- 7.62 mm AP (hard-core) projectile impact at muzzle velocity (840 m/s) on the ceramic faced armour concepts with 6.0 mm and with 2*3.0 mm thick back-up plates.
- 7.62 mm ball (soft-core) projectile impact at muzzle velocity (830 m/s) on the ceramic faced armour concept with the 6.0 mm thick back-up plate.

3.3. The experimental set-up

3.3.1. Introduction

Recent experiments with lightweight armour systems (Van Riet, 1987-1991) have shown the difficulty of using optical techniques for instrumenting impact experiments onto ceramic faced lightweight armour systems. Soon after impact, fine ceramic dust is ejected from the impacted area which obscures the view for optical high speed cameras, as is illustrated in the sequence of Imacon frames in figure 3.1 for a 7.62 mm AP projectile impacting a ceramic faced armour. Of course, the back-up plate motion can easily be observed optically before perforation. Aside from dust problems, it is impossible to obtain information regarding the actual projectile penetration into the ceramic faced armour using an optical technique.

The use of flash X-ray photography provides a solution. X-rays are a form of electromagnetic radiation, with wavelengths very much shorter (from 1/1000 to 1/100000) than that of visible light. This distinctive characteristic forms the basis of the ability of X-rays to penetrate materials which may absorb or reflect light. X-rays proceed in straight lines towards the objects; some of the X-rays pass through, others are absorbed. The intensity of X-ray radiation is reduced during transmission of material by absorption. The intensity of the transmitted radiation depends on the

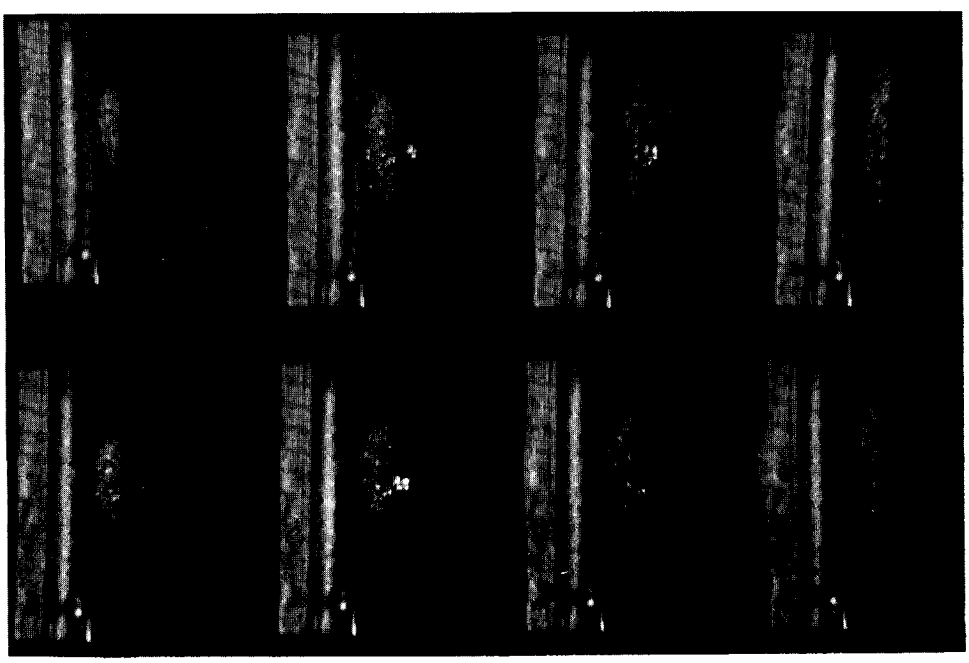

Figure 3.1 Imacon high speed camera photographs of a 7.62 mm AP projectile impacting a ceramic faced armour at 840 m/s.

intensity of the incident radiation, the material absorption coefficient and the thickness of the material traversed.
Exposure of films is realized by converting X-rays to visible light by light intensifying screens. When objects are traversed, the intensity of the X-ray radiation is attenuated, resulting in a lower degree of film exposure. The darker regions on the film represent the more easily penetrated parts of the objects and the lighter regions the more opaque. Therefore, the image recorded on the film (the flash radiograph) can be regarded as a shadowgraph of an object.

In the sixties, Wilkins conducted flash X-ray experiments with ceramic faced armours in an attempt to obtain detailed information on the penetration process. He carried out his experiments with 2-inch wide strips of alumina tiles supported by aluminium. By setting up his flash X-ray system in line with the armour's front surface (normal to the projectile's line of flight), the resulting flash radiographs presented information regarding the projectile's rear-end position, armour penetration and armour deformation. Similar results could be obtained by using the Prins Maurits Laboratory's Field Emission (model 730/2660) 600 kV flash X-ray system, since the steel core of the 7.62 mm AP projectile is visible on the flash radiograph as it is surrounded by no more than 50 mm of alumina (ρ = 3800 kg/m^3). However, experiments at PML's small calibre test range with single and multiple 50 x 50 mm tile configurations, showed a significant influence of the ceramic layer's lateral dimensions on the ballistic protection level. Figure 3.2 shows pre and post-impact photographs of two armours. The armour on top consisted of a single 8.1 mm thick alumina tile, with dimensions 50 x 50 mm, bonded to a large plate of aluminium. The other aluminium back-up plate was completely covered with 8.1 mm thick alumina tiles. The bonding layer between ceramic and back-up plate and processing were identical for both armours. Both were impacted by 7.62 mm AP projectiles at muzzle velocity (840 m/s). The back-up plate on top clearly shows a perforation, the other does not. This illustrates that a single 50 mm (approximately 2-inch) wide strip of armour material, as used by Wilkins, clearly influences the performance of the armour (in a negative way).

Additional experiments were carried out in an attempt to construct some means to apply the correct amount of lateral confinement corresponding to the situation encountered with a fully covered armour panel. The confining material had to be of low density and thickness to prevent significant absorption of the X-rays. An example of such a confinement ring around the ceramic tile is shown in figure 3.3. None of the confinement rings worked satisfactorily.

A flash X-ray set-up was therefore required which could visualize the projectile during impact for armour panels with large (155 mm x 155 mm) lateral dimensions. This was realized with flash X-ray pulsers set up in an oblique fashion so that the direction of the X-rays are at a small angle (26°) to the armour's front face. At this angle the X-rays only have to penetrate some 18 mm of alumina and 9-18 mm of aluminium aside from the projectile. This is easily achieved by a 600 kV system.

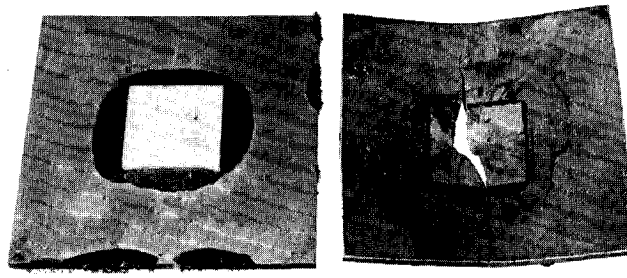

before impact after impact

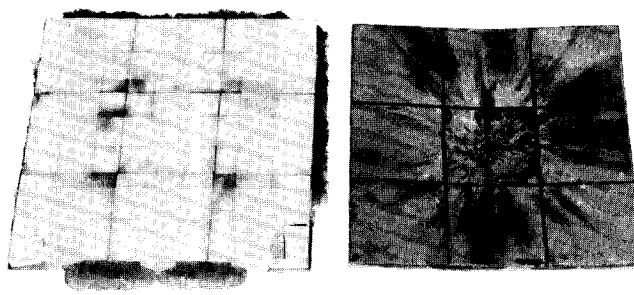

before impact after impact

Figure 3.2 Influence of armour panel ceramic facing lateral dimensions on ballistic performance of the panel when a 7.62 mm AP projectile impacts at 840 m/s.

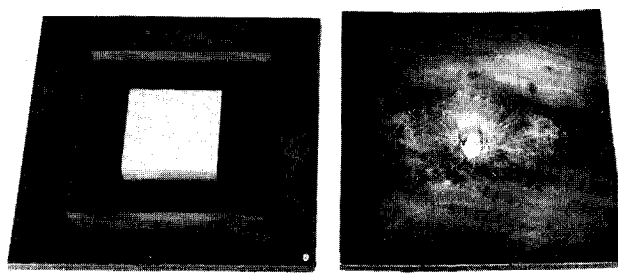

before impact after impact

Figure 3.3 The effect of a confinement ring around a single ceramic tile of a panel when a 7.62 mm AP projectile impacts at 840 m/s.

In order to be able to follow the entire penetration process in some detail, flash radiographs were generated at 2, 4, 6, 8, 10, 12, 14, 16, 20, 25, 30, 35, 40/45, and 60 μs after impact, covering the entire interesting timespan of the impact process. Of course the eroded projectile, the ceramic facing fragments and the back-up plates were recovered as well after every experiment.

3.3.2. The armour panels

The armour panels were composed of 8.1 mm thick Morgan Matroc Hilox 973 alumina and aluminium 6061-T6. For the bonding layer Scotchdamp BA-9323 from 3M was used. Based on the experimental observations discussed in the previous section, the lateral dimensions of the armour panels were set to 155 mm. Because the alumina was available as tiles of 50 x 50 mm only, nine tiles had to be used to completely cover the panel. Four back-up plate configurations were used; a single 4.0 mm thick plate, a 6.0 mm thick plate, a package of two unbonded 3.0 mm thick plates, and an 8.0 mm thick back-up plate. The material properties of the alumina and aluminium are presented in table 3.1.

To ensure proper bonding of the ceramic tiles to the aluminium plate the ceramic tiles were cleaned with methylchloroform (CH_3CCl_3). The aluminium plates were degreased (30 minutes in a bath of P_3RST (40 grams/l) at 75° C) and etched (20 minutes in a bath of chromic acid CrO_3 (55 grams/l) and sulphuric acid H_2SO_4

Table 3.1a Material properties of Morgan Matroc Hilox 973 alumina.

Density	[kg/m^3]	3810.0
H_V	[kg/mm^2]	1217 ± 67
Young's modulus	[GPa]	378 ± 15
Longitudinal sonic velocity	[mm/μs]	10.82 ± 0.22
Flexural strength	[MPa]	~230
Compressive strength	[MPa]	~1700
Grain size	[μm]	1-20
Open porosity	[%]	0
Poisson's ratio (estimated)		0.24
Bulk modulus	[GPa]	242

Table 3.1b Properties of aluminium 6061-T6.

Density	[kg/m^3]	2705.0
Ultimate yield strength	[MPa]	310
Ultimate shear strength	[MPa]	200
Failure strain	[%]	13

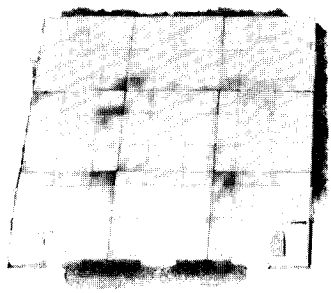

Figure 3.4 Typical example of an armour panel resulting from the vacuum bag manufacturing process (8.1 mm alumina and 4.0 mm aluminium).

(275 grams/l) at 60° C). Afterwards the aluminium plates were rinsed with cold water and dried. The bonding material was applied to the aluminium plate after which the individual tiles were placed by hand. Proper alignment was ensured by wrapping tape around the plates to prevent motion of the ceramic tiles before hardening of the bonding layer.
To ensure good bonding, a vacuumbag technique was used to apply the proper amount of pressure to all the tiles. For this purpose, the panels were placed on a thick aluminium plate, which was covered by a teflon foil. On top of the armour plates another teflon foil was placed together with a woven glass fabric. The entire plate was then covered by a thin plastic foil. By means of a small vacuum pump the enclosed volume was evacuated. For the entire 24 hours of hardening time of the bonding layer (at room temperature) the vacuum pump was left attached to the vacuumbag. The resulting bonding layer was thin (approximately 0.2 mm).
Armour panels like the one shown in figure 3.4 are the result of this manufacturing process.

3.3.3. The projectiles

The choice of the rod's geometry and material properties was based on a number of requirements. The rod was required to have similar penetration capabilities as the 7.62 mm AP projectile. This 7.62 mm AP projectile consists of a hard steel (R_C = 60) ogive-nosed core, followed by a lead plug and is surrounded by a tombac jacket (see figure 3.5). It has a maximum diameter of 7.62 mm, is 32.0 mm long, and weighs 9.55 grams.
In order to ascertain the same time-scale of events and magnitude of stress in the armour, the impact velocity of the rods was required to be close to the muzzle velocity of the standard projectile, typically some 840 m/s. The rod's length-over-diameter ratio had to be slightly higher then the 7.62 mm AP's ratio. This facilitated the determination of the projectile mass erosion during the impact process. In order to

reduce projectile-originated scatter in the experimental results, high strength steel alloys were rejected for use. These alloys are often very brittle which may result in unpredictable break-up during impact, and thus scatter with respect to the ballistic performance.

Ballistic impact experiments with various rods resulted in the selection of a rod. The selected rod weighs 7.0 grams, has a 6.0 mm diameter and is 31.5 mm long (L/D = 5.3). This rod is manufactured from steel (ETG-100; von Moos Stahl AG Luzern). The quasi-static material properties of ETG-100 are presented table 3.2. Figure 3.5 shows the steel rod.

Table 3.2 Properties of ETG-100 steel.

Density	[kg/m^3]	7800
Ultimate yield strength	[MPa]	1030
Ultimate shear strength	[MPa]	590
H_{rc}		28
Failure strain	[%]	7

Support for the selection of the 6.0 mm diameter rod was obtained by Van Zuidam (1990). Using streak photography he measured the maximum back-up plate deformation profiles of ceramic faced armours when impacted by various projectiles. The ceramic armours in his study consisted of a 10.0 mm thick alumina facing supported by 4.0 mm aluminium. Aside from the 7.62 mm AP projectile, blunt steel rods with 5 mm, 6 mm, 7 mm, and 8 mm diameters, all weighing seven grams, were fired at the armours at approximately 820 m/s. The results of these experiments are comprised in figure 3.6. The back-up plate response that resulted from the 6 mm

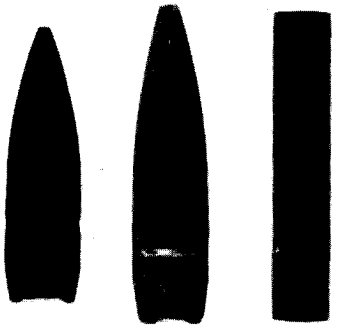

Figure 3.5 The 7.62 mm ball projectile, the 7.62 mm AP projectile and the steel rod (from left to right).

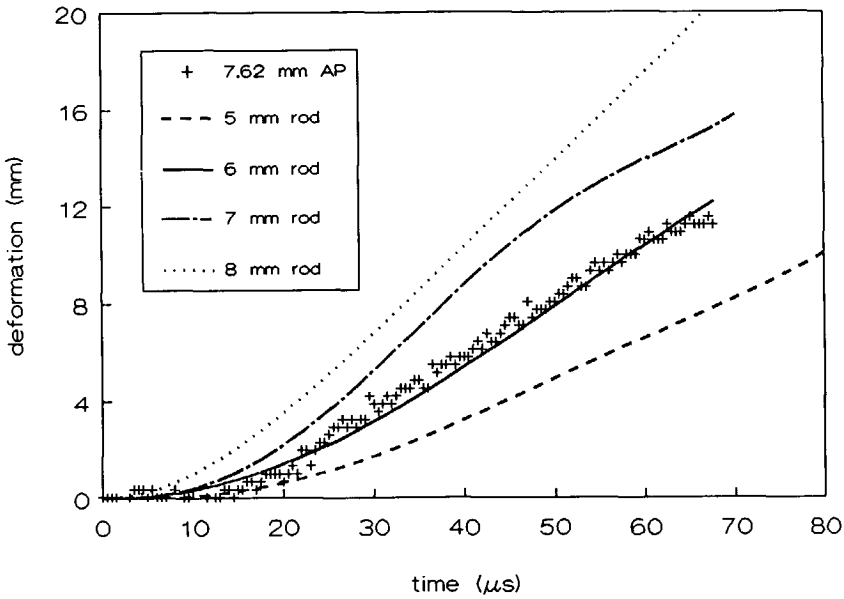

Figure 3.6 Comparison of maximum back-up plate responses of armours of 10.0 mm alumina backed by 4.0 mm aluminium when impacted by the 7.62 mm AP projectile and several blunt steel rods at a velocity of approximately 820 m/s (Van Zuidam, 1990).

diameter rod's impact followed almost completely the response caused by the 7.62 mm AP projectile.

Aside from the steel rod, two other projectiles were used with the experiments presented in this thesis: the 7.62 mm AP hard core projectile from DNAG and the 7.62 mm ball projectile (ss77) from FN Belgium. The 7.62 mm Ball projectile consists of a lead core and is surrounded by a tombac jacket. This ogive-nosed projectile has a maximum diameter of 7.62 mm, and is 28.5 mm long. It weighs 9.45 grams, and is also shown in figure 3.5.

3.3.4. Projectile acceleration techniques

The weight and length-over-diameter ratio of the rod prevent its successful acceleration to the velocity range of 700 m/s to 1100 m/s using a conventional full bore launch-tube. The highest allowable pressure in the launch-tube acting on the rear cross-section of the rod is not high enough to accelerate it to these velocities. The rod can be accelerated to higher velocities by increasing the rear cross-sectional area of the rod, using a lightweight sabot and a launch-tube with a larger bore-diameter. Hence, in this study the rod/sabot packages were launched from a 13.0 mm diameter smooth bore launch-tube.

Slender blunt rods travelling through air at supersonic velocities do not have a stable flight behaviour. The projectile will soon start to yaw due to small disturbances. Without changing the geometry of the projectile, this can only be prevented by either spinning the projectile or by placing the armour as close as possible to the launch-tube's muzzle. Spinning the projectile during launch was rejected for use within this programme. Hence, the armour had to be placed close to the launch-tube.
This, however, required that the sabot discards from the rod immediately after the rod/sabot package leaves the muzzle of the launch-tube. Otherwise the sabot will impact the armour soon after the rod, ruining the test results.

A four component sabot was developed for this purpose. This sabot uses an aerodynamic separation technique. The package is shown in figure 3.7, and consists of two fingers and a split obturator. A female conical air-scoop is added at the forward end. The ram air pressure produced by the sabot's travel through the air is contained by the cone and produces a force which causes the sabot to first pivot around its rear corners and then separate from the central rod. The sabot segments then tumble and fly away from the rod as the ensemble travels downrange. The split obturator, a unique design feature, separates into two sections after it leaves the launcher. These sections have a strong unstable flight trajectory due to their shape. At approximately 1.27 m downrange from the launcher's muzzle, the sabot segments can easily be separated from the rod by letting them impact the sabot-catcher, a thick steel plate with a 20 mm central hole which allows only the rod to continue its flight.
Unfortunately, aerodynamically opening sabots are very vulnerable to disturbances in bow to stern air flow. Disturbances in the air flow are caused by energetic gases immediately behind the rod/sabot package which can accelerate rapidly once the sabot package has left the launcher's muzzle. This energetic gas flow bursts past the rod/sabot package to form a "reverse flow" region where the atmosphere surrounding the sabot moves from the stern of the sabot to the bow. This "reverse flow" region

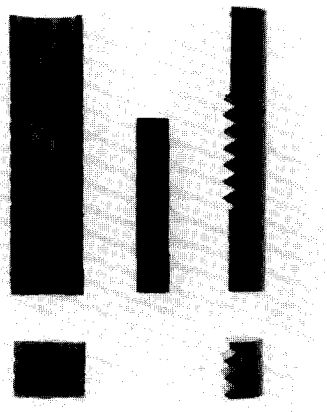

Figure 3.7 The rod/sabot package.

destabilizes the rod/sabot package during its early flight, often causing undesired tumbling of the package. In order to suppress "reverse flow", the launch-tube has been adapted. Four slots have been drilled in the launch-tube wall near its muzzle to vent almost all of the gas-charge while the rod/sabot package is still supported. This procedure was proposed by Swift & Strange (1987).
Nevertheless, the experiments showed that on many occasions the projectile impacted the armour with small amount of yaw. Rod impact with a yaw angle smaller than four degrees, however, was considered acceptable.

The 7.62 mm projectiles were launched from a standard army 7.62 mm FAL-rifle (Fusil Automatique Légère, FN Belgium), which was rigidly attached to a rig and fired automatically.

3.3.5. The flash X-ray set-up

At the time that this programme was carried out, a four channel 600 kV Field Emission (FE) flash X-ray system (model 730/2660) and two 1.2 MV Scandiflash (Sc) units (model 1200) were available at PML's Laboratory for Ballistic Research. Two flash X-ray pulsers were necessary to obtain all the information regarding projectile mass erosion, projectile position and armour deformation at a specific moment in time: the flash radiograph created by the obliquely positioned pulser provided information regarding projectile length and mass erosion, whereas the image from the second pulser set up in line with the armour panel's front surface provided information regarding the position of the projectile's rear-end, projectile debris formation and armour deformation. By using four pulsers, data was obtained at two moments in time during one experiment.
All FE pulsers were operated at their maximum voltage, 600 kV. The Sc pulsers were operated at 1100 kV. All pulsers produce a wide beam of radiation at the moment of triggering. In order to prevent X-ray cassettes from being exposed twice, diaphragms are placed such that beam widths are limited to those areas on the cassettes where the projectile armour interaction image is recorded. The diaphragms used consist of thick (20 mm) steel plates.
The X-ray pulser heads were protected by 5 mm thick aluminium plates. The X-ray cassettes, with the Kodak Lanex Regular X-ray films and Ortho-G intensifying screens, were protected from armour and projectile debris by 2 mm thick plates of aluminium. Two cassettes were used. One (300 x 900 mm) contained two films (300 x 400 mm each) to record the images of the three pulsers set up in the horizontal plane. The other cassette (300 x 400 mm) contained a full-size film to record the image from the pulser set up in the vertical plane. Figure 3.8 presents a view of the experimental set-up inside and outside of PML's medium calibre test chamber. The positions of the pulser heads, diaphragms, cassettes and armour for the experiments with the rods are presented in figure 3.9.

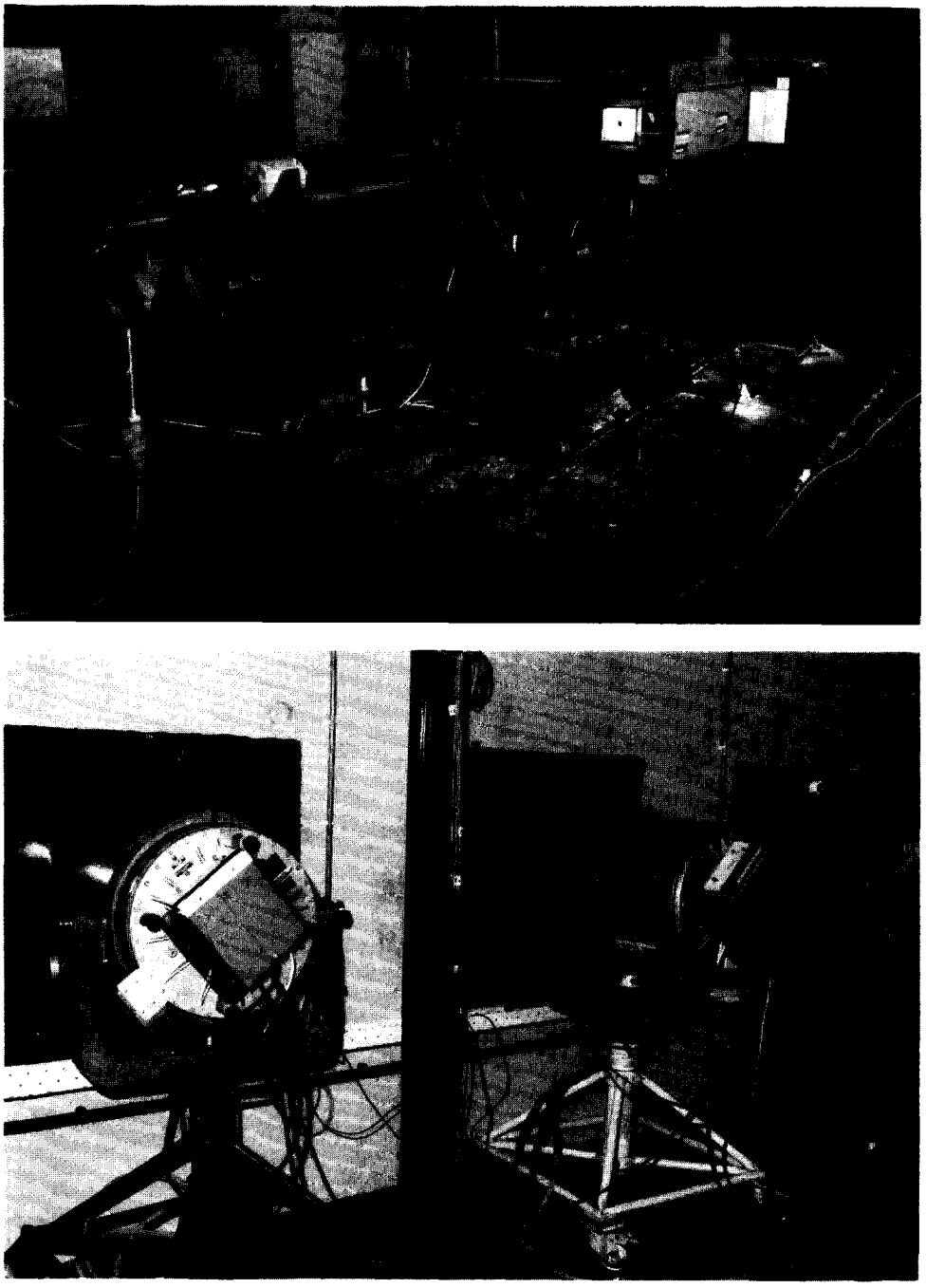

Figure 3.8 The experimental set-up in and around the test chamber during experiments.

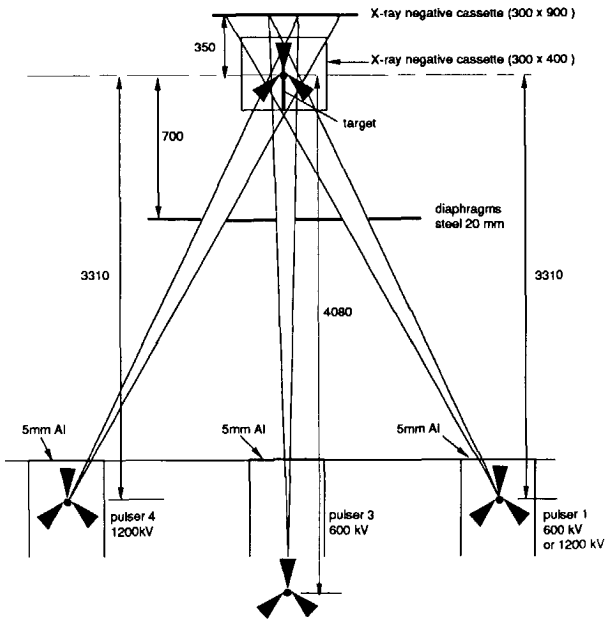

top view

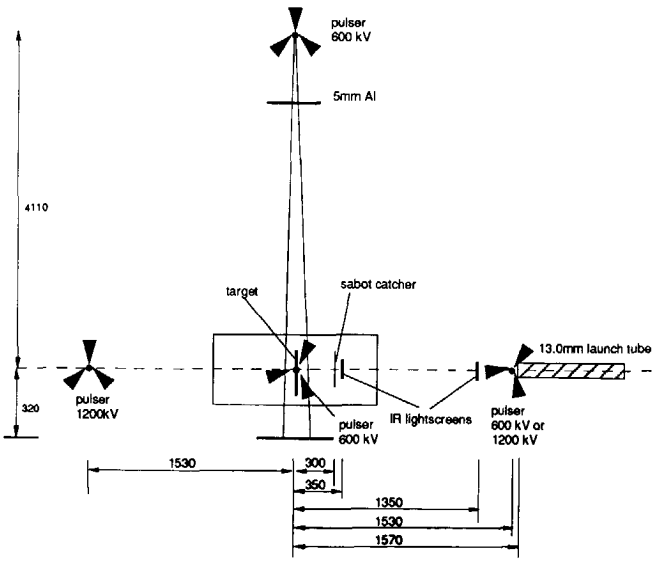

side view

Figure 3.9 Positions of launch-tube, armour, pulsers, diaphragms, X-ray negatives and velocity measurement screens, in and around the test chamber.

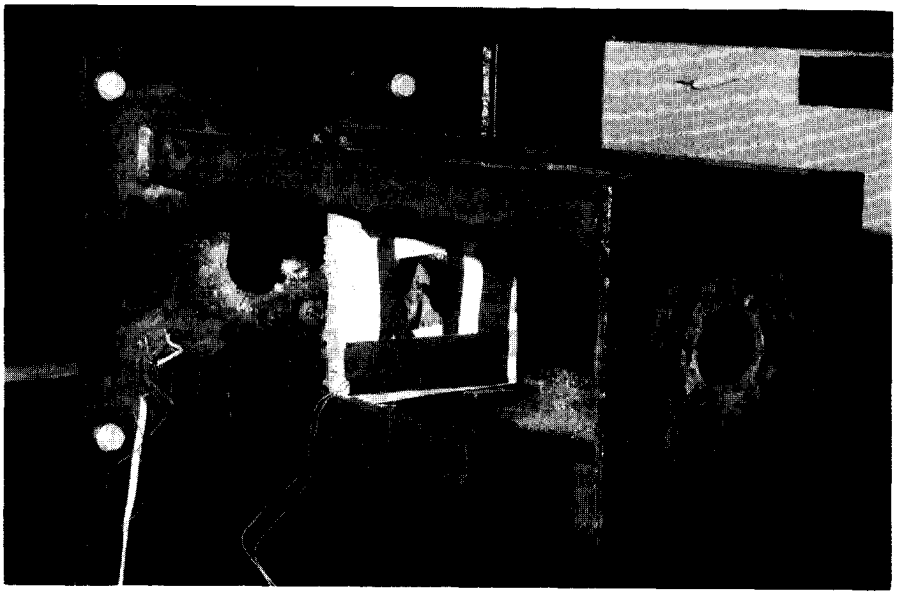

Figure 3.10 The armour panel in its supporting rig.

The armour panel had to be held in place such that the supporting structure did not obscure the projectile/armour interaction from the X-rays. This required the armour panel to be supported at the four corners only. The supports resembled table legs in order to prevent the projectile/armour interaction flash radiograph generated by the obliquely set up pulser from being obscured by the supporting rig. The armour panel in its support is shown in figure 3.10.

The experimental set-up for the tests with the standard 7.62 mm projectiles differed only slightly from the one presented here. It is described in detail in a report by this author (1990).

3.3.6. Triggering of the flash X-ray pulsers and velocity measurement

In order to be able to fire the flash X-ray pulsers at the desired moments in time after impact, an accurate triggering mechanism was needed to pin-point the moment of impact. Accurate triggering in the nanosecond regime was necessary since the pulsers were required to flash at specific moments in time (2, 4, 6, 8, 10, 12, 14, 16, 20, 25, 30, 35, 40/45 and 60 μs after impact) during consecutive experiments.
A triggerfoil technique was used for this purpose. A triggerfoil consists of two thin layers of aluminium foil separated by a thin layer of paper. These three layers are taped to the ceramic facing of the armour plate and connected to a pulse generator. As the projectile impacts, the two aluminium foils are connected causing a short-circuit, and

thus a trigger pulse. This trigger pulse was fed into four delay generators (three Hewlett Packard model 43114A digital delay generators and one Scandiflash DG-1000C delay generator), which set the delays for the flash X-ray pulsers. These pulsers were monitored by a processing storage oscilloscope (Krenz Electronics PSO 5070) to check the proper operation of the delay generators. Two of the three FE pulsers needed to flash at the first moment in time after impact while the third FE pulser had to flash at the second moment in time, together with the Sc pulser.

The projectile velocity measurement was carried out by measuring the interval of time needed by the projectile to travel a distance of 1000 mm. For this purpose, two infra-red lightscreens (Drello LS-19i) were set up in the path of the projectile (see figure 3.9). The design of these lightscreens is such that emitter and receiver are incorporated in one measuring unit. When the projectile passes the lightscreen the receiver is shaded. The signals from the lightscreens were fed into a Racal-Dana nanosecond counter (model 1991), from which the projectile velocity was easily obtained.

A schematic flowchart of the triggering and measuring equipment for the experiments with the rods is presented in figure 3.11.

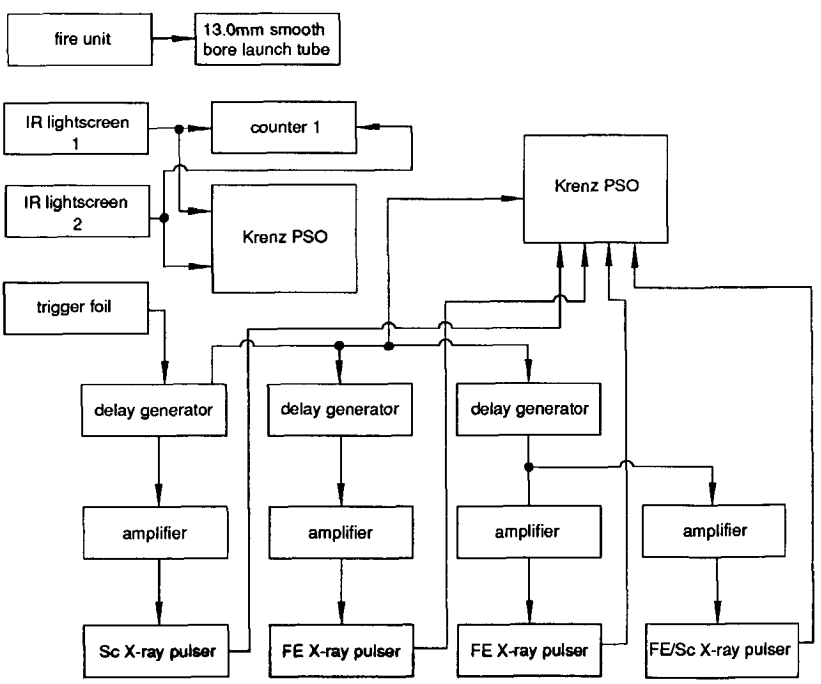

Figure 3.11 Schematic flowchart of the triggering and measuring equipment set-up.

3.4. Interpretation and analysis of the flash radiographs

Figure 3.12 shows a typical set of (cut-outs from) two flash radiograph positives from one of the experiments with the 7.62 mm AP projectile. The image on the left presents the radiograph obtained from one of the pulsers set up in line with the front face of the armour panel. Hence, the armour is seen from the side; its lateral dimensions (155 x 155 mm) prevent any X-ray radiation penetrating through it, so it is seen as a black shadow. The projectile is easily recognised in the image. The lead section in the rear of the projectile is clearly visible, due to its high density. These radiographic images were used to determine the distance between the rear-end of the projectile and the ceramic facing and the deformation of the armour plate. The diameter of the fringes of shattered projectile material flowing away laterally from the impact area were also measured from this radiograph.
The image presented on the righthandside of figure 3.12 was created by the obliquely set up pulser. They were used to determine the length of the eroding projectile. The actual penetration of the projectile into the armour is simply obtained from the difference between the projectile's length and the distance between its rear-end and the ceramic facing.

When deducing data from flash radiographs, one has to take into account that the radiographs show some image distortions (Held, 1985; Verhagen, 1988).
The appearance of the shadow picture is influenced by the relative positions of the source of radiation, the object and the film, but also by the direction of the beam of radiation with respect to the object and the plane of the film. The shadow cast by the object will be larger than the object itself because the object is not in contact with the

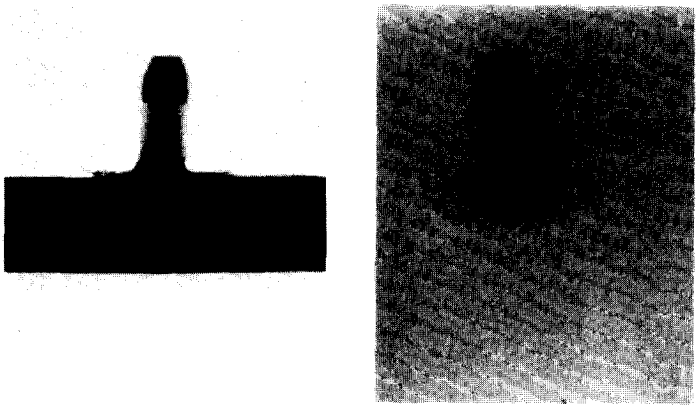

Figure 3.12 Set of flash radiograph cut-outs showing the projectile/armour interaction for a 7.62 mm AP projectile impacting 8.1 mm alumina backed by 6.0 mm aluminium at 16 μs after impact.

film; the degree of enlargement is determined by the relative distance of the object from the film and from the source. The form of the shadow may also differ according to the angle which the object makes with the incident rays. These geometric distortions were easily corrected for in the analysis of the radiographs.

The sharpness of the shadow depends on the spot size of the X-ray source and the position of the object between the source and the film. The shadows cast when the source is not a point, but a small area, are not perfectly sharp because each point of the source casts its own shadow of the object, and all of the shadows are slightly displaced relative to each other, thus producing a blurred image. All FE pulsers have a 5 mm diameter anode, i.e. a 5 mm source spot size. The Sc pulsers had 4 mm diameter anodes installed, giving them a 4 mm diameter source spot size. With the experimental set-up presented in this thesis, this unsharpeness (penumbra) is smaller than 0.5 mm. In the analysis of the radiographs, penumbra was taken into account. The blurriness of the image also depends on the displacement of the object during the exposure time. In this study, where objects move at velocities of typically 1000 m/s, the X-ray pulser's exposure time of only 20 ns prevented motion-unsharpness from becoming noticeable.

Aside from correction for geometrical distortion and penumbra, some other manipulations have to be carried out when analysing the flash radiographs. In some experiments the armour panels were slightly tilted due to misalignment; on the average this tilt angle was smaller than 1°, but as a result the armour panel appeared thicker than it should on the image of the pulser radiating in line with the armour's front surface. Because of this, the projectile's length (rear-end to ceramic facing) and the armour's deformation appeared smaller than they were on the radiographs, as is illustrated in figure 3.13. These effects were easily corrected for. However, when the armour's deformation was very small, the armour's misalignment could completely obscure it on the radiograph, and was prevented from being measured.

The images of the projectiles on the flash radiographs created by the obliquely set-up pulsers had to be analysed with extreme care. The beam of radiation made an angle of 64° (90°-26°) with the projectile's axis of flight and the X-ray negative. In the analysis of the radiographs, the obliquity was accounted for.

Analyses of flash radiographs of reference objects have shown that lengths could be measured with an accuracy of ± 0.5 mm. Due to the difficulty in determining the location of the projectile tip in the oblique radiographs, the projectile length and projectile penetration could be determined with an accuracy of ± 1.0 mm (Den Reijer, 1990). The data reduction procedure of flash radiographs using PML's image processing facilities is described extensively in a report by this author (1990).

Due to the geometric distortions, penumbra and armour misalignment, some images in the sequences of flash radiographs presented in the next chapter appear smaller or larger than others.

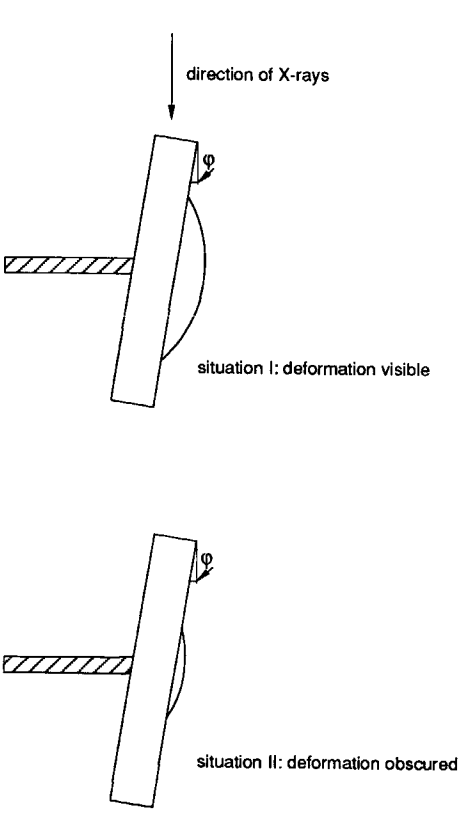

Figure 3.13 Obscured projectile length (rear-end to ceramic facing) and armour deformation due to imperfect armour alignment.

4. RESULTS OF THE EXPERIMENTS WITH THE ROD PROJECTILES

4.1. Introduction

The results of eight series of ballistic impact experiments are presented in this chapter. Armours with an 8.1 mm thick Morgan Matroc Hilox 973 alumina facing supported by four different aluminium 6061-T6 back-up plate configurations (4.0 mm, 6.0 mm, 2*3.0 mm and 8.0 mm thick) were impacted by steel rod projectiles just below and above their ballistic limit velocities.
More than 130 experiments using the X-ray equipment were necessary to obtain the data showing the projectile armour interaction process at 2, 4, 6, 8, 10, 12, 14, 16, 20, 25, 30, 35, 40/45 and 60 μs after impact for each of the eight series of experiments.

4.2. The experimental results

4.2.1. Armours of 8.1 mm alumina and 6.0 mm aluminium

4.2.1.1. Impact below the ballistic limit velocity

A complete sequence of flash radiographs was compiled from eight experiments and is presented in figure 4.1. The average projectile impact velocity was 815 m/s (± 26 m/s). In all of these experiments the projectile was stopped by the armour. Figure 4.2 presents the projectile rear-end position, armour penetration and armour deformation in time as deduced from these radiographs. The resulting projectile length reduction in time is presented in figure 4.3. On both figures, polynomials are best-fitted through the data-points. During the first 16 μs, no significant armour penetration and armour deformation could be measured. Projectile fragments are seen moving away laterally from the impact area from the moment of impact onwards. Projectile length reduction occurs until 45 to 50 μs after impact. A typical recovered projectile, as is presented in figure 4.4, weighs, on average, 2.6 grams and is approximately 12 mm long. Hence, approximately 60% of its mass has been eroded.
With all experiments the ceramic facing has completely delaminated from the back-up plate after impact. Figure 4.5 shows an example of a recovered ceramic facing viewed from front and rear. A typical example of a recovered back-up plate is shown in figure 4.6. As can be seen from the front view, some fractured ceramic material is still attached to the plate. In this example it has approximately the original ceramic thickness, indicating that the projectile was unable to penetrate the ceramic material directly in front of it. The area of back-up plate covered with ceramic material has a 20 mm radius around the impact point. This suggests that this section of the back-up plate was initially loaded by the projectile through the ceramic conoid. The area corresponds to the base area of a 65° ceramic fracture conoid. Figure 4.6 also shows the resultant back-up plate deformation. The maximum deformation is 5 mm. No cracks or shear-zones have been detected in the back-up plate.

4.2.1.2. Impact above the ballistic limit velocity

The armour is no longer capable of defeating the projectile, when the impact velocity is increased by 101 m/s to 916 m/s (± 18 m/s). The results of seven experiments were used to obtain the sequence of flash radiographs presented in figure 4.7. The projectile's rear-end position, armour penetration and armour deformation versus time are presented in figure 4.8. The projectile length reduction in time is presented in figure 4.9. Again, polynomials are fitted through the measured data.
During the first 14 μs of the impact process, no significant armour penetration or armour deformation was measured. After this period they both increase rapidly. The back-up plate deformation is limited to a relatively small area. At 60 μs, the maximum deformation is 11 mm. Back-up plate failure is noticeable in the "normal" radiograph at that time. Figure 4.10 shows a typical recovered back-up plate. A section with an approximate diameter of 10 mm has been sheared out. Figure 4.11 presents an example of a recovered projectile. It has an average weight of 2.3 grams and is 10 mm long; hence, 70% of its mass is eroded.
In most experiments in this series, the projectile pushes all ceramic material ahead of it without penetrating the material on the impact axis. After some experiments a (comminuted) ceramic plug was recovered together with the eroded projectile. Radiographs taken shortly after back-up plate perforation, show these plugs flying in front of the eroded projectile. In a few experiments, the projectile appears to have been capable of penetrating a limited thickness of ceramic. This has caused some scatter in the armour penetration data.

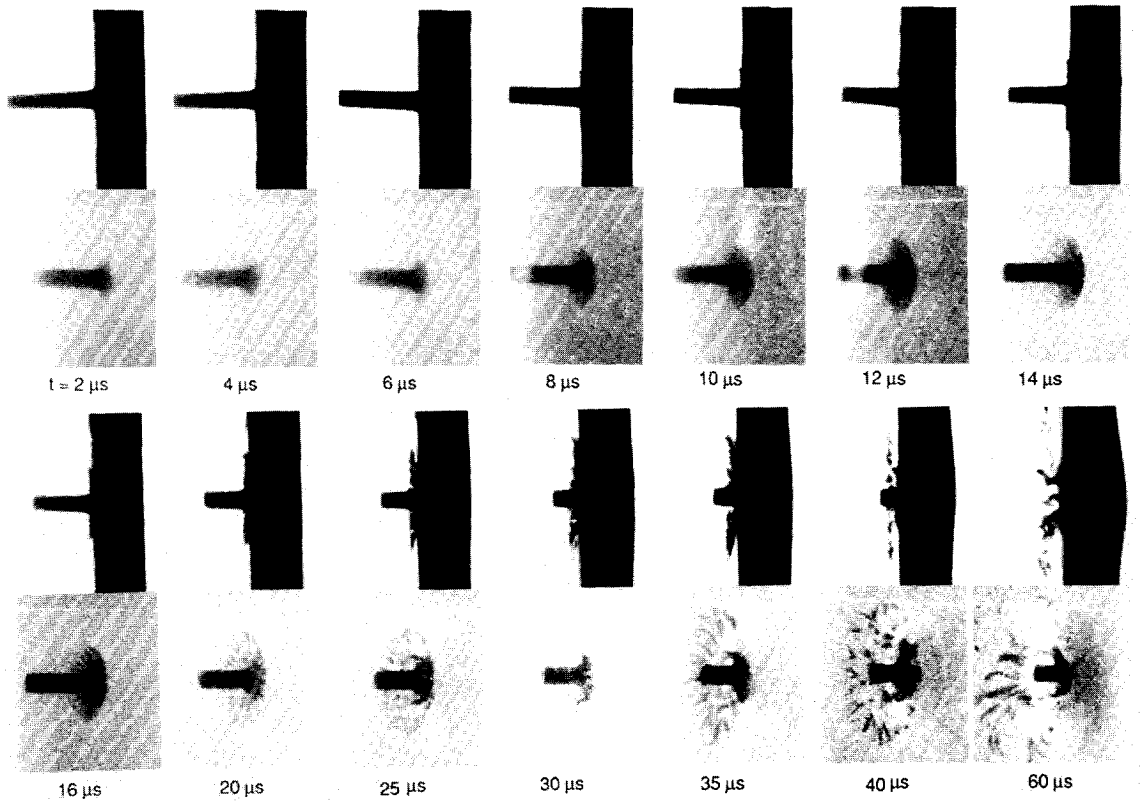

Figure 4.1 Sequence of normal and oblique (26°) flash radiographs showing the projectile/armour interaction of a steel rod impacting 8.1 mm alumina and 6.0 mm aluminium at a velocity below the ballistic limit (815 m/s).

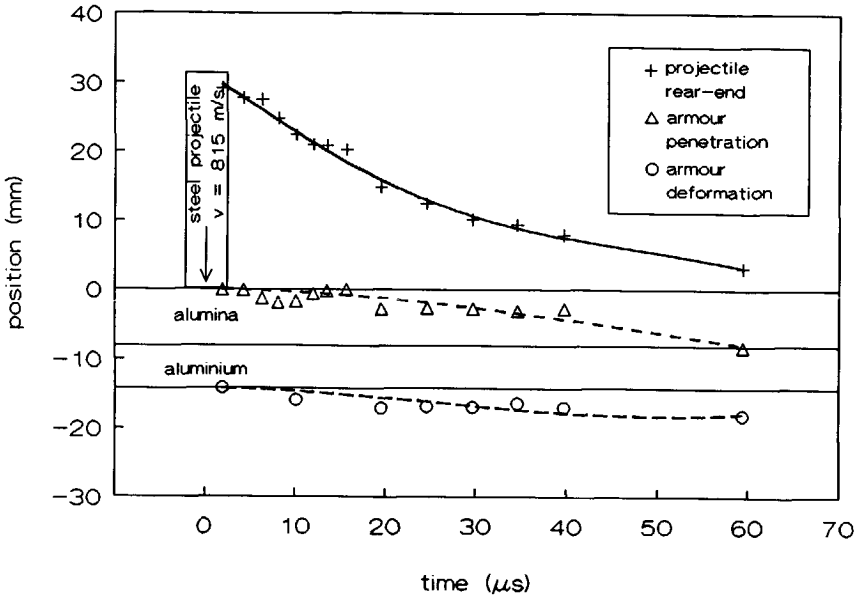

Figure 4.2 Position-versus-time curves of a steel rod impacting an armour of 8.1 mm alumina backed by 6.0 mm aluminium at a velocity below the v_{50} (815 m/s).

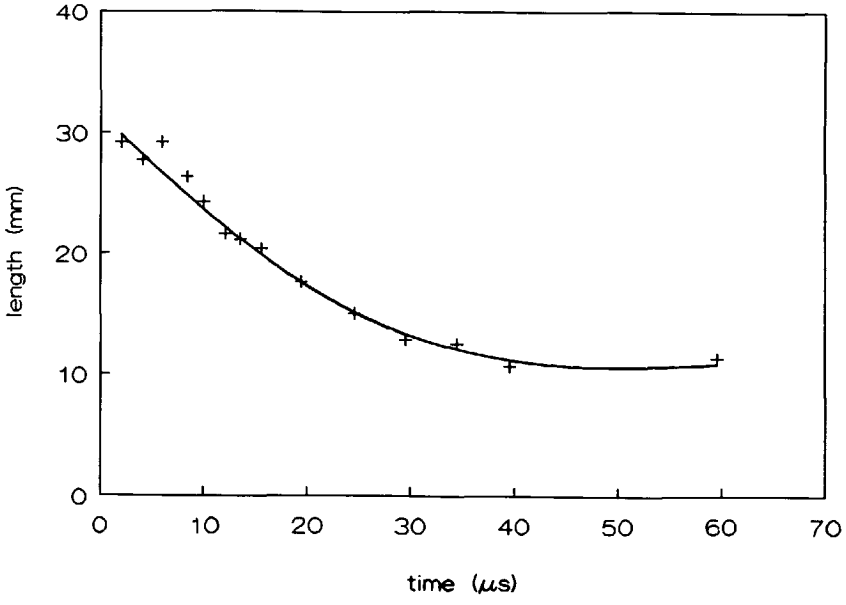

Figure 4.3 Projectile length-versus-time curve of the steel rod impacting an armour of 8.1 mm alumina backed by 6.0 mm aluminium at a velocity below the v_{50} (815 m/s).

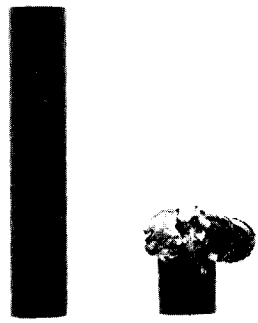

Figure 4.4 Recovered steel rod after impact of an armour of 8.1 mm alumina backed by 6.0 mm aluminium at a velocity below the v_{50} (815 m/s).

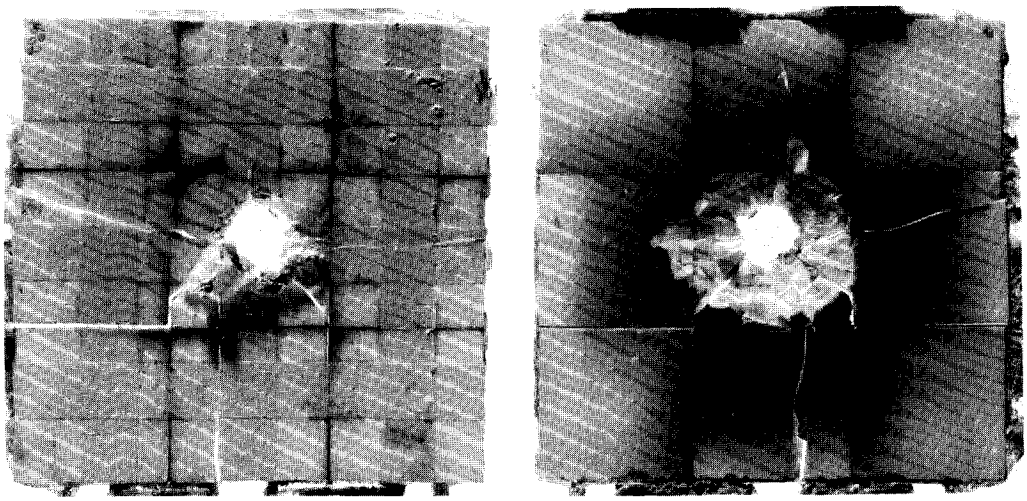

a) front view b) back-face view

Figure 4.5 Front and back-face view of an 8.1 mm thick ceramic facing recovered, after a steel rod impact on the alumina backed by 6.0 mm aluminium at a velocity below the v_{50} (815 m/s).

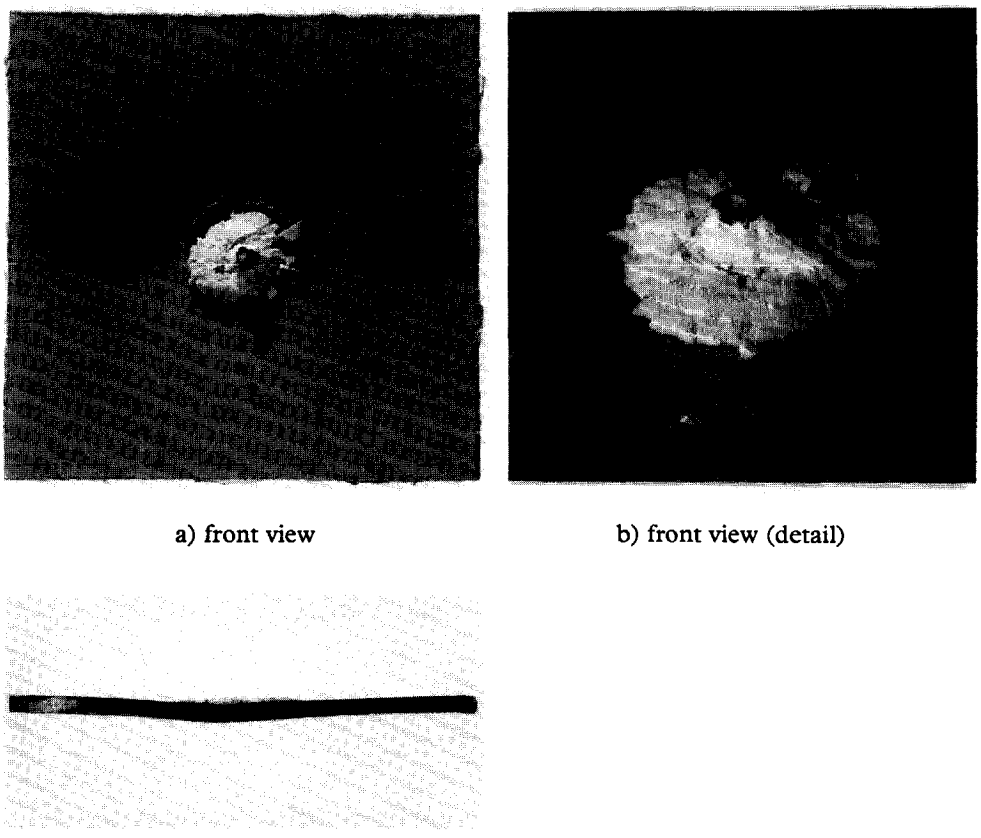

a) front view

b) front view (detail)

c) side view (cut-through)

Figure 4.6 Front (a), detail (b) and side view (c) of a 6.0 mm thick back-up plate recovered, after a steel rod impact on 8.1 mm alumina backed by the aluminium at a velocity below the v_{50} (815 m/s).

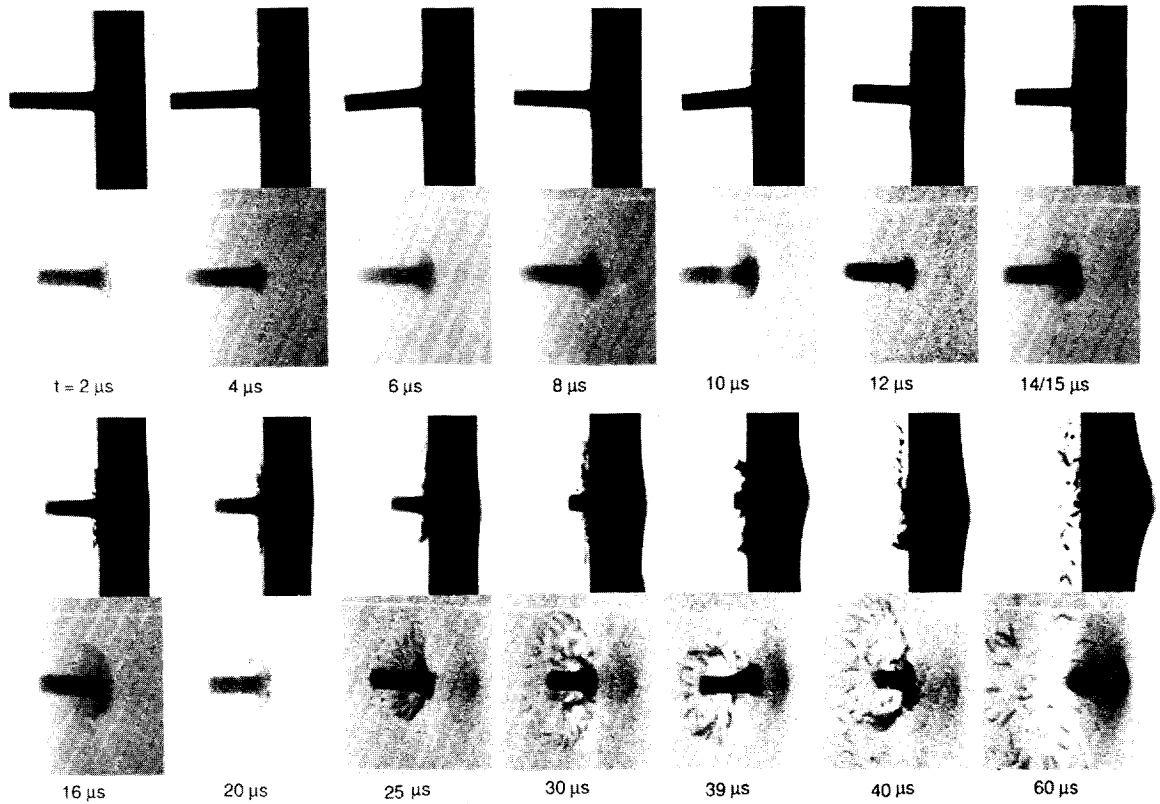

Figure 4.7 Sequence of normal and oblique (26°) flash radiographs showing the projectile/armour interaction of a steel rod impacting 8.1 mm alumina and 6.0 mm aluminium at a velocity above the ballistic limit (916 m/s).

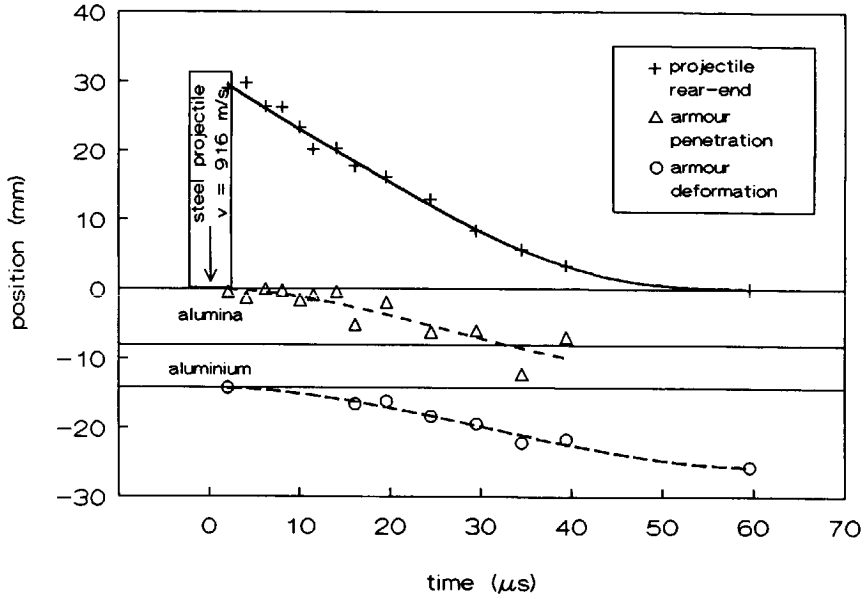

Figure 4.8 Position-versus-time curves of the steel rod impacting an armour of 8.1 mm alumina backed by 6.0 mm aluminium at a velocity above the v_{50} (916 m/s).

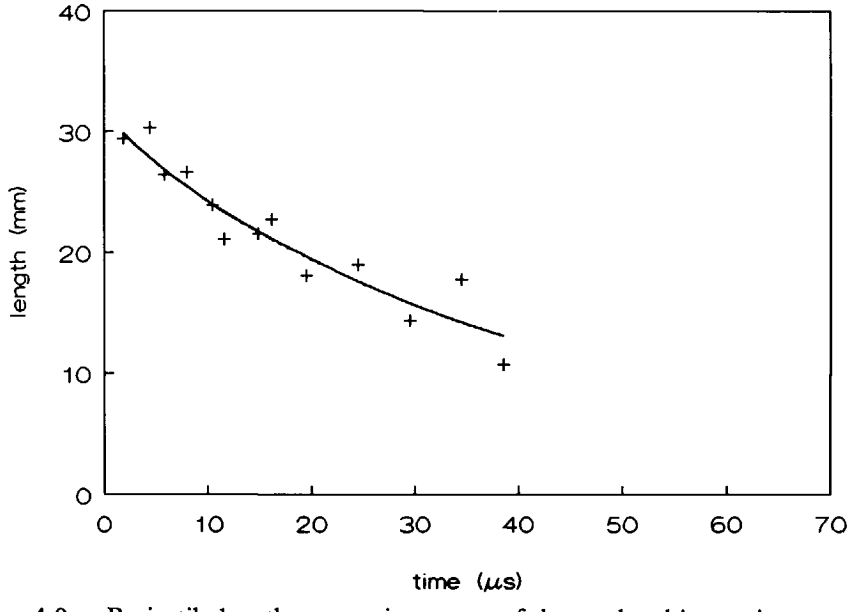

Figure 4.9 Projectile length-versus-time curve of the steel rod impacting an armour of 8.1 mm alumina backed by 6.0 mm aluminium at a velocity above the v_{50} (916 m/s).

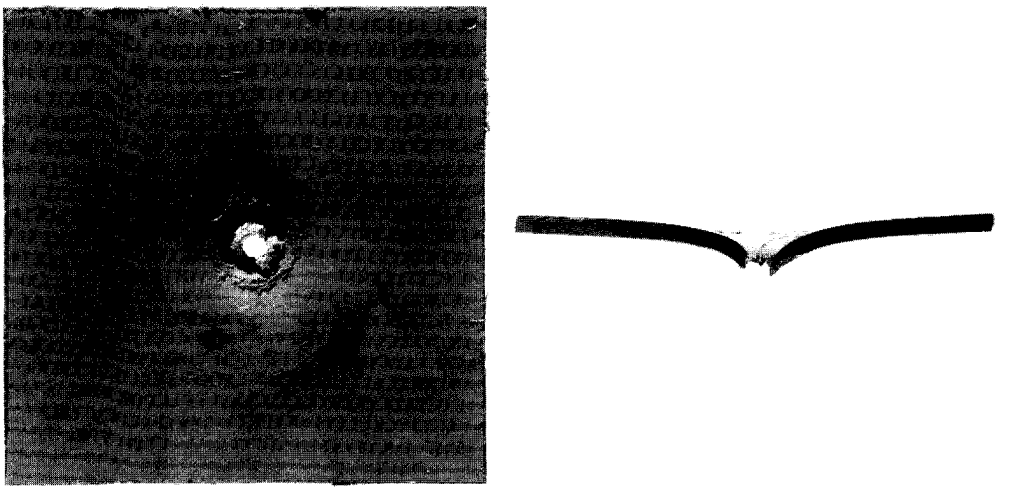

a) front view b) side view (cut-through)

Figure 4.10 Front (a) and side view (b) of a 6.0 mm thick back-up plate recovered, after a steel rod impact on 8.1 mm alumina backed by the aluminium at a velocity above the v_{50} (916 m/s).

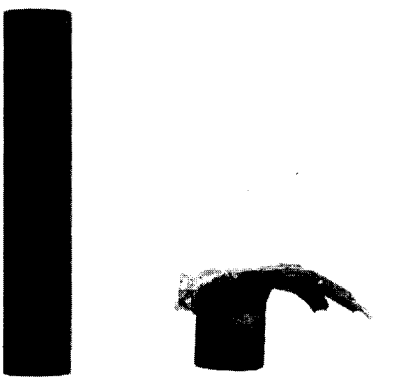

Figure 4.11 Recovered steel rod after impact of an armour of 8.1 mm alumina backed by 6.0 mm aluminium at a velocity above the v_{50} (916 m/s).

4.2.2. Armours of 8.1 mm alumina and a package of two 3.0 mm thick layers of aluminium

4.2.2.1. Impact below the ballistic limit velocity

Steel rod projectiles impacting the double back-up plate armours at a velocity as high as 819 m/s (± 13 m/s) were unable to perforate it. Hence, contrary to the expectations, this armour is not significantly easier to penetrate when compared with the armour with the single 6.0 mm thick back-up plate.
The sequence of flash radiographs, presented in figure 4.12, was compiled from seven impact experiments. Figure 4.13 presents the projectile rear-end position, armour penetration and armour deformation in time as was deduced from the radiographs. Polynomials are fitted through the data-points. The data show that the projectile was unable to penetrate the ceramic facing as the distance between the location of the projectile tip and back-up plate remains constant. The projectile length reduction in time is presented in figure 4.14. It continues for longer than 60 μs. The average recovered projectile weighs 2.4 grams and is 11 mm long (approximately 70 per cent erosion, see figure 4.15). A typical recovered back-up plate is shown in figure 4.16. A clearly visible, comminuted ceramic plug is seen still bonded to the back-up plate. The smooth ceramic front facing visible on top of this plug confirms the above observation with respect to the projectile's inability to penetrate the ceramic facing. The maximum deformation of the back-up plate was 11 mm for both layers of the back-up plate.

4.2.2.2. Impact above the ballistic limit velocity

By an increase of the impact velocity with 119 m/s, this armour was defeated by the steel rod. Eight impact experiments where rods impacted the armour at an average velocity of 938 m/s (± 23 m/s) were used to obtain the complete sequence of flash radiographs. This sequence is presented in figure 4.17. At 60 μs failure of the back-up plates become visible. At 120 μs the projectile is observed to have perforated the armour completely. The projectile rear-end position, armour penetration and armour deformation in time are presented in figure 4.18. The projectile length reduction in time is shown in figure 4.19. The radiographs show some scatter in the projectile's behaviour. The image at 30 μs shows a much larger projectile than the earlier and later radiographs. The reason for this scatter is not clear. Figure 4.20 shows one of the recovered projectiles, on average weighing 2.3 grams and measuring 10 mm in length. The radiographs show that the back-up plate deformation has a more local nature than when impacted at the lower velocity. The perforated two-layer back-up plate is shown in figure 4.21. A 10 mm hole has been created by the rod. Some star cracks can be seen radiating outward from the impact area. The two layers have failed by a combination of shear and star-cracking.

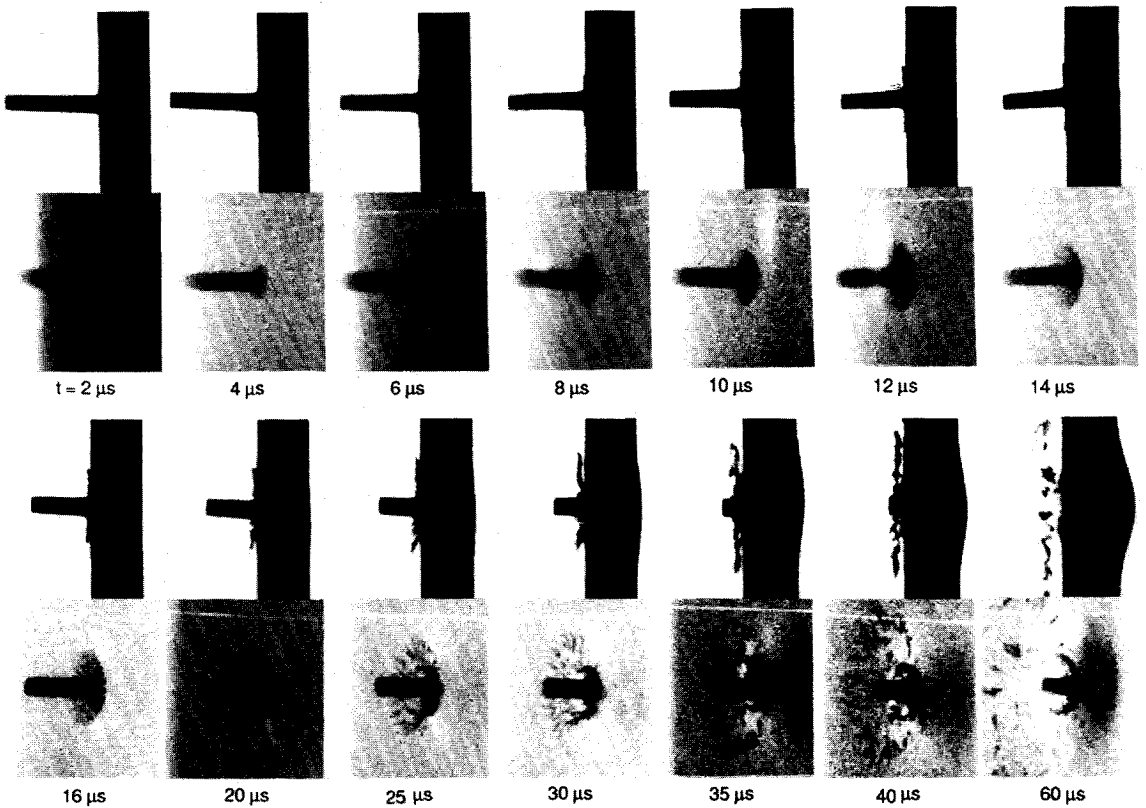

Figure 4.12 Sequence of normal and oblique (26°) flash radiographs showing the projectile/armour interaction of a steel rod impacting 8.1 mm alumina and two 3.0 mm thick layers aluminium at a velocity below the ballistic limit (819 m/s).

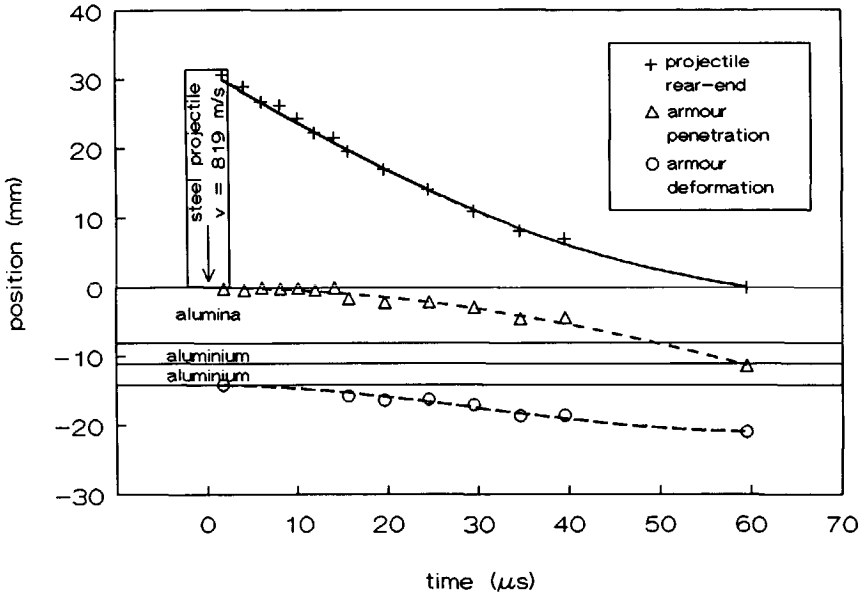

Figure 4.13 Position-versus-time curves of a steel rod impacting an armour of 8.1 mm alumina backed by two 3.0 mm thick layers aluminium at a velocity below the v_{50} (819 m/s).

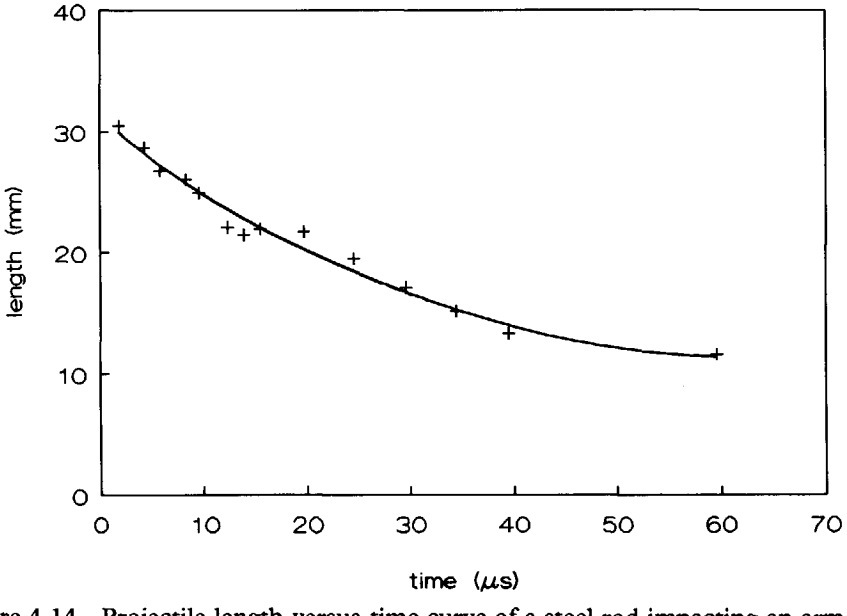

Figure 4.14 Projectile length-versus-time curve of a steel rod impacting an armour of 8.1 mm alumina backed by two 3.0 mm thick layers aluminium at a velocity below the v_{50} (819 m/s).

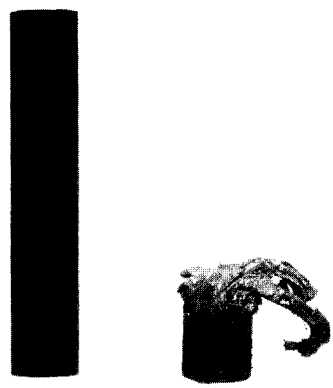

Figure 4.15 Recovered steel rod after impact of an armour of 8.1 mm alumina backed by two 3.0 mm thick layers aluminium at a velocity below the v_{50} (819 m/s).

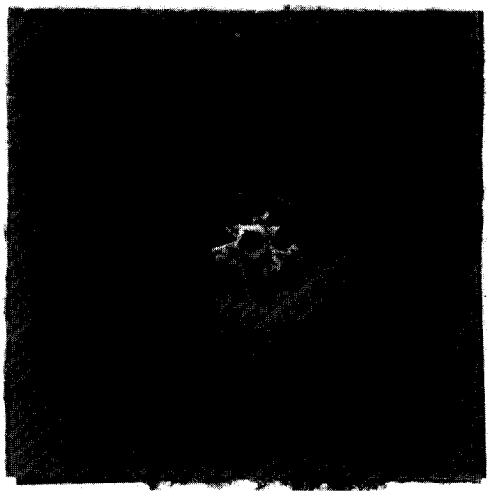

a) front view

b) front view (detail)

c) side view (cut-through)

Figure 4.16 Front (a), detail (b) and side view (c) of two 3.0 mm thick layers aluminium recovered, after a steel rod impact on 8.1 mm alumina backed by the aluminium at a velocity below the v_{50} (819 m/s).

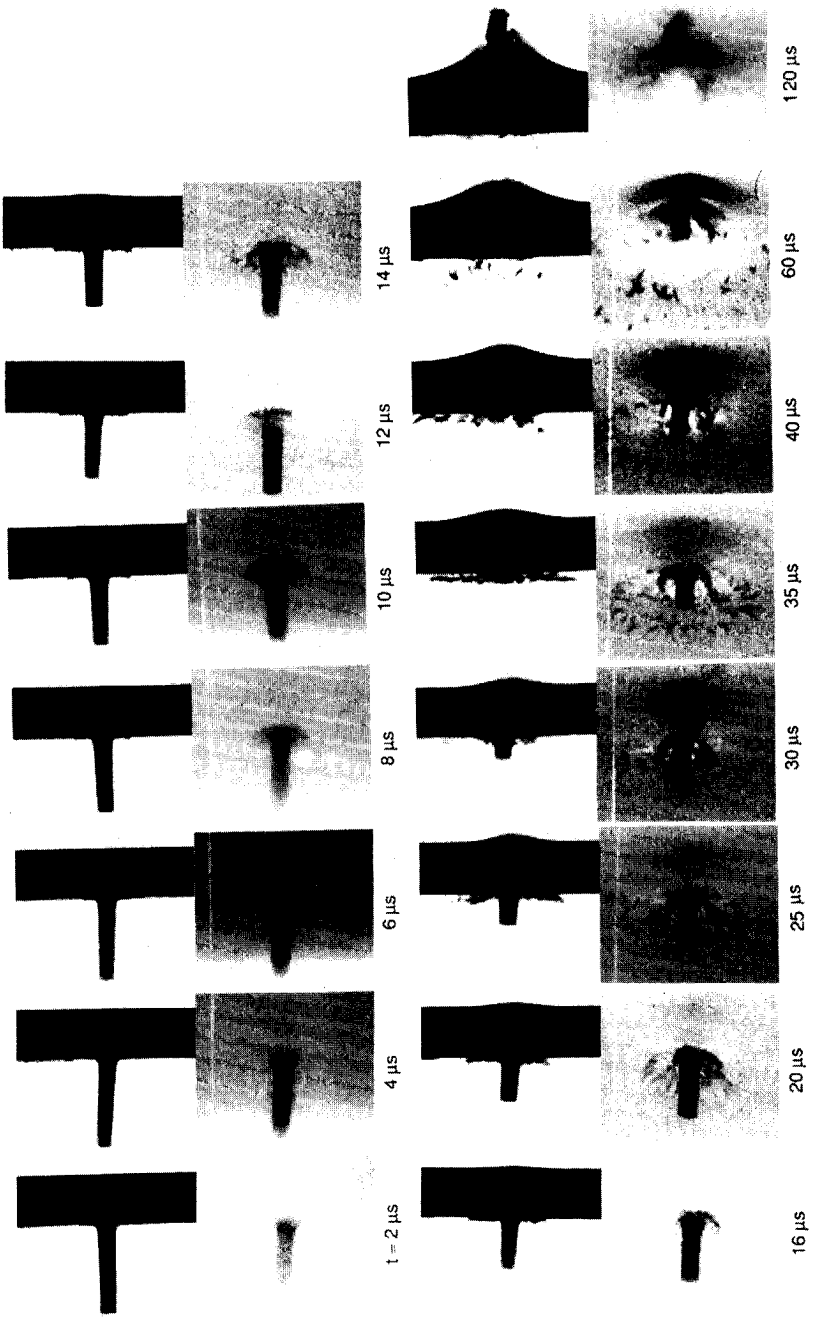

Figure 4.17 Sequence of normal and oblique (26°) flash radiographs showing the projectile/armour interaction of a steel rod impacting 8.1 mm alumina and two 3.0 mm thick layers aluminium at a velocity above the ballistic limit (938 m/s).

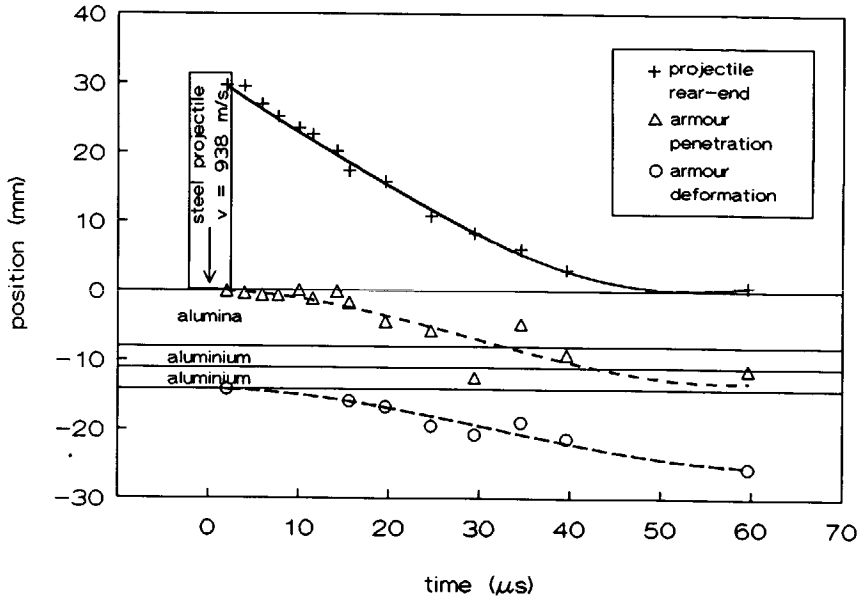

Figure 4.18 Position-versus-time curves of a steel rod impacting an armour of 8.1 mm alumina backed by two 3.0 mm thick layers aluminium at a velocity above the v_{50} (938 m/s).

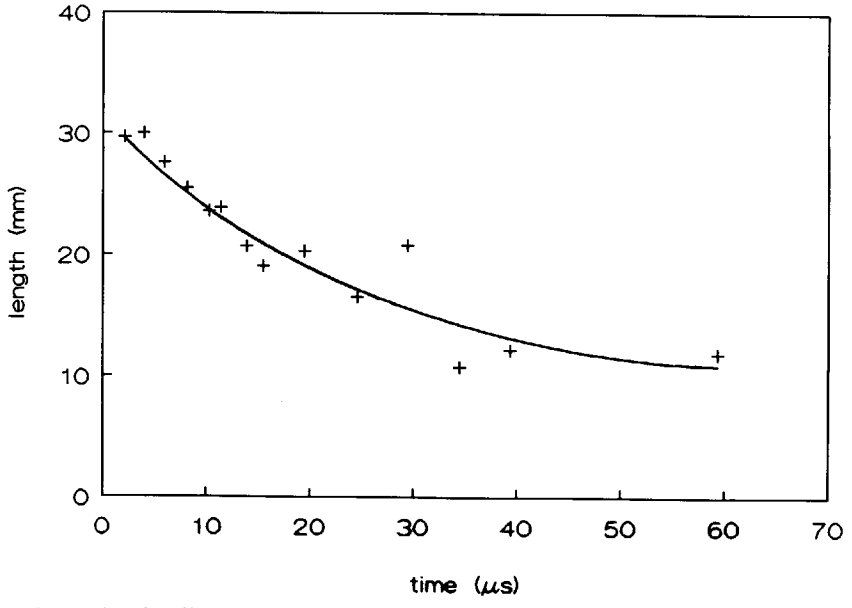

Figure 4.19 Projectile length-versus-time curve of a steel rod impacting an armour of 8.1 mm alumina backed by two 3.0 mm thick layers aluminium at a velocity above the v_{50} (938 m/s).

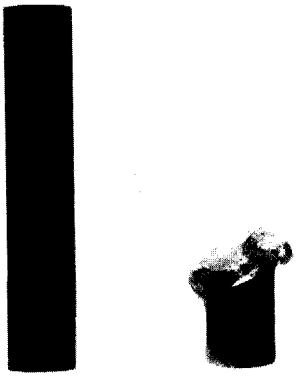

Figure 4.20 Recovered steel rod after impact of an armour of 8.1 mm alumina backed by two 3.0 mm thick layers aluminium at a velocity above the v_{50} (938 m/s).

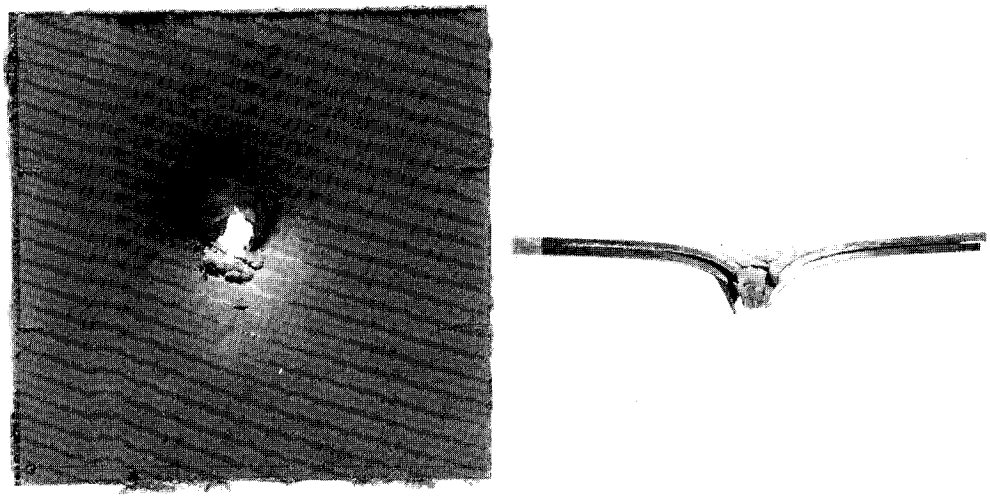

a) front view

b) side view (cut-through)

Figure 4.21 Front (a) and side view (b) of two 3.0 mm thick layers aluminium recovered, after a steel rod impact on 8.1 mm alumina backed by the aluminium at a velocity above the v_{50} (938 m/s).

4.2.3. Armours of 8.1 mm alumina and 4.0 mm aluminium

4.2.3.1. Impact below the ballistic limit velocity

The sequence of flash radiographs presented in figure 4.22 were taken from the results of nine ballistic experiments. The average projectile impact velocity was 786 m/s (± 26 m/s). All projectiles were defeated by the armour. The projectile rear-end position, armour penetration and armour deflection are presented in figure 4.23. The projectile length reduction in time is presented in figure 4.24. The projectile does not appear to penetrate the ceramic material directly underneath it. Projectile length reduction continues for more than 55 μs. A recovered projectile is shown in figure 4.25. It weighs, on average, 2.4 grams and is approximately 11 mm long. A recovered back-up plate is shown in figure 4.26. The maximum deformation is 11 mm. In some back-up plates star-cracks are visible, indicating that the armour had just failed, even though the projectile was unable to penetrate.

A few impact experiments at very low velocities (<600 m/s), show interesting details of the conoid cracks in the oblique radiograph at late times after impact (>20 μs). A representative set of radiographs, taken at 25 μs after impact, is presented in figure 4.27. In the image created by the obliquely set up pulser, two light grey lines are visible flaring out from the projectile impact area into the armour. The light grey colour of these lines indicates that at those locations the X-rays radiate through less material compared to elsewhere. Hence, these lines visualize the location of (opened) cracks in the ceramic facing. The angle that these cracks make with the impact direction indicates that they represent conoid cracks. This radiograph therefore presents the unique opportunity to measure the actual angle of this conoid. On the radiograph, the lines make an angle of approximately 58° with the impact axis. Taking the oblique projection into account, simple algebra yields that the fracture conoid has a (half) top-angle of 53°.

4.2.3.2. Impact above the ballistic limit velocity

A 43 m/s increase of the projectile velocity (to 829 m/s ± 17 m/s) resulted in armour perforation. The complete sequence of flash radiographs is presented in figure 4.28. The data deduced are presented in figure 4.29. They show that the projectile is not able to penetrate the ceramic material directly underneath it. The projectile length reduction in time is given in figure 4.30. A recovered back-up plate is shown in figure 4.31. This plate has failed by a combination of shear and star-cracking. A back-up plate area with a 35 mm diameter seems to be initially loaded by the projectile. A recovered projectile is shown in figure 4.32. It weighs 2.4 grams and is 11 mm long. According to figure 4.30, this erosion is the result of some 55 μs of length reduction.

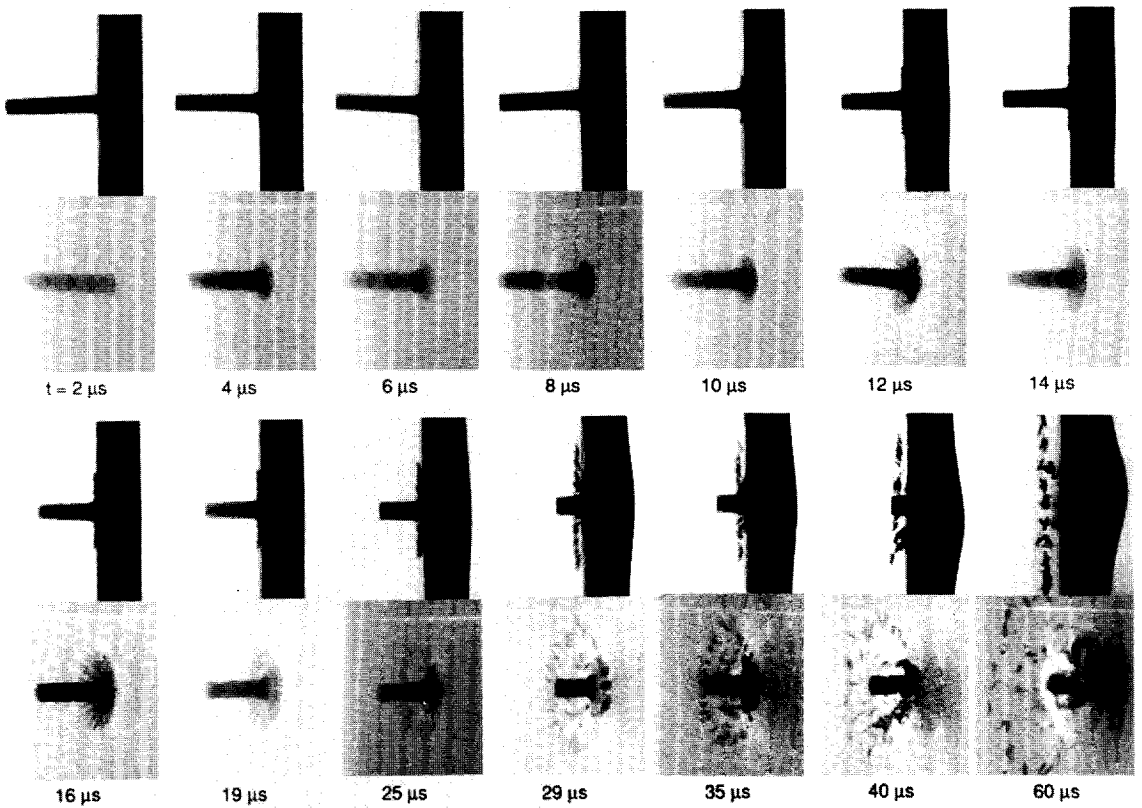

Figure 4.22 Sequence of normal and oblique (26°) flash radiographs showing the projectile/armour interaction of a steel rod impacting 8.1 mm alumina and 4.0 mm aluminium at a velocity below the ballistic limit (786 m/s).

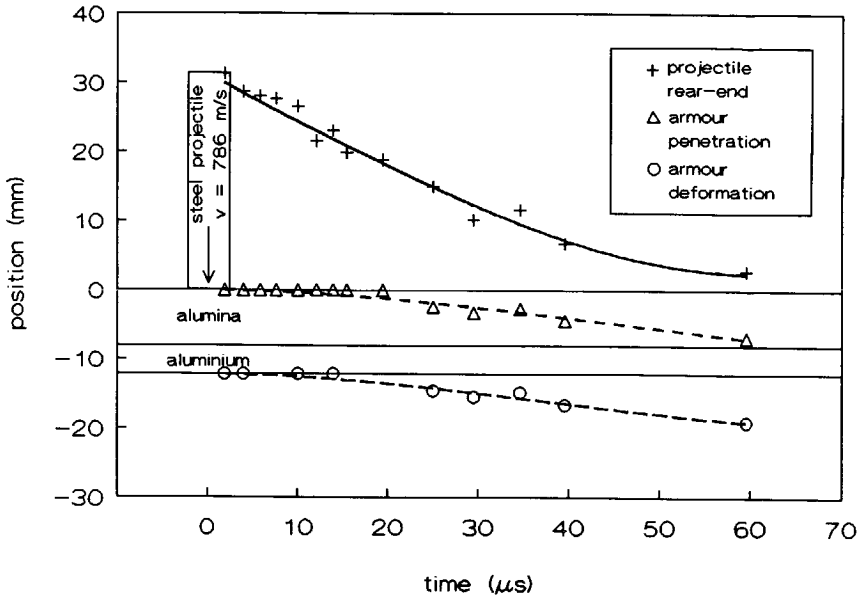

Figure 4.23 Position-versus-time curves of the steel rod impacting an armour of 8.1 mm alumina backed by 4.0 mm aluminium at a velocity below the v_{50} (786 m/s).

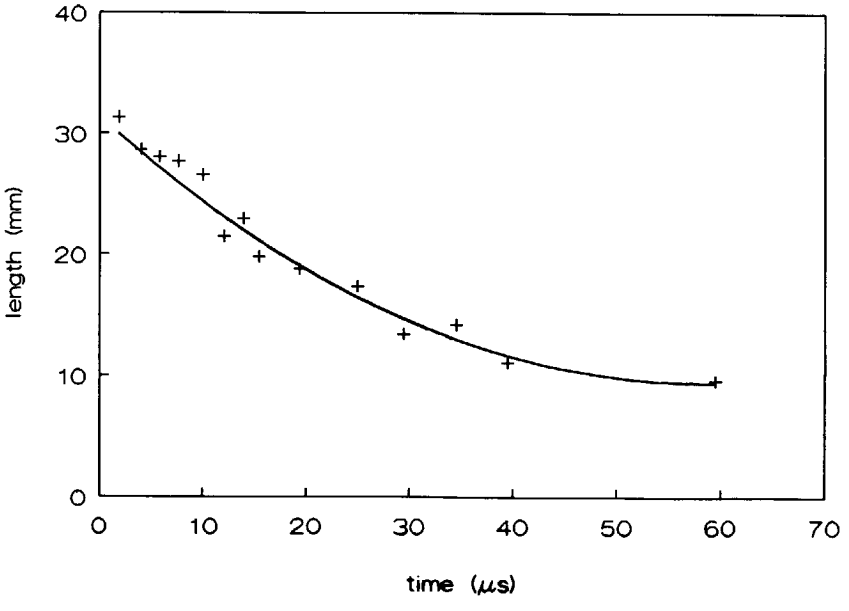

Figure 4.24 Projectile length-versus-time curve of the steel rod impacting an armour of 8.1 mm alumina backed by 4.0 mm aluminium at a velocity below the v_{50} (786 m/s).

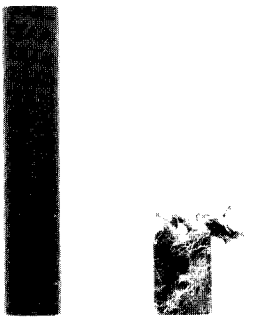

Figure 4.25 Recovered steel rod after impact of an armour of 8.1 mm alumina backed by 4.0 mm aluminium at a velocity below the v_{50} (786 m/s).

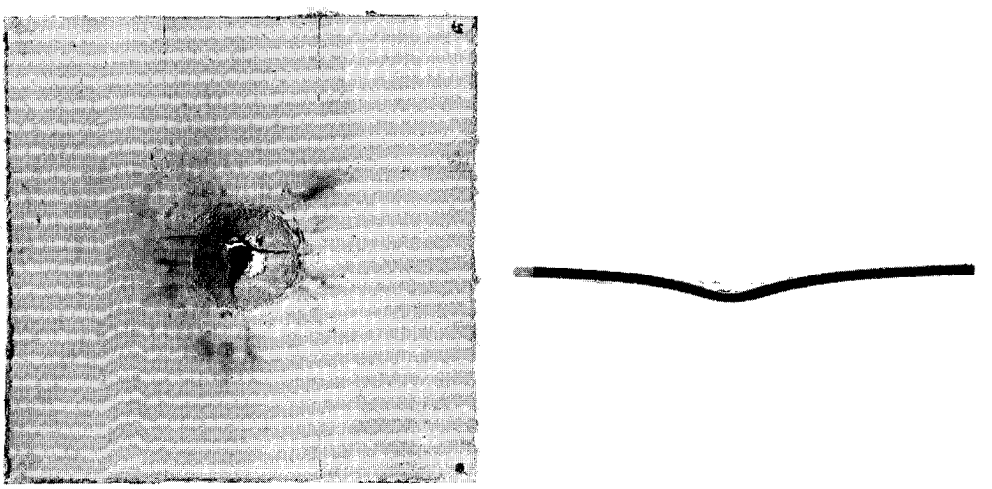

a) front view b) side view (cut-through)

Figure 4.26 Front (a) and side view (b) of a 4.0 mm aluminium back-up plate recovered, after a steel rod impact on 8.1 mm alumina backed by the aluminium at a velocity below the v_{50} (786 m/s).

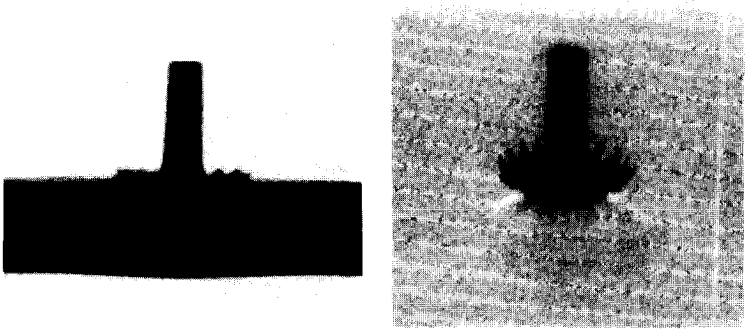

Figure 4.27 Normal and oblique flash radiograph at 25 μs after impact of a steel rod impacting 8.1 mm alumina supported by 4.0 mm aluminium. Impact velocity is 576 m/s.

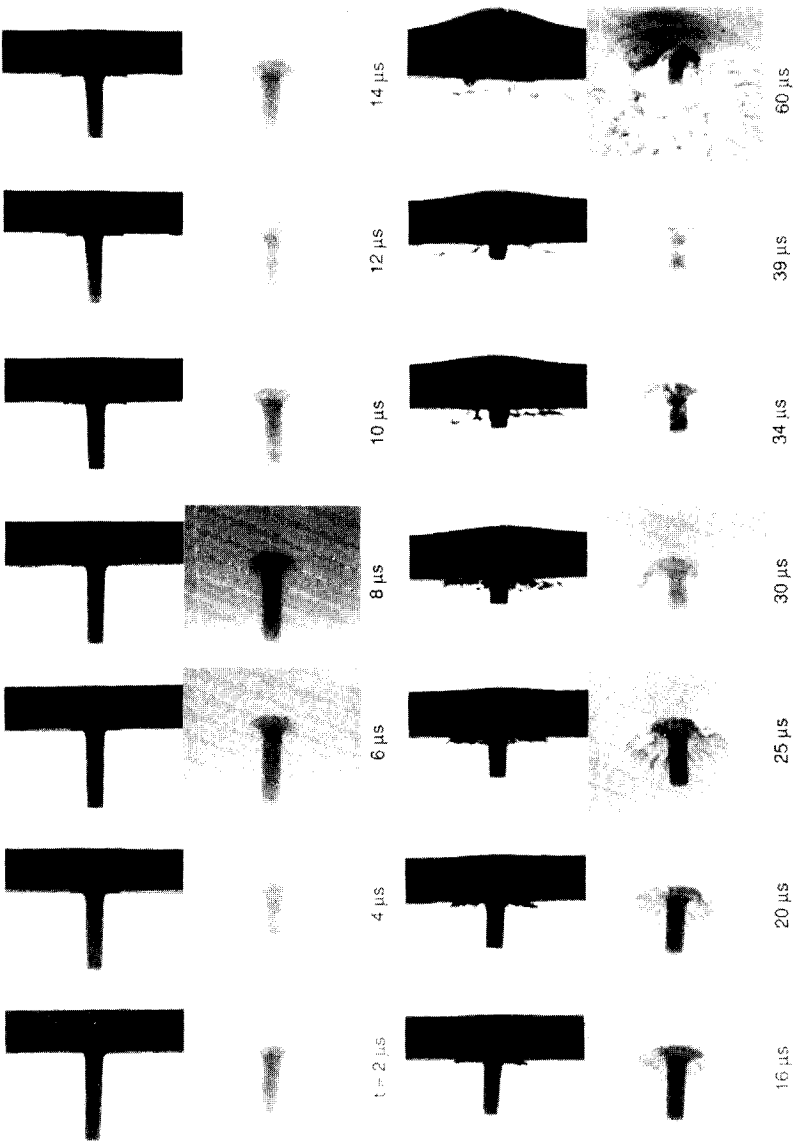

Figure 4.28 Sequence of normal and oblique (26°) flash radiographs showing the projectile/armour interaction of a steel rod impacting 8.1 mm alumina and 4.0 mm aluminium at a velocity above the ballistic limit (829 m/s).

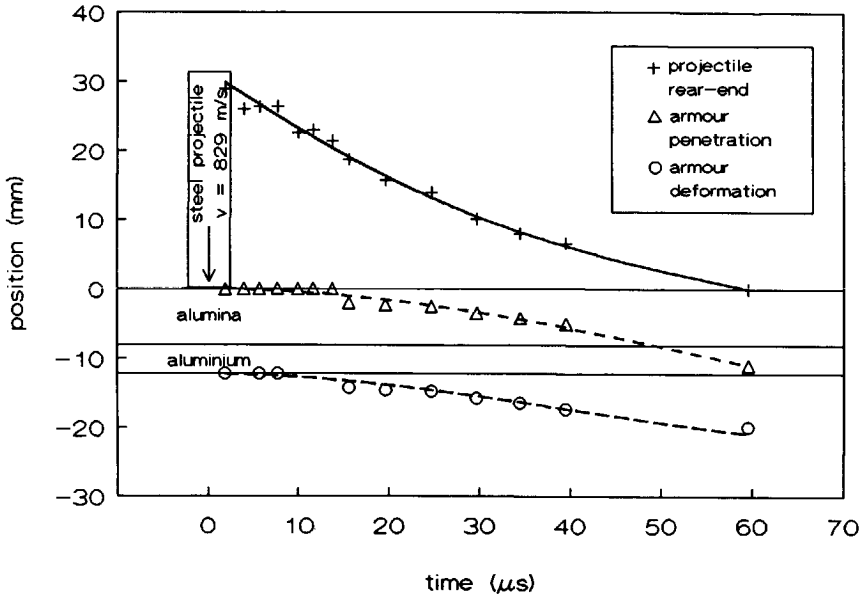

Figure 4.29 Position-versus-time curves of the steel rod impacting an armour of 8.1 mm alumina backed by 4.0 mm aluminium at a velocity above the v_{50} (829 m/s).

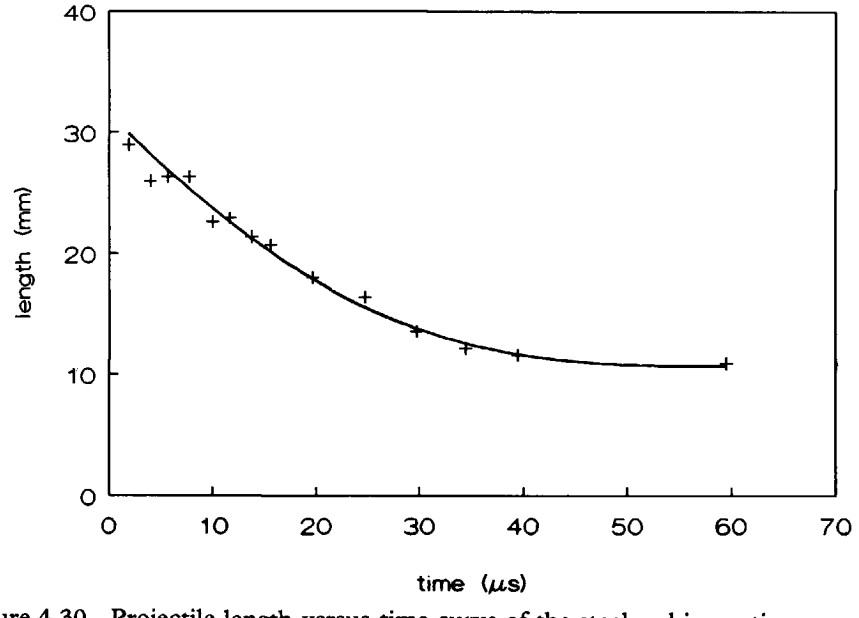

Figure 4.30 Projectile length-versus-time curve of the steel rod impacting an armour of 8.1 mm alumina backed by 4.0 mm aluminium at a velocity above the v_{50} (829 m/s).

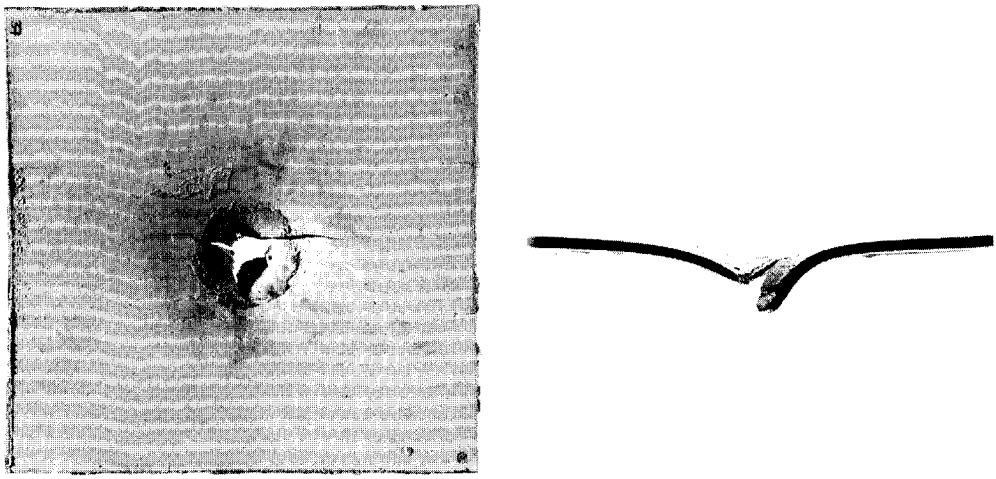

a) front view

b) side view (cut-through)

Figure 4.31 Front (a) and side view (b) of a 4.0 mm aluminium back-up plate recovered, after a steel rod impact on 8.1 mm alumina backed by the aluminium at a velocity above the v_{50} (829 m/s).

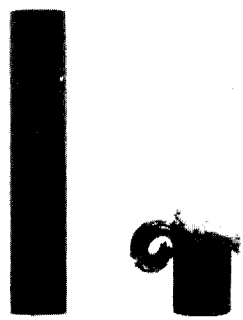

Figure 4.32 Recovered steel rod after impact of an armour of 8.1 mm alumina backed by 4.0 mm aluminium at a velocity above the v_{50} (829 m/s).

4.2.4. Armours of 8.1 mm alumina and 8.0 mm aluminium

4.2.4.1. Impact below the ballistic limit velocity

The sequence of flash radiographs presented in figure 4.33, show a steel rod impacting the armour at an average velocity of 995 m/s (± 16 m/s). At this velocity the projectile is not able to perforate the armour. The results are presented in figure 4.34. The position of the projectile-tip cannot be determined at times greater than 40 μs, since from that moment onwards the projectile's rear-end position was no longer visible in the radiographs.
Projectile length reduction in time is presented in figure 4.35. The reduction continues for less than 50 μs. A recovered projectile weighs, on average, 1.8 grams and is 8 mm long (figure 4.36). A typical example of a recovered back-up plate is presented in figure 4.37. A section of the back-up plate has been sheared off. Signs of local tensile stress failure are also observed at the back-up plate's rear face. Over an area with a 20 mm radius fragments of the bonding layer are visible. This suggests that the impact load was initially spread over this area. The results presented in figure 4.34, show that the projectile was unable to penetrate through the ceramic material directly in front of it.

4.2.4.2. Impact above the ballistic limit velocity

With an increase of 96 m/s of the impact velocity, the projectile was able to perforate the armour. The sequence of flash radiographs presented in figure 4.38, show the projectile armour interaction process for the steel rod impacting the armour at an average velocity of 1091 m/s (± 14 m/s). The data deduced from the radiographs are presented in the figures 4.39 and 4.40. After 34 μs the position of the projectile can no longer be determined. At 40 μs, back-up plate failure is clearly visible. The back-up plate deformation has a very local nature. Figure 4.41 shows an example of a recovered back-up plate. It shows some evidence of spallation. A 10 mm diameter plug is sheared out of it. The initial stages of failure resemble those observed in the previous section. The spalled back-up plates show only a minimum amount of overall back-up plate deformation. The projectile's length as observed in the oblique radiographs shows some scatter between images. This scatter is probably due to the spallation mechanism. Projectile length reduction continues for some 40 μs. A recovered projectile weighs, on average, 2.6 grams and is approximately 12 mm long (figure 4.42).

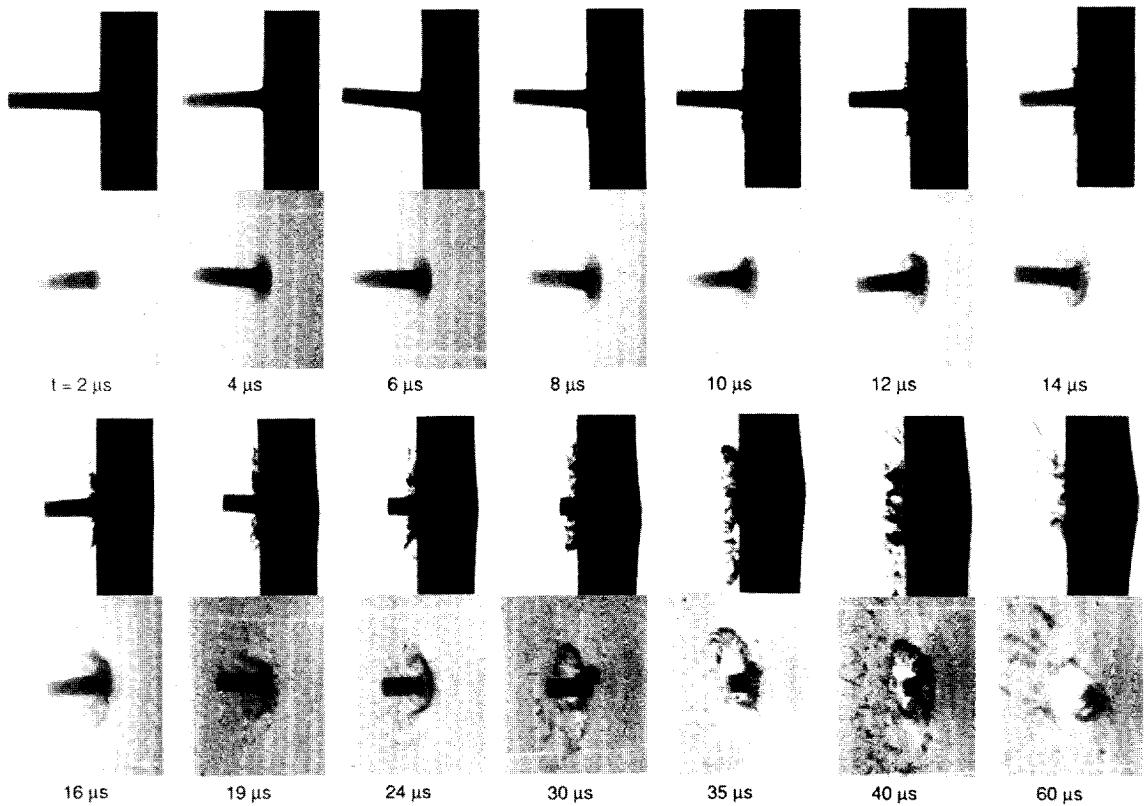

Figure 4.33 Sequence of normal and oblique (26°) flash radiographs showing the projectile/armour interaction of a steel rod impacting 8.1 mm alumina and 8.0 mm aluminium at a velocity below the ballistic limit (995 m/s).

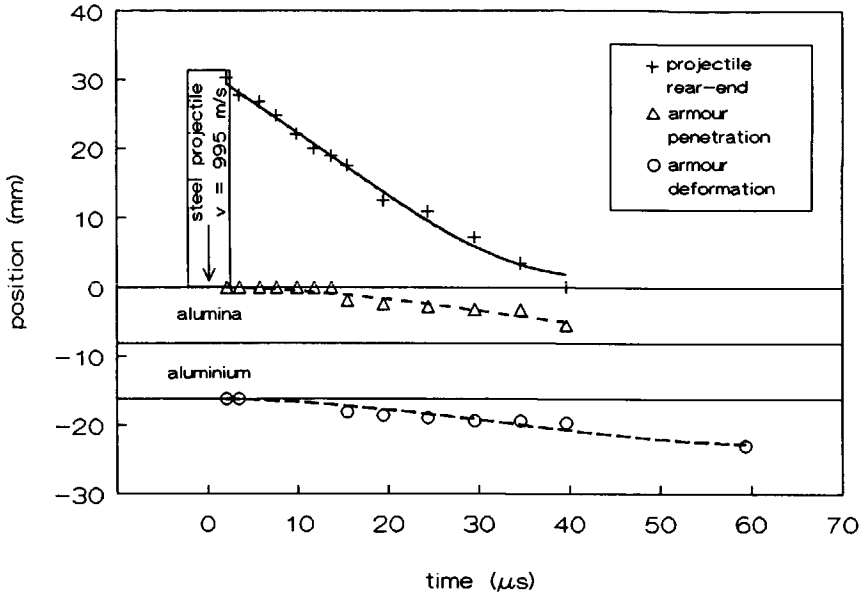

Figure 4.34 Position-versus-time curves of the steel rod impacting an armour of 8.1 mm alumina backed by 8.0 mm aluminium at a velocity below the v_{50} (995 m/s).

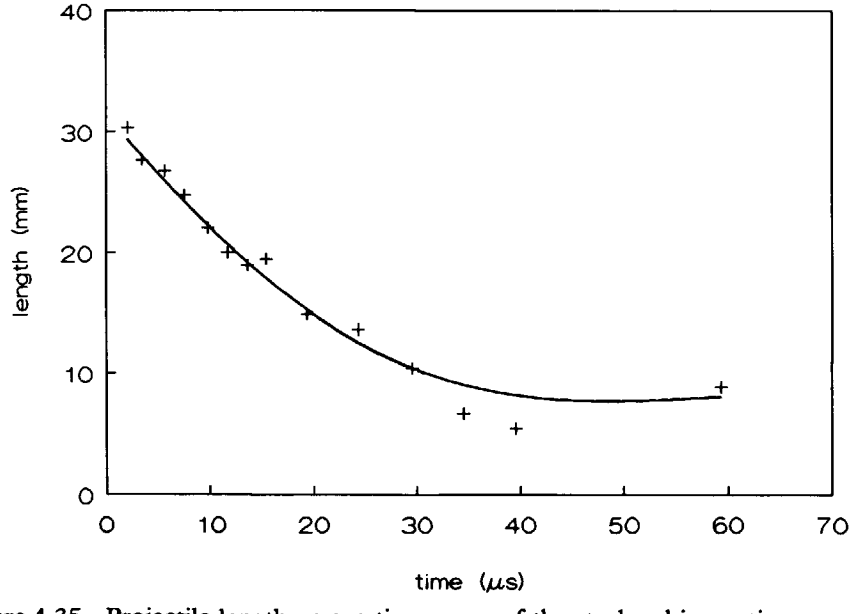

Figure 4.35 Projectile length-versus-time curve of the steel rod impacting an armour of 8.1 mm alumina backed by 8.0 mm aluminium at a velocity below the v_{50} (995 m/s).

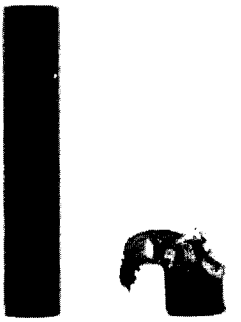

Figure 4.36 Recovered steel rod after impact of an armour of 8.1 mm alumina backed by 8.0 mm aluminium at a velocity below the v_{50} (995 m/s).

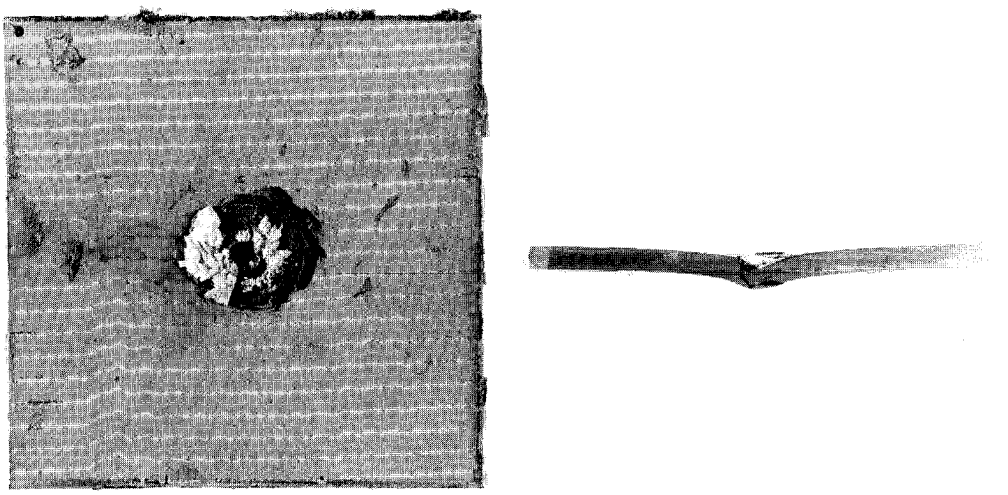

a) front view

b) side view (cut-through)

Figure 4.37 Front (a) and side view (b) of an 8.0 mm aluminium back-up plate recovered, after a steel rod impact on 8.1 mm alumina backed by the aluminium at a velocity below the v_{50} (995 m/s).

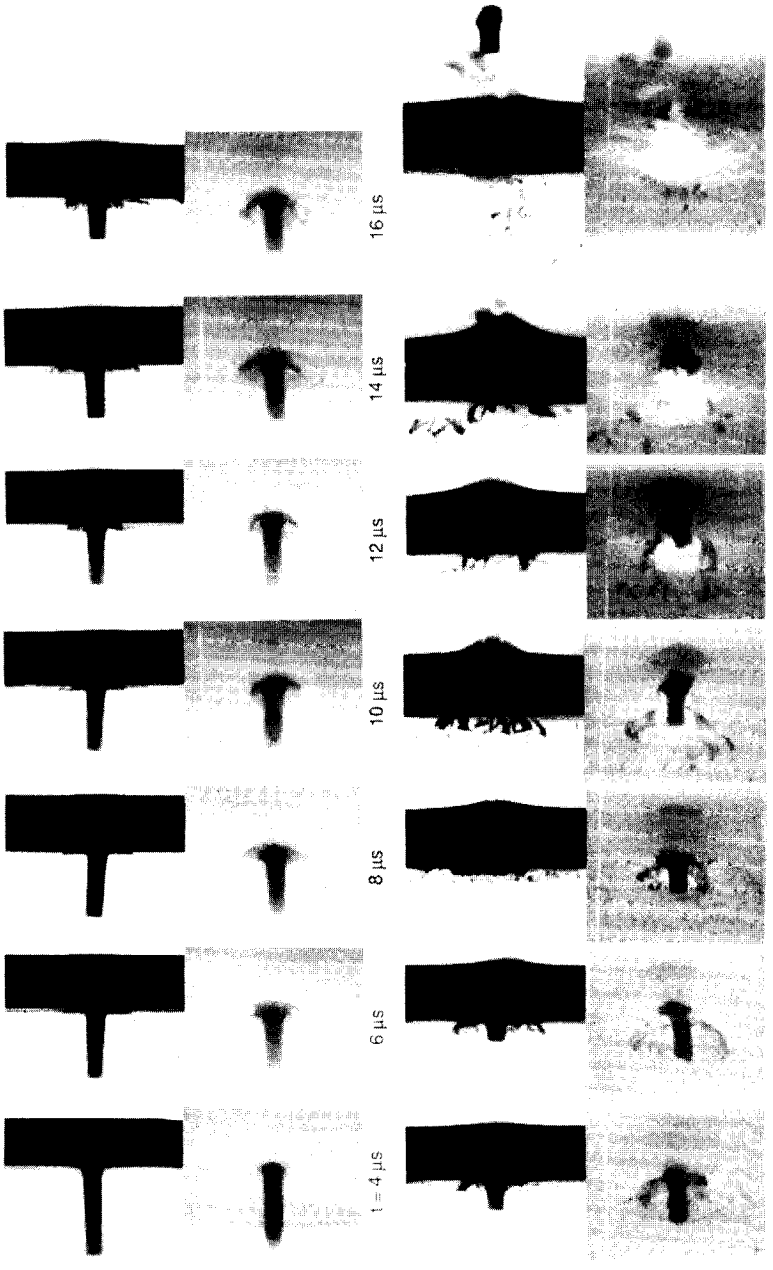

Figure 4.38 Sequence of normal and oblique (26°) flash radiographs showing the projectile/armour interaction of a steel rod impacting 8.1 mm alumina and 8.0 mm aluminium at a velocity above the ballistic limit (1091 m/s).

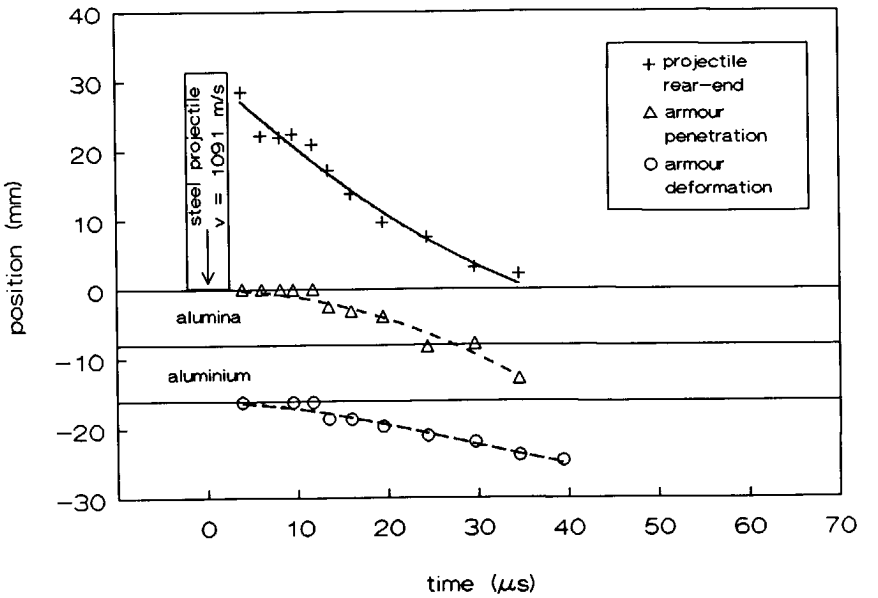

Figure 4.39 Position-versus-time curves of the steel rod impacting an armour of 8.1 mm alumina backed by 8.0 mm aluminium at a velocity above the v_{50} (1091 m/s).

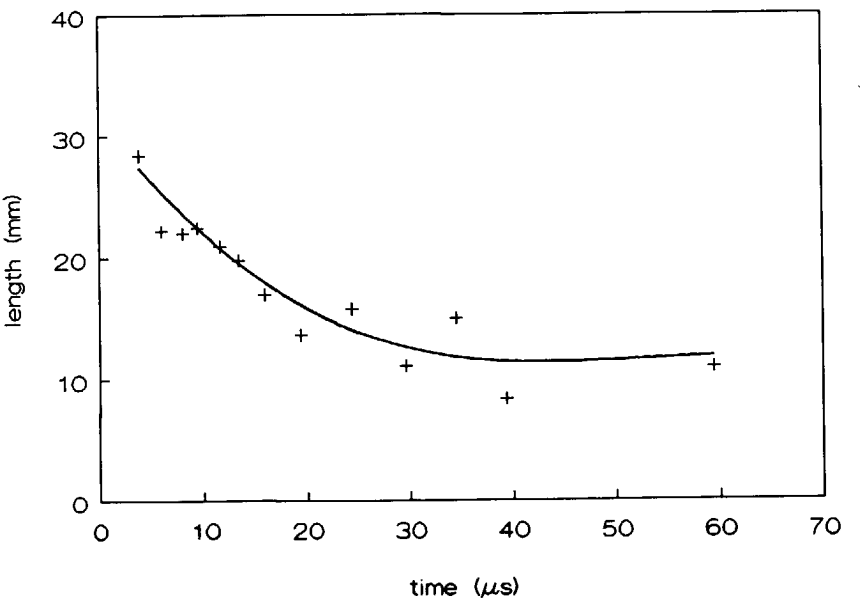

Figure 4.40 Projectile length-versus-time curve of the steel rod impacting an armour of 8.1 mm alumina backed by 8.0 mm aluminium at a velocity above the v_{50} (1091 m/s).

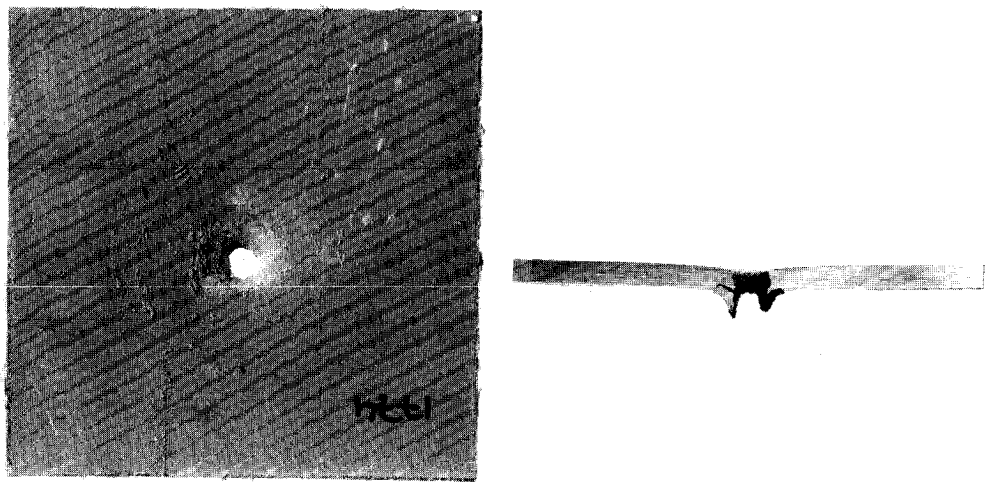

a) front view b) side view (cut-through)

Figure 4.41 Front (a) and side view (b) of an 8.0 mm aluminium back-up plate recovered, after a steel rod impact on 8.1 mm alumina backed by the aluminium at a velocity above the v_{50} (1091 m/s).

Figure 4.42 Recovered steel rod after impact of an armour of 8.1 mm alumina backed by 8.0 mm aluminium at a velocity above the v_{50} (1091 m/s).

4.3. Analysis of the experimental results

4.3.1. Introduction

The flash radiograph sequences, the differences between the deformation profiles of the various armour concepts and the recovered ceramic facings, back-up plates and projectiles, were used to analyse the projectile/armour interaction process. From these observations conclusions can be drawn about the most probable mechanism used by the ceramic facing to distribute the impact load over the back-up plate.
The influence of the various back-up plate properties on the armour's performance will be assessed by analysis of the back-up plate deformation profiles and failure modes. The deformation and erosion of the rods during impact is discussed as well.

4.3.2. The behaviour of the ceramic facing during impact

On the basis of the experimental observations, the recovered ceramic facings, the fragments found attached to the back-up plate and the literature, the following description of events is proposed for the response of the ceramic facing during the shock-wave phase and the following phase of structural response.

On impact, the stress field in the ceramic is initially elastic (the Boussinesq stress field), and the largest tensile stresses are in the radial direction (Timoshenko & Goodier, 1932; Evans, 1973). The tensile strength of ceramics is very low compared to their compressive strength. Therefore, the cracks that form (normal to the direction of maximum principal stress) are ring cracks concentric around the impact site, near the rod's periphery. According to Shockey *et al.* (1990) and Frechette & Cline (1970), these cracks are shallow, extending only a millimetre or so beneath the ceramic's surface. The ring cracks continue to grow, however, following paths normal to the direction of principal tensile stress, assuming angled trajectories from the initial normal-to-the-surface direction. Thus, several large Hertzian conoid cracks extend into the ceramic material. Frechette & Cline observed that as the impact velocity approaches the armour's ballistic limit velocity, other conoids of larger cone angle are formed around the primary conoid. Some of the recovered ceramic facings show indeed evidence of multiple overlying conoid cracks.

Star cracks, caused by high tensile hoop stresses, also run into the ceramic material. Slight discontinuities in the recovered conoid fragments at their intersections with members of the star cracks indicate that these star cracks occur earlier in time. According to Frechette & Cline, these star cracks emanate from the conoid surface, the intersection of the conoid with the back-up plate and from within the conoid enclosed volume. They assume that these cracks then spread faster than the (Hertzian) conoid cracks, in order to account for the fracture discontinuities described above. However, it is very unlikely that the star crack velocity is higher than the Hertzian conoid crack velocity as both are caused by principal tensile stresses in the ceramic. It is more likely

that the star cracks originate at the ceramic back-up plate interface, soon after the first reflection of the impact stress wave. They then spread radially and towards the impact surface. They meet the conoid cracks as these have just extended into the ceramic over a limited depth, causing the described discontinuities in the lower section of the conoid when the conoidal cracks extend. Mescall & Tracy (1986), support this reasoning with computations of their HEMP computer code, showing tensile hoop stress failure shortly after reflection of the stress wave at the ceramic back-up plate interface. Wilkins (1968) also shows failure proceeding from the ceramic back-up plate interface towards the impact face in his HEMP computations. Although he excluded failure by hoop stresses from his computation, the failure is caused by the loss of support by the back-up plate and therefore very similar to the failure described above.

The recovered sections of the fracture conoids that survived impact, see for example figures 4.6 and 4.16, show that on many occasions the projectile was unable to penetrate through the ceramic material directly in front of it. These fracture conoids include a cylindrical section of ceramic material which appears partly pulverised but recompacted. Its diameter is comparable to that of the projectile. This pulverisation of the ceramic may be explained in the following manner. Bless *et al.* (1987) showed that shocking of ceramics above the HEL (Hugoniot Elastic Limit) will introduce an extensive amount of microfracture to the material. They also showed that the HEL is exceeded in AD-85 alumina when a steel projectile impacts at a velocity above 370 m/s. Hence, in the impact velocity range used for the experiments reported on here, i.e. 700-1100 m/s, a peak shock stress is introduced into the alumina facing of the armour which exceeds the HEL to a significant degree. Taking into account that the diameter of the blunt projectile (D_p) is comparable to the thickness of the ceramic facing (h_c) and assuming that the peak transient stress falls to D_p/h_c of its peak value at the ceramic rear-surface, a substantial amount of ceramic underneath the blunt projectile is expected to experience a peak shock stress above HEL, explaining the partial comminution of the ceramic material.

When the shock waves no longer dominate the response of the ceramic, the structural response follows. The recovered pie-shaped segments of the fracture conoids show details of overlying conoid-like fractures (figures 4.6 and 4.16). The fracture pattern shows that these conoid-like cracks occur later than the star cracks. Their slope, similar to the Hertzian conoid cracks, indicate that these cracks do not originate from the ceramic's impact face. Some of the recovered fragments show initial fracture orientations perpendicular to the ceramic's back face, suggesting a tensile radial stress at the ceramic's back face as the instigator. According to Wilkins' HEMP computations, these fractures could have been generated early in the impact process. However, photographs of the development of axial cracks and conoids in alumina armours backed by thick steel plates and impacted by conical projectiles, show no signs of these rear-surface initiated cracks (Wilkins *et al.*, 1969; Frechette & Cline, 1970).
It is likely, that these conoid-like fractures start occurring some time after the primary Hertzian fracture conoid intersects with the back-up plate. The high impact load accelerates the conoid and the underlying back-up plate. The back-up plate deforms

correspondingly, introducing high tensile radial stresses near the edges of the fracture conoid's base. The relatively low tensile strength of the ceramic results in conoid-like cracks growing opposite to the direction of impact and towards the axis of impact. During this process, which is illustrated in figure 4.43, relatively thin "conoid-shell elements" are formed, which due to their constraint to follow the back-up plate's deformation, introduce a high shear load on the periphery of the central ceramic volume in front of the impact area. When lateral confinement of the "conoid-shell element" is sufficient, shear failure around this periphery occurs. As a result the impact load is now spread over a smaller area of back-up plate. The process repeats itself, depending on the loading and back-up plate response. It may end when the ceramic plug has completed its formation. This plug then loads the back-up plate over an area nearly equal to that of the projectile. As a result this plug may shear through the back-up plate or be defeated by it. Ceramic plugs have indeed been observed flying in front of the projectile on flash radiographs taken late after penetration.

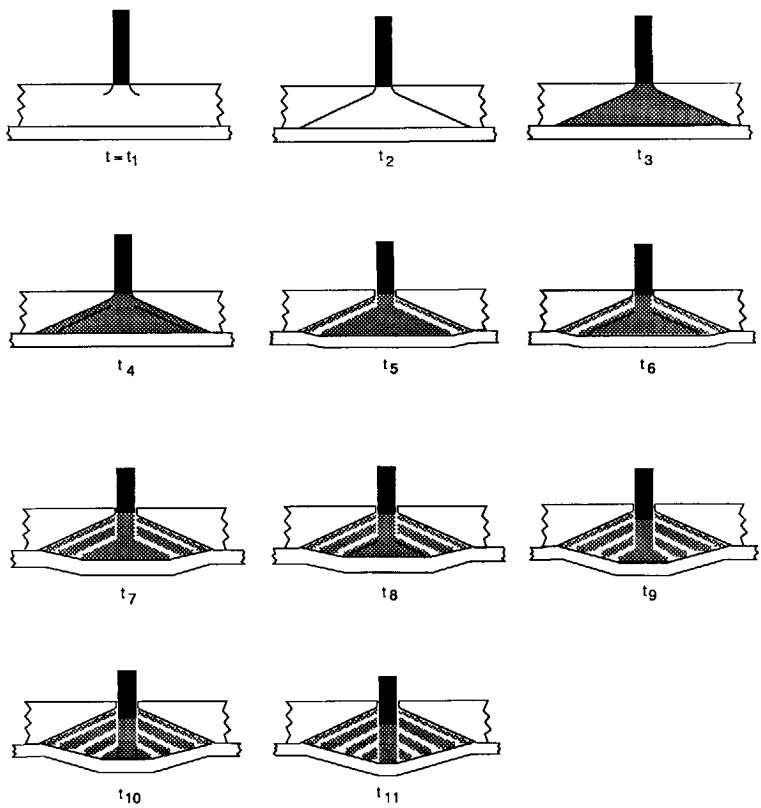

Figure 4.43 A phenomenological description of the ceramic fracturing process.

The proposed behaviour suggests that aside from a group of static properties, as proposed by Viechnicki *et al.* (1987) and Slavin *et al.* (1988), being hardness, sound velocity, Young's modulus, Poisson's ratio, density, porosity, tensile strength and compressive strength, a high shear strength is also very important for ceramic materials, in order to be able to distribute the impact load effectively. Rosenberg *et al.* (1990) confirm that ceramic materials exhibiting a lower (after shock) shear strength are easier to penetrate with blunt projectiles.

The markings on most of the recovered back-up plates indicate that they were loaded by a fracture conoid with a (half) cone angle of approximately 65°. This angle is some 20 per cent larger than the angle measured from the cracks visible on the flash radiograph taken during low velocity impact (<600 m/s). This may indicate that the cone angle is not independent of impact velocity, but increases with increasing impact velocity. Such a behaviour was observed by Townsend & Field (1987) for impacts on unsupported alumina. On the other hand, the cone angle may not be constant through the thickness and flare wide on approaching the back surface of the ceramic, as was described by Frechette & Cline (1970). The impact experiments presented were not set up to accurately measure the conoid's shape over a large range of impact velocities. Hence, further investigations are required to confirm either of the proposed mechanisms.

4.3.3. The behaviour of the back-up plates during impact

The observed back-up plate responses to rods impacting at velocities below the v_{50}'s are for the various concepts, to some extend, similar to each other. These responses are shown in figure 4.44. The reponse velocities, deduced from the polynomials, are presented in figure 4.45. Due to the moderate accuracy of the radiograph analysis procedure, an accurate analysis of the armour responses during the first 16 μs of the impact process cannot be given. After this period the responses of the armours with the 4.0 mm, 6.0 mm and 2*3.0 mm thick back-up plates may be compared to each other, as the projectiles have impacted these armours at almost identical velocities (786 m/s, 815 m/s and 819 m/s, respectively). One can see then, that the armour with the 2*3.0 mm thick back-up plate, which has the lowest bending stiffness of the three, shows the fastest response upto 40 μs after impact. The single 6.0 mm thick back-up plate, which only differs from the 2*3.0 mm thick back-up plate in its 4 times higher bending stiffness, responds slower to the impact event. The 4.0 mm thick back-up plate's response lies between the two during the first 40 μs of the impact process. Its slightly higher bending stiffness than the 2*3.0 mm combination, apparently compensates its 33 per cent lower mass, tensile and shear strength.
At 26 μs after impact, the 6.0 mm thick back-up plate starts its deceleration, followed by the 2*3.0 combination at 32 μs. The 4.0 mm thick back-up plate starts its deceleration later than 40 μs after impact, due to its relatively poor tensile-load carrying capabilities. The response of this back-up plate therefore exceeds the response of the 2*3.0 mm thick back-up plate, late after impact (>60 μs). The response of the

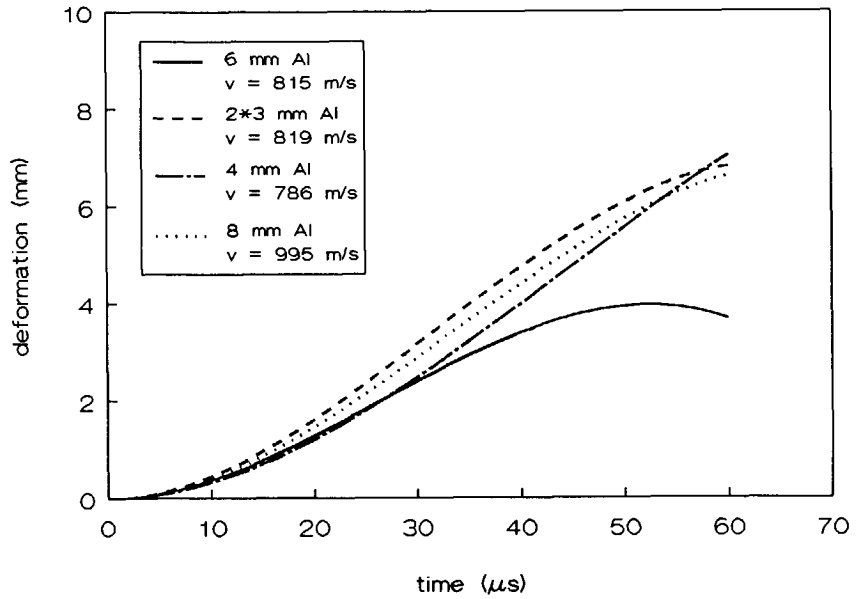

Figure 4.44 Comparison between the maximum back-up plate deformations of armours of 8.1 mm alumina backed by various aluminium back-up plates, when impacted below their ballistic limit velocities by steel rods.

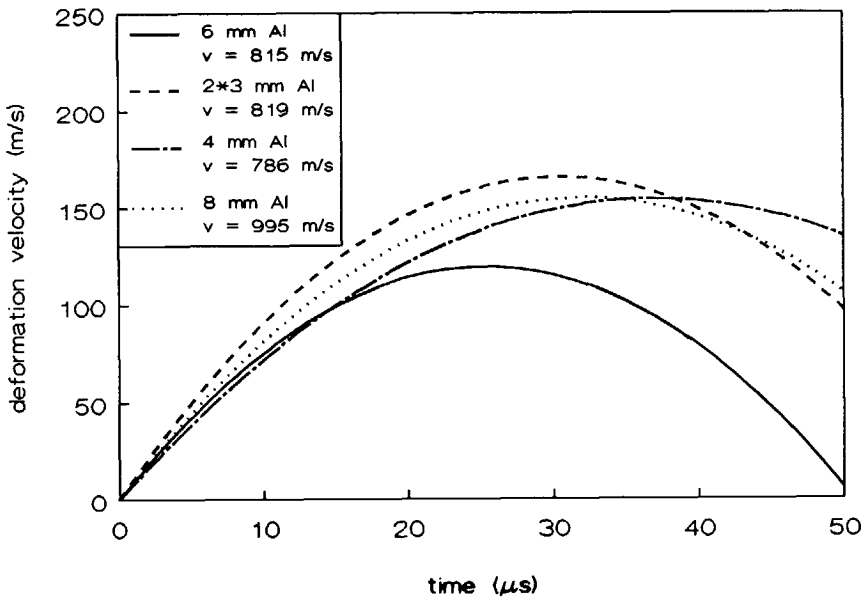

Figure 4.45 Comparison between the maximum back-up plate deformation velocities of armours of 8.1 mm alumina backed by various aluminium back-up plates, when impacted below their ballistic limit velocities by steel rods.

8.0 mm thick back-up plate lies between the others. This response is caused by an impact at 995 m/s, almost 200 m/s (24 per cent) higher then for the other armours, preventing a direct comparison with the responses of the other back-up plates.
The comparisons show that a high bending stiffness results in better support of the ceramic fracture conoid, as it reduces the deformation transient and the accumulation of strains. At later times after impact (>30 μs) the back-up plate's ability to dissipate the kinetic energy of the eroded projectile, the ceramic fracture conoid and itself becomes important. For metallic back-up plates a quick dissipation of energy is essential in order to prevent the strains to accumulate to a catastrophic level.

When the impact velocity is increased, all the armours are defeated by the rods. Their back-up plate responses are presented in figure 4.46. The response of the armour with the 4.0 mm thick back-up plate when impacted at a velocity of 829 m/s illustrates the necessity for a back-up plate to dissipate the energy quickly. Its failure can completely be attributed to the high strain accumulation during the back-up plate acceleration accompanied by its poor tensile-load carrying capabilities, which result in a too slow deceleration and energy dissipation. The other three armour responses are very similar to each other. Analysis shows that the impact load can account for this high back-up plate acceleration if only a very small area of back-up plate is involved. Hence, the shear load carrying capabilities of the back-up plate must have been exceeded by the impact loading. Very local deformation has indeed been witnessed in the flash

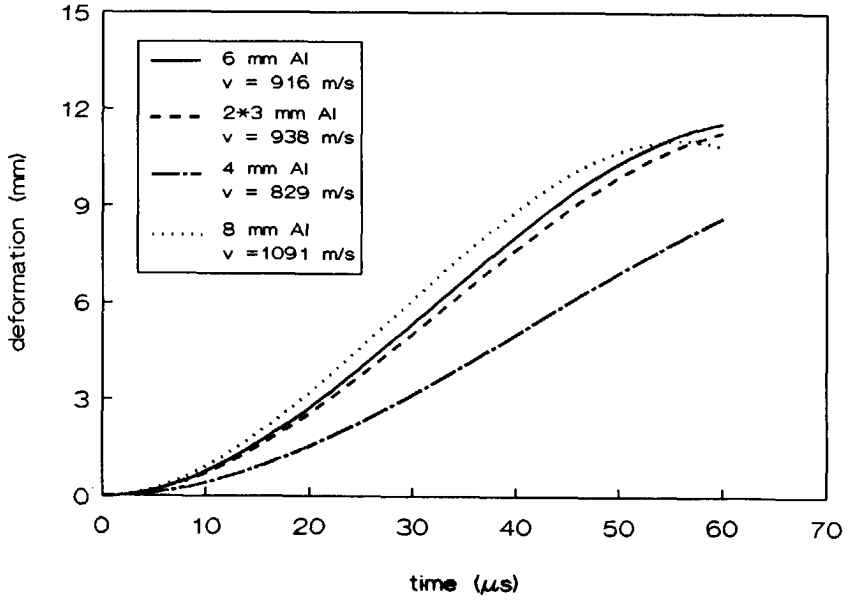

Figure 4.46 Comparison between the maximum back-up plate deformations of armours of 8.1 mm alumina backed by various aluminium back-up plates, when impacted above their ballistic limit velocities by steel rods.

radiograph sequences. Shear failure zones are also visible in recovered back-up plates. The experimental results indicate that shortly after impact (±16 μs) the ceramic facing appears to have lost its ability to distribute the high impact load over a large section of the back-up plate. Although it appears as if the ceramic facing experiences a dramatic change of behaviour when impacted at these higher velocities, its behaviour can be completely explained by the phenomenological description of events presented in section 4.3.2. The increased impact velocity results in a higher impact load, which is accordingly distributed through the ceramic conoid over a section of the supporting back-up plate. However, the increase of loading is most likely such that, at some radius of the back-up plate, significant local shear deformation results. This causes high tensile and shear stresses near the edges of the ceramic fracture conoid base. These stresses cause failure of the ceramic conoid, as described in section 4.3.2, and reduce the area over which the impact load is spread. As a result, the high impact load is now distributed over an even smaller area, immediately causing more shear deformation and more conoid base area reduction. This process may continue until only a small section of the ceramic conoid remains, distributing the load over an area of back-up plate comparable to that of the projectile. The unstable nature of this process results in a fast concentration of the impact load on a very small area of back-up plate, as was observed experimentally.

The results of the experiments indicate that there are a number of back-up plate properties, namely tensile strength, shear strength, strain to failure, density and bending stiffness, that can strongly influence a ceramic faced armour's performance. This will be discussed below.

Good tensile load carrying capabilities of the back-up plate reduce the growth of tensile strains, as they aid the back-up plate's resistance to deformation, especially when the deformation grows larger. The majority of impact experiments above the ballistic limit have shown that a too high shear load on the back-up plate, early in the impact process causes catastrophic back-up plate failure. Hence, the shear load carrying capabilities of the back-up plate are very important as well. A high strain to failure allows the back-up plate to absorb more energy before failing. The back-up plate's density has to be as low as possible. A low density allows a large back-up plate thickness to be used. The increase of thickness is accompanied by increases of the tensile load, shear load and bending moment carrying capabilities of the back-up plate.

A high bending stiffness reduces the deformation transient as the back-up plate is more reluctant to deform. It aids in the confinement of the ceramic fracture conoid to its original volume. The lateral extent of the deformation field increases with bending stiffness. Thus, a high bending stiffness effectively reduces the tensile strains in the back-up plate. However, the bending stiffness has to be considered as a subtle parameter. Both an increased and decreased stiffness may, depending on the armour configuration and materials used, improve performance.

When the armour's back-up plate fails by radial strains exceeding the material's ultimate strain, an increase of the bending stiffness of this back-up plate will improve the armour's ballistic performance as it improves ceramic confinement and hinders back-up plate deformation and thus the accumulation of strain.

On the other hand, when one considers an armour with a back-up plate that fails by plug shearing, an increase of its bending stiffness will not enhance the performance, unless it significantly increases ceramic confinement. The shear strength of the back-up plate is the weak link. Increase of the back-up plate's bending stiffness will further reduce the response of the surrounding back-up plate, shortening the time necessary to complete plug separation. However, by decreasing the back-up plate's bending stiffness such, that the shear strength remains the back-up plate's weak link, the armour's performance may be enhanced. The decrease of bending stiffness, facilitates the response of the back-up plate material surrounding the plug, thereby lengthening the time necessary to complete plug separation. As a result the projectile/plug is decelerated over a longer period of time and the back-up plate dissipates a larger amount of kinetic energy. However, the lower bending stiffness also reduces ceramic confinement which may counteract the positive effect from the increased flexibility.

The experimental results show that for armours with 6.0 mm thick and 2*3.0 mm thick back-up plates, the ballistic limit velocities lie close together. The positive effect from the increased back-up plate flexibility appears to be balanced by the negative effect caused by the reduction of the ceramic confinement.

4.3.4. The behaviour of the projectile during impact

All the series of flash radiographs presented in section 4.2 show a similar projectile behaviour. From the moment of impact onwards, projectile material is seen being ejected in radial directions from the impact area. Projectile plastic deformation appears to remain confined to a small area near the projectile/armour interface. The high circumferential stresses and the grain texture of the projectile material - long stretched grains in the axial (impact) direction - cause radial fracture of the ejected material. The high radial velocity gradient in the resulting strips of ejected material cause them to stretch and fail at some point in flight. The fringes of free-flying projectile material created by this process are visible in almost all the late-time radiographs. With the exception of fracture, the projectile's deformation process resembles that of a water jet impacting a rigid wall.
The flash radiographs and recovered projectiles indicate that the radial ejection process continues in a similar fashion after the formation of the fringes. Plastic deformation of the projectile remains limited to a small area adjacent to the projectile/armour interface. The radial fracturing process of the ejected projectile material also continues. As time progresses the strips of ejected material may either fracture, break loose or curl backwards due to their interaction with the armour. A schematic description of the projectile behaviour is given in figure 4.47.
Information on the projectile length reduction in time was obtained from the radiographs. All projectile length reduction polynomials are merged in figure 4.48. As can be seen, the differences in residual projectile lengths are very small for all situations and velocities considered. The recovered projectiles vary in length between 8 mm and 12 mm. Their shanks show very little plastic deformation (mushrooming). Some still

have a few curls of ejected material attached to them. On average, these recovered projectiles account for about 34 per cent of the projectile's original mass (7 grams). The length reduction rates are presented in figure 4.49. It shows that the length reduction process continues for a period of 40 to 60 μs. The longer length reduction periods are associated with impact on armours with more flexible supports (e.g. the 2*3.0 mm thick and 4.0 mm thick back-up plates).

The series of experiments show that the blunt steel rods appear to erode mass for a considerable amount of time. The rods do not break up into a discrete number of fragments during impact. The recovered shanks show little plastic deformation. The fringes of eroded projectile material, visible on the radiographs, fly away from the impact area at maximum velocities of 560-960 m/s, i.e. close to the impact velocity.

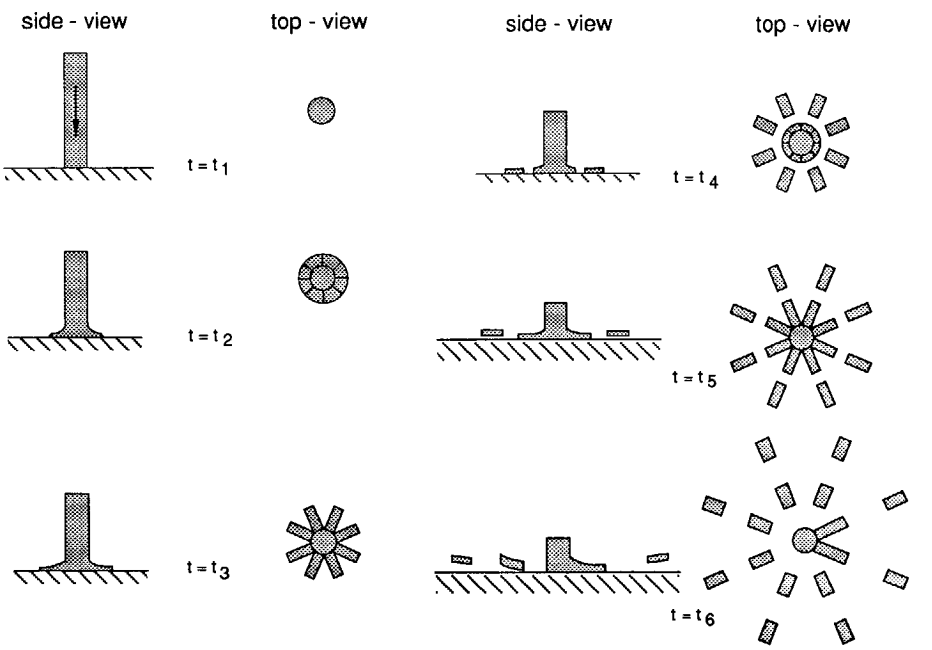

Figure 4.47 A phenomenological description of the observed projectile behaviour.

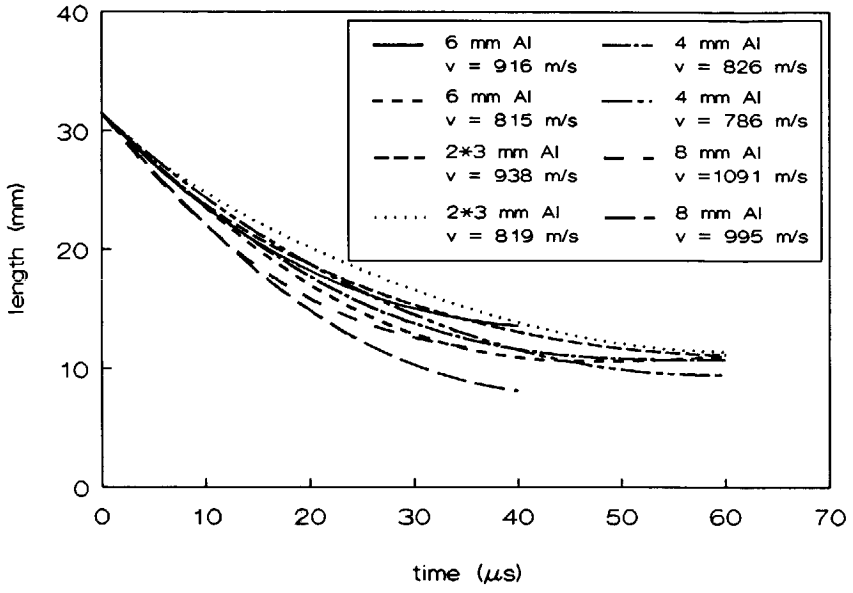

Figure 4.48 Comparison between the projectile length polynomials resulting impact at velocities below and above the ballistic limit velocities of armours of 8.1 mm alumina backed by various aluminium back-up plates.

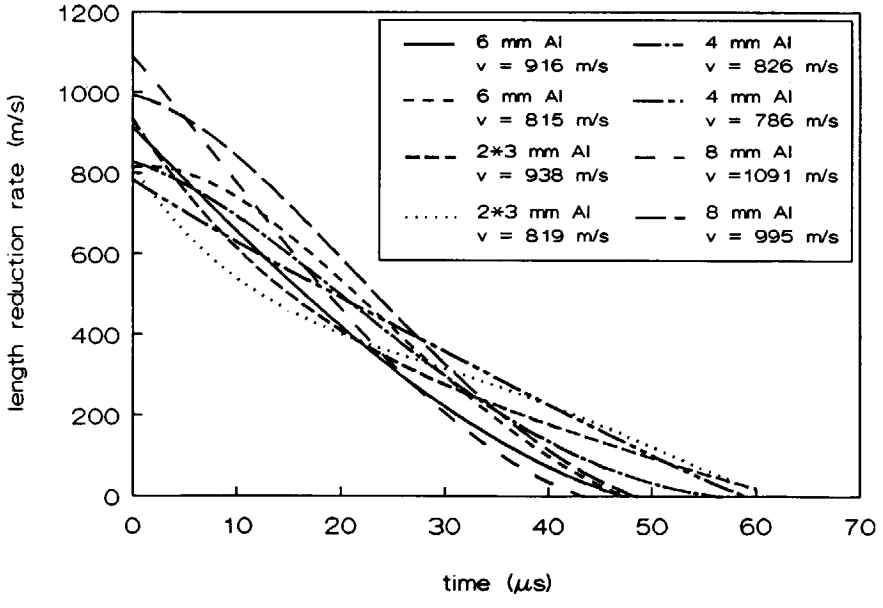

Figure 4.49 Comparison between the projectile length reduction rates resulting impact at velocities below and above the ballistic limit velocities of armours of 8.1 mm alumina backed by various aluminium back-up plates.

4.4. Conclusions

The flash radiographs presented in this chapter show that the novel flash X-ray technique provided a unique means to monitor penetration of projectiles into ceramic faced armours without limiting the lateral dimensions of the armour panels. Ceramic particles did not, as some researchers feared, obscure the projectile/armour interaction. Even though the analysis of the radiographs is time consuming, the technique provides new possibilities for observing projectile behaviour inside armour materials.

The phenomenological behaviour and break-up process of the Morgan Matroc Hilox 973 alumina facing following a rod impact is described and understood. In contrast with the experimental work with blunt rods by Wilkins (1967), the projectile was not able to penetrate through the ceramic material directly in front of it in most of the impact experiments.
The observations suggest that aside from a group of static properties, as proposed by Viechnicki *et al.* (1987) and Slavin *et al.* (1988), a high shear strength is also very important for ceramic materials, in order to be able to distribute the impact load effectively.

The influence of back-up plate properties on the protection level obtained has been discussed. An increase of the back-up plate's tensile strength, shear strength or ultimate strain can improve armour performance depending on the armour configuration. A reduction of the back-up plate's density also improves performance. The increase of bending stiffness is expected to have a positive effect on the protection level as long as the back-up plate does not fail by plug shearing. The ballistic performance of armours with back-up plates that do fail by plug shearing may be enhanced by decreasing the bending stiffness of the back-up plate. However, the lower bending stiffness also reduces ceramic confinement which may counteract the possitive effect from the increased flexibility. The tuning of the bending stiffness may becomes especially important for applique (add-on) armour systems and armours where the thickness of the ceramic facing and back-up plate are constrained.

The analysis of the experimental results showed that the shear failure mode in the back-up plate is probably caused by a catastrophic loss of load-distributing capabilities of the ceramic facing. As early as 20 μs after impact the armour's inability to defeat the projectile is clearly visible.

The erosion and deformation behaviour of the blunt steel rods is similar in all series of experiments. The rod erodes mass for a considerable amount of time (> 40 μs). On average, the rods eroded by about 66 per cent. The shanks recovered show little plastic deformation. The fringes of eroded projectile material, visible in many of the radiographs, move away from the impact area at maximum velocities of 560-960 m/s.

The smooth match between the data-points and the curve-fits indicate that the impact experiments reproduce very well. Only with a few series of experiments above the ballistic limit velocity, some scatter of the data-points is observed. Still, it is believed that the results presented in this chapter are reliable and representative.

The results and observations from the eight series of impact experiments with blunt steel rods were used to form a data-base containing detailed information on the penetration processes into ceramic faced armours. Both analytical and hydrocode modelling of impact phenomena on ceramic faced armours can benefit from this data-base.

4.5. Recommendations

Based on the observations and results presented, a number of recommendations for future research can be given.
The experimental technique used and the accuracy of the radiograph analysis procedure prevent the accurate measurement of and discrimination between early time (<16 μs) responses of the various back-up plates. Streak photography or VISAR interferometry experiments can be used to accurately measure the armour response during the first 16 μs of the impact process.

Impact experiments with short projectiles (L/D < 1) allow the development of the initial ceramic fracture conoid to be studied. Combined analysis with the streak photography or VISAR may result in an improved understanding of the events, leading to the further confirmation of the presented phenomenological description of events. In particular the events leading to the ceramic's catastrophic loss of load-carrying capabilities need further investigation.

In addition, the influence of projectile material and geometry on the ballistic limit velocity of ceramic faced armours need to be assessed. A preliminary study on this topic, showing the influence of the projectile geometry on the ballistic limit velocity, is presented by Van Zuidam (1990). According to this study, the ballistic performance changed only marginally when the blunt rod's length over diameter ratio was varied from 2.2 to 9.7. All the armours used had relatively thin back-up plates (4.0 mm aluminium 6061-T6). Their failure was observed to be primarily caused by too high tensile strains. The results presented in this chapter indicate that the failure of armours with stiff back-up plates is probably caused by a catastrophic loss of load-distribution capabilities of the ceramic facing which results in a too high shear loading of the back-up plate. It is therefore expected that a much larger influence on the ballistic protection level is experienced when stiff armours instead of armours with relatively thin back-up plates are impacted by blunt rods with various length-over-diameter ratios.

5. MODEL SIMULATION OF THE EXPERIMENTS WITH THE RODS

5.1. Introduction

Before the impact experiments with the rods could be simulated with the analytic model, a number of input parameters had to be quantified. These parameters govern the geometry, composition and material properties of the rod and the armour. In addition, the penetration resistance properties of the comminuted ceramic, as defined in section 2.9, had to be specified. After having obtained the required set of input parameters, the ballistic limit velocities were computed for steel rod impact onto 8.1 mm thick alumina supported by a whole range of thicknesses of aluminium.
In order to compare and verify details of the penetration process as predicted by the model and as experimentally observed, the analytic model was also used to simulate all eight series of impact experiments by using the same initial conditions as in the experiments.

5.2. The ALARM model input parameters

A number of parameters governing the armour and projectile material properties and impact conditions had to be quantified in order to use the model. Most of them could be obtained easily, as they describe the armour and projectile geometry and composition. A large number of the input parameters describing the material properties of the projectile, ceramic and back-up plate were obtained from available data sheets.
The fracture conoid angle had to be specified as well. The (half) conoid angle was set at 65°. At this angle, the size of its base-area matched the experimental observations of section 4.2. The radius of back-up plate allowed to respond to the impact event was set at 5/3 of the base-radius of the ceramic's fracture conoid. The flash radiographs and recovered back-up plates show that most of the plastic deformation is limited to within this area.
In the ALARM model, the projectile's elastic wave velocity is used to set the initial armour penetration velocity at the moment that the ceramic fracture conoid has completely formed, typically some 5 μs after impact. For this purpose the ALARM model uses an equation which is strictly speaking valid at the moment of impact only. In order to obtain initial penetration velocities close to the ones observed experimentally at 5 μs after impact, the elastic wave velocity is used as a tune parameter and was set at 500 m/s, which is approximately ten per cent of its original value.
Neither the steel's dynamic yield strength nor its plastic wave velocity were given in the available ETG-100 data-sheet. Hence, they had to be obtained from the experimental results. During the first 40 μs of the impact process, the experimentally observed projectile behaviour, presented in section 4.3.4, complies reasonably well with the projectile behaviour modelled in the so-called mass erosion phase of the impact process. The projectile material's dynamic yield strength was determined from the experimentally obtained projectile rear-end position and length reduction polynomials

using equation (2.11). The dynamic yield strength was found to be 0.17 10^{10} N/m^2, very close to the value of 0.19 10^{10} N/m^2 given by Rosenberg & Tsaliah (1990) for a similar but slightly stronger steel (R_C = 30 compared to R_C = 28).
At the moment that the projectile's length reduction velocity equals the plastic wave velocity, the end of the projectile mass erosion phase is initiated in the ALARM model. Therefore, the plastic wave velocity was set to 133 m/s, equal to the average length reduction rate measured from the polynomials at 40 μs after impact.

The input parameters left to be determined were the comminuted ceramic's penetration resistance properties, represented by the constants β and γ in equation (2.53), and (optional) the radius of the hole, r_{hole}, surrounding the impact point through which the ejection of comminuted ceramic may take place (equation 2.71).
These parameters cannot yet be derived from known material properties. They had to be obtained using a tuning procedure. The parameters were chosen such, that the ballistic limit velocities of the armours with the thin back-up plate (4.0 mm) and thick back-up plate (8.0 mm) matched the experimental results. The ceramic ejection option was not used.

5.3. ALARM simulation versus experiment

The ballistic limit velocities of armours composed of 8.1 mm thick Morgan Matroc Hilox 973 alumina supported by a whole variety of thicknesses of aluminium 6061-T6 were computed by the model. The results are presented in table 5.1, and compared with the experimental results in figure 5.1. The ALARM model correctly predicted that the ballistic limit velocity of the armour with the double back-up plate lies close to the v_{50} of the armour with the 6.0 mm thick back-up plate. Based on the limited amount of experimental ballistic limit velocity data, the agreement between experiment and simulation appears to be good. The ALARM model computations show that the armour with the 4.0 mm thick back-up plate failed due to the accumulation of high tensile strains, when impacted just above the ballistic limit velocity. The armour with the double back-up plate (2*3.0 mm) failed in a combined shear/tensile mode when impacted just above the ballistic limit velocity. The first back-up plate was sheared off, the second layer failed in tension. The armours with the 6.0 mm and 8.0 mm thick back-up plates both fail by plug shearing. These failure modes match those observed experimentally.

In order to compare details of the penetration processes as predicted by the ALARM model with the experimental observations, simulations were carried out for all four armour configurations at the same impact velocities that were used in the experiments. The results of these simulations are presented in table 5.2. It shows that the ALARM model correctly predicts armour or projectile defeat in all situations. Comparisons between experimentally determined and predicted projectile rear-end position, armour penetration and back-up plate deformation profiles are presented in figure 5.2 for the impacts at velocities below the ballistic limit.

Table 5.1 Comparison of the experimentally obtained and ALARM generated ballistic limit velocities and failure model for armours of 8.1 mm thick alumina supported by aluminium when impacted by blunt steel rods.

Back-up plate thickness [mm]	ballistic limit velocity [m/s]		failure mode	
	experiment	simulation	experiment	simulation
3.0		662		
3.5		728		
4.0	786 - 829	790	shear & strain	strain
4.5		837		
5.0		865		
5.5		889		
6.0	815 - 916	916	shear	shear
2*3.0	818 - 938	905	shear & strain	shear & strain
6.5		945		
7.0		975		
7.5		1008		
8.0	995 - 1091	1045	shear	shear
8.5		1086		
9.0		1131		
9.5		1183		

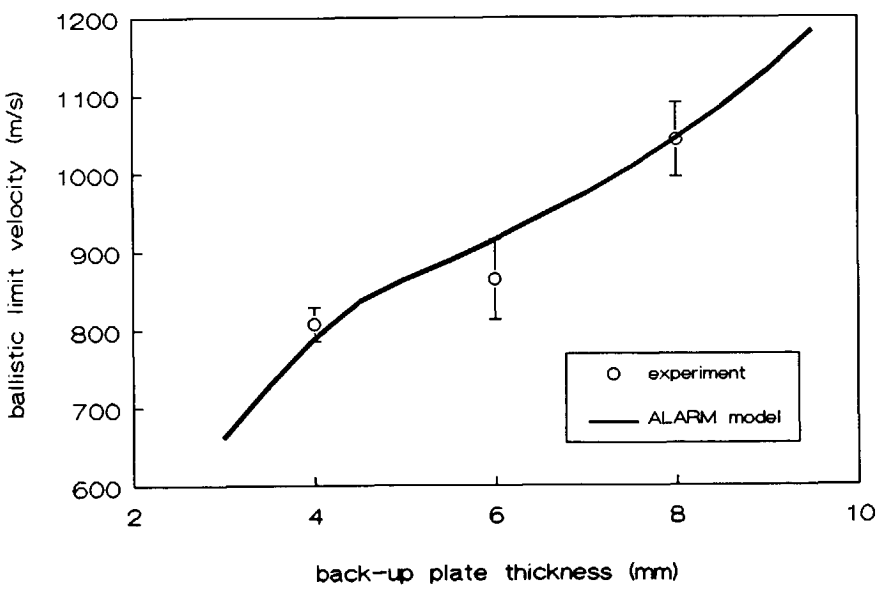

Figure 5.1 Comparison of ballistic limit velocities obtained by experiments and the ALARM model for armours of 8.1 mm alumina backed by various thicknesses of aluminium when impacted by the steel rod.

Table 5.2 Comparison of experimentally obtained and ALARM generated maximum back-up plate deformation, residual projectile mass and failure mode for armours of 8.1 mm thick alumina supported by aluminium, when impacted by blunt steel rods at velocities below and above their ballistic limit.

Back-up plate thickness [mm]	impact velocity [m/s]	max. deformation [mm]		residual projectile mass [10^{-3} kg]		failure mode	
		experiment	simulation	experiment	simulation	experiment	simulation
4.0	786	11	16	2.4	3.6	-	-
4.0	829	-	-	2.4	3.4	strain & shear	shear
6.0	815	5	5	2.6	3.0	-	-
6.0	916	-	-	2.3	2.6	shear	shear
2*3.0	819	11	12	2.4	3.2	-	-
2*3.0	938	-	-	2.3	2.7	shear & strain	shear
8.0	995	7	5	1.8	1.9	-	-
8.0	1091	-	-	2.6	2.0	shear	shear

For all four impact events, the computed back-up plates responses are somewhat slow when compared with the experimental data. This is very evident at early times after impact, as is illustrated in figure 5.3. The ALARM-model correctly predicts that the differences in back-up plate response become more significant at late times after impact. The computed positions of the rear-end of the projectile match the experimental observations very well. The armour penetration by the projectile is somewhat over-predicted by the model, especially when the (slow) back-up plate response is taken into account.

A comparison between the projectile lengths as experimentally determined and computed by the model is presented in figure 5.4. With the exception of the projectile impacting the armour with the 8.0 mm thick back-up plate, projectile length reduction is slightly under-estimated. The too high armour penetration by the projectile early in the impact process, as computed by the model, is accountable for this result. The comparison of the simulations with the experimental results show that for impact below the armour's ballistic limit velocity, the ALARM model is capable of presenting details of the impact process with acceptable accuracy.

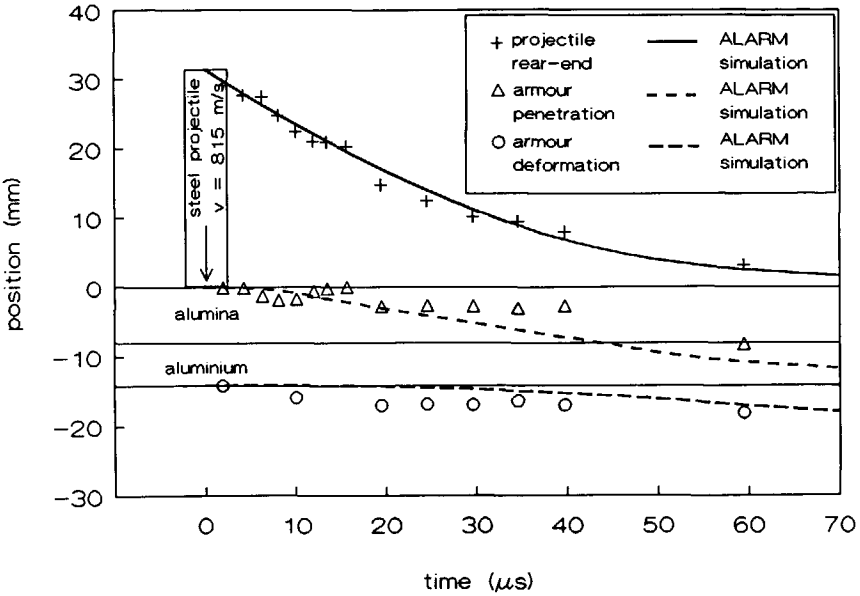

Figure 5.2a Comparison between predicted (ALARM) and experimentally obtained position-versus-time curves of the steel rod impacting 8.1 mm alumina backed by 6.0 mm aluminium at a velocity below the v_{50} (815 m/s).

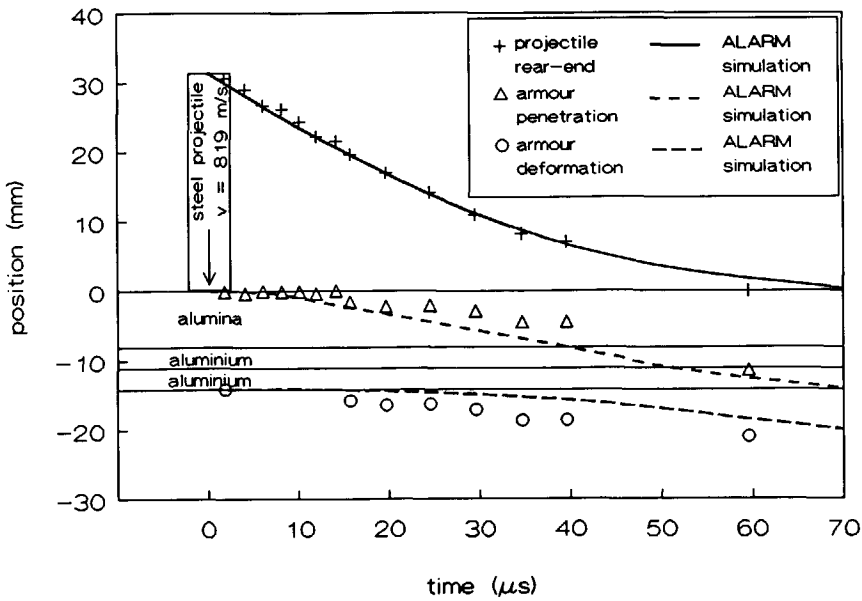

Figure 5.2b Comparison between predicted (ALARM) and experimentally obtained position-versus-time curves of the steel rod impacting 8.1 mm alumina backed by two 3.0 mm layers aluminium at a velocity below the v_{50} (819 m/s).

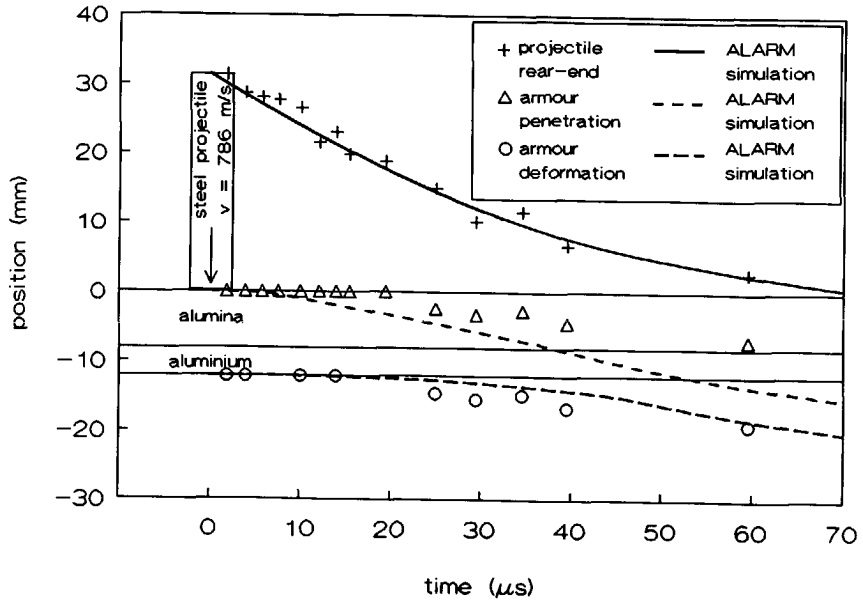

Figure 5.2c Comparison between predicted (ALARM) and experimentally obtained position-versus-time curves of the steel rod impacting 8.1 mm alumina backed by 4.0 mm aluminium at a velocity below the v_{50} (786 m/s).

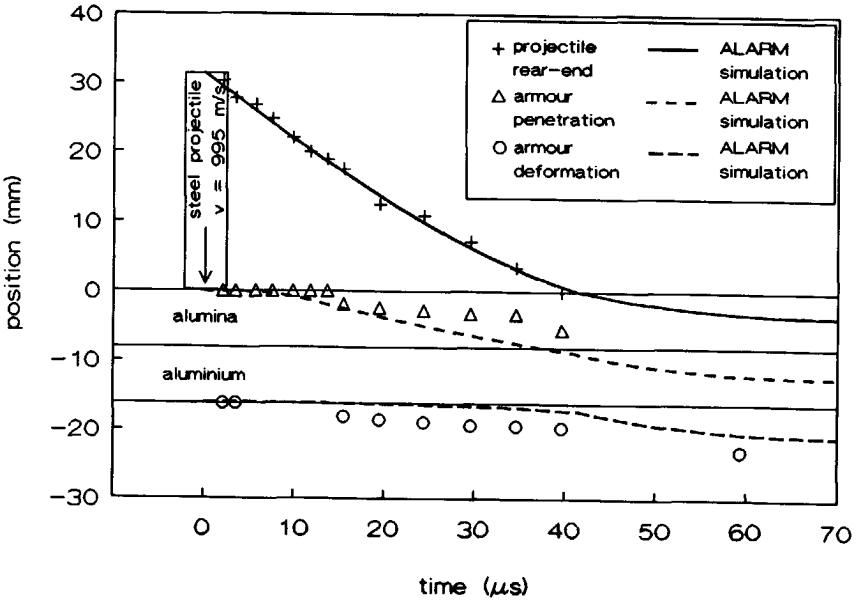

Figure 5.2d Comparison between predicted (ALARM) and experimentally obtained position-versus-time curves of the steel rod impacting 8.1 mm alumina backed by 8.0 mm aluminium at a velocity below the v_{50} (995 m/s).

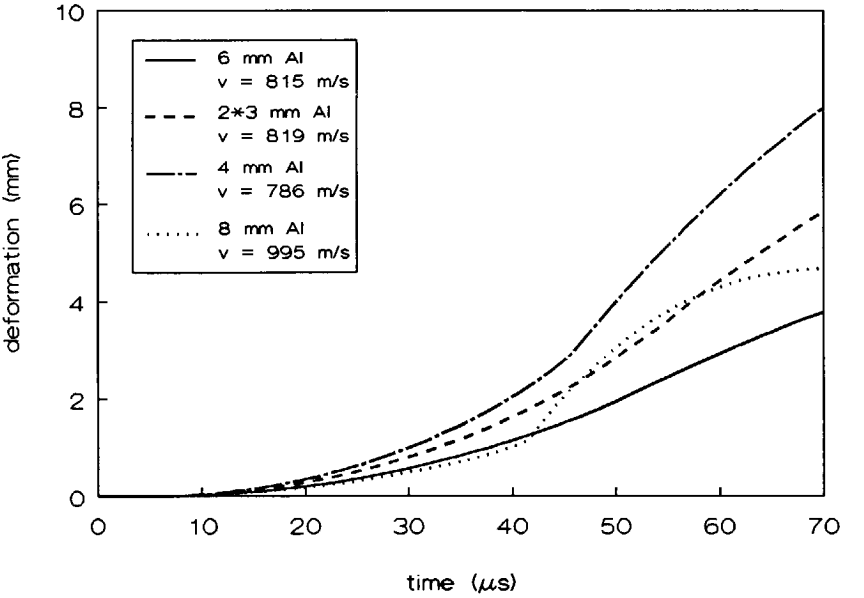

a) ALARM simulations

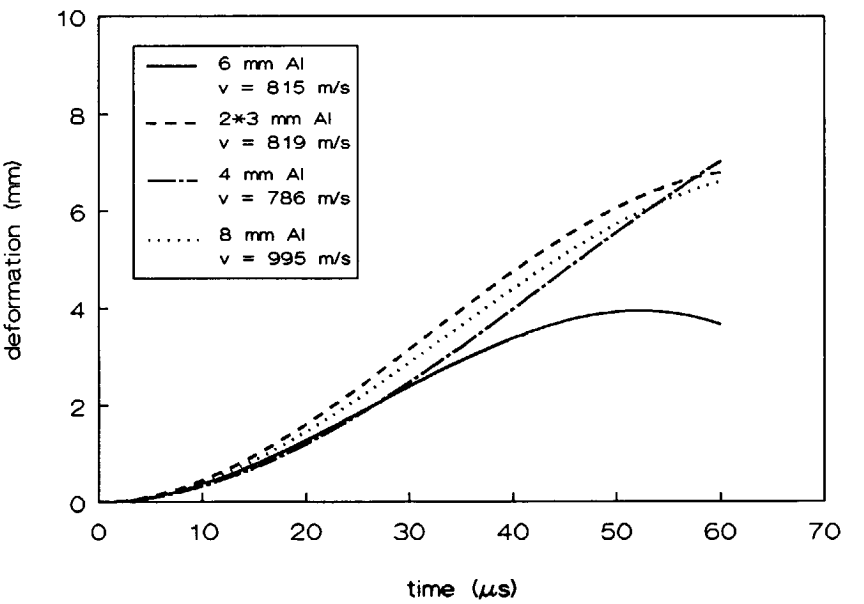

b) experimental results

Figure 5.3 Comparison between predicted (ALARM) and experimentally obtained maximum back-up plate deformations of armours of 8.1 alumina backed by various aluminium back-up plates, when impacted below their ballistic limit velocities by steel rods.

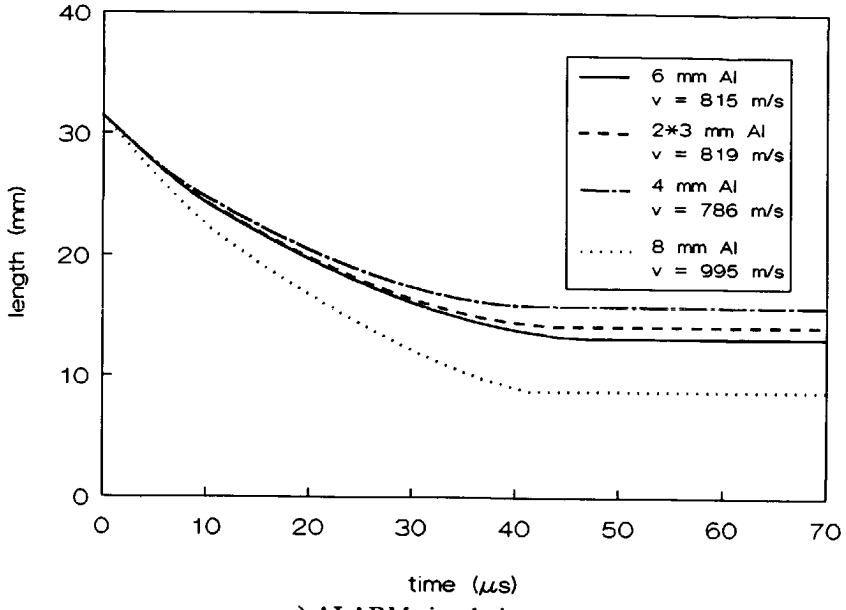

a) ALARM simulations

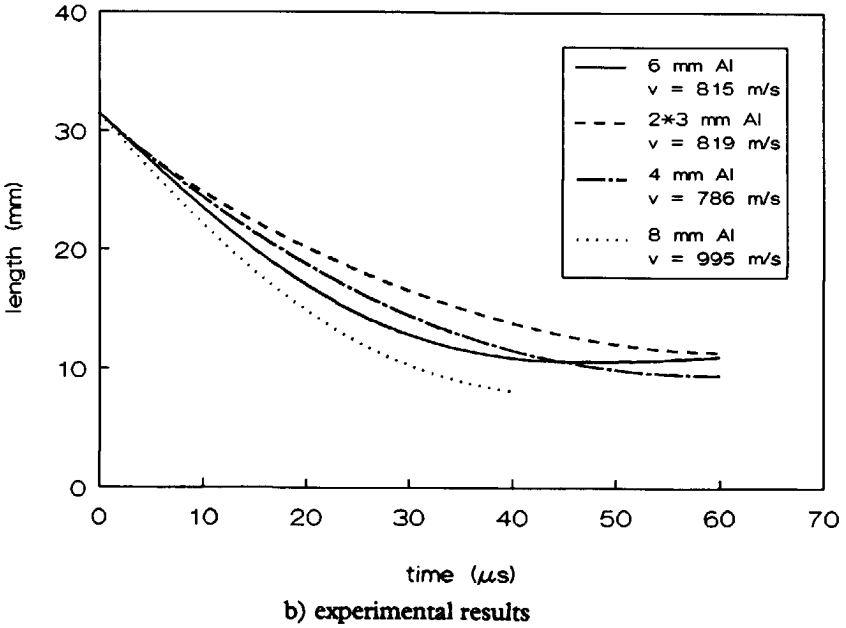

b) experimental results

Figure 5.4 Comparison between predicted (ALARM) and experimentally obtained projectile lengths resulting impacts below the ballistic limit velocities of armours of 8.1 alumina backed by various aluminium back-up plates.

ALARM simulations were also carried out for projectiles impacting at velocities above the armour's ballistic limit. The comparisons between the simulations and the experimental results are presented in figure 5.5. Also here, the computed projectile rear-end positions match the experimental data very well. The maximum back-up plate deformation, however, clearly lags behind when compared with the experimental results for all but the armour with the 4.0 mm thick back-up plate. At the specified velocities, the ALARM model predicts that the shear failure mode dominates in all four back-up plates. This failure mode was also observed experimentally for the armours with the 6.0 mm and 8.0 mm thick back-up plates. According to the experimental data presented in sections 4.2.2 and 4.2.3, the armours with the 2*3.0 mm and 4.0 mm thick back-up plates failed by accumulation of high tensile strains in combination with some plug shearing. The ALARM model predicts the correct back-up plate failure modes, when the armours are impacted at velocities just above the computed ballistic limit velocity. However, at the higher velocities used with the experiments, the model predicts the shear failure mode to be dominant. Especially for the armour with the 4.0 mm thick back-up plate, this was accompanied by large differences between simulated and measured responses as observed in figure 5.6.

This figure also shows that there exists a time-delay of approximately 25 μs between the measured and computed responses of the armours with the 2*3.0 mm, 6.0 mm and 8.0 mm thick back-up plates. The projectile length reduction and armour penetration profiles presented in figure 5.7 and 5.8 match the experimental results fairly well. The armour penetration profile calculated for the impact onto the armour with the 4.0 mm thick back-up plate is somewhat over-estimated. The armour penetration calculated for the impact into the armour with the 8.0 mm thick back-up plate is somewhat under-estimated. Due to these deviations from the experimental results, the projectile length reductions calculated for impact into these two armours differ somewhat from the experimental data.

The comparison of the simulations with the experimental results show that for impact above the armour's ballistic limit velocity, the ALARM model is also capable of presenting details of the impact process correctly, with the exception of the back-up plate response. The back-up plate response is found to clearly lag behind, especially in those situations where the experimental results indicate that the armour's back-up plate had failed by plug shearing.

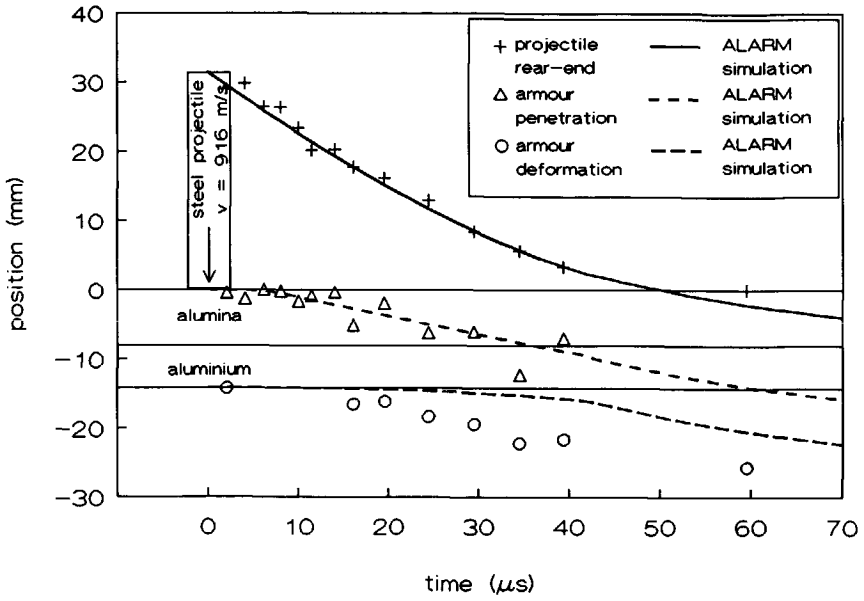

Figure 5.5a Comparison between predicted (ALARM) and experimentally obtained position-versus-time curves of the steel rod impacting 8.1 mm alumina backed by 6.0 mm aluminium at a velocity above the v_{50} (916 m/s).

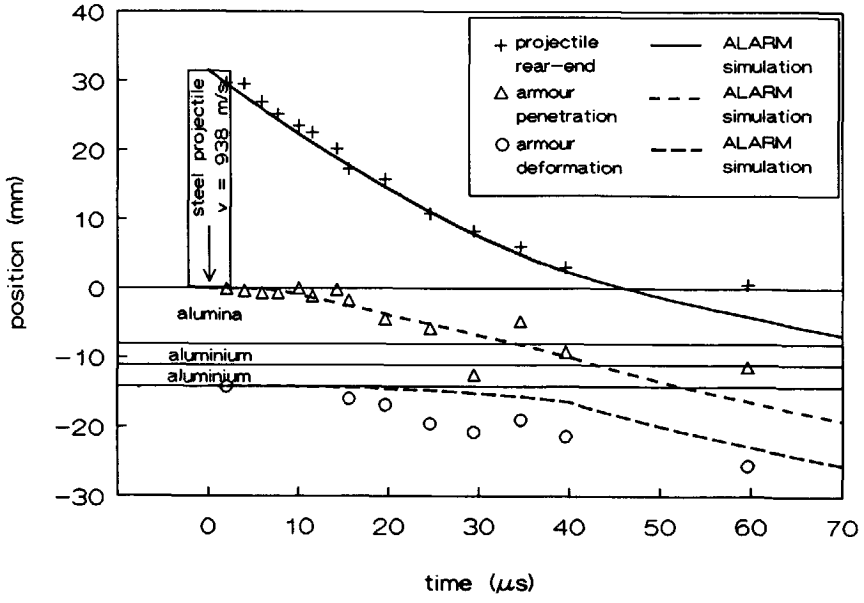

Figure 5.5b Comparison between predicted (ALARM) and experimentally obtained position-versus-time curves of the steel rod impacting 8.1 mm alumina backed by two 3.0 mm layers aluminium at a velocity above the v_{50} (938 m/s).

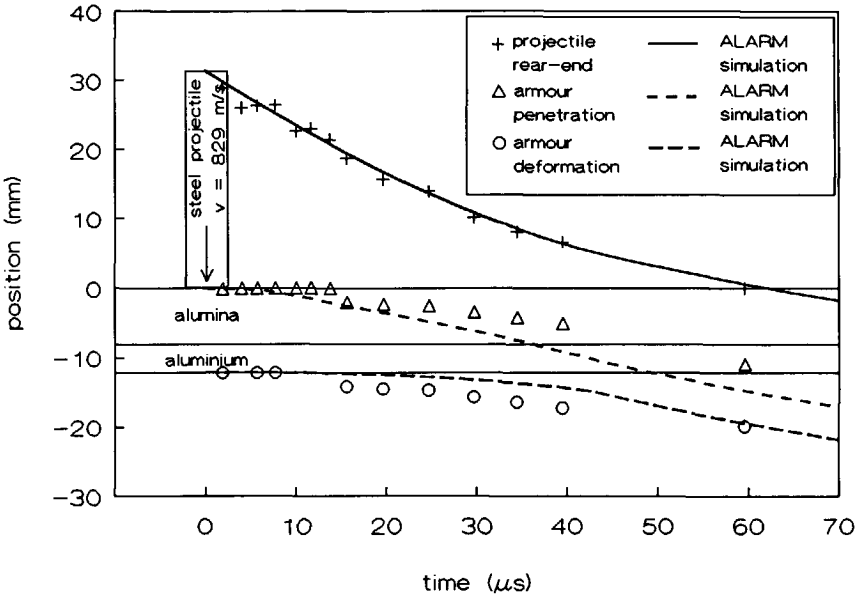

Figure 5.5c Comparison between predicted (ALARM) and experimentally obtained position-versus-time curves of the steel rod impacting 8.1 mm alumina backed by 4.0 mm aluminium at a velocity above the v_{50} (829 m/s).

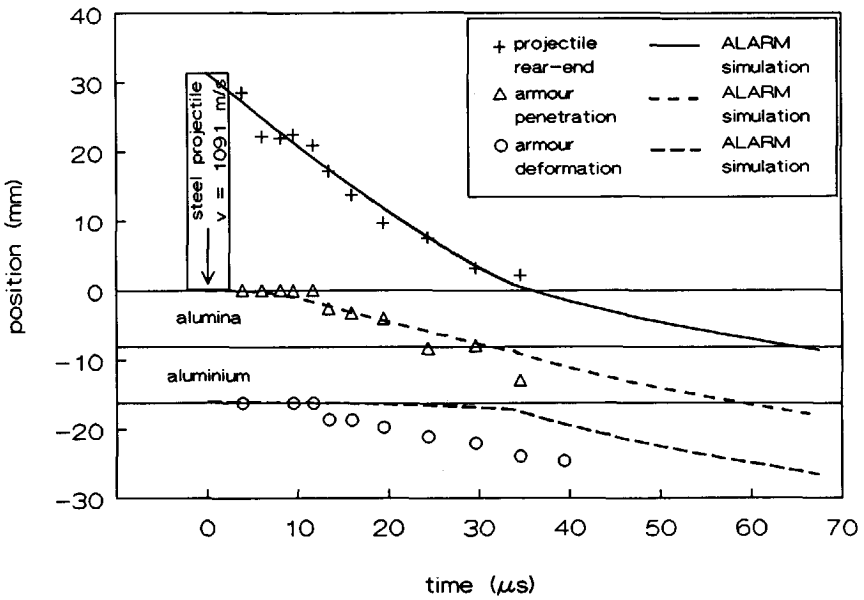

Figure 5.5d Comparison between predicted (ALARM) and experimentally obtained position-versus-time curves of the steel rod impacting 8.1 mm alumina backed by 8.0 mm aluminium at a velocity above the v_{50} (1091 m/s).

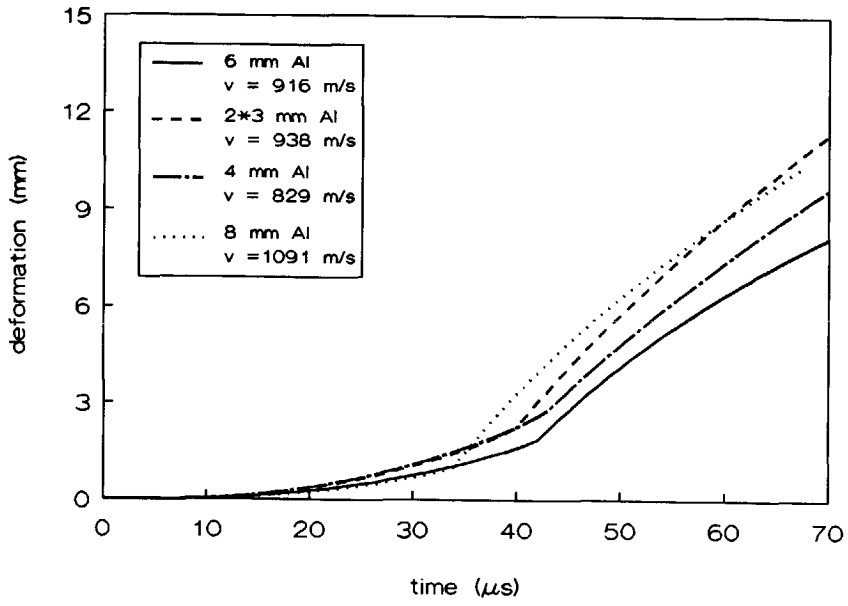

a) ALARM simulations

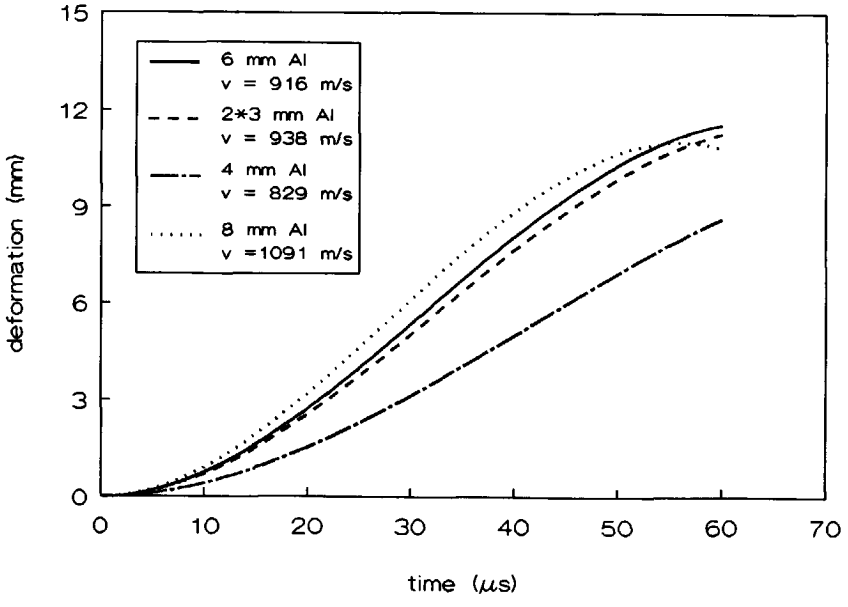

b) experimental results

Figure 5.6 Comparison between predicted (ALARM) and experimentally obtained maximum back-up plate deformations of armours of 8.1 mm alumina backed by various aluminium back-up plates, when impacted above their ballistic limit velocities by steel rods.

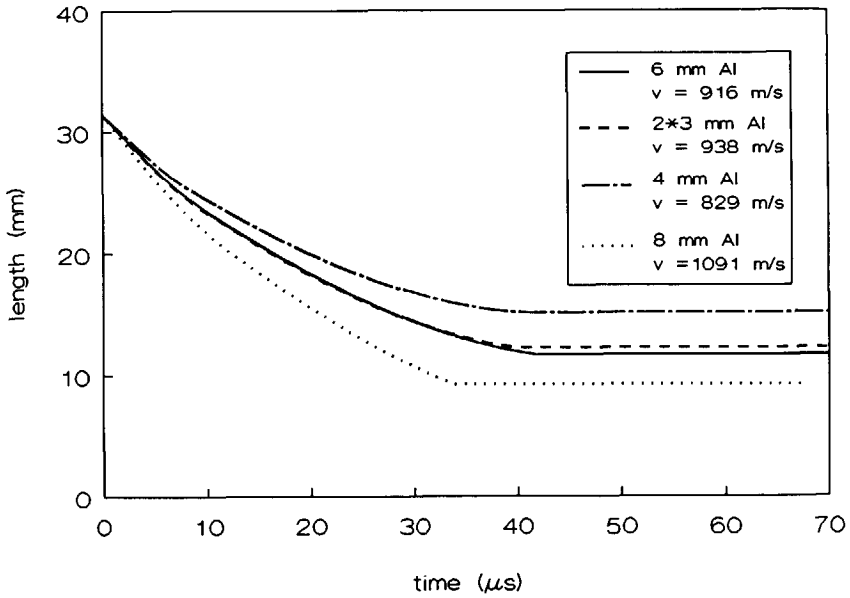

a) ALARM simulations

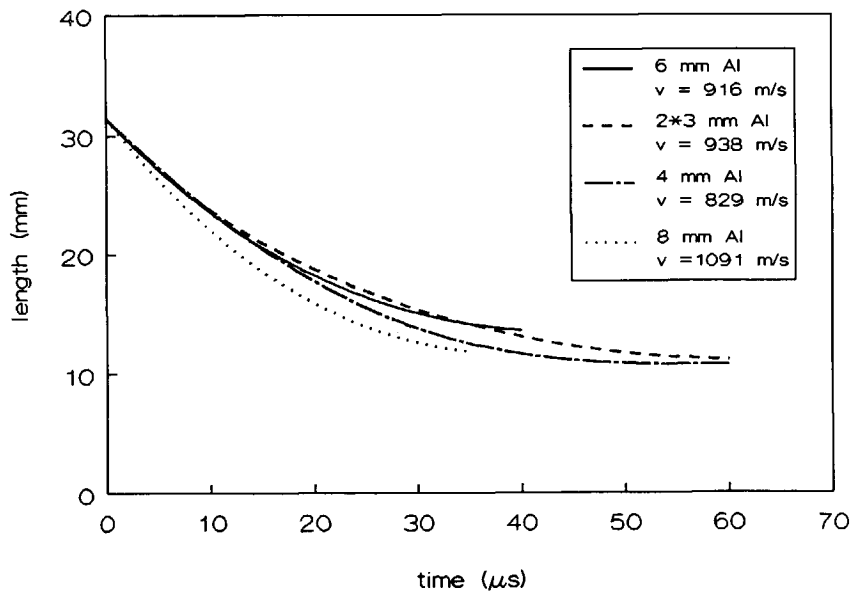

b) experimental results

Figure 5.7 Comparison between predicted (ALARM) and experimentally obtained projectile lengths resulting impacts above the ballistic limit velocities of armours of 8.1 mm alumina backed by various aluminium back-up plates.

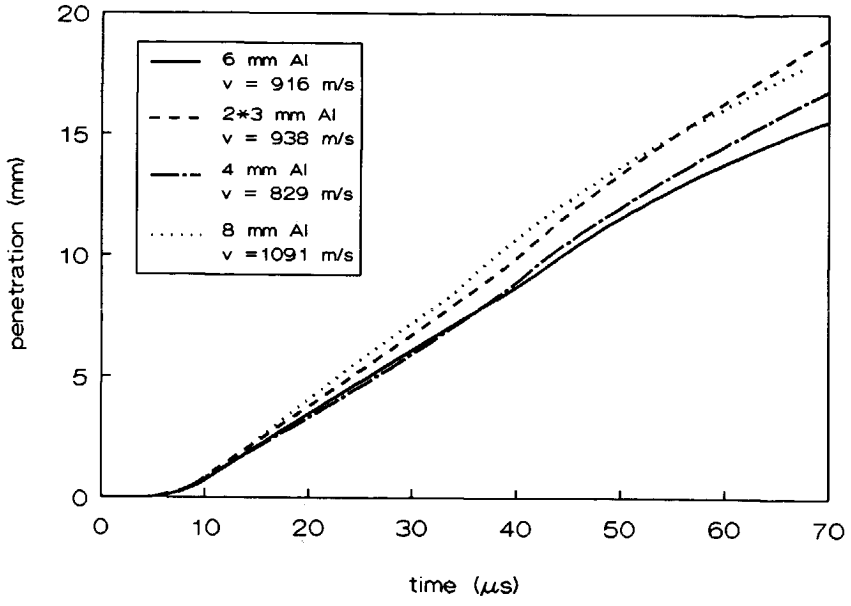

a) ALARM simulations

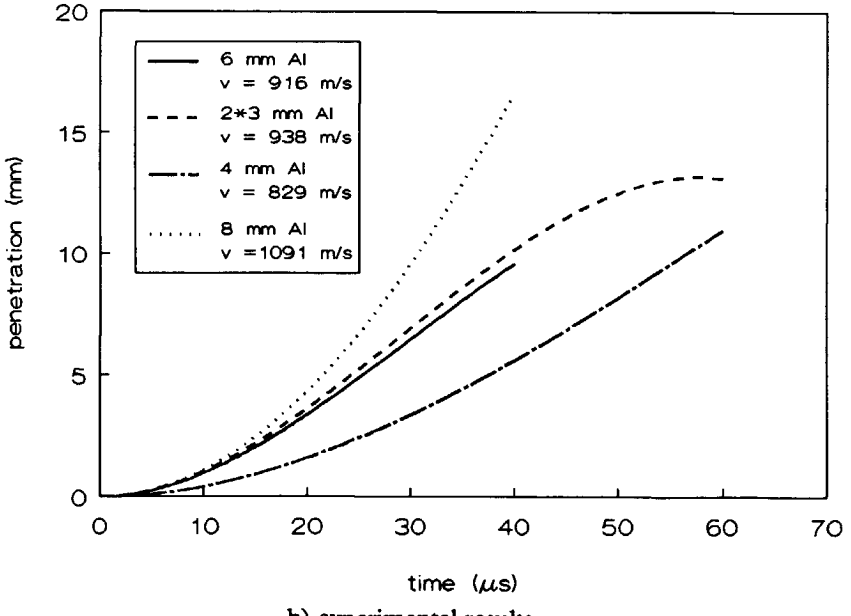

b) experimental results

Figure 5.8 Comparison between predicted (ALARM) and experimentally obtained armour penetrations of armours of 8.1 mm alumina backed by various aluminium back-up plates, when impacted above their ballistic limit velocities by steel rods.

5.4. Discussion

The results of the ALARM simulations show that the calculated behaviour complies reasonably well with the experimental observations. The ballistic limit velocities computed for the armours with the 6.0 mm thick and 2*3.0 mm thick back-up plates match the experimental data very well.
The back-up plate responses computed by the model for impacts below the ballistic limit velocity are somewhat slow when compared with the experimental observations. This may directly be attributed to the assumption of the ALARM model that the section of back-up plate, loaded by the projectile through the ceramic fracture conoid, is rigid, and cannot deform. This implies that the ceramic fracture conoid loaded by the projectile and all of the back-up plate material directly underneath it, are constrained to experience the same acceleration. However, the series of flash radiograph sequences show the back-up plate bulging from the moment that deformation becomes noticeable. Only a small central area of back-up plate seems to experience the maximum acceleration. Hence, a comparatively large section of back-up plate encounters the maximum acceleration in the model. With similar impact loading conditions, this inevitably results in a slower acceleration of the back-up plate by the ALARM model when compared with the experimental results. By introducing a modification to the back-up plate deformation field used in the ALARM model, such that it better simulates a bulging back-up plate, the model can be expected to produce a better match with the experimental back-up plate deformation data.

The discrepancies observed between the calculated and experimentally obtained armour penetration profiles are related to the projectile/armour interaction mechanism used in the model. In the series of experimental results presented in chapter 4, the projectiles appear (almost) unable to penetrate the ceramic material directly underneath it. As presented in section 4.3.2, the impact load is distributed through the ceramic conoid over a limited area of back-up plate shortly after impact. As the back-up plate deflects, the edges of the base of this ceramic conoid are no longer able to distribute the impact load. This results in the impact load being distributed over an increasingly smaller area of back-up plate, without the projectile having to penetrate through the ceramic material. The ALARM model assumes that the projectile is able to penetrate through the ceramic material inside the fracture conoid. The ceramic material in front of the projectile is assumed to distribute the impact load over an area of back-up plate. The size of this area decreases as the projectile penetrates through the ceramic material and closes in on the back-up plate. Hence, while over-estimating the ceramic penetration, the model distributes the impact load over the back-up plate in a similar fashion as is observed experimentally.

The differences between the calculated and the measured back-up plate deformation profiles, for impacts above the armour's ballistic limit velocity, are also related to the aforementioned projectile/armour interaction mechanism. The quick response of the back-up plates, observed in the experiments, is probably caused by a too high shear load on the back-up plate, which results in a quick localization of the impact load on a

small area of back-up plate, as described in section 4.3.3. This immediately initiates the plug shearing mechanism. In the ALARM model, the projectile has to penetrate through almost the complete thickness of ceramic facing before it can effectively distribute the load over a similar small area of back-up plate. On average it takes the rod projectile some 35 μs to accomplish this ceramic penetration, which reasonably matches the time-delay observed in the comparisons of the results presented in figure 5.5.

The ALARM simulations showed the correct failure modes for rod impact onto armours with 4.0 mm and 2*3.0 mm thick back-up plates at a velocity slightly above the calculated ballistic limit velocity. However, when the impact velocities of the rods were increased to match those used in the experiments, the failure modes were seen to change to plug shearing which was accompanied by large differences between the calculated and measured back-up plate responses. This change of back-up plate response and failure mode is caused by the use of a slightly too low back-up plate shear strength in the model. Simulations with an increased shear strength (15 per cent) satisfied the experimental results better.

5.5. Conclusions

The simulations with the ALARM model show that with a limited amount of empirical data, the model can reproduce the effects of (limited) variations of armour geometry on the ballistic limit velocities with an acceptable accuracy (~10 per cent).
The armour failure modes at the ballistic limit velocities calculated with the ALARM model match the experimental data satisfactorily. The projectile/armour interaction mechanism used in the model is found to deviate somewhat from the mechanism observed experimentally. However, by over-estimating the ceramic penetration, the model distributes the impact load over the back-up plate in a similar fashion as is expected on basis of the experimental results.
For impacts below the armour's ballistic limit velocity, the projectile and armour deformation processes match the experimental evidence fairly well. For rod impacts, which cause back-up plate plug shearing, the predicted deformation process shows the shear failure mode to occur later in time. In its present form, the ALARM model is not able to predict the rapid decrease of load-distribution capability of the ceramic facing as indicated by the experimental evidence.

The change of failure mode, calculated by the ALARM model for the armours with the 4.0 mm and 2*3.0 mm thick back-up plates, when the impact velocity of the rods is increased, show the importance of using the "correct" material properties. One should apply extreme care when analysing the results of simulations which include strain-rate sensitive materials, for example.

5.6. Recommendations

The comparison between experimental observations and the calculations by the model highlight a number of areas where the analytic model can be improved.
Modifications of the projectile/armour interaction mechanism used in the analytic model to match the mechanism observed experimentally more accurately are expected to improve the model's performance. However, the prediction of the armour response for impacts above the ballistic limit velocity, may already improve significantly, when only the ceramic's catastrophic loss of load-distribution capability is included in the model. This could be accomplished by instantaneously reducing the base-area of the ceramic fracture conoid to an area corresponding to that of the projectile when the shear load on the periphery of the loaded section of the back-up plate exceeds its ultimate value.
The model may also be improved by the use of a more comprehensive model for the initial phase (the first few microseconds) of the impact process. In addition, the evaluation of the back-up plate responses have indicated that a more elaborate two-dimensional (elastic-plastic) back-up plate deformation model can be expected to match the experimentally observed deformation better.
It is, however, questionable whether the implementation of such an improved model leads to more accurate predictions, considering that the ceramic break-up process, governing the creation and deterioration of the ceramic fracture conoid, is understood on a phenomenological basis only. With the behaviour of the (confined) fractured ceramic so difficult to characterise and model, the use of empirical relations are inevitable and unfortunately to some extend inaccurate. Hence, it is believed that, depending on the available resources for continued development, the best return on investment is to be expected from the inclusion of the catastrophic loss of load-distribution capabilities by the ceramic.

All of the experimental work presented has been carried out with one type of alumina (Morgan Matroc Hilox 973). In order to allow the use of other ceramic materials within the ALARM model, ballistic experiments with those materials need to be conducted in order to determine the necessary input parameters. In order to be able to assess the applicability of the model for use with armours with composite back-up plates, ballistic experiments need to be conducted with those materials too.

6. RESULTS OF THE EXPERIMENTS WITH THE 7.62 MM PROJECTILES

6.1. Introduction

The results of three series of impact experiments are presented and discussed in this chapter. Radiographs are presented for standard 7.62 mm AP and 7.62 mm ball projectiles impacting 8.1 mm of Morgan Matroc Hilox 973 alumina supported by 6.0 mm aluminium 6061-T6 at muzzle velocity. The difference between the two projectiles is that the AP projectile contains a (steel) hard-core, whereas the ball projectile has a (lead) soft-core. Both projectiles weigh 9.5 grams. The muzzle velocity for both projectiles is approximately 835 m/s. They present the same amount of kinetic energy to the armour and thus allow the influence of the projectile composition to be studied. In order to allow for the influence of back-up plate flexibility to be assessed, the 7.62 mm AP projectiles were also fired at an armour concept with two 3.0 mm thick layers aluminium.

The extend to which the steel rod used in the previously described experiments acts as a simulator of the 7.62 mm AP projectile will be assessed by comparison of the results of the impact experiments presented here with those presented in chapter 4.

6.2. The experimental results

6.2.1. 7.62 mm AP projectiles impacting 8.1 mm alumina and 6.0 mm aluminium

The fourteen sets of flash radiographs showing the penetration process of the 7.62 mm AP projectile into 8.1 mm thick alumina and 6.0 mm aluminium were obtained from eight impact experiments. In these experiments the average projectile impact velocity was 841 m/s (± 17 m/s). In all experiments the projectile was defeated by the armour. An example of a recovered back-up plate is shown in figure 6.1. A small amount of fractured ceramic material is still present on the impact axis. It is approximately 3 mm high. Details of the pie-shaped ceramic fragments are visible on the front face of the back-up plate. Some lead has been deposited on the back-up plate, typically some 30 mm away from the impact axis. It must have originated from the lead in the rear part of the projectile. Figure 6.1 also shows the deformation of the back-up plate. The maximal deformation is 9 mm. No cracks or shear zones could be detected in the back-up plate material. In all experiments the ceramic facing was found delaminated from the back-up plate after the experiment.
Figure 6.2 shows a typical example of a recovered ceramic facing viewed from the front and the back. A hole with a diameter of approximately 20 mm is visible at the impact face. The back surface shows a much larger damaged area (approximately 50 mm in diameter). The fracture pattern of the damaged area visible at the back and front surface of the ceramic facing complies with the observations in 4.3.2.

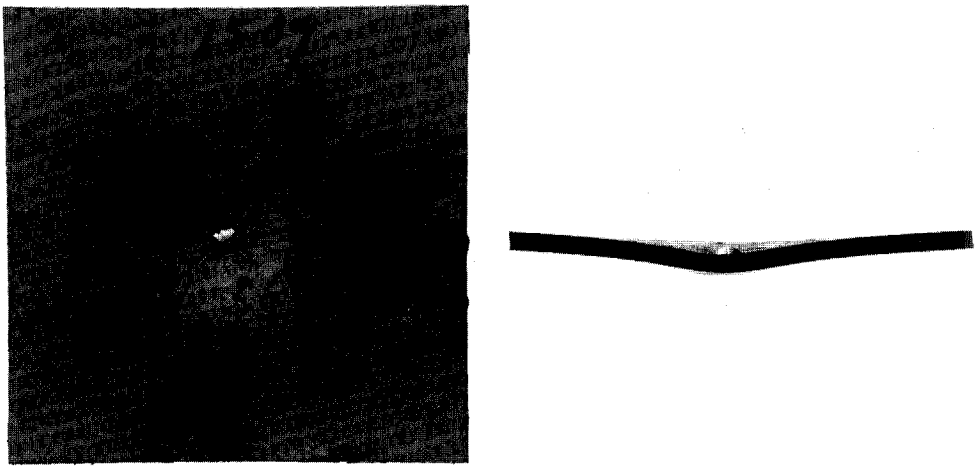

a) front view b) side view (cut-through)

Figure 6.1 Front and side-view (cut-through) of a back-up plate recovered after a 7.62 mm AP projectile impact into 8.1 mm alumina backed by 6.0 mm aluminium at 841 m/s.

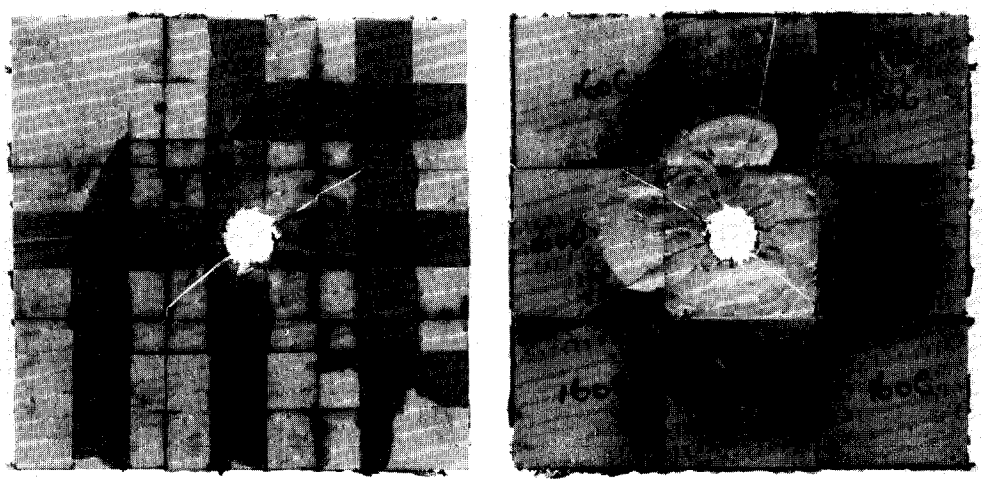

a) front view b) back-face view

Figure 6.2 Front and back-face view of a ceramic facing recovered after a 7.62 mm AP projectile impact into 8.1 mm alumina backed by 6.0 mm aluminium at 841 m/s.

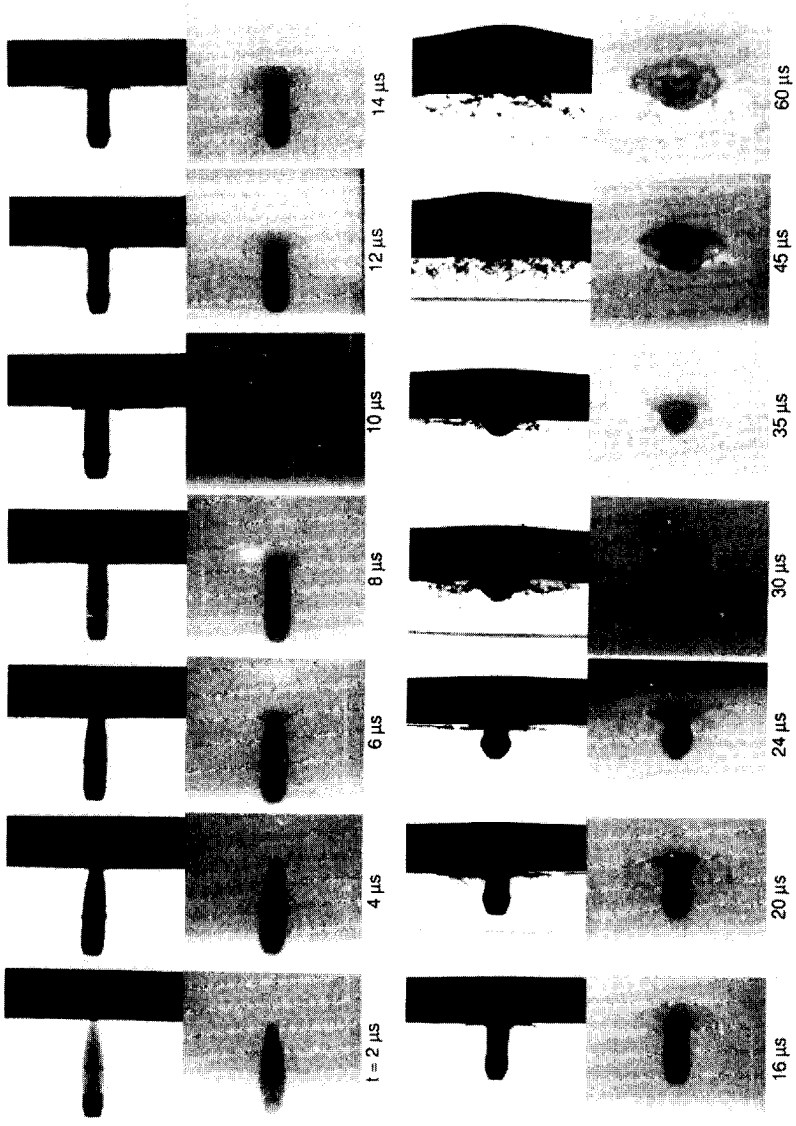

Figure 6.3 Sequence of normal and oblique (26°) flash radiographs showing the projectile/armour interaction of a 7.62 mm AP projectile impacting 8.1 mm alumina and 6.0 mm aluminium at 841 m/s.

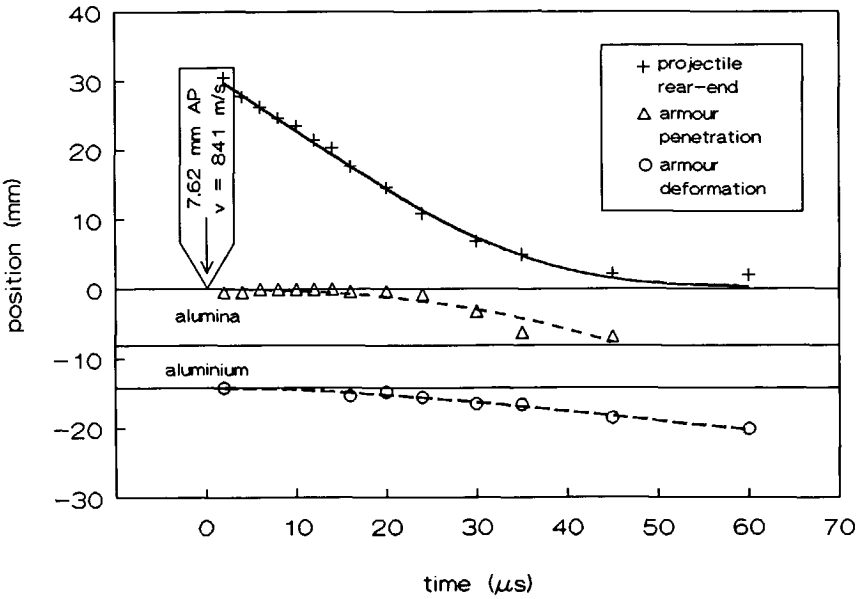

Figure 6.4 Position-versus-time curves of a 7.62 mm AP projectile impacting an armour of 8.1 mm alumina backed by 6.0 mm aluminium at 841 m/s.

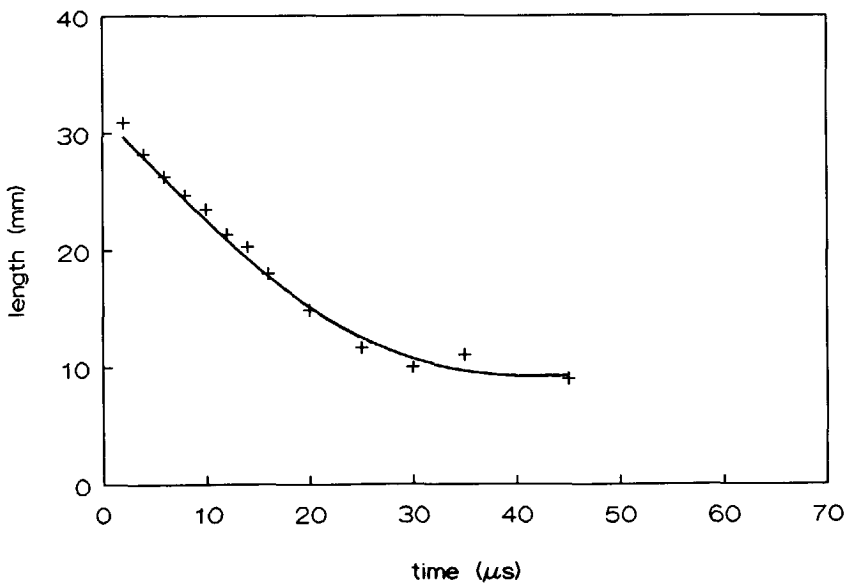

Figure 6.5 Projectile length-versus-time curve of a 7.62 mm AP projectile impacting an armour of 8.1 mm alumina backed by 6.0 mm aluminium at 841 m/s.

Cut-outs of the flash radiographs showing the projectile/armour interaction in time as captured by the normal and obliquely set up pulsers are presented in figure 6.3. Notice the bulging of the lead rear-end of the projectile at later times (>20 μs) after impact. The lead was constrained in its motion by the projectile jacket and the decelerating projectile core, which caused the bulging. Figure 6.4 presents the projectile rear-end position, the armour penetration and armour deformation in time as were deduced from the fourteen sets of radiographs. Polynomials were "best" fitted through the measured data-points.

For a long period of time, approximately 16 μs, the projectile appeared not to penetrate the ceramic material. The armour's deformation was also hardly detectable in this period of time. The projectile's length, however, reduced continuously during the first 35 to 40 μs of the impact process (figure 6.5). At 35 μs after impact, only the bulged lead section of the projectile together with some small particles are visible in the radiograph created by the obliquely set up pulser. Of course, a section of the steel projectile core may be situated inside the lead bulge, invisible for the X-rays. This projectile core section can be 10 mm long at most, since that is the average length of the remaining projectile bulge at 45 μs after impact. With only this length of projectile core surviving impact, and no significantly large broken projectile fragments visible in the radiographs, a large amount of projectile material must break up into very small particles, as in an erosion process. A typical recovered projectile is shown in figure 6.6.

Figure 6.6 Recovered 7.62 mm AP projectile after impact of an armour of 8.1 mm alumina backed by 6.0 mm aluminium at 841 m/s.

6.2.2. 7.62 mm ball projectiles impacting armours of 8.1 mm alumina and 6.0 mm aluminium

Eight experiments with 7.62 mm ball projectiles impacting 8.1 mm thick alumina supported by a 6.0 mm thick layer of aluminium were used to obtain 15 sets of flash radiographs at different moments in time. The average projectile impact velocity was 829 m/s (± 50 m/s). In all experiments the 7.62 mm ball projectile was defeated by the armour. In all experiments the ceramic facing was completely delaminated from the back-up plate after the experiment. Figure 6.7 shows a typical example of a recovered back-up plate. Notice the small section of broken ceramic facing on the impact axis, similar as in the case of the AP projectile. It is approximately 3 mm high. In a larger area surrounding the impact point, 45 mm in diameter, the bonding layer is still present on the aluminium back-up plate. This area corresponds to the area expected to be covered by the ceramic conoid base during impact. Outside this area, projectile material deposit is still visible on the back-up plate. In some sections of the back-up plate, details of the ceramic conoid pie-shaped segments are visible. Figure 6.7 also presents a post-impact side-view of the (cut-through) back-up plate. Its maximal deformation is 9 mm.

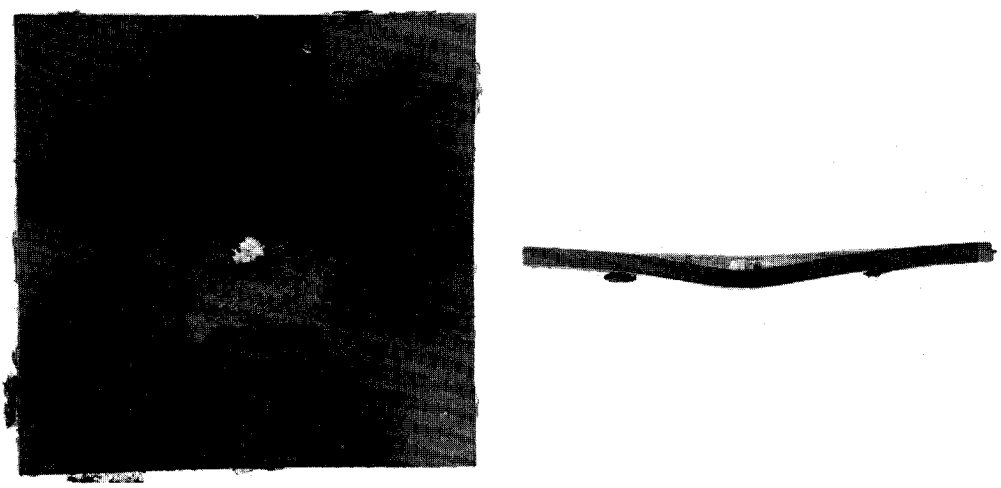

a) front view b) side view (cut-through)

Figure 6.7 Front and side-view (cut-through) of a back-up plate recovered after a 7.62 mm ball projectile impact into 8.1 mm alumina backed by 6.0 mm aluminium at 829 m/s.

Cut-outs of flash radiographs showing the projectile/armour interaction in time, as observed by the normal and obliquely set up pulsers, are presented in figure 6.8.
Figure 6.9 presents the projectile rear-end position, the armour penetration and armour deformation in time as were deduced from the fifteen sets of radiographs. The position of the rear-end of the projectile decreased linearly in time. This indicates that the projectile rear-end was not decelerated by the impact event.
In approximately 38 μs, the entire projectile was eroded, as is concluded from figure 6.10, where the projectile length is presented in time. Projectile material (jacket and lead) moved in two directions: one parallel to the front surface of the ceramic facing creating the fringes of projectile material also observed with 7.62 mm AP projectiles, and one at an angle of approximately 26° with the armour's front surface, into the armour through the Hertzian cone cracks as is schematically illustrated in figure 6.11.
The radiograph taken at 16 μs after impact was the first, where signs of projectile material flowing into the ceramic facing through the ceramic conoid cracks were visible. At later times the projectile's shape changed completely. It had flowed out over the ceramic conoid. This flowing continued when the projectile material reached the back-up plate surface, which occurred at approximately 60 μs after impact. The material continued its way in between the ceramic facing and back-up plate. This indicates that the delamination of the ceramic facing and back-up plate is progressing at that time, because the radiographs do not show any sign of complete delamination. The locations of projectile material deposit found on the back-up plate support the given description of events. Armour deformation became noticeable at 25 μs after impact. As the projectile did not penetrate the ceramic facing directly underneath the impact point, the position of the projectile tip is directly related to the deformation of the armour back-up plate.

In the situation of an armour perforation, the projectile will in most cases already be completely eroded. The armour fails in its ability to absorb the kinetic energy transferred to itself by the projectile. A debris cloud, probably primarily consisting of shattered ceramic and back-up plate material exits the armour and may cause damage.

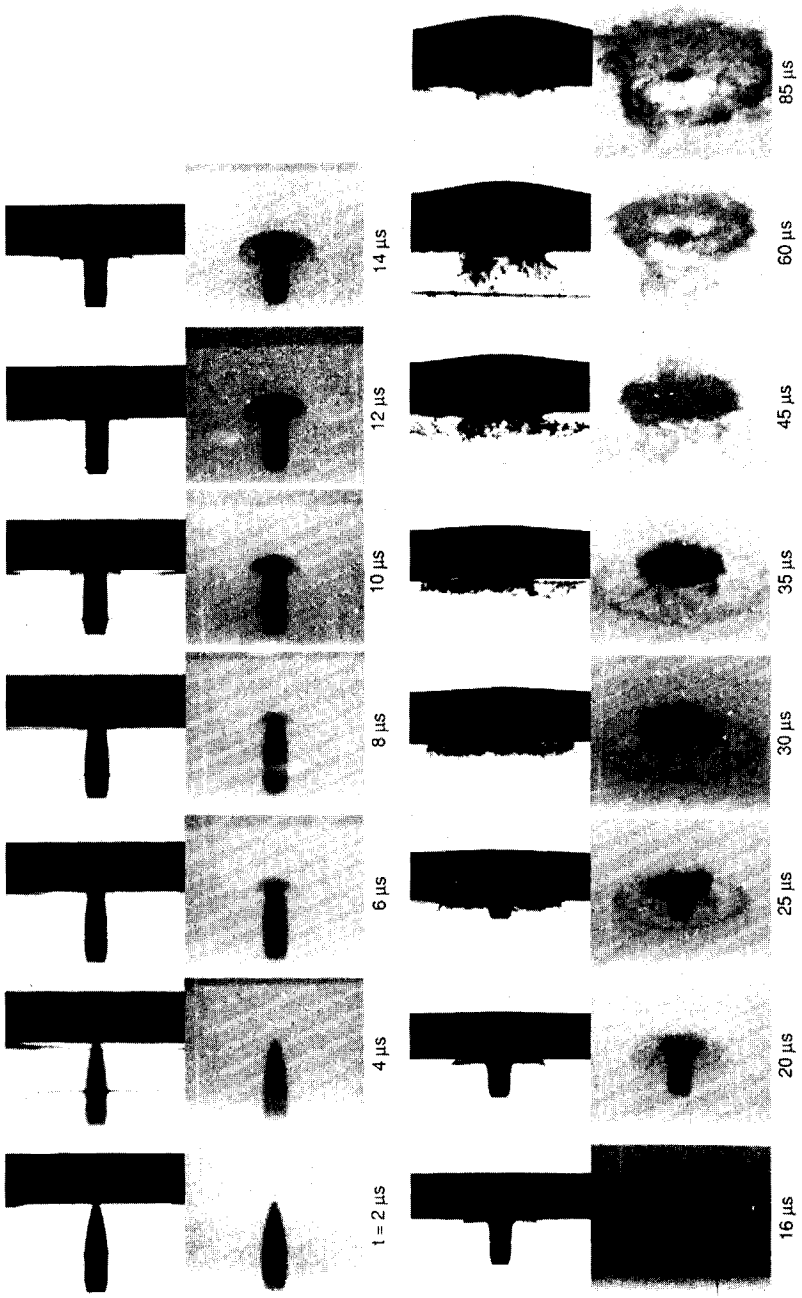

Figure 6.8 Sequence of normal and oblique (26°) flash radiographs showing the projectile/armour interaction of a 7.62 mm ball projectile impacting 8.1 mm alumina and 6.0 mm aluminium at 829 m/s.

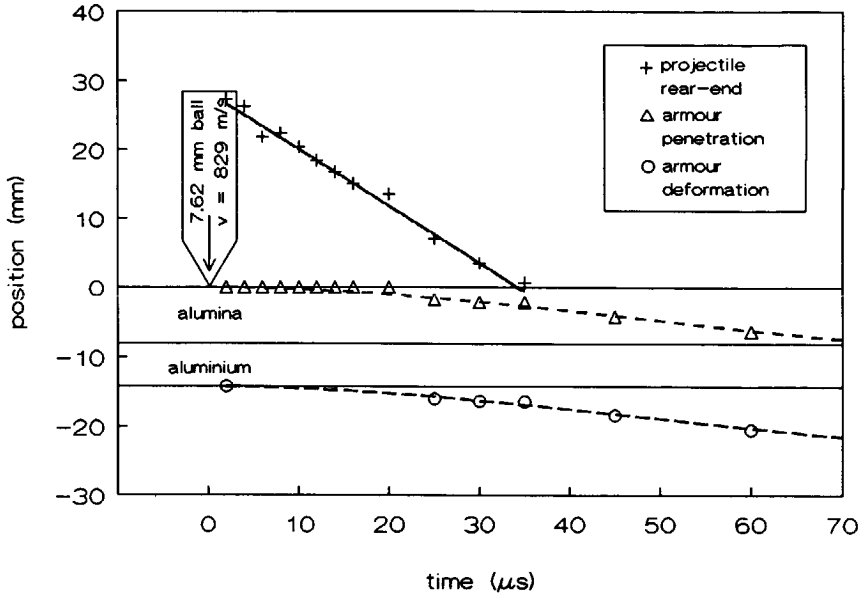

Figure 6.9 Position-versus-time curves of a 7.62 mm ball projectile impacting an armour of 8.1 mm alumina backed by 6.0 mm aluminium at 829 m/s.

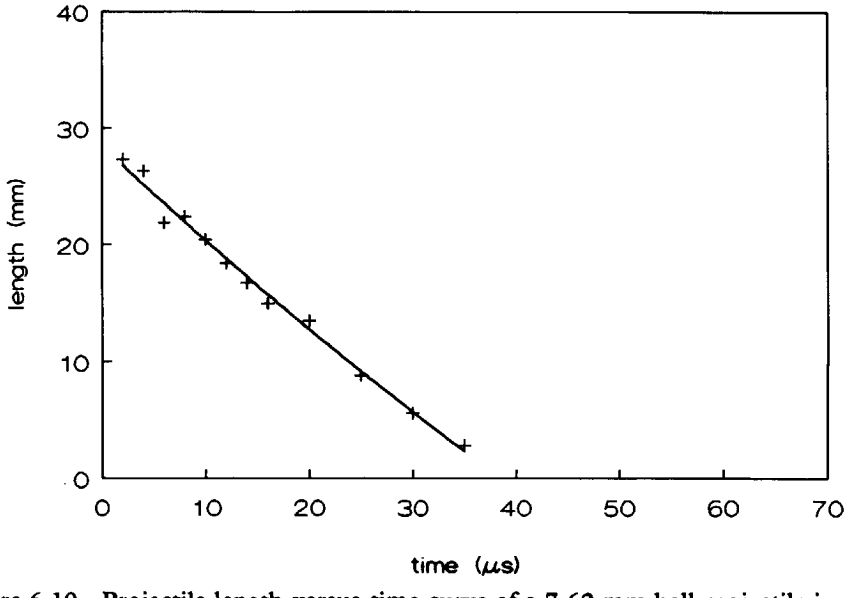

Figure 6.10 Projectile length-versus-time curve of a 7.62 mm ball projectile impacting an armour of 8.1 mm alumina backed by 6.0 mm aluminium at 829 m/s.

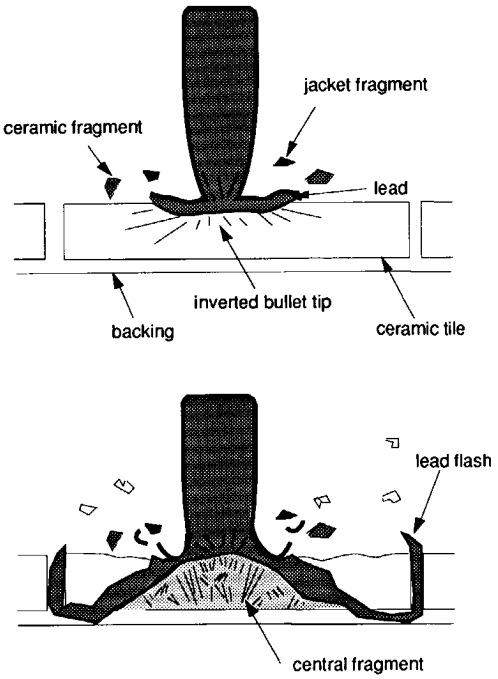

Figure 6.11 Proposed deformation mechanisms for a ball projectile impacting a ceramic faced armour (Prior, 1987).

6.2.3. 7.62 mm AP projectiles impacting 8.1 mm alumina and a package of two 3.0 mm thick layers aluminium

Nine impact experiments with 7.62 mm AP projectiles impacting 8.1 mm thick Morgan Matroc Hilox 973 alumina supported by two layers of 3.0 mm thick aluminium 6061-T6 were used to obtain 14 sets of flash radiographs at different moments in time after impact. The average impact velocity was 846 m/s (± 15 m/s). Again, contrary to expectation, every projectile was defeated by the armour. The ceramic facing was found completely delaminated from the back-up plates after the experiment. Figure 6.12 shows a typical example of a recovered back-up plate. Small fragments of ceramic facing are still bonded to it. The first layer of the back-up plate is heavily deformed and has cracked. The second back-up plate layer has a large indentation but no cracks could be detected. Figure 6.12 also shows the cut-through back-up plate from aside. The maximum deformation of the first back-up plate layer is 15 mm; the second layer's deformation is 14 mm.

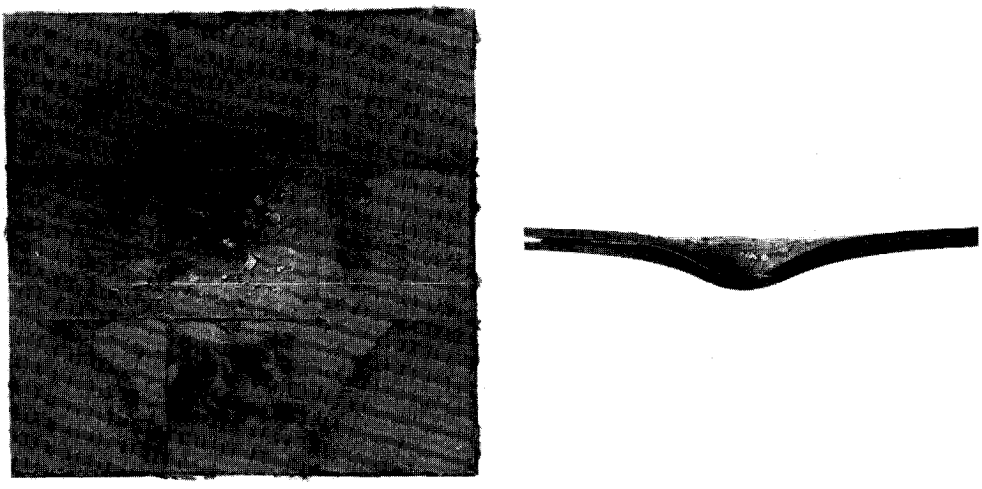

a) front view b) side view (cut-through)

Figure 6.12 Front and side-view (cut-through) of a two-layer back-up plate recovered after a 7.62 mm AP projectile impact into 8.1 mm alumina backed by two 3.0 mm thick layers aluminium at 846 m/s.

Cut-outs of flash radiographs showing the projectile/armour interaction in time are presented in figure 6.13. The bulging of the lead in the rear of the projectile as described in 6.2.1, also occurred here. Figure 6.14 presents the projectile rear-end position, the armour penetration and armour deformation in time as were deduced from the sets of radiographs. Polynomials were "best" fitted through the measured data. For a long period of time, approximately 16 μs, the projectile appeared not to penetrate the ceramic material. Notice that even though the back-up plate is much more flexible than in the other situations considered, the back-up plate response could not be measured for the first 20 μs of the impact process. The projectile length reduced continuously during the first 40 μs of the impact process, as is concluded from figure 6.15. At 35 μs after impact, only the bulged section of the projectile together with some small particles are visible in the radiograph created by the obliquely set up pulser. Of course, a section of the projectile core is still present inside the lead bulge, invisible on the radiographs. At 45 μs after impact, this section of the projectile core is (approximately) 10 mm long at most. Since no large projectile fragments are visible in the radiographs, the projectile front must have broken up into very small particles, as in an erosion process. After 45 μs the projectile was deformed in such a way that the armour penetration could no longer be determined.

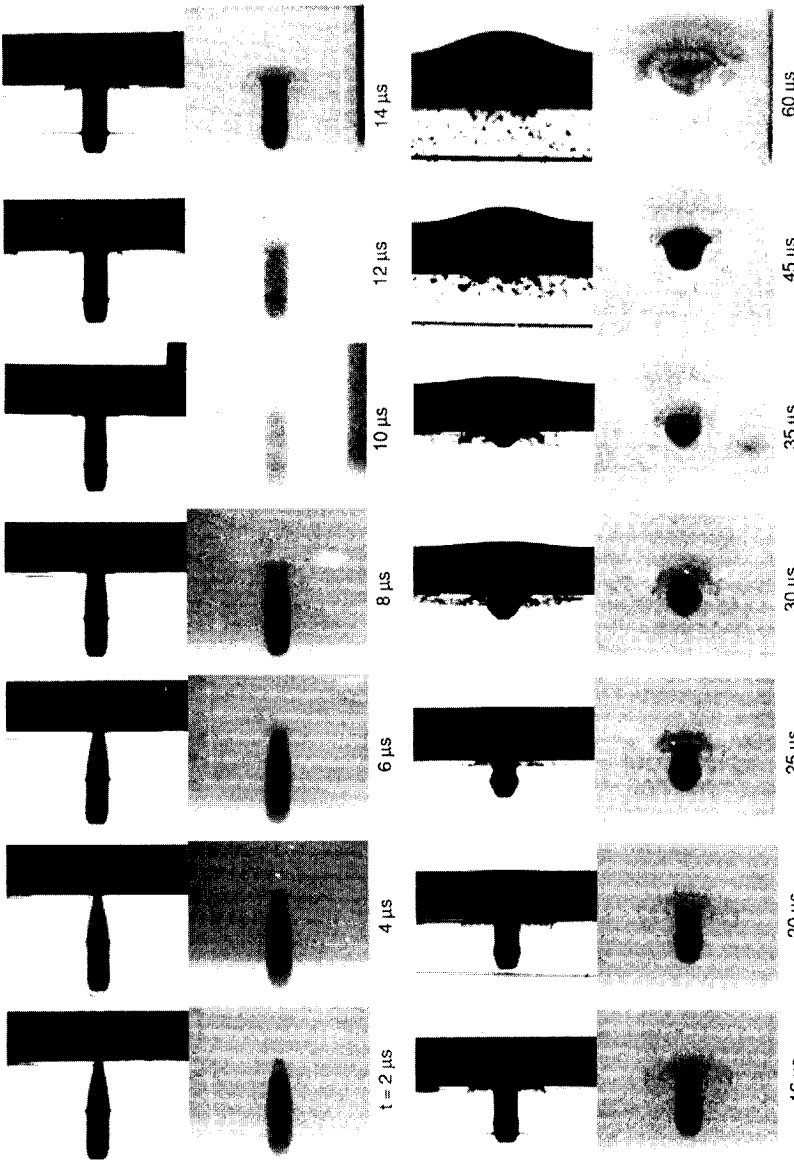

Figure 6.13 Sequence of normal and oblique (26°) flash radiographs showing the projectile/armour interaction of a 7.62 mm AP projectile impacting 8.1 mm alumina and two 3.0 mm thick layers aluminium at 846 m/s.

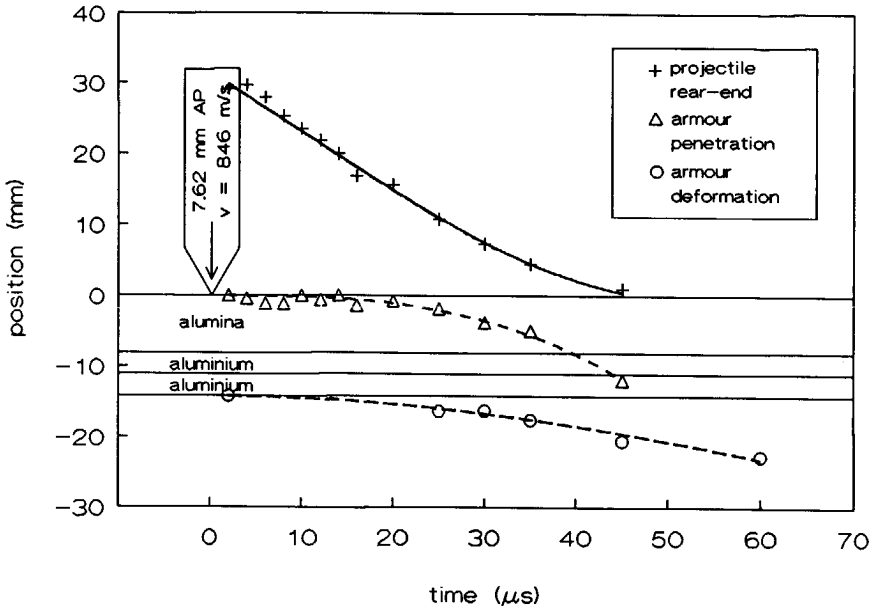

Figure 6.14 Position-versus-time curves of a 7.62 mm AP projectile impacting an armour of 8.1 mm alumina backed by two 3.0 mm thick layers aluminium at 846 m/s.

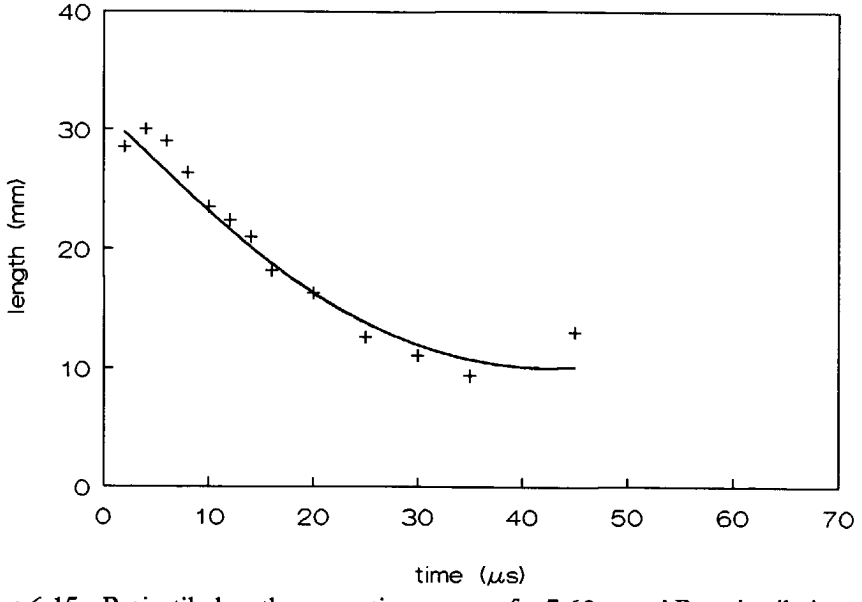

Figure 6.15 Projectile length-versus-time curve of a 7.62 mm AP projectile impacting an armour of 8.1 mm alumina backed by two 3.0 mm thick layers aluminium at 846 m/s.

6.3. Analysis of the experimental results

6.3.1. 7.62 mm AP impact versus 7.62 mm ball impact

The influence of projectile composition is assessed by examining the differences in projectile behaviour and armour response caused by either a 7.62 mm AP or a ball projectile impact. These projectiles differ in the fact that the AP projectile contains a hard steel core. Both projectiles weigh 9.5 grams. The muzzle velocity for both projectiles is approximately 835 m/s. They therefore present the same amount of kinetic energy to the armour.
Consider figure 6.16 where the projectile rear-end positions in time are presented for the two projectiles impacting the same armour. From this figure it becomes clear that for the first 25 μs of the impact process the position of the rear-end of the projectiles decrease at the same rate. Notice that the initial projectile lengths differ for AP and ball rounds. Figure 6.17 presents the projectile rear-end velocities for both projectiles as were obtained from differentiation of the curve fitted polynomials. During the mentioned period of 25 μs, the projectile rear-end velocities correspond to the initial projectile (muzzle) velocities. The lead section in the rear of the AP projectile prevents the deceleration of the AP-core from becoming visible. After this period of time the deceleration of the AP projectile becomes noticeable. The AP projectile's rear-end velocity drops to 470 m/s at 35 μs after impact. The ball projectile's velocity remains constant at approximately 829 m/s until the projectile is completely consumed.
In figure 6.18, the armour penetration in time along the impact axis is presented for the two projectiles. As described in section 6.2.2, the ball projectile does not penetrate the ceramic facing directly underneath the point of impact. Hence, the armour penetration is related to the armour back-up plate deformation. The AP projectile appears to be able to penetrate the ceramic facing. At 45 μs after impact, the projectile has penetrated some 4 mm of ceramic facing.
The back-up plate deformation caused by the AP projectile is almost identical to the deformation caused by the ball projectile as is shown in figure 6.19. The back-up plate deformation velocities deduced from the curve fits show that the back-up plates reach a maximum velocity of 127 m/s at 35 μs after impact.

In summary, the projectile composition has no significant influence on the armour's overall response. The ceramic faced armour experiences both projectiles as being "soft". The fact that the AP projectile is capable of penetrating the ceramic facing to some extend, suggests, that at higher velocities, this projectile will be able to localize the impact load on the back-up plate earlier in time. This is expected to result in a slightly better performance of 7.62 mm AP projectiles against ceramic faced armours than comparable ball projectiles, as was confirmed by Van Riet (1987-1991).

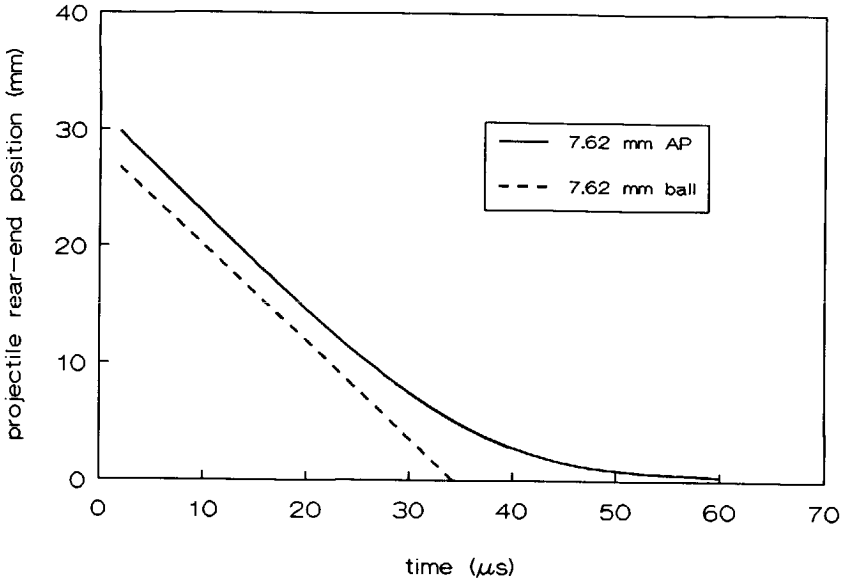

Figure 6.16 Comparison of projectile rear-end positions in time of the 7.62 mm AP projectile (at 841 m/s) and the 7.62 mm ball projectile (at 829 m/s) impacting an armour of 8.1 mm alumina backed by 6.0 mm aluminium.

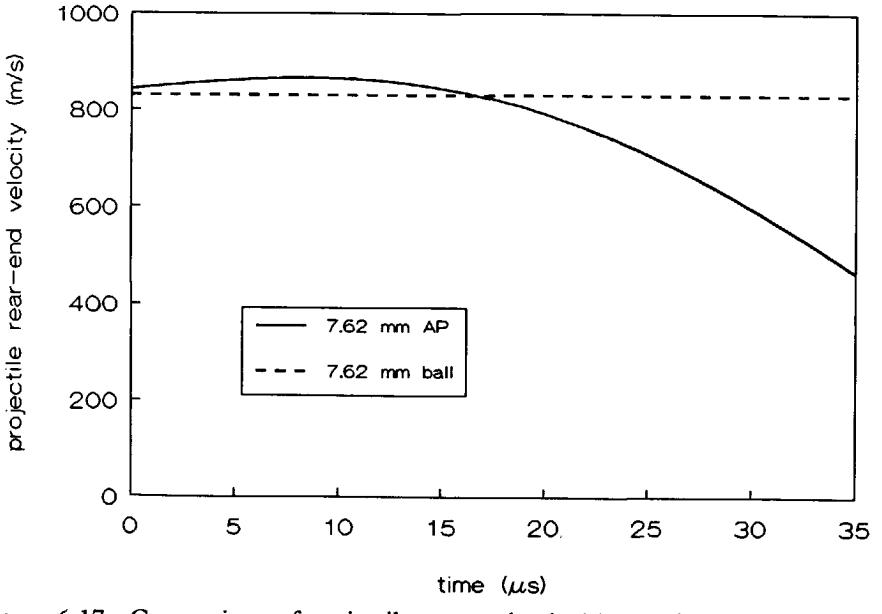

Figure 6.17 Comparison of projectile rear-end velocities in time of the 7.62 mm AP projectile (at 841 m/s) and the 7.62 mm ball projectile (at 829 m/s) impacting an armour of 8.1 mm alumina backed by 6.0 mm aluminium.

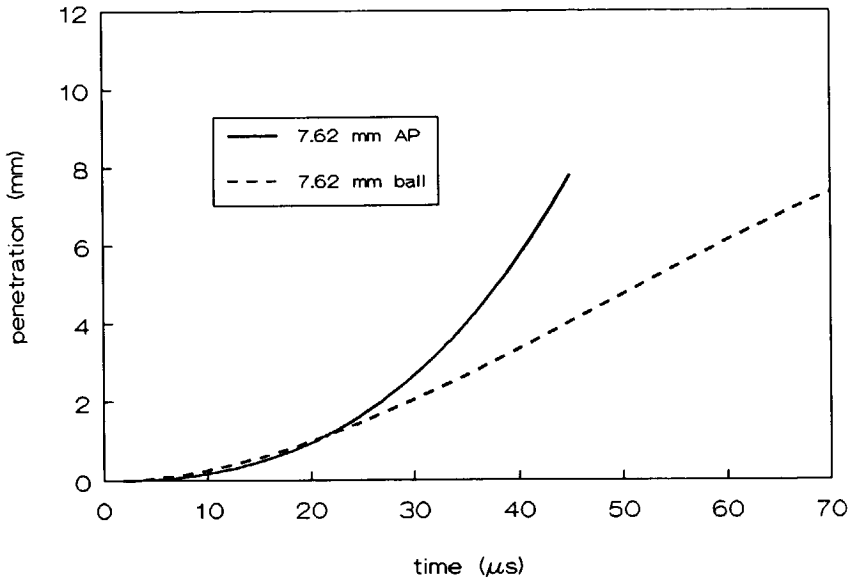

Figure 6.18 Comparison of armour penetration in time of the 7.62 mm AP projectile (at 841 m/s) and the 7.62 mm ball projectile (at 829 m/s) impacting an armour of 8.1 mm alumina backed by 6.0 mm aluminium.

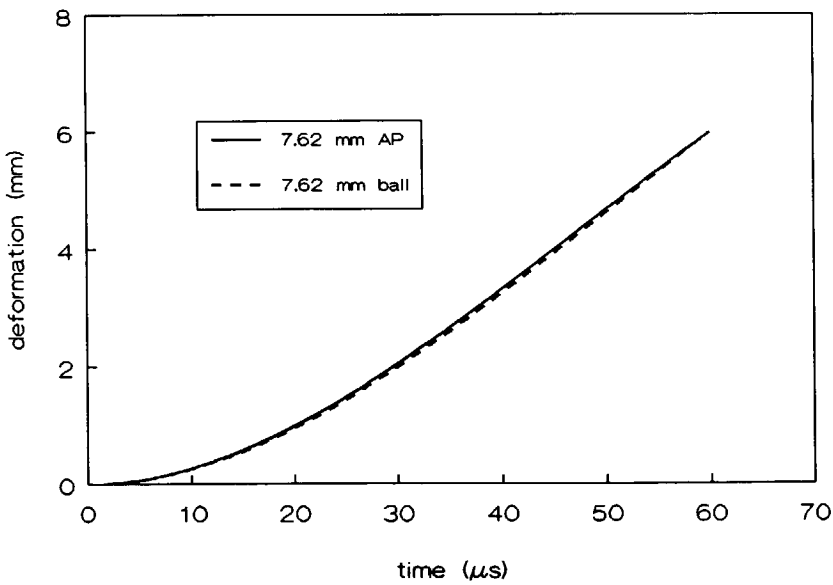

Figure 6.19 Comparison of back-up plate deformation in time of armours of 8.1 mm alumina backed by 6.0 mm aluminium when impacted by the 7.62 mm AP projectile (at 841 m/s) and the 7.62 mm ball projectile (at 829 m/s).

6.3.2. The influence of back-up plate flexibility

The 7.62 mm AP projectile was observed during penetration of armours with two different types of back-up plate; a stiff single 6.0 mm thick layer of aluminium and a more flexible back-up plate composed of two 3.0 mm thick layers of aluminium. This allowed the assessment of the influence of back-up plate flexibility on the response of projectile and armour, similar as was done with the rod projectile (see section 4.3.3).

Up to 35 μs, the projectile rear-end positions did not differ for the two situations considered (figure 6.20). After this time the projectile impacting the stiff armour decelerated slightly faster. Even though the flexibility of the back-up plates differ significantly, only a very small difference in projectile length reduction during impact was observed. When, however, the armour penetration is considered (figure 6.21), it is clear that the projectile penetrated the flexible armour faster. At 45 μs, the projectile tip is located 11.7 mm from the ceramic facing compared to 7.6 mm for the projectile impacting the stiff armour (figure 6.21). With this difference in armour penetration, one would expect a difference in projectile deceleration as well. As in the previous comparison, the lead in the rear-end of the projectile prevented differences in projectile core deceleration from becoming visible.

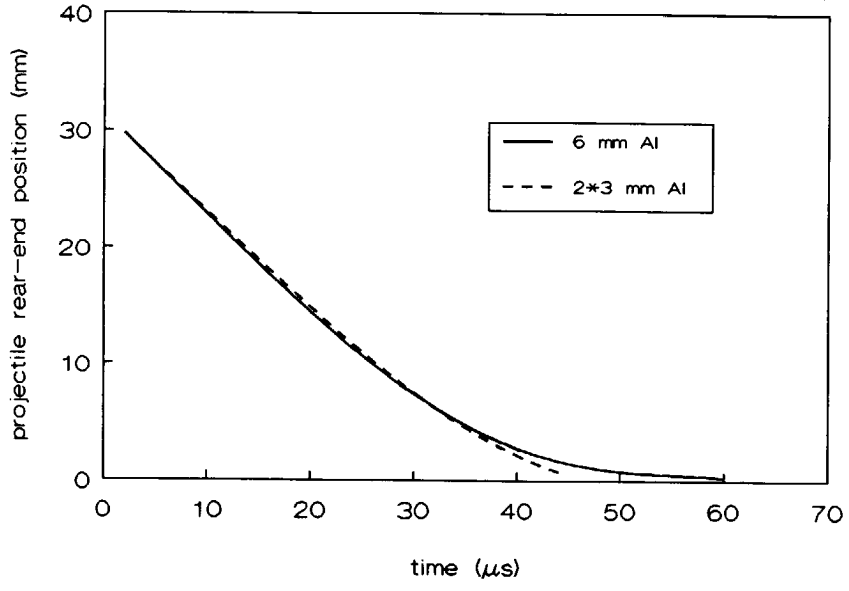

Figure 6.20 Comparison of projectile rear-end positions in time of 7.62 mm AP projectiles impacting two armours; 8.1 mm alumina backed by 6.0 mm aluminium (at 841 m/s) and 8.1 mm alumina backed by two 3.0 mm thick layers aluminium (at 846 m/s).

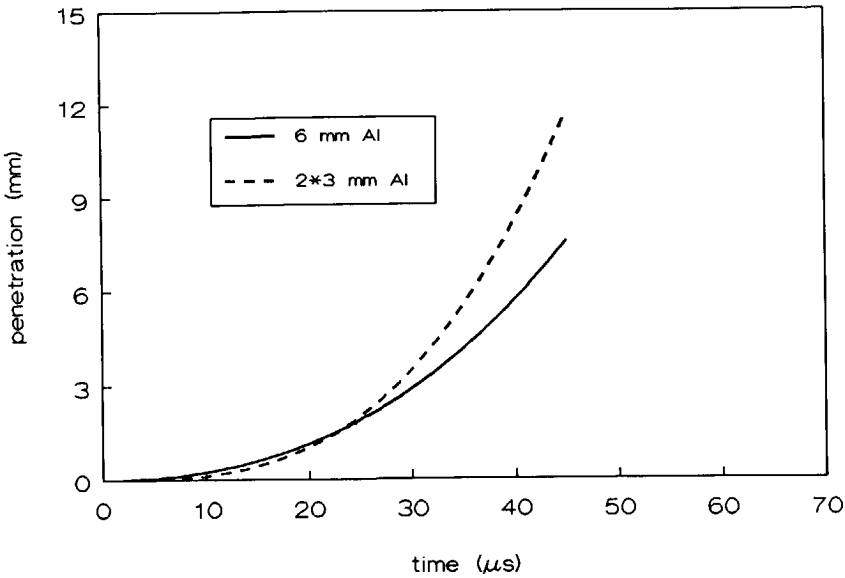

Figure 6.21 Comparison of armour penetration in time of a 7.62 mm AP projectile impacting two armours; 8.1 mm alumina backed by 6.0 mm aluminium (at 841 m/s) and 8.1 mm alumina backed by two 3.0 mm thick layers aluminium (at 846 m/s).

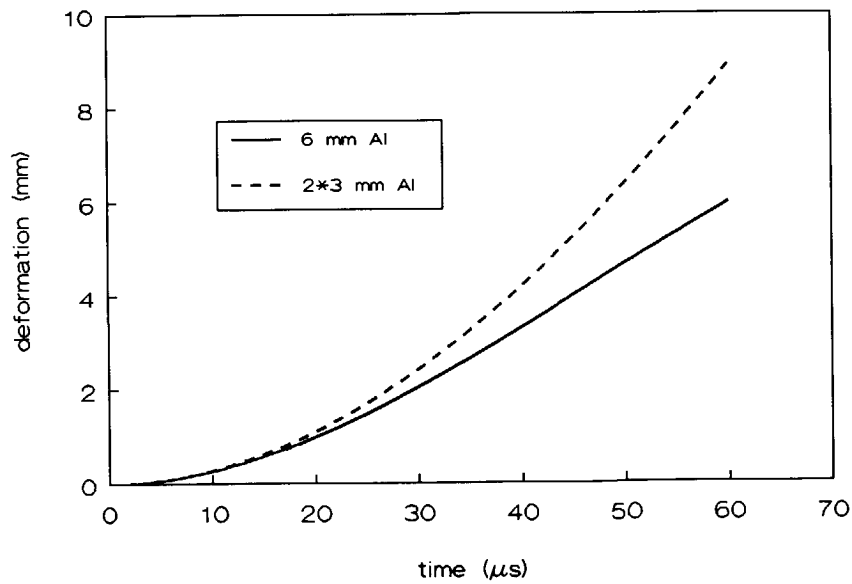

Figure 6.22 Comparison of back-up plate deformation in time following impact with a 7.62 mm AP of two armours; 8.1 mm alumina backed by 6.0 mm aluminium (at 841 m/s) and 8.1 mm alumina backed by two 3.0 mm thick layers aluminium (at 846 m/s).

The comparison of the back-up plate deformation profiles presented in figure 6.22 shows that the presence of a more flexible back-up plate becomes noticeable only after some 25 μs. At 35 μs, the flexible armour back-up plate velocity has already climbed to 180 m/s in contrast to 130 m/s for the stiff back-up plate.
With the higher armour penetration and deformation, one would expect the flexible armour's ballistic limit velocity to be lower than the v_{50} of the stiff armour. This seemed to be confirmed by post-impact visual inspection of the two-layer back-up plates, which showed that they were very close to complete failure, whereas the stiff armour's back-up plates showed no signs of failure yet. As with the rod projectile, this difference in ballistic limit velocity is not expected to be as large as the 100 m/s as was suggested by Wilkins (1968; Laible, 1980).

6.4. The blunt steel rod as a simulator of the 7.62 mm AP projectile

In 1967, Wilkins carried out experiments with blunt and sharp projectiles. He observed that the projectile nose-shape was responsible for differences of up to 40% of the ballistic limit velocity for armours with AD-85 alumina facings. Hornemann *et al.* (1984) showed that the stress wave generated in the armour depends strongly on the nose-shape of the projectile. In this section, the projectile/armour interaction process as observed for the blunt 6.0 mm diameter rod is compared with the results obtained for the ogive-nosed 7.62 mm AP projectile. This allows us to assess whether the results obtained with the blunt steel rods are representative for the penetration of the ogive-nosed 7.62 mm AP projectile.

The position-versus-time curves for the 7.62 mm AP and the 6 mm rod projectile impacts into armours of 8.1 mm alumina supported by 6.0 mm aluminium, at velocities of 841 m/s and 815 m/s respectively, are compared in figure 6.23. This comparison shows that the experimental results match very well. The armour responds almost identical to both projectiles. There are some differences in the armour penetration data. The 7.62 mm projectile appears to penetrate a limited amount of ceramic material directly underneath the point of impact, whereas the steel rod appears unable to do so. Differences are also observed between the position of the rear-end of the projectile and the rod at late times after impact (>25 μs). This can be expected as the lead plug in the rear-section of the 7.62 mm AP projectile decelerates slower than the rod as it bulges around the central hard steel core of the 7.62 mm AP.
Both projectiles were also fired onto armours of 8.1 mm alumina supported by two 3.0 mm thick layers aluminium at velocities of 847 m/s and 819 m/s, respectively. The resulting position-versus-time curves are compared in figure 6.24. Again, the experimental results for the two projectiles match very well. Hence, the armour response observed in the experiments with the blunt steel rods may be considered as representative for the response to a 7.62 mm AP projectile impact.

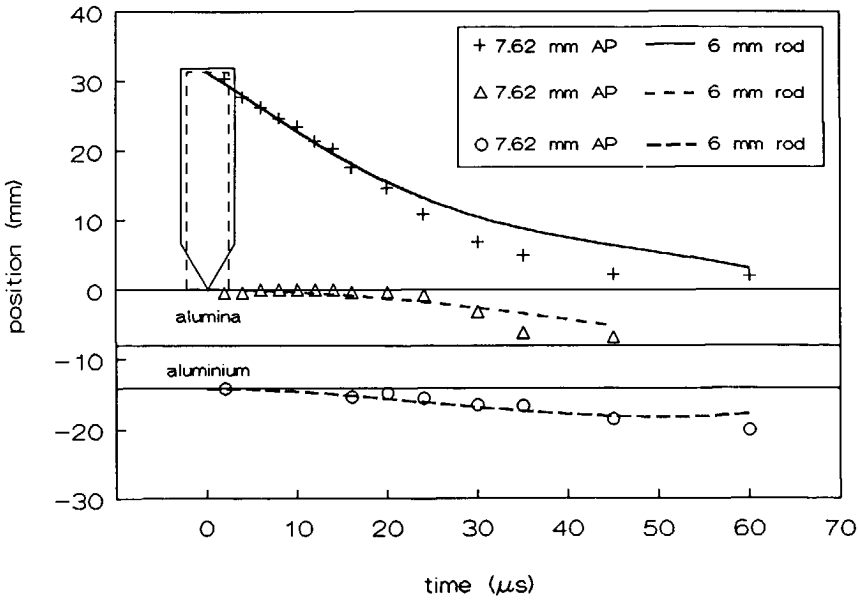

Figure 6.23 Comparison of the position-versus-time curves for 7.62 mm AP projectile (at 841 m/s) and 6.0 mm steel rod (at 815 m/s) impact onto 8.1 mm alumina supported by 6.0 mm aluminium.

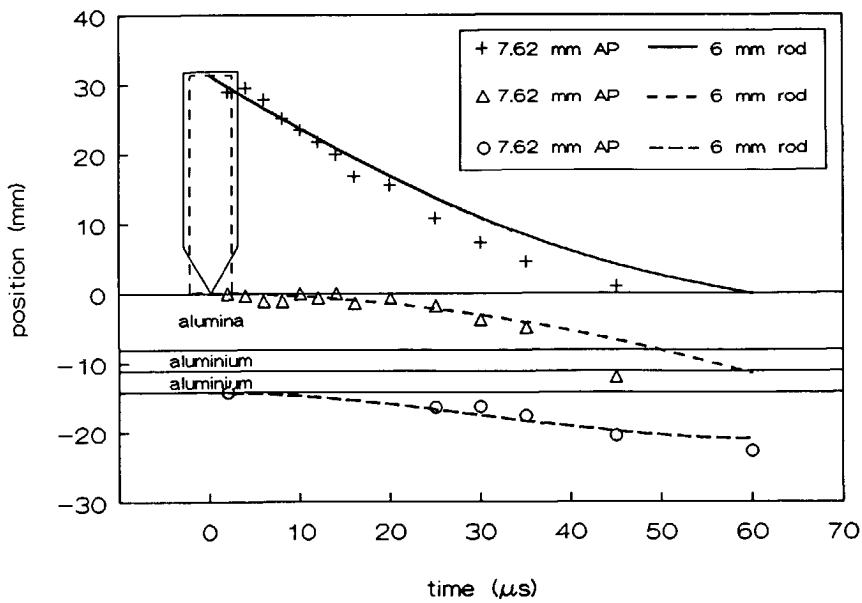

Figure 6.24 Comparison of the position-versus-time curves for 7.62 mm AP (at 846 m/s) and 6.0 mm steel rod (at 819 m/s) impact onto 8.1 mm alumina supported by two 3.0 mm thick layers aluminium.

Having obtained this result, it has to be considered surprising that a blunt steel rod (R_C = 28), weighing 7.0 grams only, inflicts a similar response to a ceramic faced armour as the ogive-nosed 7.62 mm armour piercing projectile with its hard-core (R_C = 60) and its 36 per cent higher weight (9.5 grams). The difference in projectile material composition on one hand and the influence of the projectile nose-shape on the other hand may be held responsible for this result.
The similarity between the armour responses resulting a 7.62 mm AP and ball projectile impact, presented in section 6.3.1, indicates that the use of steel or lead for the projectile's core does not influence the response significantly. Hence, it is unlikely that the (smaller) differences in material composition between the 7.62 mm AP projectile and the 6.0 mm steel rod are accountable for the better performance of the rod.
The difference in projectile nose-shape may very well have a significant influence on a projectile's performance in a ceramic faced armour. The strength and shape of the shock wave introduced into the armour by the blunt rod are different from the shock wave introduced into the armour by the 7.62 mm AP projectile. This fact is illustrated by Hornemann *et al.* (1984), who shot blunt and sharp projectiles at glass specimens. Bless *et al.* (1987) have shown that at impact velocities above 370 m/s, blunt rods (of diameter comparable to the thickness of the ceramic facing) cause much more alumina to experience a peak shock stress well above the Hugoniot elastic limit (HEL) when compared with ogive-nosed projectiles. These shocks above the HEL induce extensive microfracture in ceramics (Bless *et al.*, 1987). According to Rosenberg *et al.* (1990), this (above HEL) shock wave may even cause "catastrophic" loss of shear strength and a corresponding poor ballistic performance with some materials. Even though according to Bless (1987) alumina, when confined, retains its shear strength when shocked above the HEL, the extensive microfracture induced over a large volume in the ceramic by the blunt rod, may have degraded the ceramic such that the blunt projectile performs "better" than the 7.62 mm AP projectile.

The similarity between the armour responses resulting from an 7.62 mm AP and rod projectile impact may, however, be limited to the materials used, and the velocity regime of the above experiments. By changing the impact velocity, the peak shock stress in the ceramic changes as well. This may cause such a change of the shock degradation of the ceramic for the blunt rod projectile impact, that the similarity between the armour responses for the 7.62 mm AP and rod projectile is lost.

6.5. Conclusions

The flash X-ray experiments have resulted in detailed information regarding the penetration processes of 7.62 mm AP and ball projectiles into ceramic faced armours.
The AP projectiles impacting the armour with the 6.0 mm thick single back-up plate experienced the armour as a rigid barrier for at least 16 μs. Projectile length reduction, which does not necessarily imply mass erosion with these projectiles, continued for the first 35 to 40 μs of the impact process. The lead section in the rear-end of the AP projectile obscured the steel core's deceleration from vision. No large fragments of

the projectile core could be traced on the flash radiographs, contradicting projectile break-up in large fragments, and suggesting a continuous kind of projectile mass erosion. Post-impact analysis of the back-up plates and the other experimental results indicate that the projectile did not penetrate the entire ceramic facing nor did the back-up plate material show any signs of failure.
The 7.62 mm ball projectile mainly acted by transferring an impulse to the ceramic faced armour. It was unable to penetrate the ceramic material directly underneath the impact point. Projectile material moved into the conoid cracks and along the front face of the armour panel: this confirmed the behaviour postulated by Prior (1987). In approximately 38 μs, the original projectile was completely consumed and had (partly) squashed out over the ceramic conoid. The back-up plate responses for an AP or ball projectile impact overlapped completely when the projectiles impacted at muzzle velocity. The ceramic faced armour experiences both projectiles as being "soft". However, the hard steel core of the 7.62 mm AP projectile, causes it to perform slightly better than the the ball projectile, as other experiments have shown (Van Riet, 1987-1991).

The ceramic faced armour with the two-layer back-up plate also defeated the 7.62 mm AP projectile at muzzle velocity (846 m/s), contrary to expectation. During the first 25 μs of the impact process, the projectile rear-end position, armour penetration and back-up plate deformation almost completely matched the data obtained with the armour with the single back-up plate. After this period, the flexibility of the back-up plates resulted in a faster armour penetration and deformation. The post-impact analysis of the back-up plates showed that in most cases the layer closest to the ceramic facing had failed, indicating that the armour was almost defeated by the projectile. The large difference in ballistic limit velocity (~100 m/s) for armours with single and two-layer back-up plates, as was suggested by Wilkins (1968; Laible, 1980), was not witnessed here.

With all three series of experiments, fringes of projectile material were observed moving away from the impact area parallel to the front face of the ceramic armour. These fragments move at the initial projectile velocity.

The armour responses caused by the steel rod and the 7.62 mm AP projectile are very similar. They allow the steel rod to be used as a 7.62 mm AP projectile simulator. However, the similarity between the armour responses may be limited to the velocity regime and materials used with the presented experiments. The rod is a far more efficient penetrator than the 7.62 mm AP projectile. In addition to the fact that its steel is not as hard as the AP projectile's core, the rod weighs 36 per cent less.

7. SIMULATION OF EXPERIMENTS WITH THE 7.62 MM PROJECTILES

7.1. Introduction

One of the main reasons to set up the ALARM model was to speed up the design process for armours giving protection against 7.62 mm AP and ball projectiles. With the simplified model used in ALARM one cannot expect to handle all the geometrical and material complexities involved with these projectiles. The comparison of experimental results for 7.62 mm AP and steel rod projectile impact presented in section 6.4, showed that the steel rod can be used as a simulator for the 7.62 mm AP projectile. Therefore, also in the computer simulations the steel rod is used instead of the real projectiles.
In this chapter then, the applicability of the ALARM model for describing the penetration process of AP and ball projectiles will be assessed by simulations of the experiments that were presented in chapter 6. For the ball projectile, the rod's mechanical properties were modified to comply with those most commonly used with soft-core projectiles ($\sigma_y = 0.8\ 10^7$ N/m^2, $u_{plas} = 50$ m/s). The armour materials used in the impact experiments with the 7.62 mm projectiles are identical to the materials used for the steel rod experiments. Hence, the simulations were run with the same input parameters.

7.2. ALARM simulation versus experiment

7.2.1. Simulation of the impact experiments with the 7.62 mm AP projectile

Figure 7.1 presents the comparison of the experimentally obtained and predicted (ALARM) projectile rear-end positions, armour penetration and back-up plate deformation profiles for the 7.62 mm AP projectile impacting an 8.1 mm thick alumina facing supported by a 6.0 mm thick layer of aluminium at an initial velocity of 841 m/s. The model correctly predicts that the projectile is defeated by the armour, because it calculates the ballistic limit to be 916 m/s.
The experimental and calculated results match fairly well. The maximum back-up plate deformation is under-estimated by the model. A maximum deformation of 6 mm is predicted, whereas the back-up plates recovered from the experiments showed a maximum deformation of some 9 mm. The armour penetration is slightly over-estimated, especially early in the penetration process. The reasons for these discrepancies were discussed in section 5.4. The calculated projectile rear-end positions start to deviate from the experimental data at 20 μs after impact. This is caused by the lead in the rear-end section of the 7.62 mm AP projectile which barely decelerates and bulges around the decelerating core of the projectile. The comparison does show that during the first 20 μs of the impact process, the influence of projectile material properties with respect to the deceleration of the rear-end of the projectile early in the impact process is minimal. The model predicts that 58 per cent of the projectile simulator's mass is eroded.

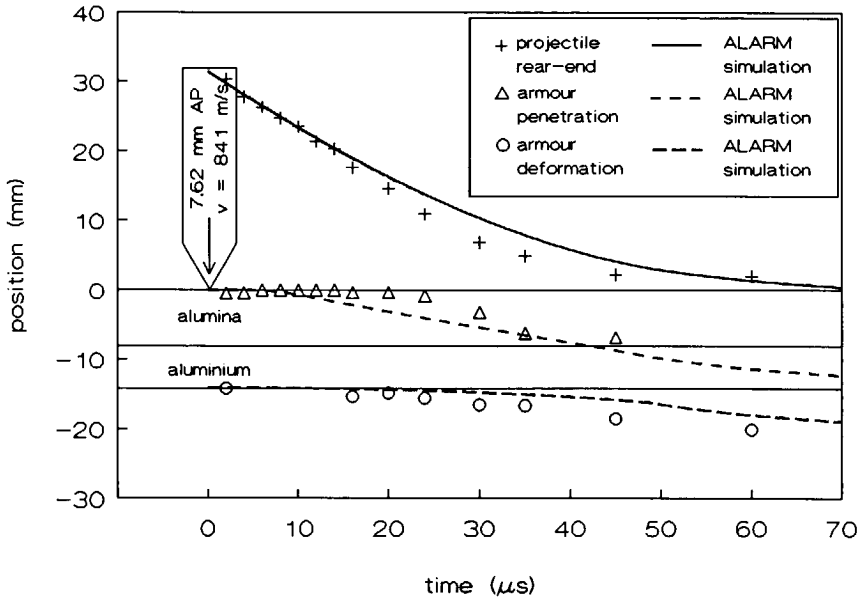

Figure 7.1 Comparison between predicted (ALARM) and experimentally obtained position-versus-time curves of the 7.62 mm AP projectile impacting 8.1 mm alumina backed by 6.0 mm aluminium at a velocity below the ballistic limit (841 m/s).

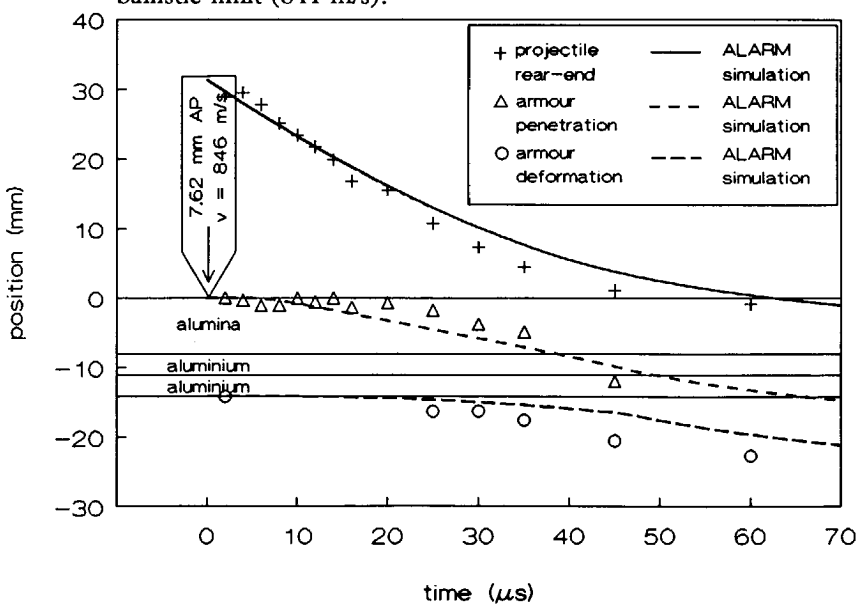

Figure 7.2 Comparison between predicted (ALARM) and experimentally obtained position-versus-time curves of the 7.62 mm AP projectile impacting 8.1 mm alumina backed by two 3.0 mm layers aluminium at a velocity below the ballistic limit (846 m/s).

The comparison between the observed and calculated response of the armour with the 8.1 mm thick alumina facing and the two-layer (2*3.0 mm) back-up plate, to impact by the 7.62 mm AP projectile at a velocity of 846 m/s is presented in figure 7.2. Again, the model correctly calculates that the projectile is defeated by the armour as it calculates a v_{50} of 905 m/s. Also in this situation, the armour penetration is slightly over-estimated by the model. The maximum back-up plate deformation lags behind compared with the experimental observations. The model predicts a final maximum deformation of 13 mm which compares well to deformation measured from the recovered back-up plates (14 mm). The model calculates that 55 per cent of the projectile simulator's mass is eroded.

7.2.2. Simulation of the impact experiments with the 7.62 mm ball projectile

The results from the ALARM simulation for the 7.62 mm ball projectile impacting a ceramic faced armour of 8.1 mm alumina and 6.0 mm aluminium at a velocity of 829 m/s are compared with the experimental data in figure 7.3. The calculation shows that the projectile is defeated by the armour (calculated v_{50} = 884 m/s). As in the other situations, the armour penetration is over-estimated and the maximum back-up plate deformation is under-estimated by the model. According to the model, the final maximum deformation is 5 mm. The recovered back-up plates showed an average

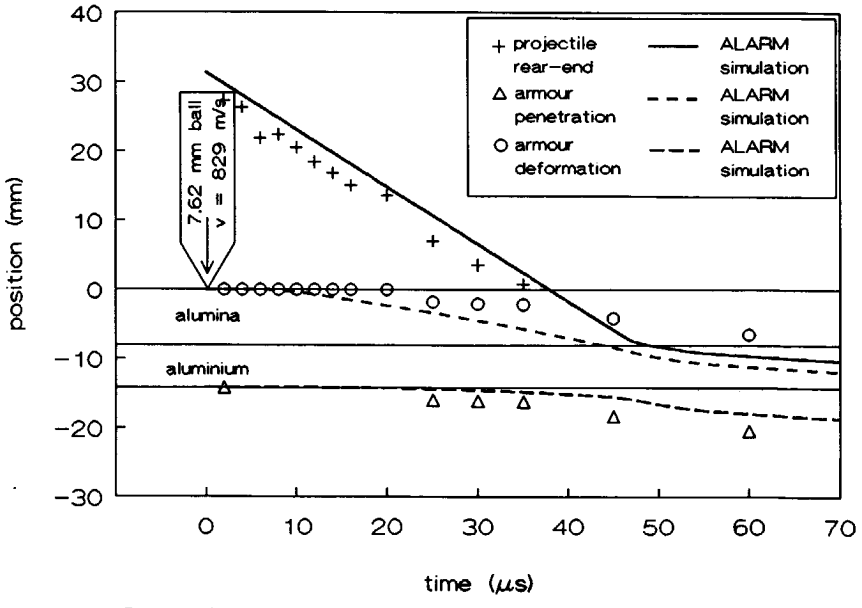

Figure 7.3 Comparison between predicted (ALARM) and experimentally obtained position-versus-time curves of the 7.62 mm ball projectile impacting 8.1 mm alumina backed by 6.0 mm aluminium at a velocity above the ballistic limit (829 m/s).

maximum deformation of 9 mm.
Due to a difference in projectile length between the 7.62 mm ball projectile (L = 28.5 mm) and the low-strength rod (7.62 mm ball simulator, L = 31.5 mm), the projectile rear-end positions do not overlap completely. The calculated projectile rear-end positions show that the projectile's rear is barely decelerated by the impact event. In 47 μs the projectile is eroded completely. The experiments showed that projectile erosion is completed in only 38 μs. The 9 μs discrepancy between experiment and simulation is caused by the projectile simulator's (larger) length and the model's over-estimation of the armour penetration.

7.3. Comparison of the simulation results

In the previous chapter the results obtained from the experiments with the 7.62 mm projectiles were analysed and compared to each other. In order to verify whether the model responds correctly to changes in projectile and back-up plate composition, the differences between the calculated projectile/armour interaction processes for 7.62 mm AP and ball projectile impact and for 7.62 mm AP projectile impact onto armours with single and two-layer back-up plates are compared to those observed experimentally.

7.3.1. 7.62 mm AP impact versus 7.62 mm ball impact

The comparison of the position-versus-time data generated by the model for impact of the hard-core and soft-core 7.62 mm projectiles onto the ceramic faced armour complies with the experimental observations presented in 6.3.1.
During the first 20 μs of the impact process, the difference in projectile rear-end positions is minimal, as in the experiments. Although the armour penetration is over-estimated for both projectiles, the model does show that the 7.62 mm AP projectile penetrates the armour slightly easier. The back-up plate deformation profiles overlap each other completely during the first 60 μs of the impact event. This was also witnessed in the experimental data.
The model predicts a ballistic limit velocity of 884 m/s for 7.62 mm ball projectile impact and 916 m/s for 7.62 mm AP projectile impact. As expected on the basis of the experimental results, these ballistic limit velocities lie closely together. However, contrary to expectation, the model predicts that the 7.62 mm ball projectile penetrates the armour easier than the AP projectile. One may conclude, that the calculated ballistic limit velocities for the 7.62 mm ball projectile will better satisfy the experimental expectations when the simulator's length is reduced to match the length of the 7.62 mm ball projectile.

7.3.2. The influence of back-up plate flexibility

The results derived from the comparison of the calculated position-versus-time data for 7.62 mm AP projectile impact onto an armour with a single layer (6.0 mm) back-up plate and an armour with a two-layer (2*3.0 mm) back-up plate, match the experimental observations presented in section 6.3.2.
For more than 35 μs, the differences between the position of the rear-end of the projectiles remain very small. It also takes approximately 25 μs before the differences in armour response become evident. The final projectile erosion is similar for both impact situations and of the same order of magnitude as witnessed in the experiments.
Even though the experiments presented in chapter 6 did not supply the ballistic limit velocities for these two armours, it was expected that they would lie close together. According to the model, the stiff armour's ballistic limit velocity is 916 m/s whereas the flexible armour's v_{50} = 906 m/s.

7.4. Conclusions

The comparison between the experimental results and the model simulations show that the results match fairly well. Taking into consideration that simple geometry, single material rods were used to simulate the complex ogive 7.62 mm projectiles, a better match cannot be expected.
The distinct similarities and differences observed experimentally for 7.62 mm AP and ball projectile impact are also evident in the comparison of the associated simulations.
The influence of back-up plate flexibility on the projectile/armour interaction process, as addressed in section 6.3.2, is also witnessed in the simulations.

Hence, also in the situations considered here, the ALARM model is capable to present the user with useful information and tendencies in the projectile/armour interaction processes.

8. PARAMETER STUDIES WITH THE ALARM MODEL

8.1. Introduction

The comparisons between the experimental data and the model simulations have shown that the model is capable of calculating the effects of limited variations of geometry and properties about a reference ceramic armour configuration with acceptable accuracy. In order to demonstrate the model's potential to assist in a projectile/armour optimization process, a number of studies are presented.

For a range of ceramic facing and aluminium back-up plate thicknesses ballistic limit velocity computations were carried out with the steel rod projectile (simulating the 7.62 mm AP) and the low strength rod (simulating the 7.62 mm ball projectile). The generated data was used to carry out armour weight optimizations, illustrating ALARM's capabilities with respect to armour optimization.
In order to illustrate the model's capabilities to aid in the optimization process of the armour's back-up plate, ballistic limit velocity computations are presented for armours with back-up plates of three different types of aluminium: 6061-T6, 2024-T4 and 7075-T6.
Finally, the influence of the rod's length-over-diameter ratio on the ballistic limit velocity is assessed.

A ceramic material optimization study is not included in this chapter. The use of another ceramic material with the model requires a number of input parameters, such as the constants in the ceramic's resistance function and the ceramic conoid angle. These parameters are not yet available for ceramic materials other than Morgan Matroc Hilox 973 and Coors AD-85.

8.2. Armour weight optimization for the steel rod (7.62 mm AP) projectile

Ballistic limit velocity computations were carried out for 4 ceramic layer thicknesses (7 mm through to 10 mm) and 17 back-up plate thicknesses, starting at 1.0 mm and increasing to 9.0 mm in 0.5 mm intervals. Hence, a total of 68 ballistic limit velocity computations were carried out using the ALARM code. The projectile and armour properties used for the comparison with the steel rod experiments were also used for the computations presented here.
The results are presented in figure 8.1. This figure shows that the steel rod is defeated by a whole range of differently composed armours when it impacts at the muzzle velocity of the 7.62 mm AP projectile (840 m/s, the horizontal line in the figure). All armours with a ballistic limit velocity above 840 m/s defeat the projectile at this velocity. The two-slope structure of the curves is related to the change in failure mode of the back-up plate.
For lightweight ballistic protection materials, the performance is preferably related to the armour's areal density. Figure 8.2, therefore, shows the performance of the armour

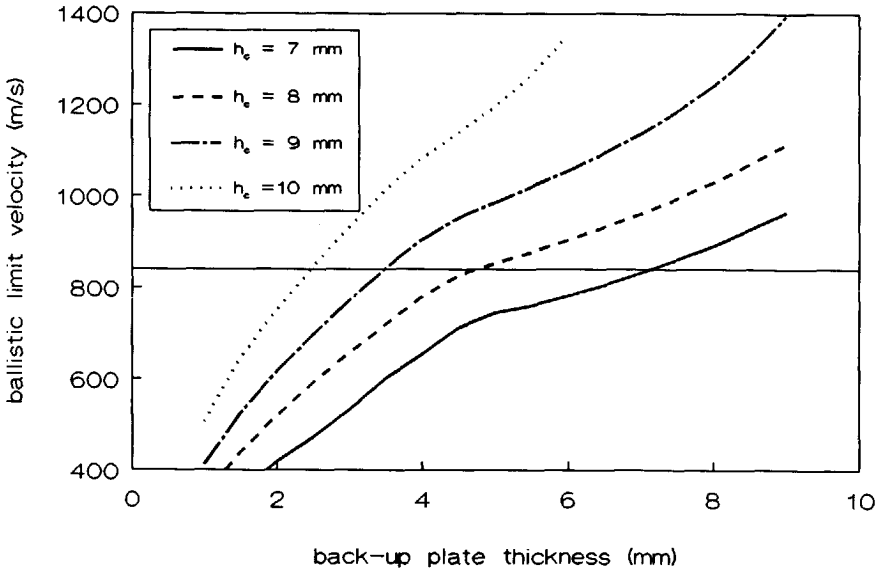

Figure 8.1 Computed ballistic limit velocities as a function of back-up plate thickness for armours of Morgan Matroc Hilox 973 alumina backed by aluminium 6061-T6, when impacted by the steel rod projectile (h_C = ceramic thickness).

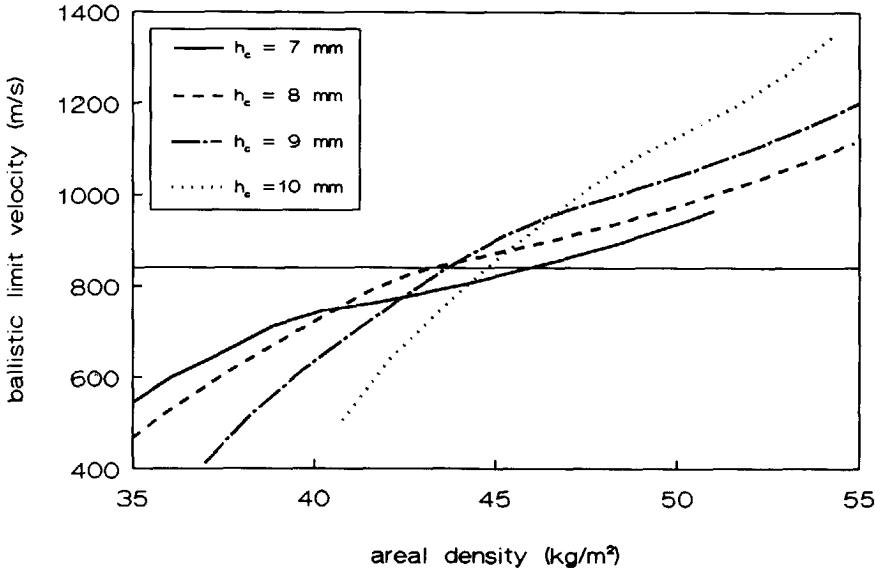

Figure 8.2 Computed ballistic limit velocities as a function of the armour's areal density for armours of Morgan Matroc Hilox 973 alumina backed by aluminium 6061-T6, when impacted by the steel rod projectile (h_C = ceramic thickness).

concepts related to their areal densities, for armours with areal densities less than 55 kg/m^2. In this figure, the increase in areal density represents increase in back-up plate thickness.
Best performance is given by an 8.0 mm thick ceramic facing backed by a 5.0 mm thick aluminium plate weighing 44.0 kg/m^2, as can be derived from this figure, since this armour defeats the projectile at the velocity of 840 m/s with the lowest areal density. If the projectile's velocity is increased by 100 m/s, however, the ALARM model predicts that an armour concept with a 9 mm thick facing performs best on an areal weight basis.

8.3. Armour weight optimization for the low strength rod (7.62 mm ball) projectile

Ballistic limit velocity computations were also carried out with the low strength rod. Its geometry and mass were taken identical to those for the steel rod. The projectile material properties were modified to simulate the 7.62 mm ball projectile's soft core, as described in section 7.1. The range of armours was identical to the one used for the computations in the previous section.

The results of the ALARM computations are presented in figure 8.3. Again there is a large number of armour configurations that defeat the projectile at a velocity of 840 m/s (the horizontal line in figure 8.3).
Figure 8.4 presents the performance of the armours against this threat as a function of their areal weight. The lightest armour capable of defeating the low strength rod projectile when it impacts at a velocity of 840 m/s, weighs 43.8 kg/m^2 (9.0 mm alumina supported by 3.5 mm aluminium). Figure 8.4 also shows that if the low-strength rod's initial velocity is decreased by 100 m/s, as if it was fired from a distance, this optimum (lightest) armour configuration is replaced by one with an 8 mm thick ceramic facing.

Comparison of the figures 8.4 and 8.2 shows that the low strength rod presents a comparable threat towards the armour as its steel counterpart. The weight of the lightest armour capable to defeat the low strength rod is approximately equal to the weight of the armour necessary to defeat the steel rod projectile. This similarity between the performance of both projectiles is quite unlike that for more conventional armours. With rolled homogeneous armour steel (RHA) the 7.62 mm ball projectile is defeated at almost half the weight necessary to stop the 7.62 mm AP round.

It is interesting to examine the behaviour of the optimum armour's behaviour in more detail, in order to illustrate some of the typical features of soft projectile impact. The ALARM generated history plots for the optimum armour configuration when impacted by the soft rod at 840 m/s are presented in figure 8.5. The velocity plot shows that the projectile's rear-end is not decelerated by the impact event. The projectile is seen to erode almost completely in 48 μs. At this same time plug shearing

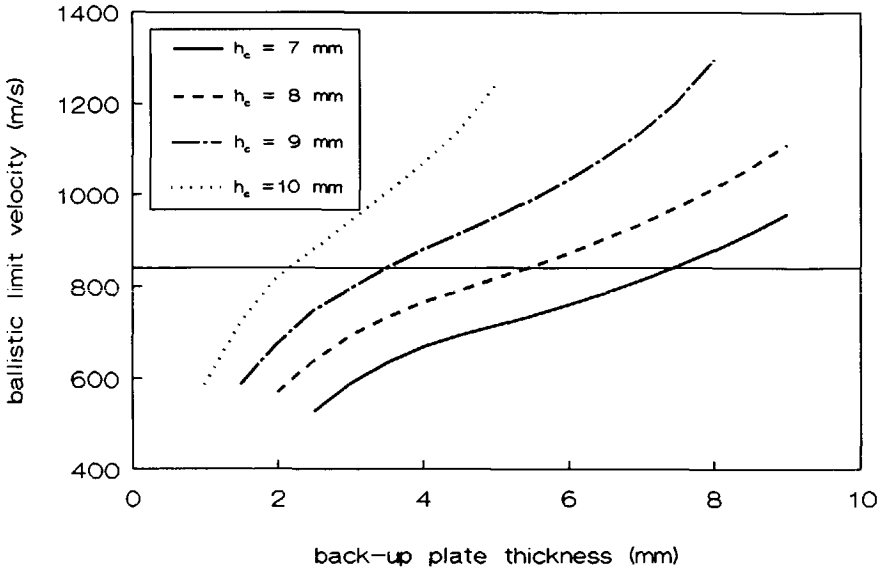

Figure 8.3 Computed ballistic limit velocities as a function of back-up plate thickness for armours of Morgan Matroc Hilox 973 alumina backed by aluminium 6061-T6, when impacted by the soft rod projectile (h_C = ceramic thickness).

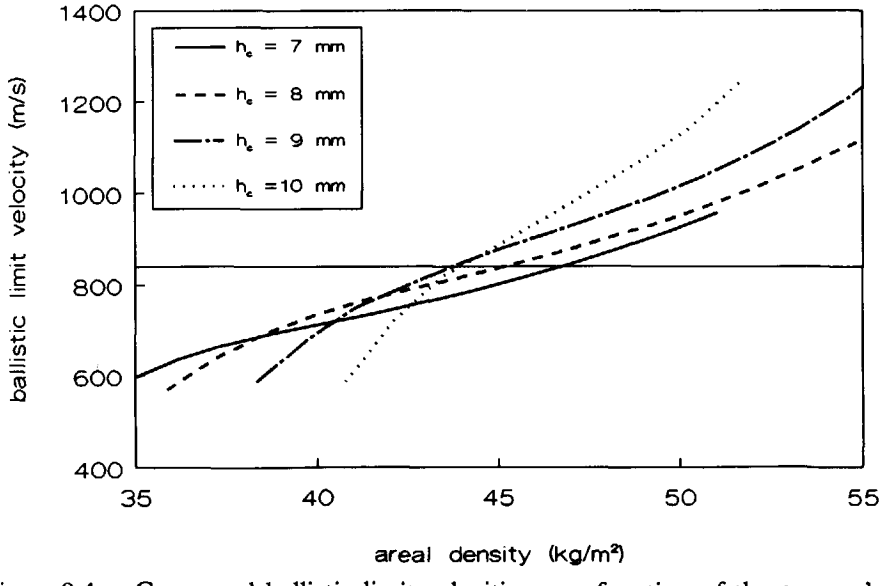

Figure 8.4 Computed ballistic limit velocities as a function of the armour's areal density for armours of Morgan Matroc Hilox 973 alumina backed by aluminium 6061-T6, when impacted by the soft rod projectile (h_C = ceramic thickness).

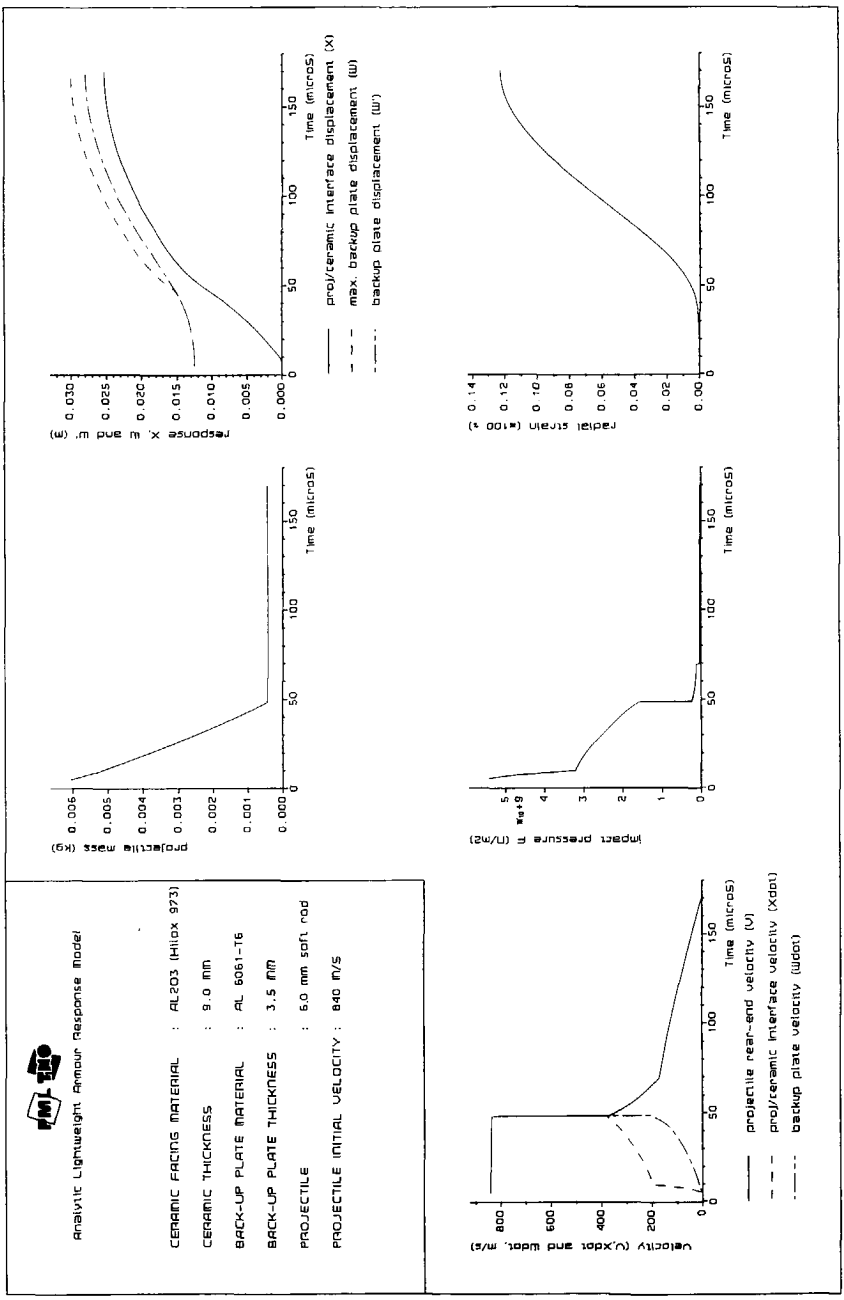

Figure 8.5 Computed mass, displacements, velocities, pressure and strain histories for an armour of 9 mm thick Morgan Matroc Hilox 973 alumina supported by a 3.5 mm thick aluminium 6061-T6 back-up plate, when impacted by the soft rod projectile at 840 m/s.

commences. The erosion is not completed because it cannot be handled by the plug shearing deformation model. At 69 μs after impact the plug shearing ends as the plug and its surroundings obtain the same velocity (175 m/s). The membrane deformation model decelerates the ensemble further. It comes to rest at 170 μs after impact, when it has accumulated some 12 per cent strain. The back-up plate's deformation is some 17 mm. A small increase of the impact velocity will result in strain failure of the back-up plate.

8.4. Back-up plate material optimization

In the requirements for an optimum back-up plate for a ceramic faced lightweight armour concept, Wilkins (1968) stated that a back-up plate has to be rigid, yet flexible. A too rigid back-up plate makes a plug shearing failure mode the weak link, a plate that is too flexible does not give optimum support to the ceramic. In this section an exercise with the ALARM model is presented which illustrates the influence of the back-up plate material on the protection level.
Simulations were run with the steel rod projectile and armours consisting of a 9.0 mm thick alumina facing supported by a range of back-up plate thicknesses, starting at 1.0 mm through to 9.0 mm. Aluminium 6061-T6, 2024-T4 and 7075-T6 were used for the back-up plates. The aluminium alloy 6061-T6 is very common in ballistics applications, the 2024-T4 alloy is more ductile with better tensile and shear-load carrying capabilities and has a higher strain to failure. The 7075-T6 alloy is very rigid with even better tensile and shear-load carrying capabilities but with a low strain to failure. Table 8.1 presents the (quasi-static) material properties used for these aluminium alloys.

Table 8.1 Quasi-static material properties of the three types of aluminium.

		6061-T6	2024-T4	7075-T6
Density	[kg/m^3]	2705.0	2705.0	2705.0
Ultimate yield strength	[MPa]	310	460	540
Ultimate shear strength	[MPa]	200	290	340
Failure strain	[%]	13	18	10

The results of the ballistic limit velocity computations are presented in Figure 8.6. Over the complete range of back-up plate thicknesses, the performance of the armour with the 6061-T6 back-up plate is worse than with the other back-up plate materials. The aluminium 6061-T6's comparatively low tensile and shear load carrying capabilities are responsible for this result.
The armours with the 2024-T4 back-up plates have higher ballistic limit velocities than the armours with the 7075-T4 back-up plates for as long as they are thinner than 3.5 mm. Membrane deformation is very important for the armours with these

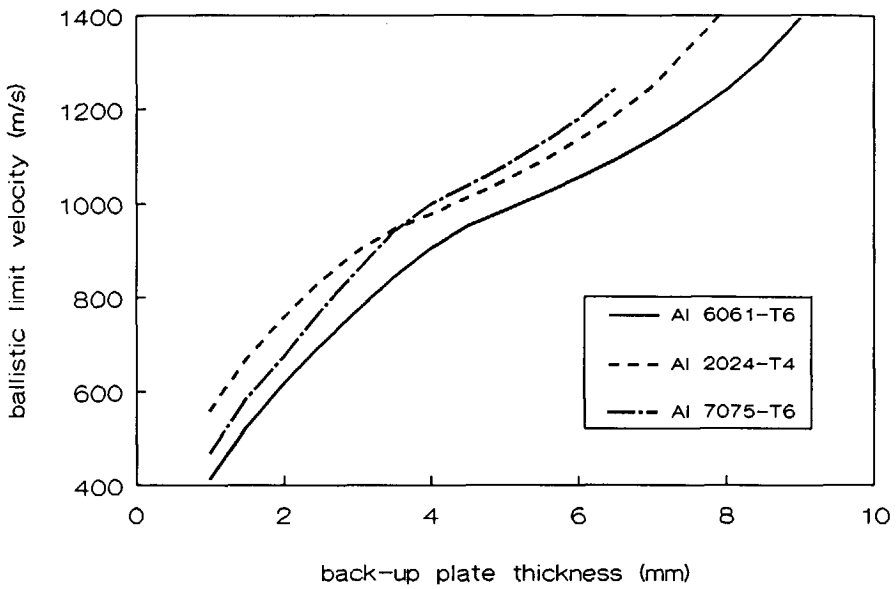

Figure 8.6 Comparison of computed ballistic limit velocities for armours with a 9 mm thick Morgan Matroc Hilox 973 alumina facing supported by back-up plates of aluminium 6061-T6, 2024-T4 and 7075-T6, when impacted by the steel rod projectile.

thin back-up plates, as is illustrated in figure 8.7. Even though the outstanding tensile and shear strength properties of the 7075-T6 back-up plate result in a faster deceleration of the projectile/ceramic/back-up plate ensemble than with aluminium 2024-T4, its poor elongation property causes the 7075-T6 back-up plates to be surpassed by the weaker but much more flexible 2024-T4 plates.

For armours with back-up plates thicker than 3.5 mm, the plug shearing deformation mechanism is very important. This is illustrated by the sequence of graphs presented in figure 8.8 for impact of the steel rod into an armour with a 4.5 mm thick aluminium 7075-T6 back-up plate. The shear strength of 7075-T6 is greater than that of the other alloys. Hence, the armours with the 7075-T6 back-up plates are found most successful in defeating the projectile in this range.

Wilkins (1968) conducted a limited number of experiments with various back-up plate materials. His experiments with armours consisting of an 8.6 mm thick AD-85 facing supported by various 6.3 mm thick aluminium back-up plates, (partially) support the observations with the model as they showed that armours with back-up plates with greater shear strength were harder to defeat.

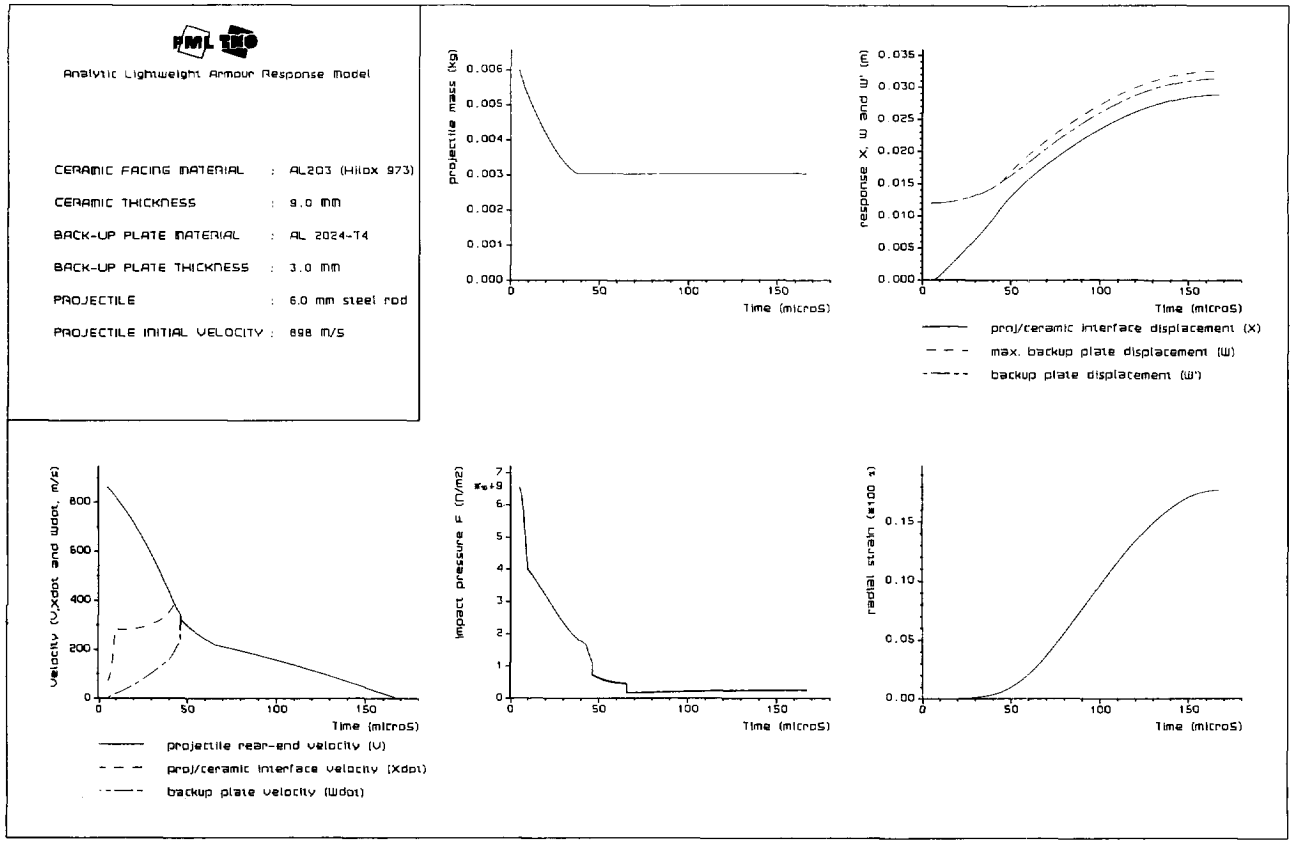

Figure 8.7 Computed mass, displacements, velocities, pressure and strain histories for an armour of 9 mm thick Morgan Matroc Hilox 973 alumina supported by a 3.0 mm thick aluminium 2024-T4 back-up plate, when impacted by the steel rod projectile at 898 m/s.

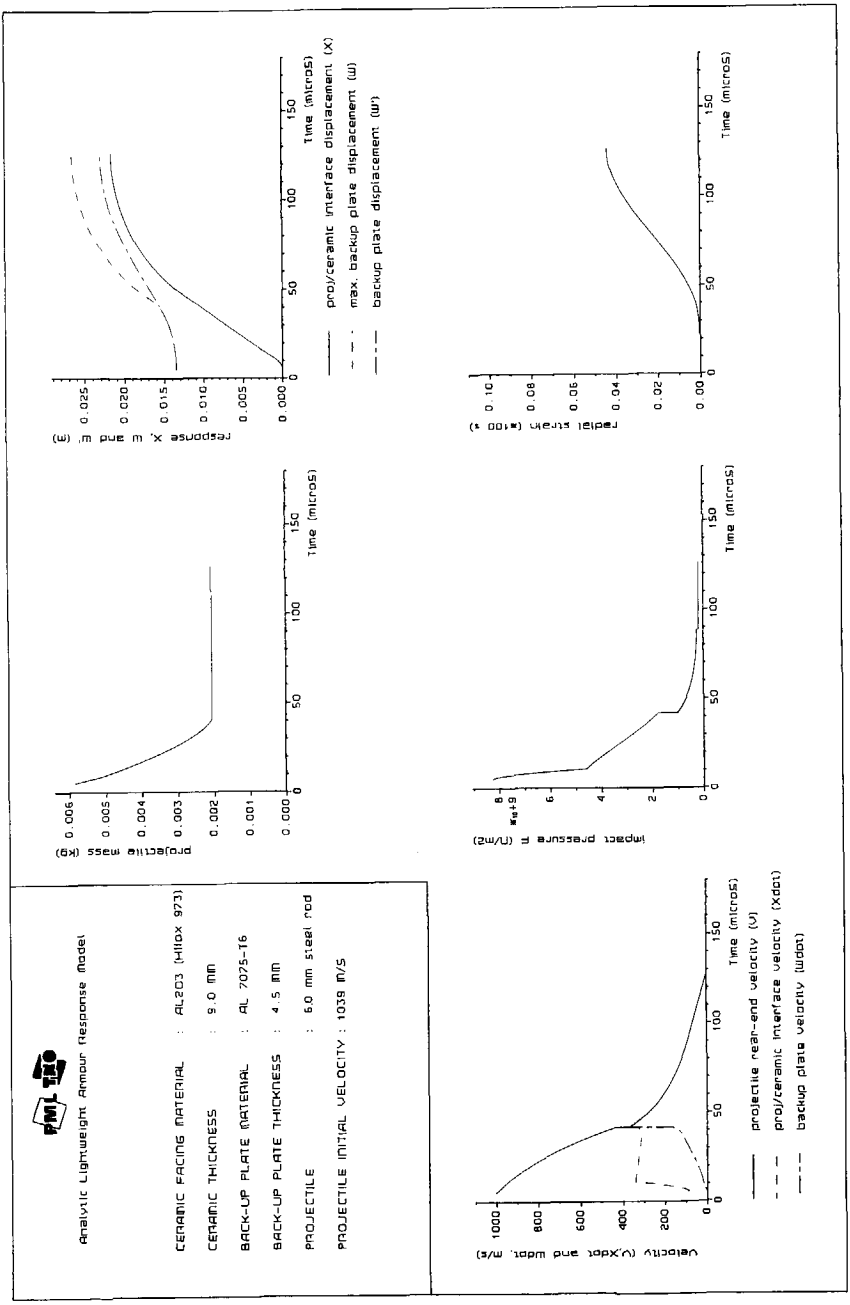

Figure 8.8 Computed mass, displacements, velocities, pressure and strain histories for an armour of 9 mm thick Morgan Matroc Hilox 973 alumina supported by a 4.5 mm thick aluminium 7075-T6 back-up plate, when impacted by the steel rod projectile at 1039 m/s.

Wilkins' experiments also showed that the ballistic performance of aluminium 2024-T4 was worse than that of 6061-T6, even though the strength of 2024-T4 is superior to that of 6061-T6. According to Wilkins (1968) the elongation property of aluminium 2024-T4 with dynamic loads is inferior and was responsible for the observed behaviour.
This experimental result is not reproduced by the model. In the ALARM simulations no strain rate effects are taken into account. The simulations, however, show that the armour's response is not very vulnerable to changes in the radial elongation property of the aluminium for armours with relatively thick (6 mm) back-up plates, such as the one used by Wilkins. Hence, based on the simulations it is very unlikely that inferior radial elongation properties can be held responsible for the poor behaviour of aluminium 2024-T4 as was proposed by Wilkins. This topic therefore needs further investigation.

8.5. The influence of the rod's length-over-diameter ratio

Preliminary computations with rods indicated that by changing the projectile's length-over-diameter (L/D) ratio the projectile can pose a higher threat to the armour. To investigate the influence of the projectile's L/D ratio on the ballistic limit velocity, computations were carried out for steel rods with L/D ratios of 4.0 (L = 26.3 mm), 5.3 (L = 31.5 mm) and 6.6 (L = 36.7 mm). The 31.5 mm long rod represents the standard projectile. The total projectile mass was kept constant for all projectiles. All computations were carried out with armours consisting of a 9 mm thick alumina facing (Morgan Matroc Hilox 973) supported by aluminium 6061-T6 back-up plates.

The results of the computations are incorporated in figure 8.9. Significant differences in the performance of these (equal mass) projectiles are immediately visible.
The rod with L/D ratio equal to 6.6 defeats the armour with a back-up plate of 5 mm thickness when it impacts at an initial velocity of 840 m/s. The two shorter rods are easily defeated by this armour at this velocity. The rod with L/D ratio of 5.3 needs an initial velocity of 987 m/s to perforate this armour. The shorter rod (L/D ratio of 4.0) has even more difficulty, it needs an initial velocity above 1200 m/s to defeat the armour. These results indicate that projectiles with high length-over-diameter ratios pose a large threat to ceramic lightweight armours.

For all three projectiles impacting an armour of 9 mm alumina supported by 5 mm aluminium at 838 m/s, the model generated history plots are presented in figures 8.10, 8.11 and 8.12. Comparison shows that the rear-end of the projectile with the largest L/D ratio is decelerated at the lowest rate. The projectile mass erosion plots show that the mass erosion rate is lower for projectiles with higher L/D ratio. Thus, the projectile with the largest L/D ratio transfers its kinetic energy to the armour at the lowest rate.

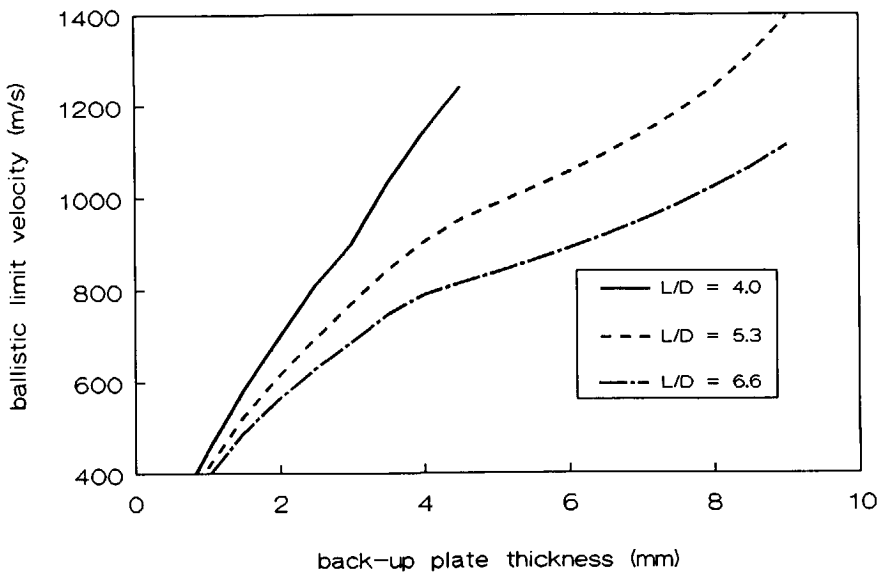

Figure 8.9 Comparison of computed ballistic limit velocities for armours with a 9 mm thick Morgan Matroc Hilox 973 alumina facing supported by aluminium 6061-T6 back-up plates, when impacted by the steel rod projectiles with length-over-diameter ratios of 4.0, 5.3, and 6.6.

The armours are seen to respond in a similar fashion during the first 30 to 40 μs after impact of either projectile. Hence, at the end of this period of time, the projectiles have accomplished approximately the same. But since the projectile with the highest L/D ratio transfers its kinetic energy to the armour at the lowest rate, it has the largest amount of kinetic energy still available to continue penetration. At 60 μs after impact, for example, the kinetic energy content of the shortest projectile (L/D = 4.0) that still has to be dissipated by the armour is 7.9 J compared to 79.0 J for the longest projectile (L/D = 6.6). Not surprisingly therefore, the projectile with the highest L/D ratio perforates the armours at a lower velocity than the others. Of course, there exists an optimum L/D ratio which gives best performance. A projectile with an extremely high L/D ratio may not be able to penetrate a ceramic faced armour at all.

It should be realized that the ALARM model may not be able to calculate the penetration behaviour correctly for blunt projectiles with very low length-over-diameter ratios (< 2). Experimental observations (Van Riet, 1987-1991) have shown that fragment simulating projectiles (FSP's) with their blunted nose and low L/D ratio (1.5) are capable of defeating a ceramic armour at a velocity below the one predicted by the ALARM model for these projectiles. This is explained as follows.

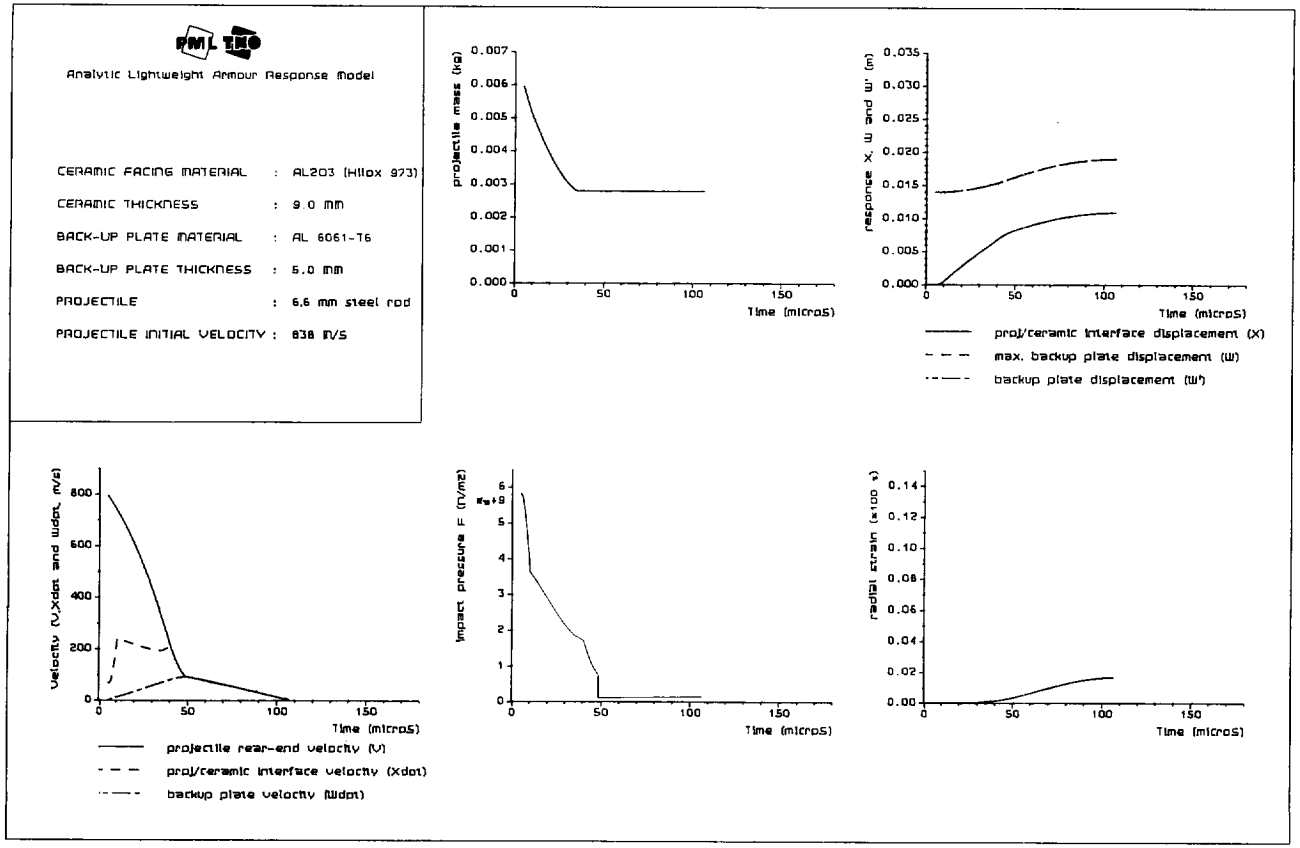

Figure 8.10 Computed mass, displacements, velocities, pressure and strain histories for an armour of 9 mm thick Morgan Matroc Hilox 973 alumina supported by a 5 mm thick Al6061-T6 back-up plate, when impacted at 838 m/s by the short steel rod projectile (L/D = 4.0).

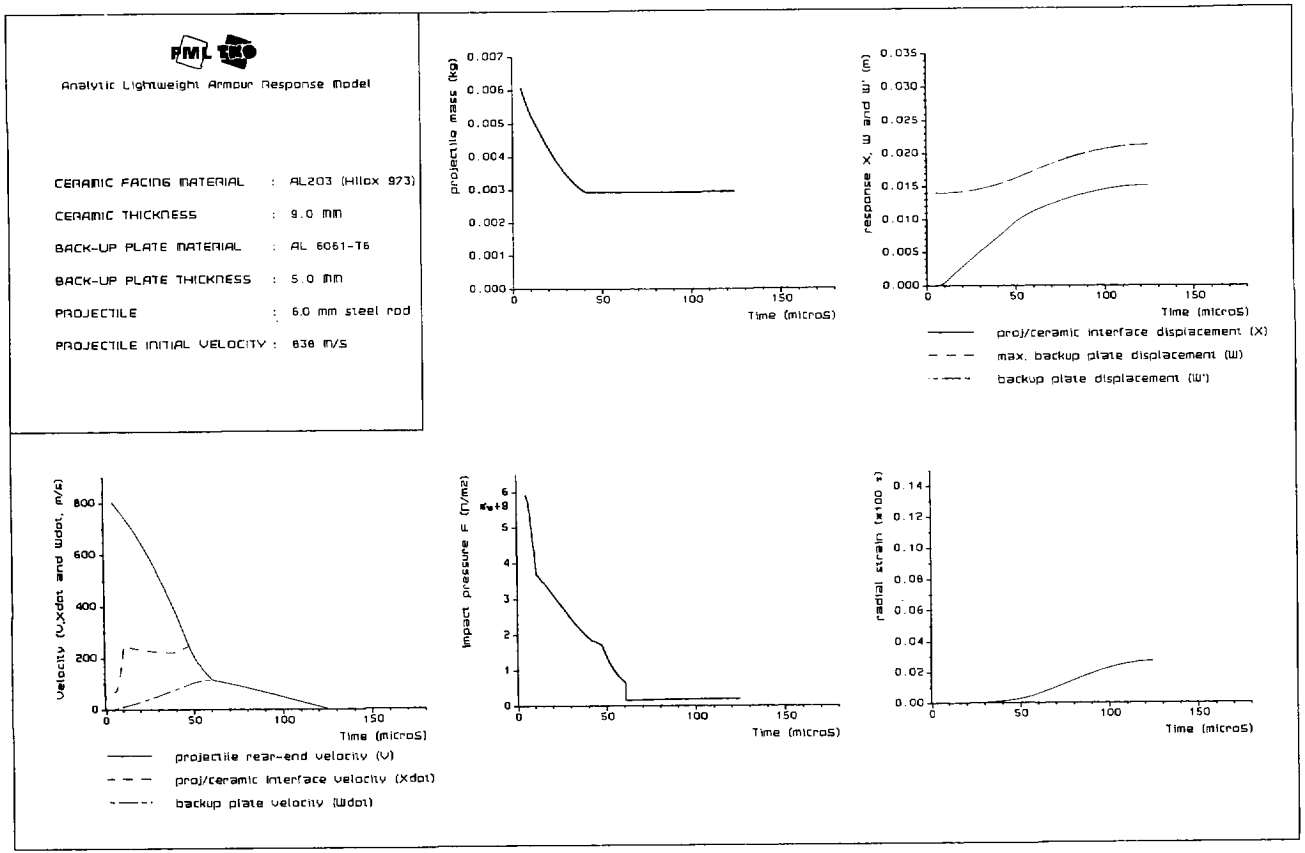

Figure 8.11 Computed mass, displacements, velocities, pressure and strain histories for an armour of 9 mm thick Morgan Matroc Hilox 973 alumina supported by a 5 mm thick Al6061-T6 back-up plate, when impacted at 838 m/s by the normal steel rod projectile (L/D = 5.3).

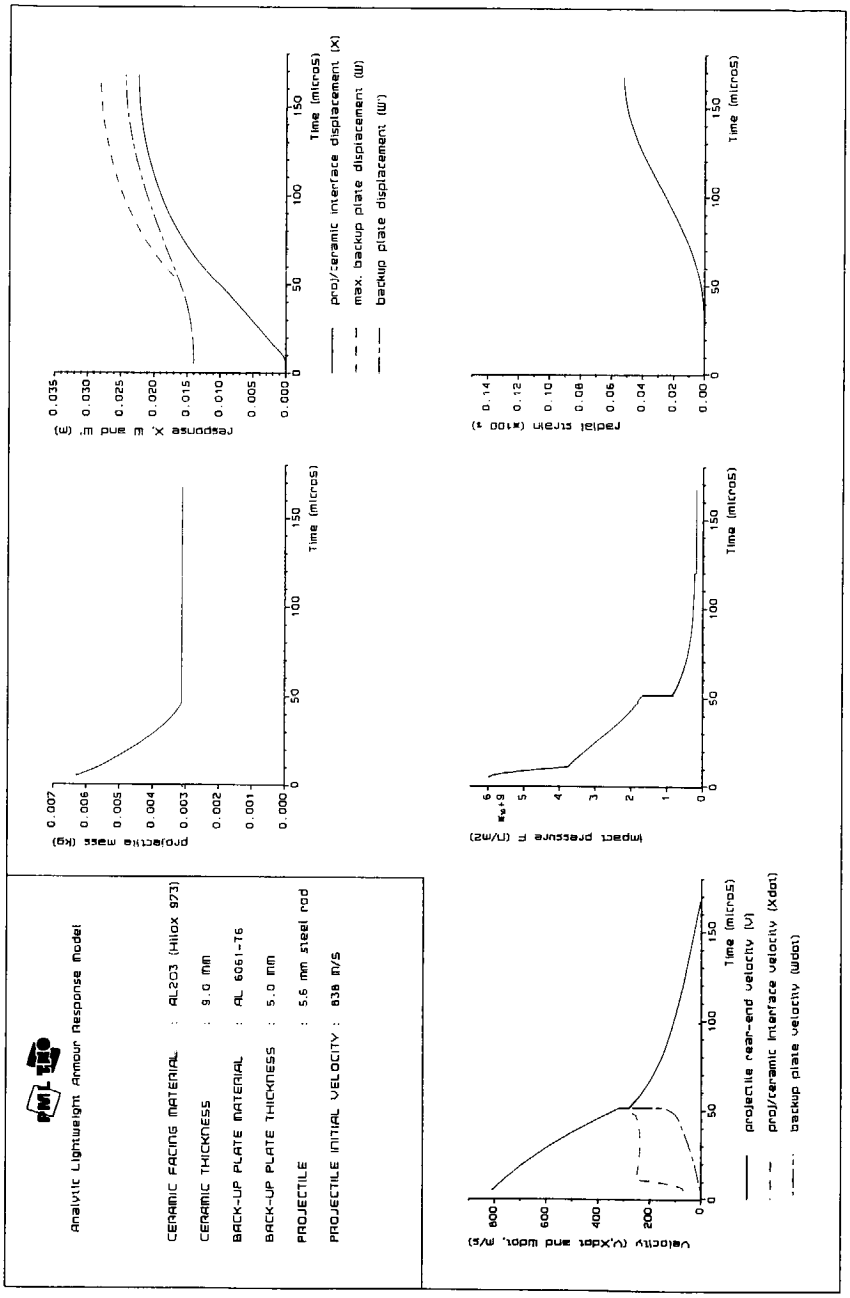

Figure 8.12 Computed mass, displacements, velocities, pressure and strain histories for an armour of 9 mm thick Morgan Matroc Hilox 973 alumina supported by a 5 mm thick Al6061-T6 back-up plate, when impacted at 838 m/s by the long steel rod projectile (L/D = 6.6).

As was discussed in section 4.3.2, shocking ceramics above the HEL (Hugoniot Elastic Limit) will introduce an extensive amount of microfracture to the material. The extend and depth of this shocked region depends on the diameter of the (blunt) projectile. Hence with low L/D ratio projectiles a much larger amount of ceramic in front of the projectile experiences a peak shock stress above HEL and is damaged. As a result the low L/D projectile may start to penetrate the armour earlier in time and with more ease. In the ALARM model, the ceramic fracturing process is assumed to be independent of the projectile geometry. In addition, the ceramic's resistance to penetration is assumed to be insensitive to the additional microfracture induced to the ceramic by a projectile geometry dependent shock wave. For short projectiles, this may result in an over-estimation of the projectile's erosion and a too slow penetration of the rod. This inevitably results in incorrect predictions, as some experiments confirm.

8.6. Conclusions

The presented results show the capabilities of the ALARM model. The model can be used to help design armour systems especially when the emphasis is placed on the back-up plate build-up and back-up plate related properties. It shows the probable mechanisms used by the armour to defeat high and low strength projectiles.

The computations show that the lightest armour (composed of a Morgan Matroc Hilox 973 alumina facing and an aluminium 6061-T6 back-up plate), capable of defeating the steel rod projectile at a velocity of 840 m/s consists of an 8 mm thick facing backed by a 5 mm thick back-up plate at an areal density of 44.0 kg/m^2. The soft rod projectile is defeated by an armour composed of a 9 mm thick facing backed by a 3.5 mm thick back-up plate at an areal density of 43.7 kg/m^2.
However, when other back-up plate materials are taken into consideration, armour performance can be improved further. Depending on the armour configuration, simulations show other aluminium alloys, such as 2024-T4 and 7075-T6, to perform better.

For as long as projectile geometry induced shock wave effects do not alter the length and appearance of the initial break-up process of the ceramic facing, the ALARM model can be used for projectile optimization studies as well. This is illustrated by the examples in section 8.5 showing a significant decrease of the armour's ballistic limit velocity when it is impacted by a projectile with an increased length-over-diameter ratio.
The design of new projectiles, such as SLAP (Saboted Light Armour Penetrating) projectiles, indeed show a tendency toward a high L/D ratio to improve performance against modern armours.

9. CONCLUSION

A combination of theoretical and experimental work on impact of projectiles onto ceramic faced armours has been presented in this thesis. The theoretical work was directed towards the development of a simple penetration model whereas the experimental work was intended to increase understanding and knowledge of the phenomena and mechanisms governing the impact event.

9.1. The ALARM model

The theoretical work has resulted in the development of the ALARM model. This one-dimensional analytic penetration model simulates the response to the impact event of both the projectile and armour.
The model allows the projectile to erode mass, to mushroom or to be rigid from the moment of impact onwards. It is assumed that the ceramic facing of the armour starts to fracture directly after the moment of impact. This fracturing process results in the formation of the ceramic fracture conoid. During this fracturing process it is assumed that the armour presents an impenetrable barrier to the projectile. In the model most emphasis is placed upon the interaction between the ceramic and the back-up plate and the response of the back-up plate itself, after the ceramic fracture conoid has been formed. It was assumed that as the projectile penetrates the ceramic facing, the impact load is distributed over an increasingly smaller area of back-up plate. The response of the armour to the impact event is simulated by four deformation models; the initial armour response model, the shear deformation model, the plug shearing model and the membrane deformation model. These models use a simplified, rigid-perfectly plastic, circular symmetric approach to structural deformation of the back-up plate. The back-up plate is allowed to fail by either one of two modes, e.g. plug shearing or strain failure. The penetration resistance experienced by the projectile as it penetrates the comminuted ceramic is expressed in terms of an empirical expression. The constants in this expression have to be obtained from a tuning-procedure by matching experimental and calculated ballistic limit velocities. The model also requires a number of other input parameters which have to be obtained from ballistic experiments with reference armours as well. The fracture conoid angle forms an example of such a parameter. Hence, in order to be able to perform penetration calculations, the results of a few ballistic experiments with reference armours, composed of the same materials, have to be available.

The comparison of the ballistic limit velocities calculated with ALARM and various other models and the experimental data supplied by Wilkins indicated that the ALARM model once tuned predicted the experimental data best. However, the comparison has shown that the calculated results may strongly deviate from the experimental values when the back-up plate thickness exceeds the thickness of the ceramic facing.

The comparison of the model simulations with the experimental results obtained for steel rod projectile impact onto armours of alumina supported by aluminium have shown that the computed ballistic limit velocities and associated back-up plate failure modes match the experimental results. For impacts below the armour's ballistic limit velocity, the calculated projectile and armour deformation profiles match the experimental evidence fairly well. The back-up plate responses are somewhat slow whereas the armour penetration is slightly over-predicted by the model. For impacts above the ballistic limit velocity that cause plug shearing, the model calculates that the shearing occurs much later in time than was observed experimentally.
The various comparisons of measured and calculated details of the penetration processes showed that the model can reproduce the effects of limited variations of projectile and armour geometry and properties about a reference armour, and thus can present the user with the tendencies and the characteristic phenomena associated with specific impact events.
The model's ability to be used for armour optimization studies was illustrated by a number of examples. The model is also capable of predicting the influence on the ballistic performance of limited variations in projectile geometry and material composition. However, the examples show that one should apply care to ensure that the variation of armour and projectile geometry and properties do not affect mechanisms which were assumed invariant in the model.

9.2. The impact experiments

The experimental work was started with the development of a novel experimental technique using flash radiography to visualize and study the penetration process of projectiles in ceramic faced armours. The unique feature of this technique is that it allows the use of armour panels with large lateral dimensions, and thus prevents the penetration process to be influenced by (unwanted) boundary effects. The flash radiographs produced with this technique proved to be very valuable.

The series of radiographs showing blunt steel rod projectiles impact ceramic faced armours with four types of back-up plates at velocities above and below the ballistic limit velocities resulted in an improved understanding of the penetration mechanisms. The results show that the blunt projectile is not able to penetrate the ceramic material directly underneath the point of impact, quite contrary to the expectations based on Wilkins' work. The rods were seen to shorten and erode for a long period of time (> 40 μs), and did not break-up into a limited number of fragments during impact. Fringes of projectile material are seen moving radially away from the impact area at a velocity slightly below the projectile's impact velocity. The remaining recovered rod shanks showed little plastic deformation.

The ceramic facings were found to fracture and a so-called fracture conoid was formed as was expected from literature. This fracture conoid spreads the high impact load over a larger section of the supporting back-up plate. A few radiographs actually show the

conoid cracks opened during impact. The recovered armours indicated that the fracture conoids had a (half) top-angle of approximately 65°. The fracture conoids recovered had largely deteriorated to the shape of a cylindrical plug with a diameter approximately equal to that of the impacting projectile. Some segments of fracture conoids showed details of overlying conoid-like fractures. Their slopes, similar to those of the conoid cracks, seem to indicate that these fractures originate from the ceramic's back-face. The height of the cylindrical plugs was found to be approximately equal to the thickness of the facing and thus confirmed the experimental data from the radiographs that showed the projectile practically unable to penetrate the ceramic.

From the experiments a deeper understanding of the ceramic's behaviour has emerged which deviates from the perception of the ceramic/back-up plate interaction process obtained from literature. On the basis of this understanding, the following phenomenological description of events that lead to the deterioration of the fracture conoid is proposed.

At some time early after impact, the Hertzian conoid cracks intersect the back-up plate and thereby complete the formation of the fracture conoid. The high impact load then accelerates the fracture conoid and the underlying back-up plate. The back-up plate deforms correspondingly and introduces high stresses near the edges of the fracture conoid's base. The relatively low tensile strength of the ceramic results in conoid-like cracks growing opposite to the direction of impact and towards the axis of impact. During this process, relatively thin "conoid-shell elements" are formed, which due to their constraint to follow the back-up plate's deformation, introduce a high shear load on the periphery of the ceramic material in front of the impacting projectile. When the lateral confinement of the "conoid-shell elements" is sufficient, shear failure around this periphery occurs. Hence, during penetration the fracture conoid deteriorates and the impact load is spread over a smaller area of back-up plate. This process may repeat itself, depending on the loading and the response of the back-up plate and ends when a ceramic plug has formed with approximately the same diameter as the projectile.

In some series of experiments at velocities above the ballistic limit, the back-up plate deformation profiles indicated that the impact load was concentrated quickly (<20 μs) over a very small area of the back-up plate. Hence, the fracture conoid must have lost its ability to distribute the high impact load over a large area of back-up plate soon after impact. Although it appeared that the ceramic facing experienced a dramatic change of behaviour when impacted at these higher velocities, its behaviour can be explained completely by the phenomenological description of events presented above.

The increased impact velocity results in a higher loading on the back-up plate. However, the increase of loading is most likely such that at some radius of the back-up plate significant local shear deformation results. This causes the fracture conoid to deteriorate as described above. As a consequence, the already too high loading is now distributed over an even smaller area of the back-up plate, which immediately causes more back-up plate shear deformation and fracture conoid deterioration. The unstable nature of this process results in the catastrophic loss of load-distributing capabilities of the ceramic facing and the fast concentration of the impact load on a small area of back-up plate, as was observed experimentally.

This description of events is very valuable, as it extends the knowledge and understanding of the (catastrophic) deterioration process of the ceramic fracture conoid and the loading process on the back-up plate during the structural response of the armour.

The measured back-up plate responses and the recovered back-up plates allowed the influence of some back-up plate material properties on the armour's structural response and performance to be assessed and clarified. The large difference in ballistic limit velocity (~100 m/s) for armours with single and two-layer back-up plates, as suggested by Wilkins (1968; Laible, 1980) was not witnessed with the blunt rod projectile experiments.

A significant amount of experimental work on ceramic faced armours presented in literature is conducted with standard 7.62 mm projectiles. The experimental work with these projectiles is often limited to the determination of ballistic limit velocities and the analyses of the recovered projectile and armour fragments. The series of flash radiographs presented in this thesis reveal the projectile/armour interaction processes of these standard projectiles during impact on ceramic faced armours.
The radiographs of the experiments with the 7.62 mm AP (hard-core) projectile impacting armours of 8.1 mm alumina supported by 6.0 mm aluminium at muzzle velocity (841 m/s) showed that the projectile is capable of penetrating a limited thickness of the ceramic facing only. The projectile is seen to shorten for some 35 to 40 μs. It does not seem to break-up into a number of large fragments. The lead part in the rear-section of the projectile bulges around the remainder of the steel core. At 35 μs after impact, the ogive-nosed projectile has been reduced to the approximate shape of a ball with a 10 mm diameter. The recovered back-up plates showed that the projectile was unable to perforate the armour.
The 7.62 mm (soft-core) ball projectile is also defeated by this armour when it impacts at 829 m/s. This projectile was seen to act by transferring an impulse to the armour. In approximately 38 μs the projectile is completely eroded. Projectile material is seen to move into two directions, along the front surface of the armour and into the conoid cracks. Eventually the projectile material reaches the ceramic/back-up plate interface and continues its path between both materials. These experimental observations confirm the behaviour postulated by Prior (1987) for ball projectile impact on ceramic-composite armours.
The back-up plates were seen to respond similar to impact of the hard-core (steel, R_c = 60) and soft-core (lead) projectiles. Hence, the ceramic faced armour experiences both projectiles as being "soft". These observations imply that one has to apply extreme care when considering a projectile's core as the only effective part of the penetrator when designing projectile simulators or simulating impact on ceramic faced armours.

The 7.62 mm AP projectile was also defeated by the ceramic faced armour with the two-layer back-up plate when it impacted at muzzle velocity. As with the steel rod experiments, the recovered back-up plates did not indicate a large difference between the

ballistic limit velocities of the armours with the single and the two-layer back-up plates. During the first 25 μs, the armour responds as if it had a single layer back-up plate. After this period, the high flexibility of this armour results in a faster armour penetration and deformation than observed with the armour with the single layer back-up plate. These observations suggest that inertial effects dominate over strength properties early in the impact process.

The comparison of the experimental results obtained for the 7.62 mm AP projectile and the steel rod projectile impacts shows that the projectile/armour interaction processes are very much alike. Hence, the steel rod is a far more efficient penetrator than the 7.62 mm armour piercing projectile. It is capable to inflict the same amount of damage to the armour as the armour piercing projectile using 36 per cent less mass (and kinetic energy). The good performance of the steel rod is mainly contributed to its blunt nose-shape.

9.3. Recommendations for future theoretical and experimental work

The improved understanding of the impact process and the comparison of the experimental results with the calculations by the model have indicated a number of areas where the analytic model can be improved.
The modification of the projectile/armour interaction mechanism used in the penetration model to match the mechanism observed experimentally is expected to improve the model's performance. The model may be improved also by the use of a more comprehensive model for the initial phase (the first few microseconds) of the impact process. In addition, the evaluation of the back-up plate responses have indicated that a more elaborate two-dimensional (elastic-plastic) back-up plate deformation model can be expected to match the experimentally observed deformations better.
Balancing the necessary efforts to implement these improvements with the expected increased accuracy of the end-result, as done in section 5.6, has resulted in the belief that the most efficient improvement is expected to come from the inclusion of the catastrophic loss of the ceramic's load distribution capabilities to the model. This will significantly improve the match between the experimental and calculated armour response for impacts above the ballistic limit velocity.

In order to further improve and verify the understanding of the penetration mechanisms and validation of the ALARM model, additional experimental data is necessary. These experiments should include other ceramic facing and back-up plate materials. The effects of projectile geometry (L/D ratio), nose-shape and material composition should also be included in such an experimental study.
In order to study the ceramic fracturing process and the events that lead to the catastrophic loss of load distribution capabilities of the ceramic facing in more detail, experiments need to be conducted using instrumentation techniques that allow a more

accurate measurement of the first 16 μs of the projectile/armour interaction process than was presented here.

9.4. Summary

In summary, the main achievements of the work presented in this thesis are:

- An analytic penetration model has been developed which can be used to study the influence of limited variations of projectile and armour geometry and composition on the ballistic performance. As such it can be used to predict tendencies and carry out optimization studies. In addition it presents the user with details on the projectile/armour interaction processes which are very helpful to increase understanding and analyse experimental observations.

- A new experimental technique using flash radiography was developed to study the projectile/armour interaction process throughout the penetration event. The unique feature of this technique is that it does not require that the lateral dimensions of the armour panels used be reduced to such an extent that boundary effects can influence the penetration process.

- A large number of experiments were conducted with steel rod projectiles and 7.62 mm AP and ball projectiles impacting ceramic faced armours with four different types of back-up plates at velocities below and above the ballistic limit. The resulting series of radiographs show details of the projectile/armour interaction process throughout the event.

- The experimental results have resulted in an improved understanding of:
  1) the ceramic's behaviour and function,
  2) the back-up plate's behaviour and function,
  3) the influence of variations of back-up plate thickness and composition on the armour's performance, and
  4) the behaviour of the 7.62 mm armour piercing projectile, the 7.62 mm ball projectile and the steel rod projectile during high velocity impact.

- The experimental data presented and the associated improved understanding of the projectile/armour interaction process represents a significant contribution to the knowledge base on impact on ceramic faced armours.

- The improved understanding of the impact event and the comparisons between the model predictions and the experimental results have resulted in the identification of a number of areas within the penetration model where the description used may be improved. On the basis of this information, recommendations for modifications to the model are proposed.

REFERENCES

Abbot, K.H. : Composite Aircraft Armor, Ordnance, pp. 582-584, May-June 1968.

Alesi, A.L. & Barron, E.R. : Plastic-Ceramic Composite Armor, SPE Journal, Vol. 24, July 1968.

Allen, W.A., Mayfield, E.B. & Morrison, H.L. : Dynamics of a Projectile Penetrating Sand, J. Appl. Physics, Vol. 28, No. 3, pp. 370-376, 1957.

Anderson Jr, C.E. & Bodner, S.R. : Ballistic Impact: The Status of Analytical and Numerical Modelling, Int. J. Impact Engng., Vol. 7, No. 1, pp. 9-35, 1988.

Bless, S.J. : Impact Behaviour of Ceramics, University of Dayton Research Institute, Dayton, Ohio, U.S.A., 1987.

Bless, S.J., Rosenberg, Z. & Yoon, B. : Hypervelocity Penetration of Ceramics, Int. J. Impact Engng., Vol. 5, pp. 165-171, 1987.

Bodine, E.G., Dunleavy, J.G. & Rolsten, R.F. : The Optimization of Composite Ceramic-Armor Materials, Proceedings of Ceramic-Armor Technology Symposium, DCIC Report 69-1 part I, pp. 21-36, 1969.

Clancy, L.J. : Aerodynamics, Pitman Publishing Limited, ISBN 0-273-01120-0, 1975.

Evans, A.G. : Strength Degradation by Projectile Impacts, Journal of the American Ceramic Society, Vol. 56, No. 8, 1973.

Florence, A.L. & Ahrens, T.J. : Interaction of Projectiles and Composite Armor, Final Report, Stanford Research Institute, Menlo Park, CA, U.S.A., AMRA CR 67-05 (F), 1967.

Florence, A.L. : Interaction of Projectiles and Composite Armor, Part II, Stanford Research Institute, Menlo Park, CA, U.S.A., AMRA CR 69-15, 1969.

Frechette, V.D. & Cline, C.F. : Fractography of Ballistically Tested Ceramics, Ceramic Bulletin, Vol. 49, No. 11, 1970.

Gerald, C.F. & Wheatley, P.O. : Applied Numerical Analysis, Addison-Wesley Publishing Company, ISBN 0-201-11579-4, 1984.

Graaf, H. van de : Validation of Ceramics Material Modelling in Impact/Penetration Calculations, Pisces International B.V., Gouda, The Netherlands, Technical report TR-88-591.2/01, 1988.

Griffith, J. & Vanzant, H. : Large Deformation of Circular Membranes Under Static and Dynamic Loading, Paper No. 702, First International Congress on Experimental Mechanics, New York, U.S.A., 1961.

Held, M. : Flash X-Radiography in Ballistics, Materials Evaluation, No. 43, pp. 1104-1123, 1985.

Hodge, P.G. : Yield Conditions for Rotationally Symmetric Shells Under Axisymmetric Loading, J. Appl. Mech., Vol. 27, No. 2, Trans. ASME, Vol. 82, Series E, pp. 323-331, June 1960.

Hornemann, U., Rothenhäusler, H., Senf, H., Kalthoff, J.F. & Winkler, S. : Experimental Investigation of Wave and Fracture Propagation in Glass Slabs loaded by Steel Cylinders at High Impact Velocities, Proceedings Third Conf. Mech. Prop High Rates of Strain, Oxford, England, 1984.

Johnson, G.R. & Holmquist, T.J. : A Computational Constitutive Model for Brittle Materials Subjected to Large Strains, High Strain Rates, and High Pressures, Proceedings Explomet, San Diego, California, U.S.A., 1990.

Johnson, W. : Impact Strength of Materials, Edward Arnold, ISBN 0-7131-3266-3, 1972.

Jones, N. : Impulsive Loading of a Simply Supported Circular Rigid Plastic Plate, J. Appl. Mech., Vol. 35, pp. 59-65, 1968.

Kennedy, C.M., Ofstedahl, K.E. & Mayseless, M. : Analysis of Impacts on Alumina, Armor and Materials Department, FMC Ordnance Division, San Jose, CA, U.S.A., 1986.

Laible, R.C. (editor) : Ballistic Materials and Penetration Mechanics, Elsevier Scientific Publishing Company, ISBN 0-444-41928-4, 1980.

Mayseless, M., Goldsmith, W., Virostek, S.P. & Finnegan, S.A. : Impact on Ceramic Faced Targets, J. Appl. Mech., Vol. 54, 1987.

Mescall, J.F. & Tracy, C.A. : Improved Modelling of Fracture in Ceramic Armours, U.S. Army Materials Technology Laboratory, Watertown, MA, U.S.A., 1986.

O'Donnell, R.G., Woodward, R.L., Gooch Jr, W.A.& Perciballi, W.J. : Fragmentation of Alumina in Ballistic Impact as a Function of Grade and Confinement, Proceedings 12th International Symposium on Ballistics, San Antonio, TX, U.S.A., 1990.

Onat, E.T. & Prager, W. : Limit Analysis of Shells of Revolution, Proceedings of the Royal Netherlands Academy of Science Parts I and II, Series B, Vol. 57, pp. 534-541, 542-548, 1954.

Prior, A.M. & Hetherington, J.G. : The Penetration of Composite Armour by Small Arms Ammunition, Proceedings 9th International Symposium on Ballistics, Shrivenham, England, 1986.

Prior, A.M. : The Penetration of Lightweight Armours by Small Arms Ammunition, Proceedings 10th International Symposium on Ballistics, San Diego, CA, U.S.A., 1987.

Ravid, M., Bodner, S.R. & Holcman, I. : Application of Two-Dimensional Analytical Models of Ballistic Penetration to Ceramic Armor, Proceedings 11th International Symposium on Ballistics, Brussels, Belgium, 1989.

Recht, R.F. : Quasi-Empirical Models of the Penetration Process, in Joint Technical Coordinating Group for Munitions Effectiveness, JTCG/ME, Working Party for KE Penetrators, Information Exchange Meeting, 13-15 February 1973 at the Ballistic Reseach Laboratories, Aberdeen Proving Ground, Aberdeen, MD, U.S.A., 1973.

Reijer, P.C. den : Ballistic Arall First Progress Report, Prins Maurits Laboratory, Rijswijk, The Netherlands, PML-1987-C101, 1987.

Reijer, P.C. den : Studiereis Keramische Pantsers in de Verenigde Staten, Prins Maurits Laboratory, Rijswijk, The Netherlands, PML 1988-RV5, 1988, in dutch.

Reijer, P.C. den : Penetration of 7.62 mm Projectiles into Ceramic Faced Armour, Proceedings 11th International Symposium on Ballistics, Brussels, Belgium, 1989.

Reijer, P.C. den : The TNO Analytic Ceramic Faced Lightweight Armour Response Model (Theory and Results), Prins Maurits Laboratory, Rijswijk, The Netherlands, PML-1989-C145, 1989.

Reijer, P.C. den : The TNO Analytic Ceramic Faced Lightweight Armour Response Model (Source and Examples), Prins Maurits Laboratory, Rijswijk, The Netherlands, PML-1989-C156, 1989.

Reijer, P.C. den : Further Development of the TNO Analytic Ceramic Faced Lightweight Armour Response Model (ALARM), Prins Maurits Laboratory, Rijswijk, The Netherlands, PML-1990-C17, 1990.

Reijer, P.C. den : An Experimental Study of 7.62 mm Projectiles Penetrating Ceramic Faced Lightweight Armours, Prins Maurits Laboratory, Rijswijk, The Netherlands, PML-1990-C79, 1990.

Reijer, P.C. den : An Experimental and Analytical Study on the Penetration of Rods into Ceramic Faced Armours, Prins Maurits Laboratory, Rijswijk, The Netherlands, PML-1991-C28, 1991.

Riet, E.J.M. van : Personal Communications to P.C. den Reijer, 1987-1991.

Rolston, R.F., Bodine, E. & Dunleavy, J. : Breakthrough in Armor, Space/Aeronautics, pp. 55-63, July 1968.

Rosenberg, Z., Bless, S.J. & Brar, N.S. : On the Influence of the Loss of Shear Strength on the Ballistic Performance of Brittle Solids, Int. J. Impact Engng., Vol. 9, No. 1, pp. 45-49, 1990.

Rosenberg, Z. & Tsaliah, J. : Applying Tate's Model for the Interaction of Long Rod Projectiles with Ceramic Targets, Int. J. Impact Engng., Vol. 9, No. 2, pp. 247-251, 1990.

Semple, C. : Property Characterization of Light Silicate Ceramic Armors, U.S. Army Materials and Mechanics Research Center, Watertown, MA, U.S.A., AMMRC TR 76-19, 1976.

Shockey, D.A., Marchand, A.H., Skaggs, S.R., Cort, G.E., Burkett, M.W. & Parker, R. : Failure Phenomenology of Confined Ceramic Targets and Impacting Rods, Int. J. Impact Engng., Vol. 9, No. 3, pp. 263-275, 1990.

Slavin, M.J., Viechnicki, D.J. & Tracy, C.A. : Processing, Microstructure and Property Relationships of Armor Ceramics, U.S. Army Materials Technology Laboratory, Watertown, MA, U.S.A., 1988.

Swift, H.F. & Strange, D.E. : Analysis of Sabot Operation, Physics Applications Inc., Dayton, Ohio, U.S.A..

Swift, H.F. & Strange, D.E. : Sabot Discard Technology, Physics Applications Inc., Dayton, Ohio, U.S.A., 1987.

Tate, A. : A Theory for the Deceleration of Long Rods After Impact, J. Mech. Phys. Solids, Vol. 15, pp. 387-399, 1967.

Taussig Jr., J.K. : Breakthrough in Armor, Ordnance, p.71, July-August 1970.

Taussig Jr., J.K. : Ceramics for Defense, Ordnance, pp. 292-294, July-August 1970.

Timoshenko, S.P. & Goodier, J.N. : Theory of Elasticity, McGraw-Hill, ISBN 0-07-Y85805-5, 1932.

Townsend, D. & Field, J.E. : Investigation of the Impact Performance of Various Glass and Ceramic Systems, Cavendish Laboratory, Dept. of Physics, University of Cambridge, Cambridge, England, AD-A178 115, 1987.

Tracy, C., Slavin, M. & Viechnicki, D. : Ceramic Fracture during Ballistic Impact, Proceedings of Conference on Fractography of Glasses and Ceramics, Alfred University, New York, NY, U.S.A., 1986.

Verhagen, Th.L.A. : Determination of Fragment Mass Distributions in Absolute Units from Flash X-Ray Shadowgraphs with Digital Image Processing, Prins Maurits Laboratory, Rijswijk, The Netherlands, PML 1988-IN20, 1988.

Viechnicki, D., Blumenthal, W., Slavin, M., Tracy, C. & Skeele, H. : Armor Ceramics 1987, Proceedings of the Third TACOM Armor Coordinating Conference, 17-19 February 1987, Monterey, CA, Published by Battelle Columbus Division, Columbus, U.S.A., 1987.

White, M.P. : Impact Force of a Rigid-Plastic Missile, J. Appl. Mech., Vol. 51, pp. 102-106, 1984.

Wilkins, M.L., Honodel, C. & Sawle, D. : An Approach to the Study of Light Armor, Lawrence Radiation Laboratory, University of California, Livermore, CA, U.S.A., UCRL-50284, 1967.

Wilkins, M.L. : Second Progress Report on Light Armor Program, Lawrence Radiation Laboratory, University of California, Livermore, CA, U.S.A., UCRL-50349, 1967.

Wilkins, M.L. : Third Progress Report on Light Armor Program, Lawrence Radiation Laboratory, University of California, Livermore, CA, U.S.A., UCRL-50460, 1968.

Wilkins, M.L., Cline, C.F. & Honodel, C.A. : Fourth Progress Report on Light Armor Program, Lawrence Radiation Laboratory, University of California, Livermore, CA, U.S.A., UCRL-50694, 1969.

Wilkins, M.L., Landingham, R.L. & Honodel, C.A. : Fifth Progress Report on Light Armor Program, Lawrence Radiation Laboratory, University of California, Livermore, CA, U.S.A., UCRL-50980, 1971.

Wilkins, M.L. : Use of Boron Compounds in Lightweight Armor, in Boron and Refractory Borides, edited by V.I. Matkovich, Springer-Verlag, 1977.

Wilkins, M.L. : Mechanics of Penetration and Perforation, Int. J. Engng. Sci., Vol. 16, pp. 793-807, 1978.

Wilkins, M.L. : Personal Correspondance to P.C. den Reijer, 1988.

Wimmer, J.M., Bransky, I. & Tallan, N.M. : Impact Resistance of Structural Ceramics, Air Force Materials Laboratory, WPAFB, Ohio, U.S.A., AD-A037165, 1976.

Woidneck, C.P. : Keramikbeschichtete Metall- und Faserverstärkte Panzerungen, Deutch-Französisches Forchungsintitut Saint-Louis (ISL), Saint-Louis, France, ISL-S-CO-916/78, 1978.

Woodward, R.L. : A Simple One-Dimensional Approach to Modelling Ceramic Composite Armour Defeat, Int. J. Impact Engng., Vol. 9, No. 4, pp. 455-474, 1990.

Yatteau, J.D. : Improved Multiple Plate Penetration Model for Spin-Stabilized Projectiles, Laboratories for Applied Mechanics, Denver Research Institute, Denver, CO, U.S.A., 1985.

Zuidam, D-J.A. van : Een Onderzoek naar de Invloed van de Projectielgeometrie op de Penetratiecapaciteit in Keramische Pantsers, Koninklijke Militaire Academie, Breda, The Netherlands, 1990, in Dutch.

ACKNOWLEDGEMENT

The first three and a half years of this research were sponsored by the National Technology Project "Ballistisch Arall" which was initiated and led by AKZO Fibre and Polymers Division (New Business). The final phase of this research was sponsored by TNO Defence Research. Some international travelling of the author was sponsored by the Prof. Dr. Ir. J.M.J. Kooy-fund of the Royal Netherlands Institute of Engineers (K.I.V.I.).

The research presented in this thesis was conducted during the authors tenure at the Prins Maurits Laboratory TNO. The experimental work was carried out at TNO's Laboratory for Ballistics Research at Ypenburg Air-Force base.

The author thanks Prof. Dr. J. Arbocz and Dr. R.R. IJsselstein for their supervision during the past four and a half years of research. The staff of the Prins Maurits Laboratory, the members of the Ballistics section in particular, is thanked for its support, interest and contributions to this research.

SUMMARY

Ceramic faced armours can, when properly designed, significantly reduce the weight of classical ballistic protection as used for instance in armoured vehicles. This thesis presents a combination of theoretical and experimental work on the principal processes that give these armours their enormous protective properties.

The theoretical work described in this thesis has resulted in the development of a one-dimensional penetration model which simulates the response to the impact event of the projectile and the armour in an approximate manner. The penetration model accounts for: 1) mass erosion, mushrooming and rigid body behaviour of the projectile; 2) drag, confinement and bulking (dilatation) of the ceramic facing; 3) bending, shearing and stretching of the back-up plate.

The various comparisons of measured and calculated details of the penetration processes have shown that the model can reproduce the effects of variations of projectile and armour geometry and properties about a reference projectile and armour. Hence, the information on the characteristic phenomena associated with a specific impact event generated by the model presents the user with guide-lines for armour and projectile design optimization.

The experimental work was directed towards increasing the knowledge base and understanding of the mechanisms governing penetration into ceramic faced armours. For this purpose a novel experimental technique was developed that used flash radiography from several angles to visualize the projectile/armour interaction process at discrete moments in time throughout the impact event. The unique feature of this technique is that it does not require that the lateral dimensions of the armour panels used be reduced to such an extend that (unwanted) boundary effects influence the penetration process. This technique was used to visualize and study the projectile/armour interaction process of steel rod projectiles impacting alumina/aluminium armours. The effects of four different types of back-up plates and velocities above and below the armour's ballistic limit were investigated. The penetration processes of the 7.62 mm AP and 7.62 mm ball projectiles, which are often used in experiments with ceramic armours, were also visualized, analysed and discussed.

These experiments have resulted in an improved understanding of the projectile/armour and ceramic/back-up plate interaction mechanisms. On the basis of this understanding, a new phenomenological description of events that lead to the deterioration of the ceramic fracture conoid and the associated impact load concentration is proposed.

The improved understanding of the impact event, and the comparisons between the model predictions and the experimental results have also resulted in the identification of a number of areas within the penetration model where the description used may be improved. On the basis of this information, recommendations for modifications to the model are proposed. In order to further improve and extend the understanding of the projectile/armour interaction processes, and to aid the modelling efforts, recommendations for future experimental research are presented as well.

SAMENVATTING (summary in Dutch)

Keramische lichtgewichtpantsers kunnen wanneer zij goed ontworpen zijn, het gewicht van de ballistische bescherming zoals gebruikt in gepantserde voertuigen sterk verlagen. Dit proefschrift presenteert een combinatie van theoretisch en experimenteel onderzoek naar de voornaamste processen die deze pantsers hun bijzondere beschermende eigenschappen geven.

Het in dit proefschrift beschreven theoretische werk heeft geresulteerd in de ontwikkeling van een één-dimensionaal penetratiemodel, dat het gedrag van het projectiel en het pantser na inslag op een benaderende wijze beschrijft.

Het penetratiemodel houdt rekening met: 1) massa-erosie, paddestoelvorming en starlichaamgedrag van het projectiel; 2) weerstand, opsluiting en uitzetting (dilatatie) van de keramische toplaag; 3) buiging, afschuiving en rek van de achterlaag.

De vele vergelijkingen tussen gemeten en berekende details van de penetratieprocessen hebben laten zien dat het model in staat is om de invloed van variaties van de geometrie en eigenschappen van zowel het projectiel als het pantser om een referentiesituatie te reproduceren. De aldus door het model gegenereerde informatie met betrekking tot de bij het inslagfenomeen behorende karakteristieke verschijnselen kan ook door de ontwerper gebruikt worden om de richting te bepalen waarlangs de optimalisatie van projectiel of pantser het meest succesvol zal zijn.

Het experimentele onderzoek was gericht op het uitbreiden van de kennis en het begrip van de mechanismen die het penetratieproces in keramische lichtgewichtpantsers beheersen. Voor dit doel werd een nieuwe experimenteertechniek ontwikkeld die gebruik maakt van röntgenflitsfotografie uit verschillende richtingen om het projectiel/pantser interactieproces op discrete momenten in de tijd te visualiseren. Het bijzondere van deze techniek ligt in het feit dat de (zijdelingse) afmetingen van het pantser niet zodanig aangepast moeten worden, dat ongewenste randverschijnselen het penetratieproces kunnen beïnvloeden.

Deze techniek werd gebruikt om het penetratieproces van eenvoudige stalen staafprojectielen in aluminiumoxyde/aluminium pantsers te visualiseren en te bestuderen. Zowel de invloed van vier verschillende achterlagen als van inslagsnelheden boven en onder de ballistische limietsnelheid van het pantser werden bestudeerd.

De penetratieprocessen van de veel gebruikte 7.62 mm AP (pantserdoorborende) en 7.62 mm ball projectielen zijn ook gevisualiseerd, bestudeerd en beschreven.

De experimenten hebben geresulteerd in een verbeterd begrip van de interactiemechanismen tussen projectiel/pantser en toplaag/achterlaag. Op basis hiervan is een nieuwe fenomenologische beschrijving van het proces voorgesteld dat leidt tot de afbrokkeling van de keramiekkegel en inslag-belastingconcentratie op de achterlaag.

Het verbeterde begrip van het penetratieproces en de vergelijkingen tussen de modelberekeningen en de experimentele resultaten, hebben geleid tot de identificatie van een aantal plaatsen waar de gebruikte modelbeschrijving zou kunnen worden verbeterd. Uitgaande van deze informatie worden aanbevelingen voor modificaties aan het model voorgesteld. Teneinde het begrip van de projectiel/pantser interactieprocessen verder te verbeteren en te verbreden en het modelleerproces te ondersteunen zijn ook aanbevelingen voor experimenteel onderzoek opgesteld.

ABOUT THE AUTHOR

The author of this thesis was born in The Hague in The Netherlands on January 30, 1962. In 1980 he graduated with honours from the Atheneum of the Lodewijk Makeblijde College in Rijswijk, The Netherlands.
In the same year he started to study Aerospace Engineering at the Delft University of Technology in Delft, The Netherlands. In 1984 he joined the research group "Sterkte & Trillingen" (structural mechanics) under the supervision of Professor Dr. J. Arbocz. The author's engineering thesis was titled: *On the Buckling of Axially Compressed, Iso - or Orthotropic, Thin-walled, Circular Cylindrical Shells or An Attempt to Calculate Non-linear Mode Interactions*. He graduated with honours.
In 1987, while fulfilling his (mandatory) military service as a reserve officer (R.O.A.G.) of the Royal Netherlands Army, he was attached to the Ballistics section of the Prins Maurits Laboratory TNO. At that time he started his PhD-research on ceramic faced armours under the supervision of Professor Dr. J. Arbocz and Dr. R.R. IJsselstein. In 1989 he became a research scientist at the same institute and continued his work on ceramic faced armours. The results of that research are described in this thesis.